Lancaster University

Magnetospheric Plasma Dynamics: Investigating Ion and Electron Flow in the Magnetotail

by

Jonathan Doyle

A thesis submitted in partial fulfillment for the
degree of Doctor of Philosophy

in the

Space and Planetary Physics
Department of Physics

September 2019

Declaration of Authorship

I, Jonathan Doyle, declare that this thesis titled, 'Magnetospheric Plasma Dynamics: Investigating Ion and Electron Flow in the Magnetotail', and the work presented in it are my own. I confirm that:

- This work was done wholly or mainly while in candidature for a research degree at this University.
- Where any part of this thesis has previously been submitted for a degree or any other qualification at this University or any other institution, this has been clearly stated.
- Where I have consulted the published work of others, this is always clearly attributed.
- Where I have quoted from the work of others, the source is always given. With the exception of such quotations, this thesis is entirely my own work.
- I have acknowledged all main sources of help.
- Where the thesis is based on work done by myself jointly with others, I have made clear exactly what was done by others and what I have contributed myself.

Signed: _____

Date: _____

Magnetospheric Plasma Dynamics: Investigating Ion and Electron Flow in the Magnetotail

Jonathan Doyle

Abstract: An investigation was carried out using moment data from the Cluster CIS and PEACE instruments, examining earthward and tailward directed ion and electron flows within the terrestrial magnetotail. For a time interval spanning 2001-2006, the study looked at the distribution of ion bulk velocity vectors in the magnetotail, separating the region up into discreet slices in the XY plane, and later in the XZ plane. Key features of the ion velocity distribution and flow directions were uncovered, highlighting how ions behave within the magnetotail over large time periods and helping to form a greater understanding of the overall picture of the Earth's magnetosphere. The results found are in general agreement with a number of similar studies previously carried out on topic, and found that overall, the magnetosphere is a rather stagnant system.

An important mechanism in the terrestrial magnetosphere is the transportation of energy and momentum throughout the system. Magnetospheric substorms have been linked to much of this transportation and as such, the investigation in this thesis shifts the focus from the occurrence of plasma flow for all times, to just during substorm events, concentrating on the three substorm phases, the growth expansion and recovery phase. The duration of each phase is quite short, meaning that the amount of data available was somewhat limited. This led to the time interval used to be increased to 14 years. Observations of key differences in the velocity distributions and flow patterns between each substorm phase were made, and the dominant direction of ion flow was found, both at the equatorial plane and further out into the magnetospheric lobes.

The final investigation looked at how the data availability could be increased in order to improve the quality and reliability of the results. Following the frozen-in theorem, all charged particles are constrained to their local magnetic field lines and as such, they should all follow the same general flow pattern. An attempt was made to recreate the results of the first study instead using PEACE electron moments. If it was found to be possible, both data sets could be combined to greatly increase the resolution of the results. The electron velocity distribution was investigated and the dominant electron flow direction was found to be tailward within the plasma sheet, the opposite of ion flows. A further examination of the results was carried out to establish what could be causing tailward flow dominance in this region and in conclusion, it was decided that until a more in-depth investigation is carried out, PEACE electron moments are unsuitable for large time scale analysis of magnetospheric plasma flows.

Acknowledgements

I would like to thank the following people without whom the this thesis would not have been completed:

Prof. Jim Wild, for his guidance and support throughout the last six years, and for going out of his way to help me out in times of need; without him I would not have got very far. Also a huge thanks must go to Dr. Chris Arridge for showing his support and encouraging me to persevere, even when I thought all was lost. Thanks also to my past and present colleagues in the group: Gareth Dorrion, Neil Rogers, Paddy Cannon, Dave Hartley, Carl Bryers, Marianna Felici, Nathan Case, Carley Martin and Maria Walach for putting up with my stupid questions, providing insight into work and life, and being there to have a bloody good time at the pub. Also thanks to honorary SPP member Becky Case for the sublime Mars Bar cakes!

I would also like to thank my colleagues and friends; Hannah Laurens, for not only kicking my ass into gear throughout my undergraduate degree, but also providing invaluable moral support throughout my PhD, and being there for me, even when life wasn't always running smoothly. It's been an honour and a pleasure sharing the journey with her. Thanks must also go to Becky Gray for being such an outstanding friend, for being there to listen to me and providing Bounty chocolate bars when they were needed most. Also thanks to Joe Kinrade, he may have been a later addition to the team, but he provided such merriment, sophistication and whiskey to the group; also did you know he was from the Isle of Man?! I am proud to call all three of you my friends and I truly hope we remain so for many years to come.

Of course a huge thank you must go out to my family, and especially parents, whose support, encouragement and guidance went unparalleled. Thank you for always being there for me, through the good times and especially the bad times; without you, I don't know where I would be. Also, thank you for not making me get a real job. Also thanks to Sarah for putting up with me for almost 27 years! An extra thank you must also go to Aunty Heather for proof reading my thesis, not a job for the faint hearted, you did a fantastic job finding so many of my mistakes.

I would also like to thank my climbing crew: Matt Amos, Ben Cianchi, Aoife Marrett, Keelan Tootell, Dan Dry, Martin Paley, Dexter Williamson, Joe Fennell and Lizzy Goldsbrough for joining me on many a wonderful adventure and sharing the passion of the great outdoors with me. The combined influence of all of you have enhanced my life to no end and have changed my perspective on the world. I can only imagine what adventures we will find ourselves on in the future. In addition, I need to extend my thanks

to Conor Scrivener, Dr. Jenni Carter, Alex Pilling and Jonnie Critchley, for not only supporting me through university, but for being excellent friends and sharing many an evening sampling the finest ales Lancaster has to offer. Thanks to Dr. Chris Oldfield, for being a genuinely fantastic human being, going above and beyond to support me during my times of need; surely the best friend a person could ever ask for. Finally, a huge thank you to Tash for revolutionising my life, for showing me the way to becoming the person I want to be and for believing in me even when I did not believe in myself. Without you, I am certain I would not have made it out the other side.

Contents

List of Figures

List of Tables

This thesis is dedicated to Mum and Dad, and the memory of Kenneth Shaw (1929-2016) and John Dixon Doyle (1928-2016)

Chapter 1

Introduction and Background

1.1 Introduction

This thesis focuses on plasma flows within the terrestrial magnetosphere, specifically undertaking large scale analyses of plasma flow dynamics within the Magnetotail. The first investigation carried out was the observation of ion flows for all times between 2001 and 2006. This study was implemented to ensure the procedures utilised throughout the research produced results which generally agreed with previous plasma flow studies. The second investigation conducted was a study observing the average tailward and earthward ion flows during substorm events, focussing on the growth, expansion and recovery phases. The study took advantage of the Cluster spacecraft's broad spatial coverage within the Magnetotail, providing details on the plasma dynamics within the region. The final investigation carried out attempted to recreate the initial ion flow results using electron velocity moments. The inspiration for this final topic of research came from the realisation that the amount of data available for the substorm study was severely limited. If the electron moments could provide comparable results to the ion moments (using the assumption that both ions and electrons follow the frozen-in theorem), then the two data sets could be combined, greatly increasing the amount of data available. In turn, this would improve the spatial coverage, resolution and reliability of the results collected by future studies.

The first chapter is an overview of solar-terrestrial system, reviewing the space-plasma environment in which this thesis is set. The second chapter carries out a review of the motion and characteristics of plasma interacting with electromagnetic fields, and discussed the structure and behaviour of plasmas contained specifically within the terrestrial magnetosphere.

1.2 Solar-Terrestrial Physics: An Overview

1.2.1 The Sun, Solar Wind and Interplanetary Magnetic Field

The Sun is the largest body in the solar system, holding 99.86% of its mass with just 0.5% of its angular momentum (*Woolfson*, 2000). It is predominantly composed of Hydrogen (73.81%) and Helium (24.85%) (*Asplund et al.*, 2009) and is host to a very interesting phenomenon within the penultimate layer of the star, the chromosphere. The temperature at its outer boundary spikes by two orders of magnitude and following the equation of state, its density decreases proportionally. It is still unclear exactly what causes this phenomenon. From here, the temperature stabilises and remains around $1\text{x}10^6\,\text{K}$ across a few solar radii. This extremely hot solar region is called the corona and is the source of the solar wind (*Meyer-Vernet*, 2007).

The solar wind is a pressure-driven continuous stream of ionised plasma flowing radially out from the Corona. As the solar wind has a high electrical conductivity, the solar magnetic field is frozen into it and as a result, the field is dragged out into the solar system with the expansion of the solar wind. This magnetic field is called the Interplanetary Magnetic Field[1] (IMF) and directly connects the Sun to the Earth (*Owens and Forsyth*, 2013). The IMF does not exhibit a radial configuration throughout the solar system, in fact it is perturbed by the rotation of the Sun. Through the frozen-in theory (see section 2.4.3), the IMF slowly winds around the sun as it rotates, creating an archimedean spiral configuration often called the Parker Spiral (Figure 1.1) (*Parker*, 1958). The solar wind flow-speed falls into two categories, slow and fast streams with velocities of 300-450 $\text{km}\,\text{s}^{-1}$ and 600-900 $\text{km}\,\text{s}^{-1}$ respectively (*Phillips et al.*, 1995). Near the Earth, electron density is often measured to be around $n_e \approx 5\,\text{cm}^{-3}$ and temperature to be of the order $10^5\,\text{K}$ (*Baumjohann and Treumann*, 1997). The solar wind extends throughout the solar system and terminates at the heliopause where it eventually merges with the interstellar medium.

1.3 The Terrestrial Magnetosphere

Earth's magnetic field can be approximated to the first order as a magnetic dipole, not dissimilar to a bar magnet. It is tilted by about 11° from the Earth's rotational axis with its north pole currently located on Ellesmere Island in northern Canada. The magnetic field is orientated such that in the northern hemisphere, it is directed towards the Earth and in the southern hemisphere, it is directed away from the Earth.

[1] The IMF is also known as the Heliospheric Magnetic Field.

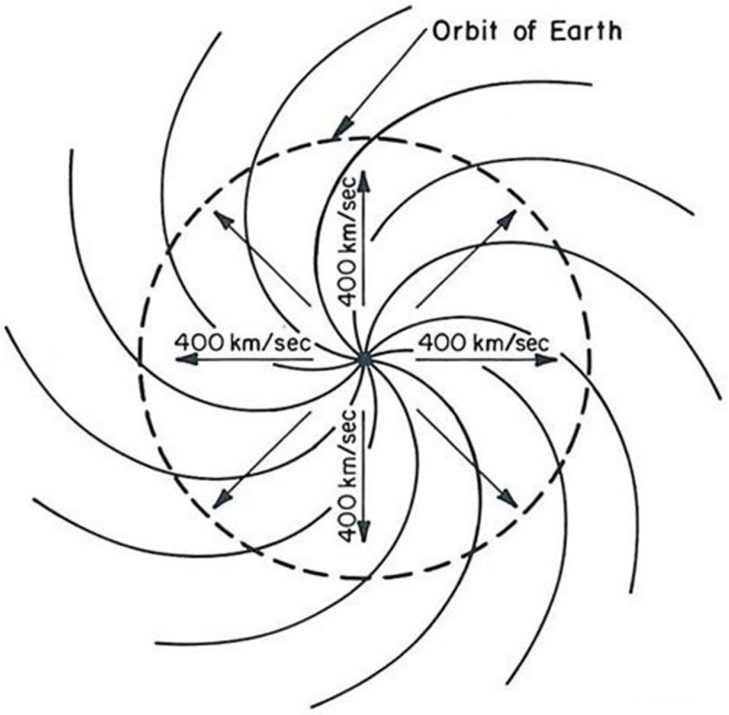

FIGURE 1.1: The Parker Spiral. The configuration of the IMF in the solar-equatorial plane due to the rotation of the Sun. Adapted from *Parker*, 1963.

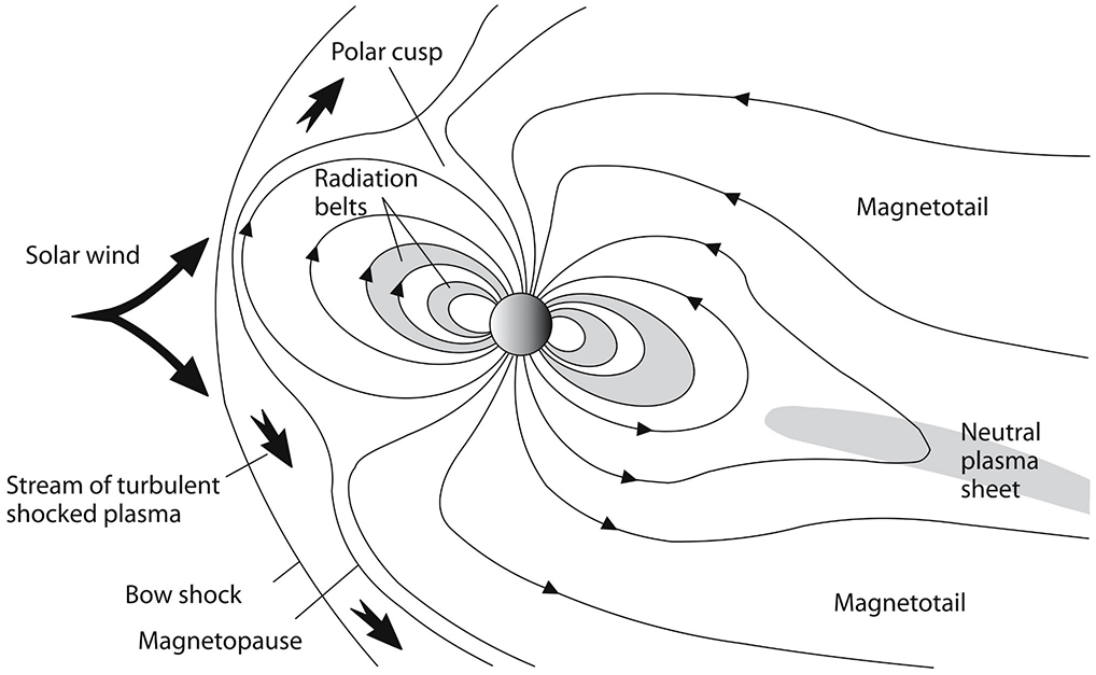

FIGURE 1.2: A schematic of the Earth's magnetosphere looking at the noon-midnight meridian plane, *Narinder*, 2016

As the solar wind meets the Earth, its magnetic field acts as a barrier to the solar wind (*Chapman and Ferraro*, 1931a), effectively deflecting it around the planet. This interaction creates a cavity in which the Earth's magnetic field dominates over the IMF and this cavity is known as the magnetosphere (Figure 1.2). The ram pressure of the solar wind compresses the dayside magnetosphere and its tangential component (acting along the magnetopause) stretches the nightside into a shape reminiscent of a tear-drop. As the solar wind (moving at supersonic speeds) reaches the Earth and interacts with the magnetosphere, it is decelerated to subsonic speeds and a shock, know as the **bowshock** is created upstream. At this point, the density of the region increases as the solar wind plasma piles up and the temperature also increases as much of the solar wind's kinetic energy is converted into thermal energy. This shocked, dense and hot region is known as the **magnetosheath** and the boundary between this and the magnetosphere is the **magnetopause**. The frozen-in theory (see section 2.4.3) states that plasma of different origins cannot mix, meaning that solar wind plasma and magnetospheric plasma may never populate the same region at the same time. This is often described as the closed magnetospheric system.

1.3.1 The Magnetotail Configuration

The Magnetotail is situated on the nightside of the Earth and stretches out approximately $1000\,\mathrm{R}_e$ (*Dungey*, 1965) and is a region of great importance as it stores a great deal of the magnetospheric system's plasma and energy. A typical radius of the Magnetotail has been estimated to be around $29\,\mathrm{R}_e$ (*Corontini and Kennel*, 1972), see Figure 1.2.

1.3.2 The Plasma Sheet

The plasma sheet (Figure 1.2) occupies the majority of the closed[2] region of the magnetosphere and is made of two parts, the central plasma sheet and the plasma sheet boundary layer. At its centre is the central plasma sheet, an area with generally isotropic ion and electron distributions. The region is largely thought to be more densely populated (0.1-$1\,\mathrm{cm}^{-3}$) with ions having bulk-flow energies in the keV range and relatively low plasma-flow velocities. The plasma sheet boundary layer predominantly sits on closed field lines although it is commonly seen as the transition region between the central plasma sheet and the magnetospheric tail lobes. It is a region of high flow velocities, often of the order of hundreds of kilometres per second. The plasma density is often a little lower, with values around $0.1\,\mathrm{cm}^{-3}$.

[2] A closed region or field line is one which is connected to one magnetic field source at both ends.

1.3.3 The Tail Lobes

The magnetospheric tail lobes occupy the regions either side of the plasma sheet (Figure 1.2) and lie on open[3] magnetic field lines. They are populated with cold plasma flowing away from the Earth and they are regions of very low density plasma, often much lower than 0.1 cm^{-3}, making it difficult to take reliable plasma measurements. (*Kivelson and Russell*, 1995; *Eastman et al.*, 1984).

1.4 The Ionosphere

The Ionosphere is a region of cold dense plasma occupying the area between altitudes of 60-600 km embedded within the neutral atmosphere. Incident solar radiation leads to the creation of this region through photo-ionisation and impact-ionisation. As a result, it is predominantly an ionised medium home to charged ions and free electrons, and many neutral particles too. Particle recombination is also prevalent in this region, creating new neutral particles. While this process is dominant at night when photo-ionisation is not present, on average, the rate of ionisation is greater than or equal to that of recombination and thus, a permanently ionised plasma is maintained. The electrodynamic system of the ionosphere is also very different from the completely neutral atmosphere. When neutral particles collide with drifting charged particles, they alter their trajectory, which can often lead to charge separation, resulting in the creation of new current systems within the region (discussed further in section 2.2.2).

The Ionosphere is in fact not a uniform region (Figure 1.3), it is split up into separate layers based upon factors such as the rate of ion production, loss and recombination. The Ionosphere varies with altitude because the layers are independently produced through the absorption of solar radiation by the variety of neutral particle species spread throughout the region. The different neutral particles respond differently to incident photons of different energies, meaning altitude as well as plasma density play a significant role in how the Ionosphere is populated. There is an altitude at which maximal ion production is achieved for the various ion species, these layers are known as Chapman layers. In reality, the Chapman layer theory falls short, for example, it cannot describe the major peak in the F-layer as it only considers recombination and does not account for other important chemical processes which also occur. (*Baumjohann and Treumann*, 1997).

[3] An open magnetic field line is one connected to the terrestrial magnetic field at one end and the solar wind magnetic field at the other.

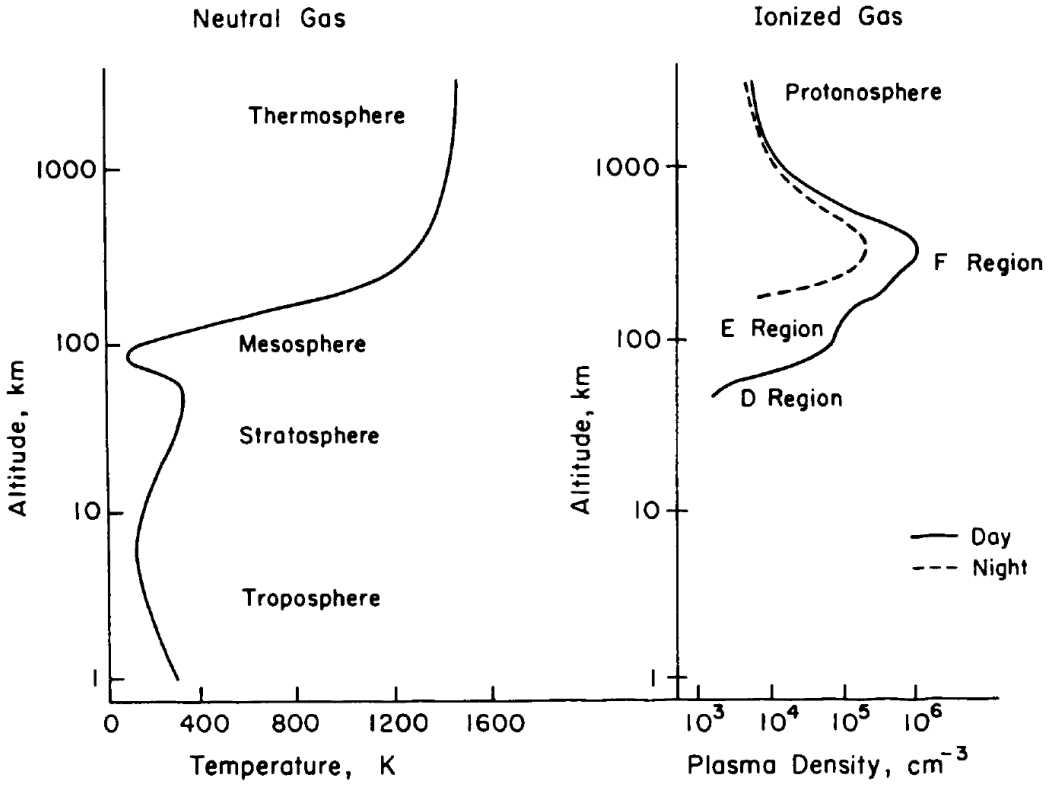

FIGURE 1.3: Profiles of neutral atmospheric temperature and ionospheric plasma density indicating the layered structure of the region. (from *Chen* (2012))

1.5 Summary

As the solar wind flows out from the Sun, it carries with it the interplanetary magnetic field out into the solar system. When the solar wind reaches the Earth, its magnetic field stands in its way and as such, the solar wind must flow around it. The cavity which the terrestrial magnetic field creates is known as the magnetosphere and contained within it is a complicated dynamical system of plasma flows, currents and electric fields. At lower altitudes, the Earth's atmosphere is partially ionised by solar radiation to create the Ionosphere. The dynamics of the magnetosphere will be further discussed in the following chapter.

Chapter 2

Fundamentals of Magnetospheric Dynamics

2.1 The Concepts of Plasma Physics

Plasma is a fundamental state of matter, just as a solid, liquid or gas is. It exists in the form of an ionised gas whereby its electrons and ions have become disassociated from their pre-existing atomic structure. However, not all ionised gasses may be classed as a plasma.

It is possible for plasma to exhibit a net charge across small scales as the freely-charged particles are not always evenly distributed throughout the body of matter. However, on a large scale, it is observed as neutrally charged because the charges of the constituent positive ions and negative electrons cancel each other out.

Every charged particle exhibits an electric field and if it is moving, it also exerts a magnetic field. When a group of charged particles are moving together, their fields can combine to create a single much stronger one. In order for a particle to feel the influence of such large scale magnetic fields, it must be free, meaning that it's not influenced by its neighbouring particles and as a result, must also remain collision-free, which means the charged particles are predominantly constrained to a particular magnetic field line.

In order for a gas to be defined as a plasma, it must satisfy four criteria: it must appear to be neutral across large scales, consist of free, charged particles, remain collisionless and exhibit collective behaviour (although some collisional plasmas do occur in solar physics). For a plasma to be net neutral, it must have roughly equal positive and negative charges per volume element. Each charge in a volume shielded from other nearby charges. When considering a Debye sphere about a charged particle, its radius

is given by the Debye length (equation 2.1); beyond this region, the charged particles are screened from each other. From this, it can be seen that in order for a plasma to remain quasi-neutral and as such be classified as a plasma, the physical dimensions of the system must be much greater then the Debye length. If this is not the case, there is not enough space for collective shielding to occur and thus the system is just classed as an ionised gas. This is called the first plasma parameter. The second plasma parameter says that there must be enough particles within the Debye sphere for collection shielding to occur; if there are not enough, neutrality cannot occur.

$$\lambda_D = \left(\frac{\epsilon_0 k_B T_e}{n_e e^2} \right)^{\frac{1}{2}} \tag{2.1}$$

Where it is assumed $n_e \approx n_i$ and $T_e \approx T_i$ (*Baumjohann and Treumann*, 1997).

2.1.1 Maxwell's Equations

Electromagnetic fields play a fundamental role in plasma-transport and behaviour within the Earth's magnetosphere. Maxwell's equations describe how these electric and magnetic fields, **E** and **B** respectively, interact with the charged particles which make up the plasma.

$$\nabla \cdot \mathbf{E} = \frac{\rho_q}{\epsilon_0} \qquad \text{Gauss' Law for electricity} \tag{2.2}$$

$$\nabla \cdot \mathbf{B} = 0 \qquad \text{Gauss' Law for magnetism} \tag{2.3}$$

$$\nabla \times \mathbf{E} = -\frac{\partial \mathbf{B}}{\partial t} \qquad \text{Faraday's Law} \tag{2.4}$$

$$\nabla \times \mathbf{B} = \mu_0 \mathbf{j} + \epsilon_0 \mu_0 \frac{\partial \mathbf{E}}{\partial t} \qquad \text{Ampère-Maxwell's Law} \tag{2.5}$$

Equations 2.2 and 2.3 describe the sources of the electric and magnetic fields. **Gauss' Law for electricity**, equation 2.2, states that the source of the electric field is the charge density, ρ_q, which is the difference between ion and electron density, and ϵ_0 is the permittivity of free space in a vacuum. **Gauss' Law for magnetism**, equation 2.3, states that there are no sources of magnetic fields, meaning that all magnetic fields

should form closed systems, meaning they no longer possess north and south poles. This law is also known as the '**No Monopoles Law**'.

Equations 2.4 and 2.5 show that electric and magnetic fields are intrinsically connected in that they are coupled by their spatial and temporal variations. **Faraday's Law**, equation 2.4, describes how the spatial variation of the electric field induce a temporal change in the magnetic field. **Ampère-Maxwell's Law** describes how a temporally varying electric field induces a magnetic field with **j** being the electric current density, (*Griffiths*, 2013).

2.2 Magnetospheric Current Systems

Magnetospheric plasmas move under the influence of external forces and interactions. Charged particles can move together in the same direction (such as in the solar wind) as well as in opposite directions, and following the assumption that frozen-in-flow applies (see section 2.4.3), they also convect with the Earth's magnetic field. In general the relative motion of the charged particles can often give rise to electric currents. These currents are integral to magnetospheric dynamics as they play a key role in the transportation of charge, mass, momentum and energy. The motion of charged particles (currents) can lead to the creation of new magnetic fields (Figure 2.1) which interact with the pre-existing magnetic field structure, resulting in a rearrangement of the field-geometry. Current sheets also separate oppositely directed magnetic fields and therefore are important in the identification of region boundary crossings.

2.2.1 Current Sheet Creation

Moving positively-charged ions create electric currents along their direction of motion and magnetic fields are created as a result(Figure 2.1). When many charged particles are travelling together, they can be treated as a current element and as such, the total magnetic field at a distance of r from the current element can be calculated by the **Law of Biot and Savart**:

$$\mathbf{B} = \frac{\mu_0}{4\pi} \int \frac{I d\mathbf{l} \times \hat{\mathbf{r}}}{r^2} \qquad (2.6)$$

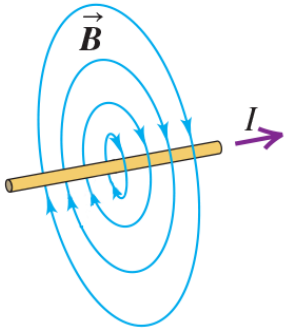

FIGURE 2.1: Magnetic field created by a moving electric field (*Young et al.*, 2012).

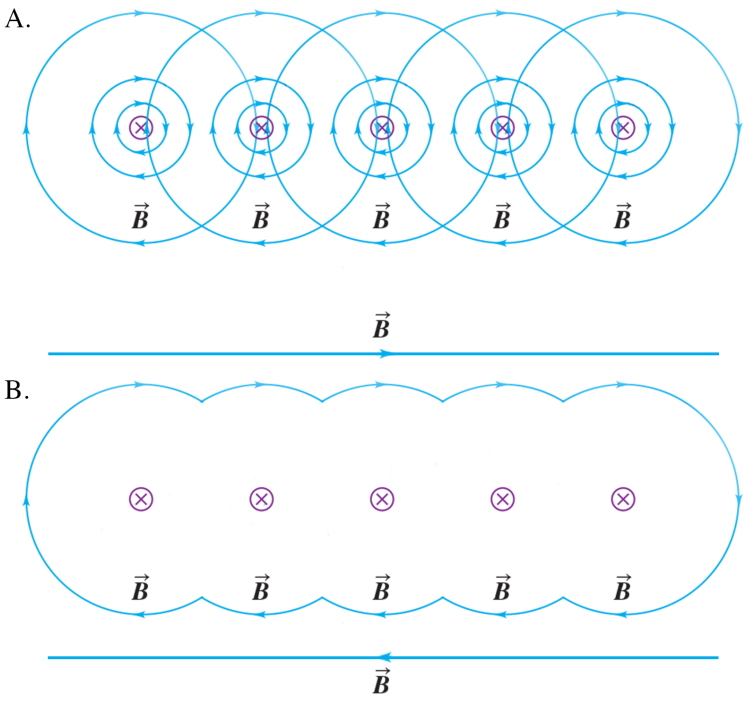

FIGURE 2.2: Multiple current line-elements in close proximity forming a current sheet with the electric current directed into the page. Adapted from *Young et al.* (2012).

where I is the current in the element, d**l** and $\hat{\mathbf{r}}$ is the unit vector (equal to the vector from the current element to the field point divided by its magnitude: $\hat{\mathbf{r}} = \mathbf{r}/\mathrm{r}$).

Figure 2.2A illustrates the set-up of multiple current line-elements in close proximity to each other. Note that the orientation of the closed magnetic field loops follow the **right hand grip rule** and thus as the electric current is directed into the page, the magnetic field is orientated in a clockwise direction. It is clear that each electric current element's associated magnetic field line crosses over with its neighbours'; since oppositely directed magnetic field lines cancel out, there is a rearrangement of the magnetic field line topography as seen in 2.2B. The magnetic field lines have combined to create a single field still orientated in the clockwise direction, and at the centre, the current line-elements have formed a line of current known as a **current sheet**.

2.2.2 Currents in the Terrestrial Magnetosphere

Current systems are prevalent throughout the terrestrial magnetosphere and play an important role in the transportation of charge, mass, momentum and energy, Figure 2.3.

As the solar wind comes into contact with the Earth's magnetic field at the magnetopause boundary, a gradient in the magnetic field system can be formed due the IMF being

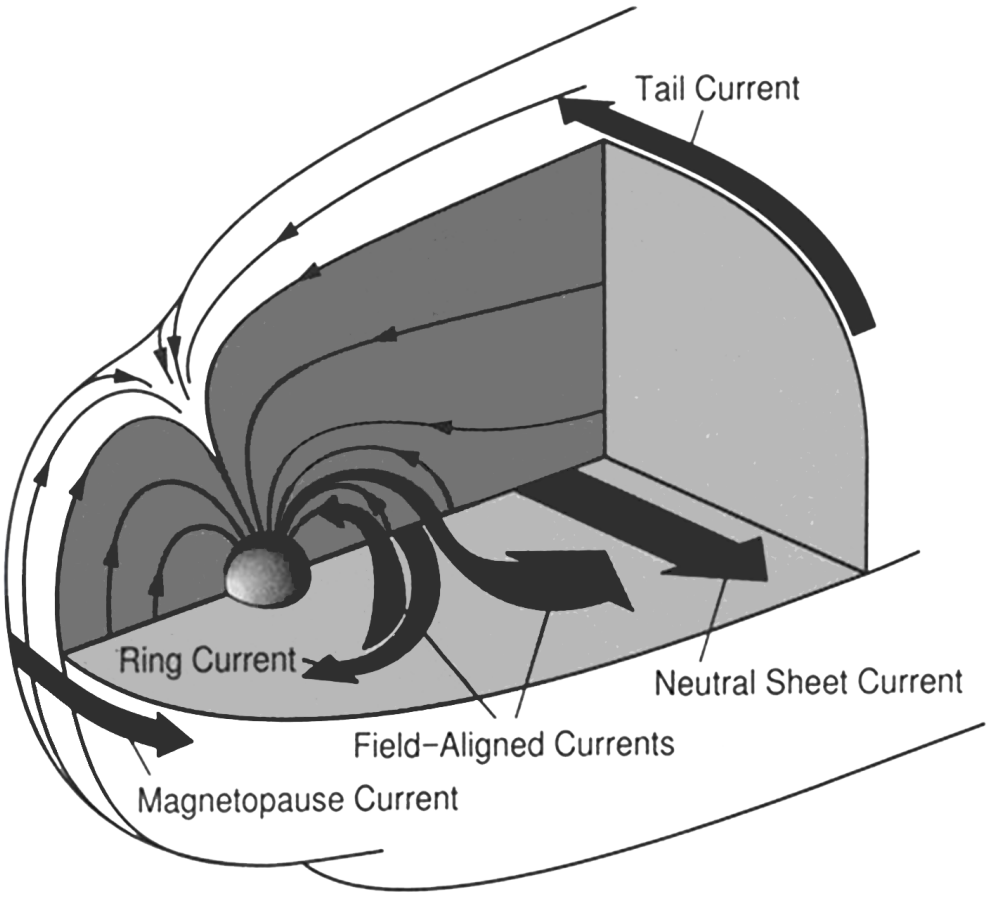

FIGURE 2.3: Schematic of magnetospheric current systems, *Baumjohann and Treumann* (1997).

predominantly directed southward and the terrestrial magnetic field directed northward. Looking at Ampere's law (equation 2.5) and using the right-hand-curl rule, it is clear that this system generates a duskward directed current at the most sunward position (the west-side of the Earth when looking along the Earth-Sun line).

In addition to this there is another current system which flows along the magnetopause in a single sheet, forming a boundary between the magnetic fields of the Earth and solar wind. When solar wind particles meet the Earths magnetic field, the Lorentz force bends them from their path. Since the particles are coming from the Sun and the direction of the Earths field is directed northward, the incident particle gyration (ions gyrate in a left-handed sense around a magnetic field and electrons in a right-handed sense) creates an electric current eastward in the equatorial plane. The field of this current decreases the Earths field outside the boundary and increases it inside. The current then occupies a thin sheet everywhere on the dayside of the Earth. This current sheet is known as the magnetopause current, or the Chapman-Ferraro current (*Chapman*, 1918; *Chapman and Ferraro*, 1930, 1931b).

In addition to these dayside currents, large-scale current systems also exist within the magnetotail (see Figure 2.3). The first of these, the tail-current, is generated by magnetic field gradients in the tail, causing a dawnward current flow across the magnetotail along the magnetopause. The tail-current is connected with the neutral-sheet current, situated within the plasma sheet and directed in the duskward direction, as seen in Figure 2.3. Together these two current sheets form a closed θ-shaped system. The neutral sheet current also acts to separate the earthward and tailward directed magnetic fields in the northern and southern hemispheres respectively. Figure 2.2B shows a schematic of how this field separation occurs and it is clear that a current sheet must always be present between two oppositely directed magnetic fields.

Another important current system is the ring current, situated within the inner magnetosphere. The ring current is made up of hot electrons and ions drifting about the Earth (via curvature drift, which is discussed in section 2.3.5) in opposite directions. This motion creates a charge differential which gives rise to the westward-directed ring current.

As well as the perpendicular currents systems, there are also currents sheets which are directed along the field lines. These are the field-aligned currents, often called **Birkeland currents** (*Birkeland*, 1908) and are split into two regions, region 1 and region 2, Figure 2.4. Region 1 describes the high latitude portion of the field aligned current system and is associated with the distant boundaries of the plasma sheet. Region 2 describes the lower latitude portion of the field aligned current system and close with the low latitude ring currents. These current systems are formed as a direct response to the stress exerted on the magnetosphere by the solar wind and are integral for the exchange of energy and momentum into the ionosphere and upper atmosphere as well as between the ionosphere and magnetosphere. It must be noted that there are two ionospheric current systems which are driven by Birkeland currents, the high latitude horizontal Pedersen and Hall currents which flow in response to the electric fields created by magnetosphere-ionosphere coupling. The former is formed by ions flowing along the electric field, and the latter is the horizontal current associated with the transverse convective flows driven by $\mathbf{E} \times \mathbf{B}$ drift, seen in Figure 2.4, (*Kamide*, 1982; *Baumjohann and Treumann*, 1997; *Le et al.*, 2010).

2.3 Single Particle Motion

The equation of motion for a single charged particle of charge q in an electromagnetic field is given by:

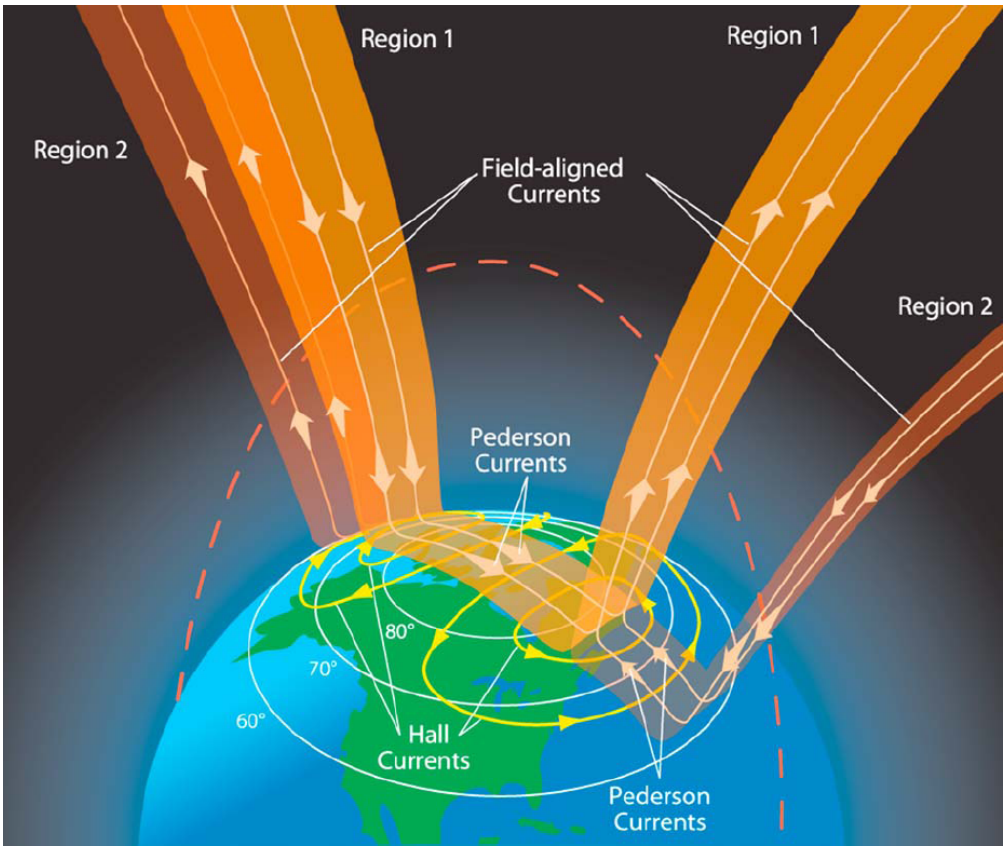

FIGURE 2.4: Schematic of field aligned and ionospheric current systems, *Le et al.*, 2010.

$$m\frac{d\mathbf{v}}{dt} = q(\mathbf{E} + \mathbf{v} \times \mathbf{B}) \tag{2.7}$$

where m is the particle's mass, $\frac{d\mathbf{v}}{dt}$ is the rate of change of velocity, $\mathbf{v}$, of the particle, $\mathbf{E}$ the electric field and $\mathbf{B}$ is the magnetic field exerted on the system. The electromagnetic force is predominantly the dominant force acting on an individual particle, with the effect of other forces often being negligible (except for in regions such as the solar corona or planetary ionospheres). Equation 2.7 is a combination of the Coulomb and Lorenz force and is the source of motion a single particle can experience while under the influence of electric and magnetic fields (*Baumjohann and Treumann*, 1997).

2.3.1 Gyromotion

Neglecting the electric field for the time being, a charged particle under the influence of a uniform magnetic field will experience an electromagnetic force perpendicular to both $\mathbf{B}$ and $\mathbf{v}$. This is a centripetal force and as such, it causes a charged particle to follow a circular trajectory (assuming there is no velocity component parallel to the magnetic field line) about a magnetic field line with speed, $v_\perp$, in the perpendicular direction to $\mathbf{B}$,

Figure 2.5. The direction of gyration is dependant on the charge of the particle, meaning that a positively charged particle will gyrate in the opposite direction to a negatively charged particle.

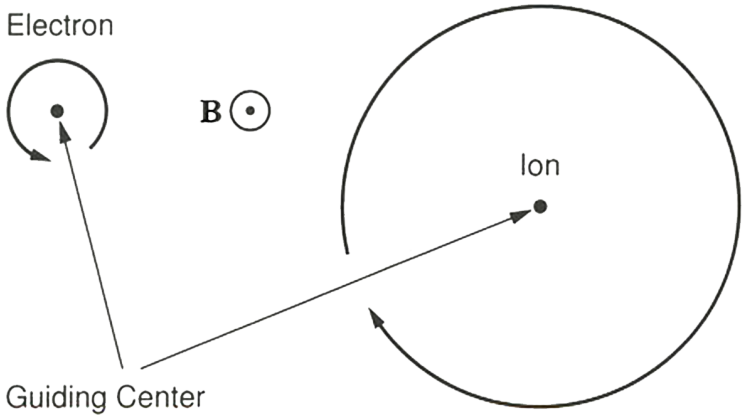

FIGURE 2.5: Gyration of a charged particle about a guiding centre with only a perpendicular velocity component. From *Baumjohann and Treumann* (1997).

Solving equation 2.7 for a non-varying magnetic field and no electric field, the gyrofrequency of the charged particle can be found. This is the angular frequency at which the particle gyrates about the magnetic field line and is given by:

$$\omega_g = \frac{qB}{m} \tag{2.8}$$

From equation 2.8, it can be seen that particles experiencing stronger magnetic fields will have a higher gyrofrequency, as will lighter particles.

The radius of gyromotion is governed by the particle's perpendicular velocity and its gyrofrequency and is given by:

$$r_g = \frac{v_\perp}{|\omega_g|} = \frac{mv_\perp}{|q|B} \tag{2.9}$$

It is clear that more massive particles experiencing a large magnetic field will have larger gyroradii, for example, in the solar wind (where $\mathbf{B} \sim 5\,\mathrm{nT}$ and $\mathrm{E}_k \sim 10\,\mathrm{eV}$, where E_k is kinetic energy), electrons experience a typical gyroradii of about 2 km whereas ions typically experience gyroradii of the order of 100 km. In the terrestrial magnetospheric environment (where $\mathbf{B} \sim 100\,\mathrm{nT}$ and $\mathrm{E}_k \sim 1\,\mathrm{keV}$), it can be seen from equations 2.8 and 2.9 that electrons will have a much higher gyroperiod ($\sim$ 18,000 $\mathrm{rad\,s^{-1}}$), but a smaller gyroradius ($\sim 1\,\mathrm{km}$) than ions ($\sim 10\,\mathrm{rad\,s^{-1}}$ and $\sim 50\,\mathrm{km}$ respectively) under the influence of the same magnetic field. Finally, in the ionosphere (where $\mathbf{B} \sim 50{,}000\,\mathrm{nT}$ and

kinetic energy $\sim 0.1\,\text{eV}$), electrons typically have a gyroradii of $\sim 2{\times}10^{-5}\,\text{km}$ whereas protons (atomic oxygen) have a gyroradii of $\sim 0.004\,\text{km}$.

2.3.1.1 Pitch Angle

When a constant parallel velocity component is introduced, a charged particle will travel along the magnetic field line following a helical trajectory, Figure 2.6.

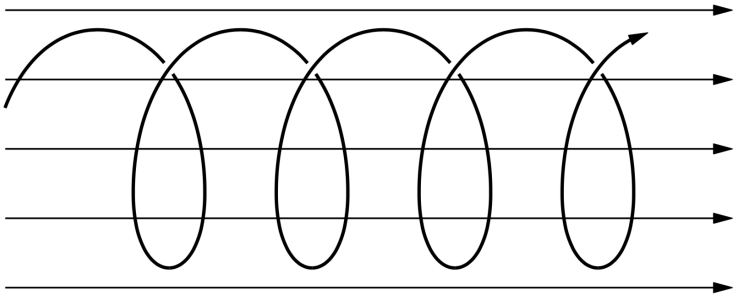

FIGURE 2.6: Helical trajectory of a charged particle with parallel and perpendicular velocity components. From *Baumjohann and Treumann* (1997).

The angle between the particle velocity vector and the magnetic field vector, **B**, is defined as the pitch angle (*Farley and Sanders*, 1962), α and is given by:

$$\alpha = \tan^{-1}\left(\frac{v_\perp}{v_\parallel}\right) \tag{2.10}$$

It is clear that pitch angle is dependent on the ratio of parallel and perpendicular velocities.

2.3.2 Magnetic Mirroring and Bounce Motion

While still considering the absence of any electric field, charged particles experience another form of motion when under the influence of a spatially varying magnetic field, magnetic mirroring.

Consider the guiding centre (the point around which a particle gyrates) travelling along a magnetic field line within a non-uniform magnetic field, by observing its magnetic moment:

$$\mu = \frac{mv_\perp^2}{2B} = \frac{mv^2 sin^2\alpha}{2B} \tag{2.11}$$

The magnetic moment is an adiabatic invariant, meaning that it can be treated as a constant as long as the magnetic field varies slowly in time compared to the gyrofrequency.

Note that a particle's total energy is a constant of motion. This can be shown by taking the scalar product of equation 2.7 with **v**:

$$m\frac{d\mathbf{v}}{dt}\cdot\mathbf{v} = q\mathbf{v}\cdot(\mathbf{v}\times\mathbf{B}) = 0 \tag{2.12}$$

The right side of the equation is equal to zero because **v** is perpendicular to **v** x **B**.

$$m\frac{d\mathbf{v}}{dt}\cdot\mathbf{v} = m\frac{d}{dt}\left(\frac{1}{2}\mathbf{v}\cdot\mathbf{v}\right) = \frac{d}{dt}\left(\frac{1}{2}mv^2\right) = 0 \tag{2.13}$$

Equation 2.13 shows that in a spatially varying magnetic field, the kinetic energy of a particle does not change with respect to time and therefore its total speed remains constant along its trajectory. This occurs because the force acting on the particle is perpendicular to **v** and therefore there is no work being done on the particle in the direction of motion.

In order to describe magnetic mirroring, it is important to understand how the force on a dipole magnetic moment can be used to describe how gradients in magnetic field strength in the direction of **B** affect particle motion.

$$\mathbf{F} = -\mu\frac{d\mathbf{B}}{dz} \tag{2.14}$$

It can be seen from equation 2.14 that the force, **F** is always directed along the magnetic field and away from the direction of increasing strength.

Consider a converging magnetic field geometry, Figure 2.7: as the magnetic field lines draw closer to each other, the overall magnetic field strength increases. Applying the knowledge that a particle's speed remains constant along its trajectory to equation 2.11, it is clear that when the magnetic field changes, only the pitch angle, α, can change with it. So as a charged particle enters a region of increased magnetic field strength, the pitch angle increases to account for this. Looking at equation 2.10 , in order for this to occur, $v_\perp$ must increase with $v_\parallel$ decreasing so that overall speed remains constant. Eventually, the pitch angle will reach 90°, at which point $v_\parallel = 0$ and the parallel component of the force on a dipole magnetic moment (from equation 2.14) starts the particle moving back in the direction it originally came from. This is magnetic mirroring.

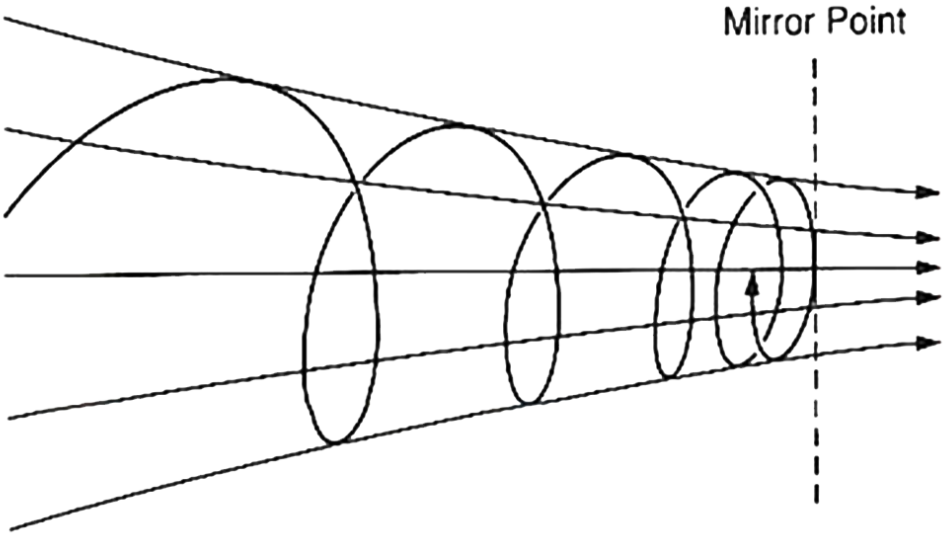

FIGURE 2.7: Ion orbit and reflection in a converging magnetic field (*Baumjohann and Treumann*, 1997)

Finally, because the magnetic moment is the first adiabatic invariant and a particle's speed remains constant in the direction of the magnetic field (from equation 2.13), a particle's pitch angle can be calculated at a specific location by taking the ratio of the field strengths of the particle's position and at its mirror point:

$$B_m = \frac{B}{sin^2\alpha} \tag{2.15}$$

Assuming the Earth dipole field follows a symmetrical magnetic field geometry (although technically the Earth Field isn't exactly symmetrical), avoiding collision a particle can become trapped between two mirror points, leading to the phenomena of magnetic mirroring, or bounce motion as it is sometimes called.

2.3.3 E × B Drift

Consider a charged particle in the presence of a constant electric and magnetic field, when looking for solutions to equation 2.7, the perpendicular and parallel components of **E** can be treated separately with respect to **B**. The parallel component, equation 2.16, describes the acceleration of a particle along a magnetic field line.

$$m\frac{dv_\parallel}{dt} = qE_\parallel \tag{2.16}$$

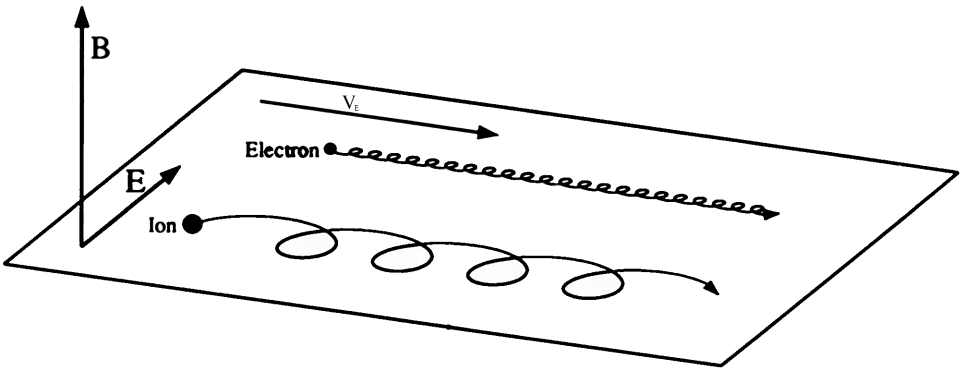

FIGURE 2.8: A schematic showing $\mathbf{E} \times \mathbf{B}$ drift, the motion of electrons and ions in a uniform magnetic field in the presence of a uniform electric field perpendicular to $\mathbf{B}$ (*Baumjohann and Treumann*, 1997)

However, in geophysical plasmas, such as in the magnetosphere, most parallel electric fields cannot be maintained electrons and ions move under the influence of the electric fields, and as such, they are cancelled out by the electric fields created by the ions and electron motion. As a result of this, it is possible to assume that $E_{\parallel}$ vanishes and therefore the electric field only acts in the perpendicular direction to $\mathbf{B}$ (*Baumjohann and Treumann*, 1997).

Now consider the effect a perpendicular electric field (however $\mathbf{E}$ does not need to be exclusively perpendicular to $\mathbf{B}$, it just needs a component in that direction) has on the motion of charged particles. The magnetic field force instigates gyration of charged particles. When an electric field is applied perpendicular to the direction of the magnetic field, illustrated in Figure 2.8, further forces are added in to the system. The force due to the electric field acts in the direction of $\mathbf{E}$ (from equation 2.7) and thus for half of a particle's orbit, it is accelerated, meaning that its gyroradius is increased, and for the other half of the orbit, the particle is decelerated, reducing its gyroradius. This motion distorts the particle's orbit and over a number of orbits, leads to the motion of the particle's guiding centre perpendicular to the field line, and thus particle drift occurs. This motion is often referred to as $\mathbf{E} \times \mathbf{B}$ drift and the particles drift velocity, $\mathbf{V}_E$ can be shown as:

$$\mathbf{V}_E = \frac{\mathbf{E} \times \mathbf{B}}{B^2} \tag{2.17}$$

It can be seen from equation 2.17 that $\mathbf{V}_E$ is independent of charge and particle energy, hence when the magnetic field is uniform and straight, ions and electrons drift with the same velocity as the magnetic field, as depicted in Figure 2.8.

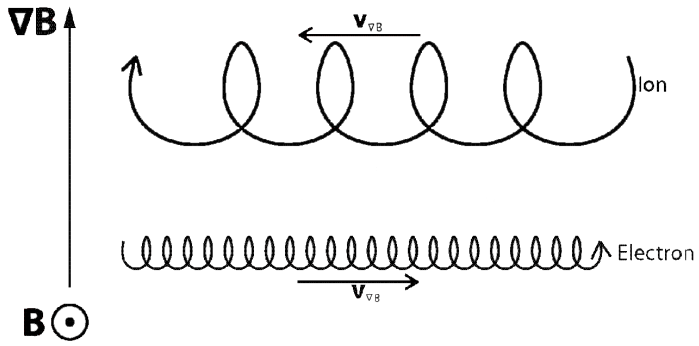

FIGURE 2.9: Illustration of an ion and electron drifting due to a gradient in the magnetic field perpendicular to the magnetic field direction. Adapted from *Baumjohann and Treumann* (1997).

2.3.4 Gradient Drift

As a charged particle gyrates, it will encounter regions of varying magnetic field strength. Looking at equation 2.9, when this occurs, its gyroradius will decrease in the upward direction (when considering a magnetic field system as seen in Figure 2.9). As a result of this effect, the upper half of the gyroradius will be smaller than the lower half. As a result of this imbalance, the guiding centre of the particle's gyroradius is displaced perpendicularly to both ∇B and $\boldsymbol{B}$, translating into a drift of the particle, as seen in Figure 2.9. This drift motion is referred to as the gradient drift and its velocity is given by:

$$V_{\nabla B} = \frac{mv_{\perp}^2}{2qB^3}(\mathbf{B} \times \nabla B) \tag{2.18}$$

From equation 2.18, it can be seen that the direction of the drift is charge dependent, meaning that ions and electrons drift in opposite directions perpendicular to the direction to both the direction of magnetic field and the magnetic field gradient. This drift motion also gives rise to currents in the perpendicular direction caused by the relative motion of the particles. The amount of drift which occurs is proportional to ∇B, so if this value is zero, there will be no drift, whereas drift will become much more prominent which a large change in magnetic field across a smaller distance. It is also shown by equation 2.18 that the gradient drift velocity is proportional to the perpendicular kinetic energy, meaning more-energetic particles experience a greater drift velocity. This is because more energetic particles have a larger gyroradius (equation 2.9) and therefore experience a greater difference between the maximum and minimum field strength, thus their drift will be increased. An important implication of gradient drift is that if a magnetic field line is initially associated with a collection of gyrating particles, over time the particles

will drift off the initial magnetic field line, leading to the mixing of plasma and as a result, a breakdown of the frozen-in flux theory (more on this in section 2.4.3).

2.3.5 Curvature Drift

Magnetic field lines are often curved, and when this occurs, a curvature drift appears. As it has already been shown, a particle with perpendicular and parallel velocity drifts along a magnetic field line. When that field line is curved, it also experiences a centrifugal force

$$\mathbf{F}_R = m v_\parallel^2 \frac{\mathbf{R}_c}{R_c^2} \tag{2.19}$$

where $\mathbf{R}_c$ is the local radius of curvature. This force is directed perpendicularly to the magnetic field and its curvature, illustrated in Figure 2.10. Similar to gradient drift, the centrifugal force, which controls the gyration (equation 2.19), will increase the gyroradius of one side of the gyration, and act to reduce it on the other side. Over several orbits, this motion gives rise to the particle's guiding centre drifting in the direction perpendicular to $\mathbf{B}$ and the field line's radius of curvature, $\mathbf{R}_c$. The curvature drift velocity is given by:

$$\mathbf{V}_R = \frac{m v_\parallel^2}{q} \frac{\mathbf{R}_c \times \mathbf{B}}{R_c^2 B^2} \tag{2.20}$$

Curvature drift is analogous to gradient drift in that the direction of the drift is charge dependant, so that ions and electrons drift in opposite directions perpendicular to the direction to both the direction of magnetic field and the magnetic field gradient as well as giving rise to currents in the perpendicular direction caused by the relative motion of the particles. The amount of curvature drift is also proportional to the parallel energy of the particles, as seen in equation 2.19, the more energy a particle has, the greater the amount of drift it experiences. The force acting on a particle generated by the curvature of a magnetic field is inversely proportional to the amount the field is curved, so the greater the radius of curvature, $\mathbf{R}_c$ or the straighter the magnetic field is, the smaller the force applied to the particle is. This is also true for the curvature drift velocity as in equation 2.20, it can be seen that $\mathbf{V}_R$ is inversely proportional to R_c so again the greater the radius of curvature, the lower the curvature drift velocity. Finally, as with gradient drift, due to the charge dependency of the drift direction, the electrons and ions will drift onto adjacent magnetic field lines as the initial field line cannot drift with the particles in opposite directions at the same time. This motion leads to the mixing

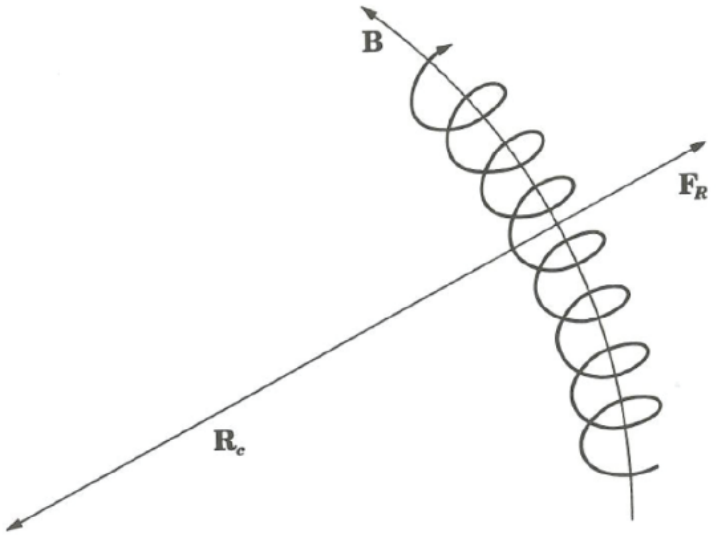

FIGURE 2.10: Illustration of the centrifugal force experienced by a particle moving along a curved magnetic field line. From *Baumjohann and Treumann* (1997).

of plasma across field line and so once again leads to th break down of the frozen-in theorem (discussed in section 2.4.3).

2.3.6 Diamagnetic Drift

When considering a multi-fluid system, i.e. a plasma of ions and electrons, a non-guiding centre drift can be present. Consider a plasma consisting of gyrating particles of one species, all particles gyrate in the same direction around the field. So in a homogeneous plasma, exactly the same number of particles would have exactly the same but oppositely directed transverse velocities, leaving the average velocity to be zero. However, in a non-uniform plasma, a change in transverse (to the magnetic field) pressure caused by either a gradient in plasma density or transverse temperature. If a density gradient is present, it introduces an asymmetry because in the area of decreased particle density, there are less particles gyrating, meaning they cannot average out the transverse velocity in the more densely populated region. As a result, the excess particle gyration velocity leads to a drift motion in the perpendicular direction to the magnetic field. In the event of a temperature gradient, decreasing temperature leads to smaller transverse gyroradii and velocities which therefore means again, the transverse velocity throughout the region cannot reduce to zero, giving rise to further diamagnetic drift.

2.4 Magnetohydrodynamics

Magnetohydrodynamics (MHD) describes the bulk motion of charged particles subject to the presence of internal and external magnetic fields. This is an alternative method for describing the motion of charged particles, instead of examining the motion of single particles, MHD treats the plasma as a single conducting fluid.

The one-fluid theory assumes that plasma is made up of two particle species, ions and electrons (subscripted as i and e respectively) and for simplicity, it assumes ions are singly-charged, and neglects the difference between the two constituent particles. It also considers the plasma as a conducting fluid carrying magnetic and electric fields and currents. When considering this quasi-neutral plasma, the key variables are given for

$$n = \frac{m_e n_e + m_i n_i}{m_e + m_i} \tag{2.21}$$

$$m = m_e + m_i = m_i \left(1 + \frac{m_e}{m_i}\right) \tag{2.22}$$

$$\mathbf{v} = \frac{m_i n_i v_i + m_e n_e v_e}{m_e n_e + m_i n_i} \tag{2.23}$$

$$\rho_q = e(n_i - n_e) \tag{2.24}$$

$$\mathbf{j} = e(n_i \mathbf{v}_i - n_e \mathbf{v}_e) \tag{2.25}$$

where n is the fluid number density, m is the fluid mass, $\mathbf{v}$ is the fluid velocity, ρ_q is the charge density, and $\mathbf{j}$ is the current density (*Baumjohann and Treumann*, 1997).

The **continuity equation** is given by

$$\frac{\partial \rho}{\partial t} + \nabla \cdot \rho \mathbf{v} = 0 \tag{2.26}$$

where $\rho = \text{nm}$ is the fluid mass density. This equation shows that the one-fluid theory satisfies the conservation of mass in that the amount of mass entering the system is equal to the amount of mass leaving the system plus some accumulation of mass within it (*Pedlosky*, 1992).

The equation of motion for electrons is given by

$$n_e m_e \frac{d\mathbf{v}_e}{dt} = n_e m_e \mathbf{g} - \nabla \cdot \mathbf{P}_e - n_e e \mathbf{E} - n_e e \mathbf{v}_e \times \mathbf{B} \tag{2.27}$$

and the equation of motion for ions is given by

$$n_i m_i \frac{d\mathbf{v}_i}{dt} = n_i m_i \mathbf{g} - \nabla \cdot \mathbf{P}_i + n_i e \mathbf{E} + n_i e \mathbf{v}_i \times \mathbf{B} \tag{2.28}$$

where ρ is the mass density, ρ_q is the charge density, $\mathbf{P}$ is pressure, $\mathbf{j}$ is current density and $\mathbf{g}$ is the acceleration due to gravity.

In order to calculate the overall motion of a plasma, equations 2.27 and 2.28 must be added together. It must also be assumed that the plasma is charge neutral, meaning $\mathrm{n}_e \simeq \mathrm{n}_i$. Finally, by applying equations 2.24 and 2.25, the **momentum equation** for a quasi-neutral plasma is formed

$$\rho \frac{d\mathbf{v}}{dt} = -\nabla \cdot \mathbf{P} + \rho \mathbf{g} + \mathbf{j} \times \mathbf{B} \tag{2.29}$$

This equation describes the change of the centre of mass velocity of a quasi-neutral plasma element (*Schunk and Nagy*, 2009).

2.4.1 Ohm's Law

The generalised Ohm's law describes the variation of current density with electromagnetic fields and is found by multiplying equations 2.27 and 2.28 by m_e and m_i respectively and then subtracting them from each other:

$$\mathbf{E} + \mathbf{v} \times \mathbf{B} = \eta \mathbf{j} + \frac{1}{ne} \mathbf{j} \times \mathbf{B} - \frac{1}{ne} \nabla \cdot \mathbf{P}_e + \frac{m_e}{ne^2} \frac{\partial \mathbf{j}}{\partial t} \tag{2.30}$$

Where η is the resistivity, $\mathbf{P}_e$ is electron pressure tensor. The equation actually consists of several terms on the right-hand side; the first term is the resistive term, the second is the Hall term, the third term is the anisotropic electron pressure and the final term is the contribution of electron inertia to the current flow. The algebra is also simplified by neglecting terms with small mass ratios, $\mathrm{m}_e/\mathrm{m}_i \ll$ and assuming quasi-neutrality, $\mathrm{n}_e \simeq \mathrm{n}_i \simeq \mathrm{n}$.

When considering the case of ideal MHD, the plasma resistivity reduces to zero ($\eta = 0$), and as such the conductivity (σ) must tend to infinity , there is no electron pressure gradient and current density is assumed to vary slowly in time. In addition, the electric field cannot have a component parallel to the magnetic field and there is no electric field in the plasma's rest frame. Furthermore, the magnetic flux through a surface S (lying perpendicular to $\mathbf{B}$) must remain constant, even if the surface changes shape or position.

If all of the above assumptions are used, then the last three terms in equation 2.30 drop out and Ohm's law reduces to

$$\mathbf{j} = \sigma(\mathbf{E} + \mathbf{v} \times \mathbf{B}) \tag{2.31}$$

where σ, plasma conductivity is the inverse of η, plasma resistivity (*Baumjohann and Treumann*, 1997).

2.4.2 Magnetic Pressure and Tension

The Hall term in equation 2.30, $\mathbf{j} \times \mathbf{B}$ introduces an effect specific to MHD called **magnetic tension**. Using equation 2.5, the Hall term can be rewritten as

$$\mathbf{j} \times \mathbf{B} = \frac{1}{\mu_0}(\nabla \times \mathbf{B}) \times \mathbf{B} = -\nabla \frac{B^2}{2\mu_0} + \frac{1}{\mu_0}(\mathbf{B} \cdot \nabla)\mathbf{B} \tag{2.32}$$

The first term in equation 2.32 gives the gradient in **magnetic pressure**, P_B, where:

$$P_B = \frac{B^2}{2\mu_0} \tag{2.33}$$

The second term is the **magnetic tension**, T_B

$$\mathbf{T}_B = \frac{B^2}{\mu_0}\frac{\hat{\mathbf{n}}}{R_c} \tag{2.34}$$

where R_c is the radius of curvature and $\hat{\mathbf{n}}$ is the outward normal. Magnetic tension acts towards the centre of curvature, meaning that the force acts to straighten curved magnetic field lines.

The ratio of plasma pressure to magnetic pressure is called the **plasma beta**, β, where

$$\beta = \frac{p}{B^2/2\mu_0} \tag{2.35}$$

$\mathrm{p} = \mathrm{k}(\mathrm{n}_i\mathrm{T}_i + \mathrm{n}_e\mathrm{T}_e)$ and k is the Boltzmann constant. A plasma is said to be cold if $\beta \ll 1$ and hot if $\beta \geq 1$ (*Kivelson and Russell*, 1995).

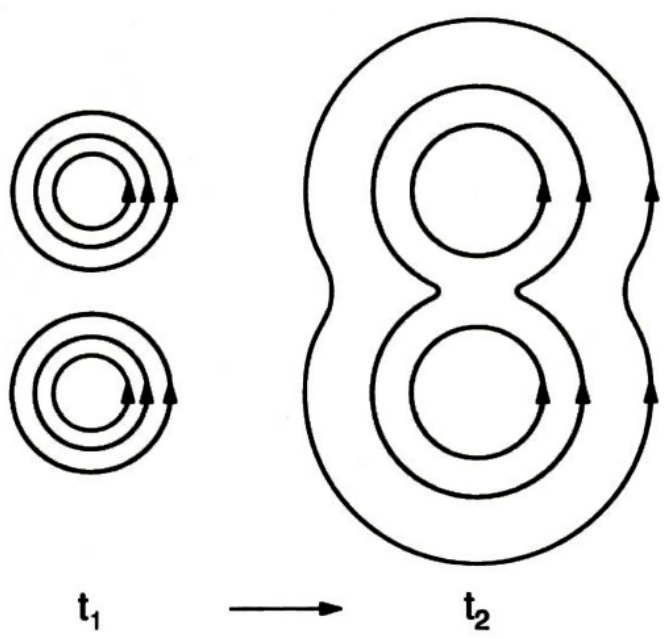

FIGURE 2.11: Diffusion of magnetic field lines (*Baumjohann and Treumann*, 1997).

2.4.3 Diffusion and Frozen-in Flux

The transportation of magnetic field lines and plasma can be investigated through the combination of Ohm's law, Ampère-Maxwell's law and Faraday's law, equations 2.30, 2.5 and 2.4 respectively to create the **induction equation**.

$$\frac{\partial \mathbf{B}}{\partial t} = \nabla \times (\mathbf{v} \times \mathbf{B}) + \frac{1}{\mu_0 \sigma} \nabla^2 \mathbf{B} \tag{2.36}$$

The right-hand side of this equation contains terms for convection and diffusion of magnetic fields.

Magnetic fields tend to diffuse across plasma when met with finite resistance and act to smooth out local inhomogeneities, as in Figure 2.11. This change in topological structure occurs over a period of time called the **magnetic diffusion time**

$$\tau_d = \mu_0 \sigma L_B^2 \tag{2.37}$$

Where L_B is the characteristic length of the plasma.

In collisionless geophysical plasma regions, conductivities can often be very high and length scales very large, so from equation 2.37 it is clear that large τ_d values can arise, meaning magnetic fields may no longer diffuse across the plasma. When this occurs, the diffusion term in the induction equation (equation 2.36) tends to zero and only the convection term is left

$$\frac{\partial \mathbf{B}}{\partial t} = \nabla \times (\mathbf{v} \times \mathbf{B}) \tag{2.38}$$

This is the condition for frozen-in flux (*Alfvén*, 1942) and it implies that when convection is dominant, plasma and magnetic field lines are intrinsically connected together meaning that they experience frozen-in flow, where plasma must move with the magnetic fields and therefore the magnetic fields must also move with the plasma. This theorem is often referred to as the **hydromagnetic theorem**, the **Frozen-in flux theorem** and also **Alfvén's theorem**.

The frozen-in theorem gives rise to the notion of flux tubes, which are essentially a generalised cylinder containing a constant amount of magnetic flux. It implies that all particles and magnetic flux within the volume of a flux tube must remain in that tube independent of any motion the tube experiences or any distortion to its overall shape. Faraday's law, equation 2.4, can be used to replace the partial differential in equation 2.38 to produce an equivalent form of the frozen-in flux condition:

$$\mathbf{E} + \mathbf{v} \times \mathbf{B} = 0 \tag{2.39}$$

Equation 2.39 indicated that in an infinitely conducting plasma, electric fields are zero in a frame moving with the plasma. The condition also demonstrates through its cross product that there are no electric fields parallel to magnetic fields when in an infinitely conducting plasma.

The induction equation, equation 2.36 indicated that the motion of plasma is governed by both diffusion and convection. By considering the ratio of these properties, a more precise definition of frozen-in can be established, providing the **magnetic Reynolds number**:

$$R_m = \mu_0 \sigma_0 L_B v \tag{2.40}$$

This value enables the determination of whether diffusion or convection is dominant within a plasma. If $R_m \gg 1$, convection dominates and diffusion can be entirely neglected, meaning that magnetic field lines flow with the plasma. When $R_m \approx 1$ then diffusion cannot be ignored and may become dominant, meaning that the frozen-in theorem is not satisfied and magnetic field lines may slip across the plasma. However, because space plasmas generally involved large scale lengths, in this regime it can readily be assumed that convective flow dominates and the contribution from diffusion is negligible (*Baumjohann and Treumann*, 1997).

2.4.4 Particle Motion Summary

In general, the MHD theory offers an accurate description of plasma behaviour, holding true for plasmas as long as magnetic fields vary slowly in space and time in comparison to particle gyroradii and gyroperiods. The solar wind is a perfect example of this, with few collisions and relatively consistent magnetic field over large spatial scales, it satisfies the frozen-in theory. However, the breakdown of the frozen-in theory is an important mechanism to facilitate the mixing of plasma and the initiation of magnetic reconnection. An example of this is seen when the solar wind meets the Earth's magnetopause, it experiences sharp magnetic field gradients and when the IMF is directed southward, there is also a shear in the magnetic field system. The magnetic shear configuration is a precursor to magnetic reconnection, where magnetic diffusion of plasma from the field line gives rise to plasma mixing (when the diffusion term in Eqn 2.38 becomes significant). Both phenomena signify the breakdown of the frozen-in theory, which is key to solar wind - magnetosphere coupling. This is MHD.

2.5 Magnetospheric Plasma Sources and Transportation

2.5.1 Magnetospheric Convection

The key assumption made when using the frozen-in theory is that magnetic fields must vary slowly in space and time in comparison to particle gyroradii and gyroperiods. This is true throughout much of the magnetospheric system, although at the magnetopause this is not quite the case. As discussed previously, there is a large magnetic shear at this boundary, meaning magnetic gradients in this region are of comparable length scales to particle gyroradii and as a result, the frozen-in conditions break down. This allows the diffusive term of the induction equation, (equation 2.36) to become dominant and as a result, magnetic field lines from the IMF and magnetosphere diffuse across the boundary and construct an x-type magnetic field geometry, as seen in Figure 2.12. This process

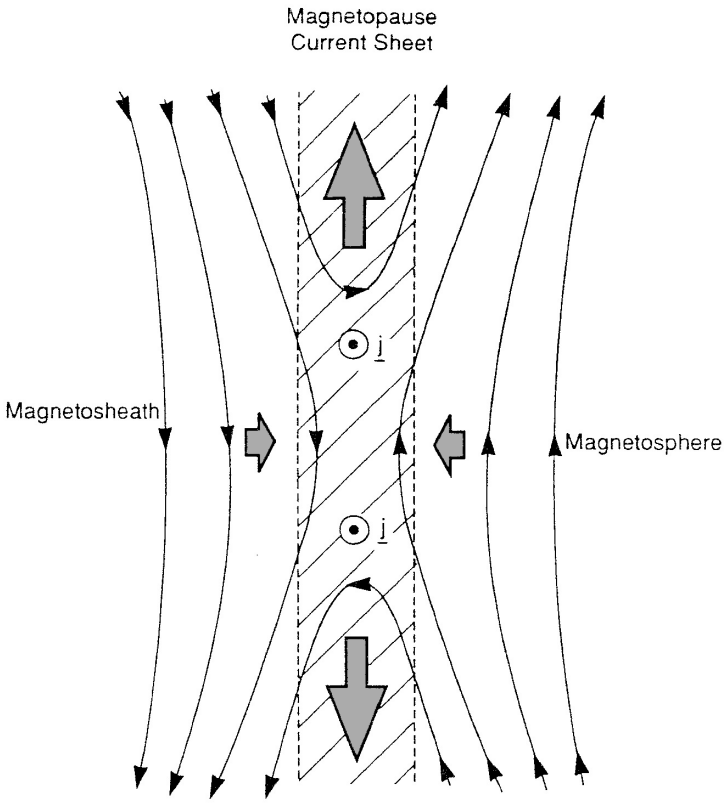

FIGURE 2.12: Magnetic reconnection at the magnetopause current sheet. Diagonal shading lines represent the current sheet with the current density point out of the page. The black solid lines show the magnetic field lines with the large grey arrows showing their direction of motion. From *Cowley et al.* (2003).

was first introduced by *Dungey* (1961) who called it **magnetic reconnection**. The reconnection site is cleared of newly opened magnetic field lines by magnetic tension acting to straighten the highly curved fields, pulling them along the magnetopause current sheet and allowing more IMF and magnetospheric field lines to replace them ready to continue the process. The contracting magnetic field lines transfer magnetic energy to the particles frozen into the field, exciting and accelerating them, leading to a heating of the plasma.

A key consequence of the breakdown of the frozen-in theorem is the mixing of solar wind and magnetospheric plasma as the newly reconnected field lines contain plasma from both regions. These new field lines are open, meaning that one end remains connected to the Earth's magnetic field up in the high latitude polar region and the other end is still connected with the solar wind and they satisfy the frozen-in flux conditions away from the reconnection region.

Magnetic reconnection has a large contribution to magnetospheric dynamics and drives convection throughout the magnetosphere. Consider the configuration of solar wind and magnetospheric magnetic fields depicted in Figure 2.13 where the IMF is directed

southward. Magnetospheric convection begins at the dayside of the system; when both ends of the field line are connected to the magnetosphere, it is closed. As this field line reaches the magnetopause, it undergoes reconnection and merges with an IMF field line and at this point, one end of the newly formed field line is still connected to the magnetosphere and the other is now connected to the IMF. It is now open and is illustrated by point 2 in Figure 2.13. The newly opened field line is swept anti-sunward via the momentum of the solar wind, and over time it becomes elongated. From here, kinetic energy of the solar wind is converted into magnetic energy, stretching the magnetotail into a tear drop shape up to about 1000 R_E in length (*Dungey*, 1961, 1965). As more magnetic field lines convect around the Earth and populate the tail, magnetic pressure forces them to lower latitudes and anti-parallel lines from the northern and southern hemispheres come into close proximity. They form the tail current sheet and reconnection X-line field structure somewhere beyond 100 R_E downtail. Tailward of this point, the disconnected section of magnetic field line, whose ends are now both connected to the IMF continue flowing downstream away from the Earth and rejoin the solar wind. Earthward of the reconnection point, the magnetic field is now closed again and magnetic tension draws the field lines sunward and around the Earth to eventually repeat the process again. This convective motion, seen in the insert of Figure 2.13, can be mapped to the ionosphere and is seen as a twin-cell convection pattern. The open magnetic field lines convect anti-sunward at high latitudes and the closed field lines convect sunward at lower latitudes.

Magnetic reconnection is not a steady-state process, in fact it is highly variable and depends on solar wind and IMF conditions. The rate of dayside reconnection is independent of the nightside reconnection rate, and while on average the two processes are balanced, at any given moment, either process could be dominant in driving magnetospheric convection (*Cowley and Lockwood*, 1992). While southward directed IMF produces the highest rate of reconnection, during periods of northward directed IMF, reconnection still occurs even though the magnetospheric and IMF magnetic field lines are directed parallel to each other, but instead of happening at the subsolar point, it is at higher latitudes that IMF field lines and southward pointing open magnetic field lines reconnect (*Dungey*, 1963). It is important to note that the IMF can have a component in the dawn-dusk and earthward-sunward directions and thus has implications on magnetospheric flows. When this occurs, it introduces asymmetries in the magnetospheric structure due to magnetic tension exerting a torque on the newly formed open field lines (*Cowley*, 1981a,b).

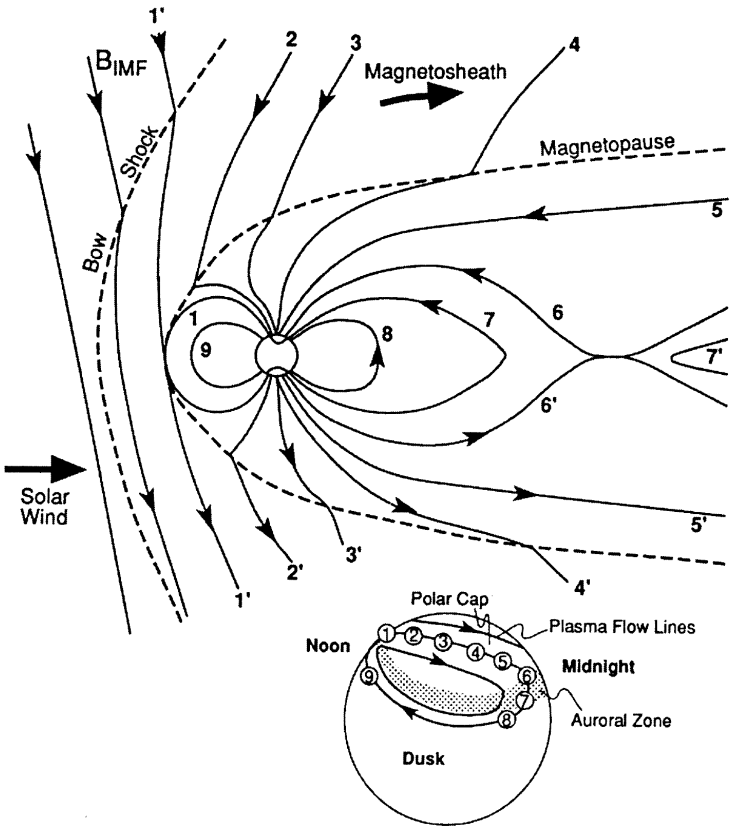

FIGURE 2.13: Illustration depicting the flow of plasma within the Earth's magnetosphere due to magnetic reconnection. The numbered magnetic field lines show the evolution of reconnection beginning at 1 as it is transported tailward. 6 indicates the region of reconnection in the tail. The insert highlights the ionospheric footprint of the open field lines in the northern hemisphere. From *Hughes* (1995a).

2.5.2 Corotation

Corotation is the dominant plasma transportation mechanism in the inner magnetosphere. As the Earth rotates, friction between its surface and the atmosphere causes the neutral atmosphere to rotate with the Earth. Collisions between the atmospheric neutral atoms and ion transfer momentum from the neutral particles to the ions, resulting in the ions approximately moving with the neutrals. Because frozen-in flux (section 2.4.3) usually applies in the ionosphere, the magnetic field is affected with the ions, thus this motion is communicated to the magnetospheric plasma along field lines.

Convective motion and corotation both contribute to the magnetospheric structure and plasma flow. Corotation dominates at lower latitudes whereas convection prevails at larger distances from the Earth. Figure 2.15 illustrates the combination of the convective and corotational motions. On the dawn side, both regimes work to make the plasma drift sunward, but on the dusk side, they are competing to make the plasma drift in

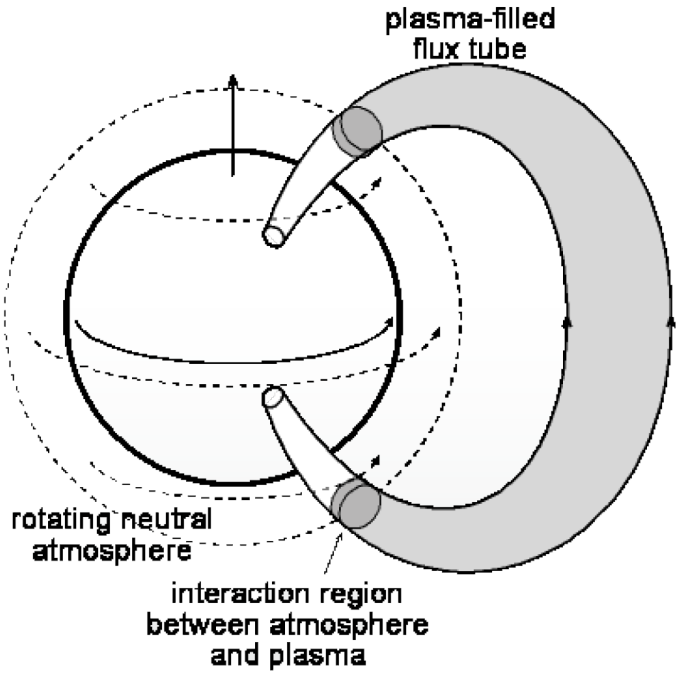

FIGURE 2.14: Earth's corotation environment. Depicting the rotating neutral atmosphere with the corotating flux rope and magnetospheric plasma. Adapted from *Wild* (2015).

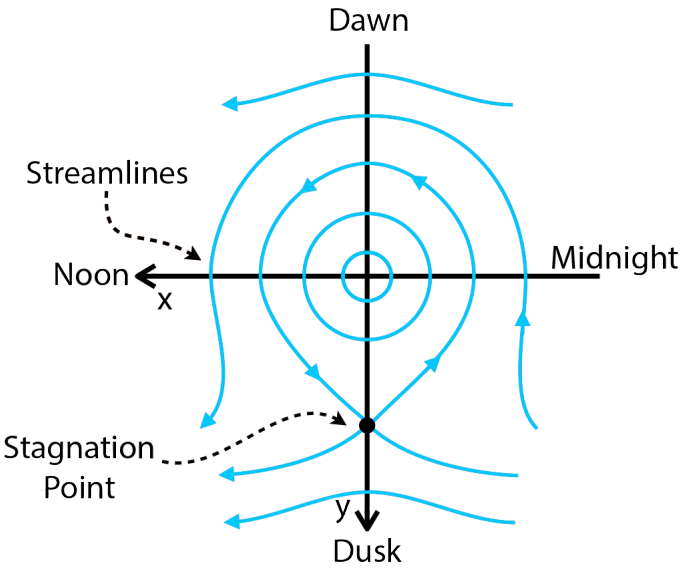

FIGURE 2.15: Illustration of the combination of convective and corotational magnetospheric flows looking in the equatorial plane. Adapted from *Kavanagh et al.* (1968).

opposite directions. There is a point on the dusk side where the plasma velocity is zero, highlighting a clear balance between the convective and corotational processes.

In a time independent picture, no cold plasma is able to cross the boundary between the corotational and convective regions, this boundary is called the separatrix. The particles within this boundary continue to corotate with the Earth and make up the plasmasphere. The separatrix and by definition the plasmasphere expands and contracts with magnetospheric activity, the more active the system, the smaller the separatrix. Note that the separatrix and plasmasphere are not always the same size. This is because while the separatrix reacts instantaneously to a change in magnetospheric activity, the physical plasmasphere takes longer to adjust (*Kivelson and Russell*, 1995; *Baumjohann and Treumann*, 1997).

2.5.3 Magnetospheric Plasma Sources and Losses

2.5.3.1 Magnetospheric Plasma Sources

There are two sources from which plasma is injected into the magnetosphere, the ionosphere and the solar wind. The ionosphere is the most important source of terrestrial magnetospheric plasma (*Chappell*, 2015). The main processes are ionic outflow along the Earth's magnetic fields and are grouped into different classes; bulk up-flow, conics and beams.

Ionic bulk up-flow is split into two key processes, the polar wind and the auroral bulk up-flow. The first describes the outflow of H^+ and He^+ ions at both poles along open magnetic field lines in the polar ionosphere (100 - 2000 km in altitude and above $\sim 50^\circ$ latitude (*Heelis*, 1982)). The process is caused by the ion-acceleration by a bipolar electric field formed by the separation of ions and electrons. The latter describes the outflow of O^+ ions in the topside auroral ionosphere (about 500 km altitude).

Ion beams and conics differ from ionic bulk flow primarily by the altitudes at which they are observed. Ion beams are typically observed about 5000 km and are up-flowing ions along the upward magnetic field direction. Ion conics have a peak flux in the direction at an angle to the upward magnetic field direction and have been observed between the altitudes for 1000 km to a couple of Earth radii (*Yau and André*, 1997; *André and Yau*, 1997; *Seki et al.*, 2015).

The second major source of magnetospheric plasma is the solar wind. There are two main methods in which this occurs, magnetic reconnection (see section 2.5.1) and anomalous diffusion across the magnetopause via a non-linear instability such as the Kelvin-Helmholtz instability (KHI). Anomalous diffusion via KHI occurs at low latitudes and

requires solar wind plasma to be transported perpendicularly to the local magnetic field in order for it to occur. The KHI is driven by a flow shear between the magnetosphere and magnetosheath and a non-linear KHI vortex can allow diffusion to occur within it and thus the mixing of solar wind and magnetospheric plasma (*Seki et al.*, 2015).

2.5.3.2 Magnetospheric Plasma Losses

There are three main processes enabling plasma to leave the Earth's magnetosphere: reconnection, charge exchange and pitch angle scattering.

Magnetic reconnection in the terrestrial magnetotail is one of the key processes for plasma loss from the magnetosphere. During periods of high geomagnetic and auroral disturbance of heightened dayside magnetic reconnection, nightside reconnection can occur earthward of the quiet-time X-line position. When this occurs, any magnetospheric plasma attached to a field line between the two reconnection points will be trapped in a closed magnetic loop structure called a plasmoid. This bubble like object can be anywhere between 1 and 10 R_E in diameter (*Ieda et al.*, 1998), and travels tailward out into the solar-system, taking the magnetospheric plasma with it (*Hones*, 1976).

There is a lower-altitude region in the Earth's magnetosphere where highly energised particles are trapped by the Earth's dipolar magnetic field called the ring current (*Frank*, 1967). In this region, an efficient loss mechanism is present in the form of **charge exchange**. This process sees charged ring current ions collide with neutral exospheric hydrogen atoms (from the outermost region of the Earth's atmosphere), whereby the charged ion strips an orbital electron from the neutral atom, forming an energetic neutral particle. They are then charge-neutral, they are unaffected by electric and magnetic forces, meaning they are free to leave the ring current, no longer trapped in the geomagnetic field. Through the process of charge exchange, the exosphere behaves as an mass sink, removing plasma from the magnetosphere (*Dessler and Parker*, 1959).

Particles are also lost from the magnetosphere via **pitch angle scattering**. If a particle's pitch angle (equation 2.10) is smaller than the loss cone[1] angle, α_{lc}, that is to say particles inside the loss cone, then the particle will penetrate down to lower altitudes and interact with the Earth's atmosphere via collisions and will be lost. The loss cone angle is defined by

[1]The loss cone is a range of angles where a particle will collide with the atmosphere and no longer be trapped in the magnetosphere, while particles with pitch angles outside the loss cone will remain trapped in the magnetosphere.

$$\alpha_{lc} = \left(\frac{B}{B_m}\right)^{\frac{1}{2}} \tag{2.41}$$

where B is the magnetic field strength at the specified position and B_m is the magnetic field strength at the magnetic mirror point. Particle precipitation occurs at higher latitudes and is the cause of the aurora, seen as curtains of light from the ground (*Hughes*, 1995b).

2.6 Magnetospheric Substorms

Over large time scales Dungey's convection model stands true, so the average magnetic reconnection rates on the dayside and nightside magnetosphere are balanced. However, the IMF direction and solar wind flow are incredibly variable, so over short time scales the dayside and nightside reconnection rates are rarely balanced. During periods of southward-directed IMF, there is a heightened rate of dayside reconnection, adding open flux into the magnetotail. Conversely, during period of northward-directed IMF, the reconnection rate is much reduced and little open flux is added to the tail. Regardless of the amount of flux contained within the magnetotail, only a small amount of it is instantaneously reconnected and returned to the dayside (*Rostoker and Eastman*, 1987a). As such, during periods of southward IMF, flux is piled up in the tail region and eventually this stored energy is released in an explosive event and the newly closed magnetic field lines are convected back to the dayside ready to start the cycle again. This process is known as a **magnetospheric substorm**.

2.6.1 Substorms: A Brief History

Substorms were first documented by *Birkeland* (1908) when during his 1902 polar expedition he used a network of magnetometers to observe northward and southward deviations of magnetic field strength and coined the phenomenon 'polar elementary storms'. It took another 53 years for the phenomenon to gain more interest with *Akasofu and Chapman* (1961) referring to it as the 'polar magnetic substorm' before *Akasofu* (1964) reduced the name to just 'substorm', which eventually stuck. *Akasofu* (1964) was the first to define the substorm according to auroral morphologies and outlined the characteristic events associated with the storms. The first event was the **auroral onset**, the time at which there is a rapid brightening of the most equatorward arc in the auroral oval, usually situated near local midnight. Over the next five minutes, a very bright aurora develops at the arc's most westward position and surges poleward and westward.

The period over which the arc travels poleward is called the **expansion phase** and usually lasts between 10 and 30 minutes. The final stage of the substorms observed by Akasofu is the **recovery phase**. This is the longer part of the process and can last anything up to a number of hours after the expansion phase terminates. It is seen as a relaxation of the system whereby the auroral bulge shrinks and the arcs begin to migrate equatorward once more (*Kennel*, 1996).

It was not until 1966 that substorm events were correlated with southward directed IMF by *Fairfield and Cahill* (1966) and it was at this point that magnetospheric convection and substorms were interlocked. Four years later *McPherron* (1970) completed the description of the substorm by introducing the **growth phase**. This precedes the auroral onset and later *Meng and Makita* (1986) showed that the auroral oval expands equatorward for 30-60 minutes during this phase (*McPherron*, 1995).

2.6.2 Phenomenological Models of Magnetospheric Substorms

There have been many substorm theories since their first observations in 1908 and they can generally be separated into four categories: (i) internally triggered or externally driven processes in the near-Earth region, (ii) those based on magnetic reconnection occurring in the mid-tail, (iii) those based on ionosphere-magnetosphere coupling and (iv) those based on abstract ideas of non-linear dynamics. This section presents a number of these substorm models which attempt to explain how the storms are triggered and evolve.

2.6.2.1 The Driven Model

Through the interconnection of the solar wind and magnetosphere due to magnetic reconnection, the interplanetary electric field is directly applied to the ionosphere. When there are divergences in this electric field or discontinuities on the ionospheric conductivity, field-aligned currents (FAC) will be induced. **The driven model** of substorms was initialised by *Perreault and Akasofu* (1978) to explain the strong correlation between magnetic indices sensitive to the field aligned currents and the solar wind. In this model, a southward turning IMF enhances the coupling of the solar wind electric field and the ionosphere and as such the strength of the ionospheric currents. In order to explain the sudden auroral enhancement during the expansion phase, *Akasofu* (1979, 1980, 1981) proposed that an outward FAC near midnight creates a field aligned potential drop when the current density reaches some crucial value. This potential drop accelerates electrons downward, leading to an increase in current and ionospheric conductivity. This higher conductivity requires more current for a fixed solar wind electric

field, which further increases the FAC and its potential drop. Akasofu suggested that this instability corresponds to the substorm expansion phase (*McPherron*, 1995).

2.6.2.2 The Boundary-Layer-Dynamics Model

The boundary-layer-dynamics model (BLD) is another reconnection model devised by *Rostoker and Eastman* (1987b) to explain why fast plasma flows in the magnetotail are most frequently observed in the earthward direction (*Eastman et al.*, 1985). From the evidence of this paper, Eastman et al thought the source of substorm expansion was at a great distance from Earth. The model utilised magnetic field mapping where the dusk high-latitude ionospheric convection reversal and the Harang discontinuity near midnight were mapped to the same magnetospheric topological feature. As the dusk convection reversal maps to the inner edge of the low-latitude boundary layer on the dusk-side of the plasma sheet, to maintain the continuity of mapping, the Harang discontinuity at midnight must map to a location near to the distant X-line. From this, Eastman et al suggest that the expansion phase is triggered by a sudden burst of reconnection at this distance X-line. The reconnection will cause energised plasma to launch earthward and enhance the velocity shears at the inner side of the low-latitude boundary layer. These shears can become unstable as the Kelvin-Helmholtz instability grows, vortices are created, especially on the dusk-side and with this, FACs flow away from the velocity shear on the dawn-side and into the newly formed vortices on the dusk-side. As with the driven model, outward FACs give rise to the downward acceleration of electrons, creating the westward travelling surge. Unfortunately, the Boundary-Layer-Dynamics model uses a magnetic field mapping model which was later found to be incorrect (*Fairfield and Mead*, 1975) as it maps the Harang discontinuity near-midnight to the geosynchronous orbit distance, not the distant X-line (*McPherron*, 1995).

2.6.2.3 The Thermal-Catastrophe Model

Another reconnection-related model is the **thermal-catastrophe model** which was introduced by *Smith et al.* (1986) and *Goertz and Smith* (1989), although the only role reconnection plays in this model is to drive convection and instead, energy is injected into the magnetotail via surface-wave perturbations of the tail magnetopause.

The wave energy propagates across the magnetic field lines of the plasma-sheet boundary layer, and where the driving frequency matches the resonant frequency of the magnetic field, the energy is transferred into the plasma. This energy heats up the plasma which then convects into the central plasma sheet and over time, earthward. The substorm

growth phase begins when the intensity of the compressional waves crossing the magnetospheric lobes increases. Once a characteristic temperature is met, the boundary layer becomes opaque and as such, it is able to absorb all frequencies of waves. As a result, the boundary layer absorbs an increased amount of energy and quickly increases the temperature of the plasma because convection is not able to maintain an equilibrium. The plasma sheet reconfigures topologically in order to adjust to the new raised temperatures and at this point, the opacity decreases and therefore convection is once again about to transport the energy deposited by the waves away. The boundary layer adjustment from one temperature with a constant energy is labelled as the thermal-catastrophe and marks the duration of the expansion phase. While there have been a number of attempts at correlating wave power in the lobes with substorm activity, there is little compelling evidence in support of the thermal-catastrophe model (e.g. *Chen and Kivelson* (1991) and references therein) (*McPherron*, 1995).

2.6.2.4 The Near-Earth Neutral-Line Model

The **Near-Earth Neutral-Line Model** (NENL) is arguably the most developed substorm model to date (*McPherron et al.*, 1973; *Russell and McPherron*, 1973) and focusses on creating an internally consistent description for most of the magnetospheric phenomena. With this, it does concentrate on mid-tail substorms and as such describes this region much better than the inner magnetosphere.

A southward turning of the IMF indicates the beginning of the expansion phase in the NENL model. This dynamic change initiates magnetic reconnection at the dayside magnetopause and the newly formed open field lines are swept tailward. This process acts to erode away the dayside magnetosphere while piling up additional flux in the tail, causing it to expand outwards in size. The dayside erosion leads to the flaring of the magnetosphere (*Coroniti and Kennel*, 1972), increasing the angle of attack on it from the solar wind (Figure 2.16), which in turn increases the dynamic pressure at this boundary. This increased pressure compresses the magnetotail and must be balanced by an increase in tail-lobe magnetic-pressure and this increased lobe-pressure is in turn applied to the plasma sheet, causing it to thin. Plasma and magnetic flux transported through the plasma sheet to the dayside also contributes to the thinning of the nightside plasma sheet. The removal of magnetic flux from the dayside and thus a reduction in closed flux in the region can be observed in the ionosphere as an increase in size of the polar cap (*Akasofu*, 1968), the auroral oval moves equatorward (*Feldstein and Starkov*, 1967), and the aurora becomes more intense. As the growth phase progresses, the near-Earth current sheet becomes thinner and more intense. This causes a great deal of the magnetic flux crossing this region to close at much greater radial distances and the

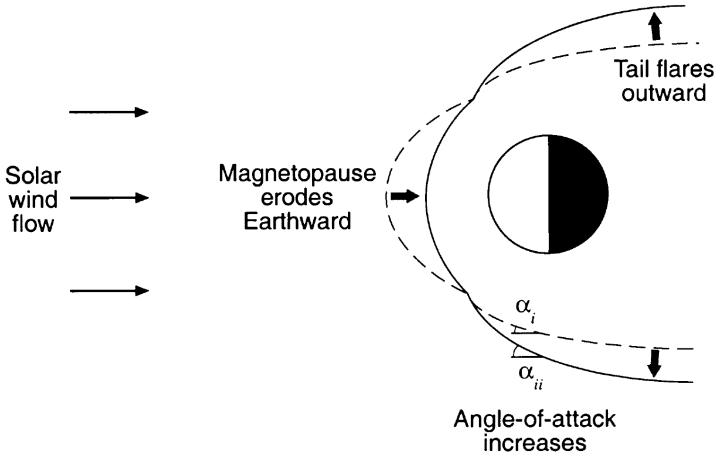

FIGURE 2.16: The change in magnetospheric shape during a southward turning IMF. The dashed/solid lines represent the shape before/after the southward turning. Thick arrow shows motion of magnetopause due to IMF repositioning. α_i/α_{ii} represent the solar wind angle of attack before/after following the turning. From *Wild* (2000).

field becomes weak and tail-like in the equatorial plane (*Kokubun and McPherron*, 1981; *Baker et al.*, 1994). The configuration of the magnetosphere during the growth phase according to the NENL mode is depicted in Figure 2.17(a).

Clearly the reorganisation of magnetic flux cannot proceed forever as described above. The dayside magnetosphere would eventually be stripped of all closed field lines and the nightside plasma sheet would thin to the scale of ion gyroradii. Before this can occur, a global instability is triggered, allowing the closed field lines in the magnetotail to return to the dayside. The NENL model instability is the initiation of magnetic reconnection.

Magnetic reconnection is triggered spontaneously once the current sheet reaches an appropriate threshold and occurs at the centre of the current sheet earthward on the quiet-time neutral line at around 20-30R_E, this is the NENL, Figure 2.17(b). Within the region between the NENL and the distant neutral line (DNL), regions of closed flux are formed, o-lines, which can appear cylindrical in shape when considered in three dimensions. They can also be formed earthward of the NENL as reconnection does not occur in a static position and as a result, additional regions of closed flux can also be trapped here. As reconnection progresses, closed magnetic field lines in the plasma sheet form loops around the o-line and shorter closed field lines flowing earthward of the X-line. Within the plasma sheet, field lines flow vertically into the X-line and horizontally out of it.

The expansion phase of the NENL model has a unique feature to the previous model discussed, the creation of a plasmoid. This is a bubble-like structure of closed magnetic flux which is ejected from the plasma sheet during this phase. Reconnection continues

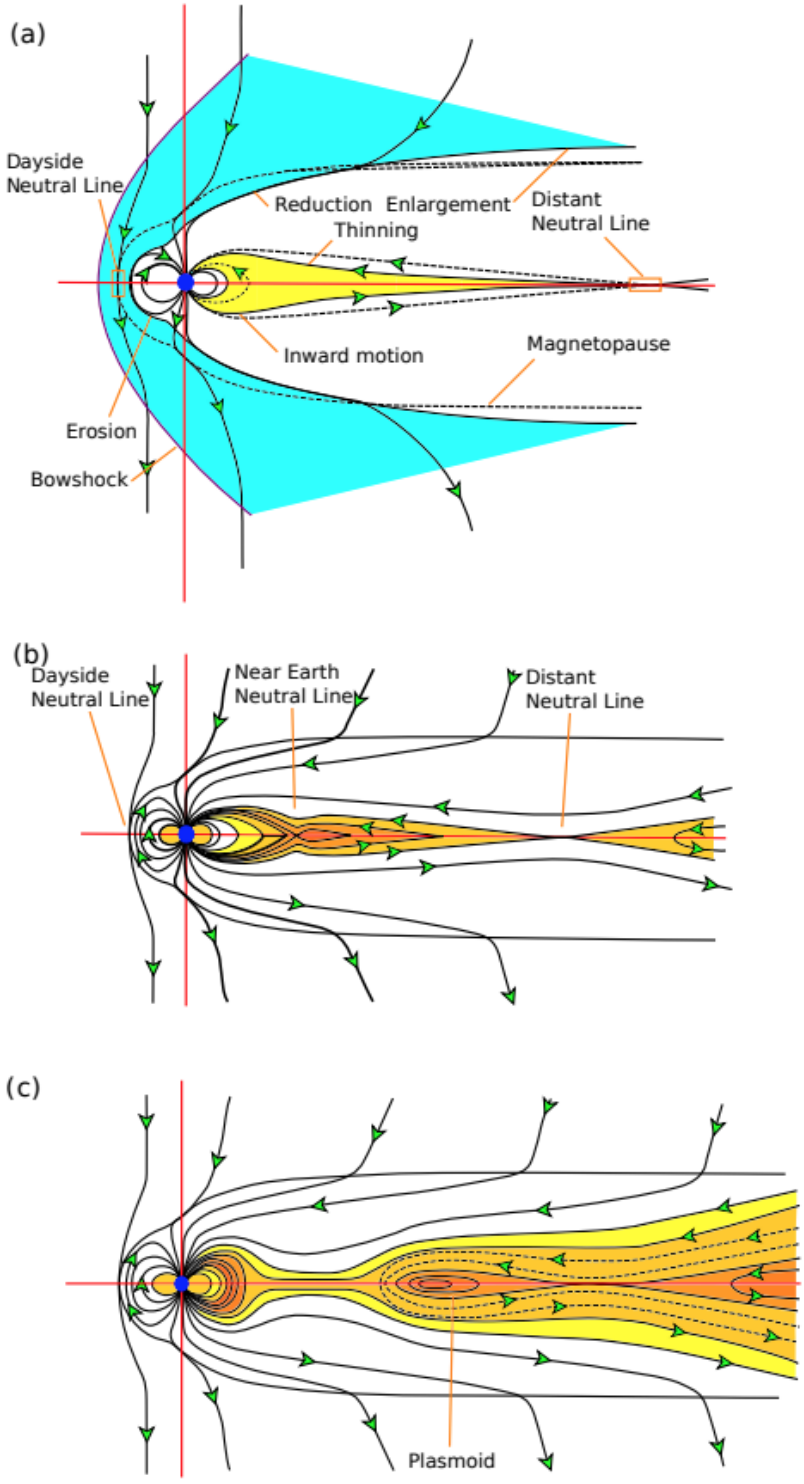

FIGURE 2.17: A schematic of magnetospheric configurations according the the NENL model, from *James* (2015). (a) the magnetospheric configuration during the substorm growth phase. (b) The formation of the near earth neutral line following the thinning of the plasma sheet. (c) Magnetospheric configuration for the substorm expansion phase.

at the NENL and the plasmoid expands until the final field lines are closed and at this point, the plasmoid is entirely detached from the magnetosphere and is accelerated under the influence of already existing plasma pressure gradients and by freshly reconnected field lines following the plasmoid detachment sweeping tailward, Figure 2.17(c).

The substorm current wedge (SCW) is another important factor introduced by the NENL model. It comes as a consequence of a localised X-line as when it forms, the net current across the tail in the meridian of the X-line is reduced (*Birn and Hesse*, 1991). In order to maintain current continuity throughout the magnetotail, current must be diverted. This can be done by diverting the original cross-tail current along magnetic field lines connecting each end of the X-line to the ionosphere via the **substorm electrojets**. Plasma flowing earthward from the X-line occupies a narrow channel with strong flow-velocity shears at the channel boundaries. The sense of the flow-shears is such that more current is diverted into the growth of the SCW. When the flow reaches the inner magnetosphere, it is slowed and compressed by the strong central dipolar magnetospheric field. As the flow evolves, the moving plasma polarises and creates a dawn-to-dusk (westward) electric field across the flow channel and propagates to the ionosphere as an Alfvén wave, which is seen in ground magnetic data as Pi2 pulsations (*Baumjohann and Glassmeier*, 1984). When the electric field reaches the ionosphere, it instigates ionospheric-plasma flow in the equatorward direction. This flow is quickly retarded by inertia and the electric field is mostly reflected and as a result the initial wave reverberates between the plasma sheet and the ionosphere a number of times to establish the DC current needed to drive the equatorward flow against the ionospheric resistance.

Tailward of the interface between dipolar and tail-like fields, the turbulent plasma population precipitates into the ionosphere to create unstructured aurora of the auroral bulge and the interface corresponds to the poleward edge of the auroral bulge. Additional closed flux is added to the dipolar field through continual earthward flow and as such, the interface moves tailward. This causes the position of particle precipitation in the ionosphere to migrate polewards. Within the auroral bulge, the particle precipitation leads to the enhancement of the ionospheric conductivity relative to the surrounding ionosphere because the more charge carriers there are in a region, the easier current is able to flow. The westward electric field created by high-velocity earthward flows projects into this region and drives Pederson currents westward and Hall currents poleward *Ohtani et al.* (2000).

The recovery phase begins when the plasmoid starts to move tailward and in the mid-tail region, rapid plasma sheet expansion (*Sauvaud et al.*, 1984) and earthward plasma flows (*Hones Jr.*, 1985) have been observed and associated with the beginning of this phase.

Further support to this model was given by *Slavin et al.* (1993) with his observations of tailward moving plasmoids, or travelling compression regions in the distant tail. In the near-Earth region, the recovery phase manifests as a decay of the substorm current wedge and a slow return to the quiet-time magnetic field configuration after the neutral time has begun to move tailward (*Baker et al.*, 1996).

2.6.2.5 The Current Sheet Disruption Model

A competing model to the NENL model is the **current sheet disruption model**. The AMPTE CCE spacecraft made some observations just beyond the magnetospheric synchronous orbit showing inconsistencies in particle and field signatures which disagree with the NENL model (*Takahashi et al.*, 1987; *Lui et al.*, 1988). *Lui* (1991) introduced the current sheet disruption model in an attempt to correct for these inconsistencies by postulating that instabilities in the current sheet give rise to substorm onset.

In this model, it is suggested that a thin current sheet evolves in the inner magnetosphere during the substorm growth phase, just as it does in the NENL model. As it thins, non-adiabatic ions and electrons stream across the current sheet in opposite directions and interact via the kinetic cross-field-streaming instability producing lower hybrid waves (*Lui et al.*, 1990). At the same time, the density gradient on the boundary of the plasma sheet drives the lower-hybrid-drift instability. The combination of these two types of waves lead to an anomalous resistance in the plasma sheet that disrupts the cross-tail current, sending it along field lines, especially those of the SCW.

According to *Lopez and Lui* (1990), the current sheet disruption begins near to synchronous orbit and expands radially out into the tail. This is the location at which the expansion phase is initiated and this position is the main difference between the current sheet disruption model and the NENL model. This idea has been supported by two spacecraft observations of substorm-related tail-lobe reconfigurations made by Lopez and Lui. Furthermore, *Jacquey et al.* (1991) have modelled these lobe variations, adding additional support to the model. Auroral observations made by *Elphinstone et al.* (1991) are also consistent with an expansion phase onset located near Earth. In addition, magnetic field models support the current sheet disruption model as they project the position of the auroral oval and therefore expansion onset just tailward of synchronous orbit, a region likely to host the current sheet disruption. Finally *Murphree et al.* (1991) provided evidence suggesting that at least the initial stage of substorm expansion occurs on closed magnetic field lines.

The current sheet disruption model concludes with suggesting that the substorm expansion phase does not initially involve magnetic reconnection on the tail-lobe open field

lines. Instead a rarefaction wave is initiated and propagates downtail creating a thinning of the plasma sheet and a reduction in the north-south magnetic field. Importantly, near the end of the expansion phase, or indeed at the start of the recovery phase, these effects initiate reconnection and the subsequent creation of a plasmoid.

2.6.2.6 Substorms Summary

All of the substorm models described offer different mechanisms for the expansion and recovery phase of the geomagnetic events. For example, the driven model does not talk about nightside reconnection and its effects; the boundary-layer-dynamics model begins reconnection at a distant X-line at expansion onset; the thermal-catastrophe model initiates reconnection at a distant X-line soon after it begins on the dayside; the NENL model begins reconnection late in the growth phase on closed field lines and the expansion phase occurs when the last closed field line is released; the current-sheet-disruption model suggests that the expansion phase is initiated by an instability of the near-earth current sheet which diverts current through the ionosphere. Even with all of these different models, a universal model has not been created and there is still no clear universal description that incorporates all observed substorm phenomena (*McPherron*, 1995).

It is clear that the mechanism which triggers substorm onset is still a strongly debated topic, with many new studies frequently being carried out (*Angelopoulos et al.*, 2008; *Nishimura et al.*, 2010; *Rae et al.*, 2014). The two most widely supported substorm models are the NENL and current disruption (CD) models. The main difference between the two is their causality chain: for the NENL model, reconnection at greater distances from Earth trigger a current disruption closer in, whereas for the CD model, the current disruption triggers the reconnection process. Overall however, the NENL model seems to have the strongest support and measurements made by the Geotail spacecraft have shown evidence of the existence of a NENL during substorms at a distance of 20-30 R_E (*Baumjohann et al.*, 1999). Furthermore, steps have been taken to re-evaluate the NENL reconnection process. While the original description of the NENL model suggested that reconnection at the NENL was a fairly steady and consistent event, later observations of intermittent fast Earthward flows imply that perhaps this is not the case. These variable fast flows are named **Bursty Bulk Flows** (*Baumjohann et al.*, 1990; *Angelopoulos et al.*, 1992, 1996) and will be discussed in more detail later.

2.7 Summary

In this chapter, the fundamental physics of magnetospheric dynamics has been discussed in detail. The information ranges from the configuration of the Earth's magnetosphere to how plasma, momentum and energy are transported about the system, as well as how substorms influence convection during a southward turning of the IMF. Along with the phenomenological descriptions of these processes, this chapter delves into the small scale structure and behaviour of the terrestrial magnetosphere, discussing the motion and interactions of singular particles. It then moves onto talking about how these ions and electrons move together, behaving as a single fluid as described by magnetohydrodynamics. It is important to understand not only how the magnetospheric processes are initiated and how they progress, but also how the data providing the information is obtained and thus how the space-plasma instruments operate and collect the data required for investigation. This will be discussed in the next chapter.

Chapter 3

Instrumentation and Datasets

3.1 Introduction

This chapter will provide a brief introduction to the Cluster mission including a more detailed summary of the in-situ instruments used throughout the investigation presented in this thesis. It also introduces the additional datasets used to carry out some of the data analysis during the research.

3.2 The Cluster Mission

The Cluster mission was originally launched in 1996, but quickly aborted, leading to the destruction of all four satellites. A second identical mission, Cluster II, was re-launched, two satellites at a time in 2000 and declared as operational on 1st February 2001. The mission was made up of four identical spacecraft and followed an elliptical polar orbit at an initial perigee of $4\,R_E$ (26,000 km) and apogee of $19.6\,R_E$ (125,000 km) with an orbital period of 57 hours (*Escoubet et al.*, 1997).

The Cluster mission's orbital characteristics and tetrahedral formation are two of the main factors in selecting the mission for my research. The other candidate multi-craft mission for this research project is THEMIS (Time History of Events and Macroscale Interactions during Substorms), which has similar mission objectives as the Cluster mission, making large scale multipoint observations of the interaction between the solar wind and the magnetosphere (*Sibeck and Angelopoulos*, 2008). However, THEMIS' orbit is restricted to the Earth's equatorial plane, so it does not have the necessary spatial coverage to observe plasma convection in the noon-midnight meridian, a region which Cluster frequently visits.

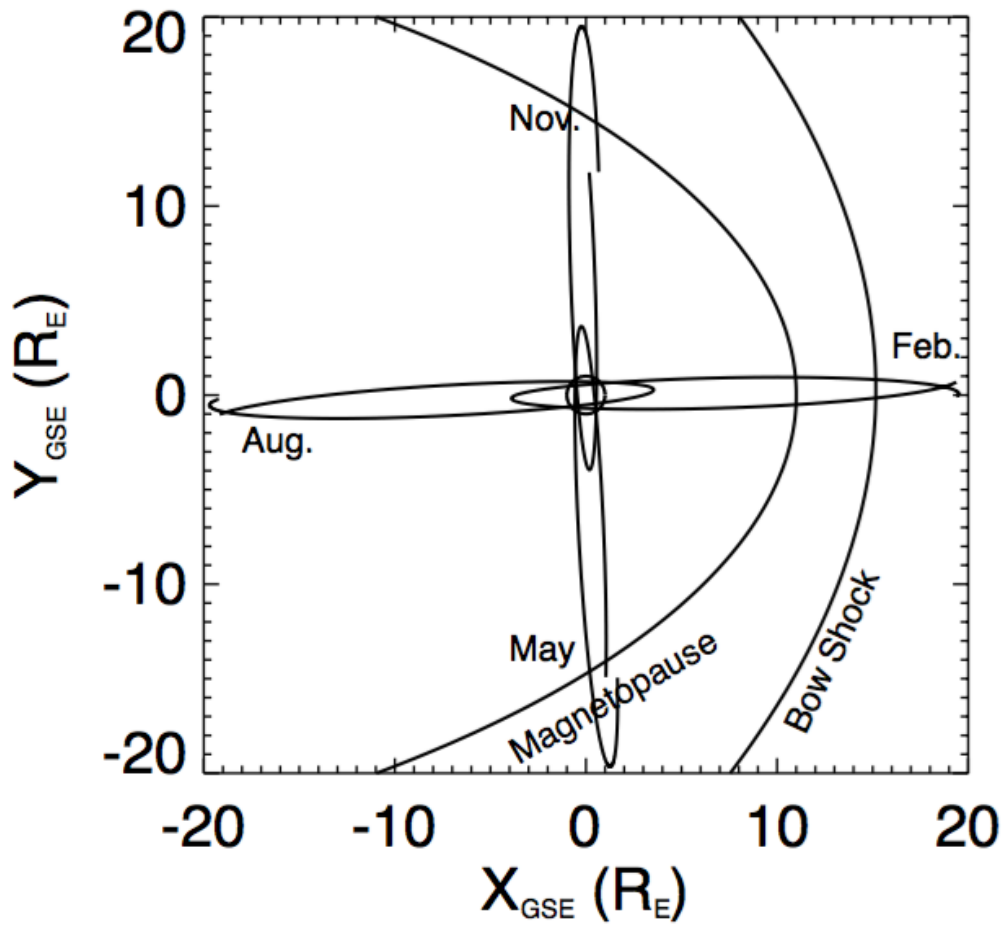

FIGURE 3.1: Cluster spacecraft orbits projected onto the equatorial plane. The orbits are shown at three-month interval (*Escoubet et al.*, 1997).

The Cluster mission's orbit is fixed in inertial space and achieves a complete 360° view of the near-Earth environment via the Earth's orbit about the Sun. Cluster's orbital plane rotates with respect to the Earth-Sun line as seen in Figure 3.1. Observations of specific magnetospheric regions can therefore only be made at certain times of the year. For example, if one would like to take measurements of the magnetopause, this could only be carried out between the months of November and June, the 'dayside' season. Likewise, if it is the magnetotail which is the observation target, data can only be collected between the months of June and November, the 'nightside' season, see Figure 3.1. This behaviour is caused by the relative position of the Earth's magnetosphere with respect to the Sun, which rotates once per year in an inertial reference frame.This thesis focuses on the night-side magnetosphere out to a distance of about 20 Earth radii.

Cluster is a multi-craft mission with all four satellites possessing 11 identical instruments as summarised in Table 3.1 below. They can be used together to study the small-scale plasma structures in three dimensions in key plasma regions.

TABLE 3.1: List of the instruments on Cluster and their principal investigators from (*Escoubet et al.*, 1997).

Instrument	Principal Investigator
ASPOC (Spacecraft potential control)	K. Torkar (IFR, A)
CIS (Ion Composition)	H. Rème (CESR, F)
EDI (Plasma Drift Velocity)	G. Paschmann (MPE, D)
FGM (Magnetometer)	A. Balogh (IC, UK)
PEACE (Electrons)	A. Fazakerley (MSSL, UK)
RAPID (High energy electrons and ions)	P. Daly (MPAe, D)
DWP * (Wave processor)	H. Alleyne (Sheffield, UK)
EFW * (Electric field and waves)	M. André (IRFU, S)
STAFF * (Magnetic and electric fluctuations)	N. Cornilleau (CETP, F)
WBD * (Electric field and wave forms)	D. Gurnett (IOWA, USA)
WHISPER * (Electron density and waves)	P. Décréau (LPCE, F)
* wave experiment consortium (WEC)	

3.2.1 Top Hat Electrostatic Analyser

The top hat electrostatic analyser, as used in the PEACE and CIS instruments, is a design of charged particle detector frequently used in the study of space plasmas. This model of electrostatic analyser was selected for its 'fly-through' geometry of the input aperture and its design enables better low energy performance than the 'Triquadrispherical' type used on other missions. The top hat analyser's improved low energy performance is due to incident particles (whose energies are too high to pass through the analyser plates) being able to travel right through the instrument without impacting any part of the structure. In effect, minimising the number of secondary electrons created within the analyser, improving the measurement of low-energy electrons (*Johnstone et al.*, 1997).

The basic geometry of the Top Hat analyser consists of an inner and an outer hemispherical plate, a collimator 'cover' above them as well as an annular microchannel plate and position-sensitive readout detector, see Figure 3.2. For electrons, the inner hemisphere is charged positively while the outer hemisphere is grounded, giving the systems a potential difference. This allows the detection of electrons as at a specific potential difference, only the trajectory of electrons with specific energies can be deflected cleanly between the two plates and impact onto the position-sensitive detector (anode) at the end of the track. The trajectories of electrons with higher energies than selected will be deflected less and therefore impact with the outer hemisphere while electrons with lower energies will be deflected more and therefore impact with the inner hemisphere. This method allows the construction of an electron velocity distribution and the potential difference can be swept from high to low values, allowing the selection of electrons with varying energies. Energy sweeps are carried out an integer number of times per

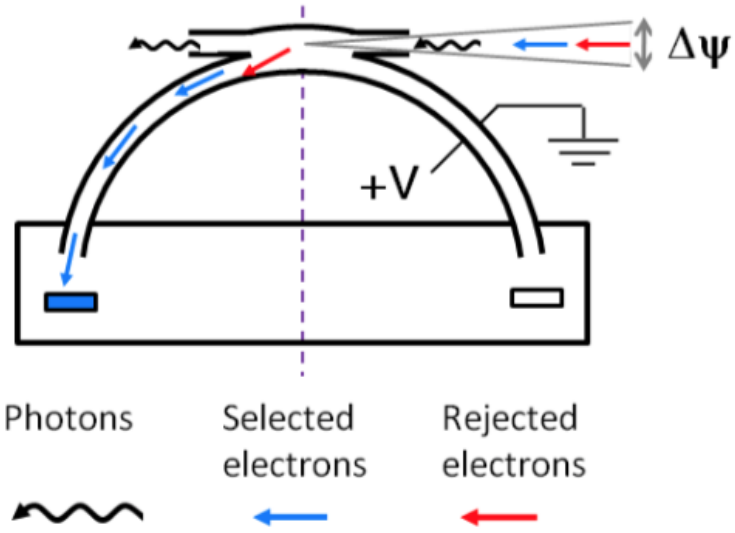

FIGURE 3.2: Geometry of the PEACE Top Hat electrostatic analyser (*Fazakerley et al.*, 2013).

spacecraft spin. The instrument's energy range is split into 88 discrete energy levels. The first 16 are spaced linearly between 0.59eV and 9.45eV and the other 72 levels are spaced logarithmically over the remainder of the energy range (*Johnstone et al.*, 1997; *Carlson et al.*, 1982).

Detecting the impact of a single particle is very difficult, as a result, these analysers employ the mechanism of a particle cascade in order to increase the probability of successfully detecting an incident electron. It uses two microchannel plates (MCP) layered on top of each other and placed between the two hemispheres and the readout detector. MCPs are electron multipliers and are manufactured from a lead glass and full of tiny hollow channels angled slightly off-vertical to the MCP input surface. As an incident electron strikes the inside of one of the channels, it triggers the emission of secondary electrons. These then shower down onto the second MCP, causing the same emissions to happen again. This 'shower' of electrons is significantly easier to detect than a single incident electron and hence improving the probability of making reliable particle detections (*Wiza*, 1979).

3.3 Cluster's Particle Detection Instruments

Both of the Cluster particle detection instruments used in the research presented in this thesis employ spectroscopic analysers based on the top hat electrostatic analyser design. The primary difference between PEACE (Plasma Electron And Current Experiment)

and CIS (Cluster Ion Spectrometry experiment) is that PEACE is an electron detector, so the mass of the particle to be detected is already known. For CIS, an ion detector, particle mass varies greatly and so it is important for CIS to have the ability to distinguish between ion species. This section will give a brief overview of the particle detection instruments used in this investigation.

3.3.1 CIS Instrument

The CIS experiment (*Rème et al.*, 1997; *Rème et al.*, 2001) is a highly versatile plasma experiment, carried on all of the Cluster spacecraft, capable of measuring the full three-dimensional ion distribution every spin. It was incorporated into the Cluster mission in order to provide considerable contributions to the study of magnetospheric interactions, dynamics and reconnection events as well as plasma sheet dynamics and current sheet phenomena. CIS consists of two top hat electrostatic analysers, CODIF (COmposition and DIstribution Function analyser) and HIA (Hot Ion Analyser), providing a wide dynamic range which allows the instrument to detect particles in sparsely populated regions such as the magnetospheric lobes.

3.3.1.1 CODIF

CODIF is a highly sensitive mass-resolving spectrometer instrument with the capability of measuring a full 3D distribution of the major ion species (H, He^{+}, He^{++}, and O^{+}) every spin of the spacecraft and covers the energy range between 0.02 and 40 keV/charge. The instrument is made up of two 180° field-of-view segments operating at two different sensitivities, this allows CODIF to take measurements over a large dynamic range from low density regions such as the magnetospheric lobes, to highly-dense regions such as the magnetosheath. The two segments feed ions into an electrostatic analyser which provides energy-per-charge. The particles then reach the time-of-flight section (*Mobius et al.*, 1985) which measures the mass per charge ratio, allowing the distinction between ionic species. The time of flight detector allows the discrimination between particles of mass with the same momentum using their time of flight between scintillators attached to photomultiplier tubes. Energy via ionisation is released when a charged particle crosses the first scintillator, which absorbs the particle's energy and emits photons. These photons travel down through the scintillator to the photomultiplier tube (PMT). Once the photons reach the PMT, the emission of electrons is induced and amplified by the PMT to produce a measurable electrical pulse. The particle's time of flight is the time difference between the initial interaction with the scintillator and the final electrical pulse.

	C1	C2	C3	C4
CODIF	Operations until 25 Oct. 2004	Not operational	1 deficient MCP quadrant, operational until 11th Nov. 2009	Normal operations
HIA	Normal operations	Not operational	Normal operations until 11th Nov. 2009	Not operational

TABLE 3.2: A summary of CIS instrument status for all Cluster spacecraft (*Dandouras and the CIS Team*, 2017).

CODIF also has a Retarding Potential Analyser (RPA) allowing the detection of ions with energies lower than 15eV. When the RPA is active, CODIF cannot detect higher energy ions, and in practice the system was hardly ever used.

3.3.1.2 HIA

HIA is an ion spectrometer which uses electrostatic deflection in a symmetrical quadrispherical analyser (similar to PEACE's top hat geometry) to find ion energy per charge in order to detect incident ions with a fast imaging particle detection system. HIA provides an instantaneous 2D distribution every 1/64 of one spin with a full 360deg distribution in the energy range of 0.005keV/charge to 32keV/charge at spin resolution. Unlike CODIF, HIA cannot discriminate between ion species, although it does have higher energy and improved angular resolution. Finally, the operationality of the CIS instruments across all four Cluster spacecraft is described in Table 3.2.

3.3.2 PEACE Instrument

The PEACE instrument was incorporated into the Cluster mission to measure the electron distribution in the near-Earth environment as accurately and with the best spatial, temporal and energy resolution possible. The main aims were to explore the nature and causes of processes such as acceleration, scattering and diffusion of electrons, all of which affect the charged particle's distribution.

PEACE is an electron spectrometer made up of two sensors, HEEA (High Energy Electron Analyser) and LEEA (Low Energy Electron Analyser) and also a DPU (Digital Processing Unit). The instrument uses differential electrostatic analysers with electron multipliers to measure the three-dimensional electron velocity distribution in the energy range 0.59eV to 26.4keV at spin resolution (about every four seconds) (*Johnstone et al.*, 1997). The HEEA and LEEA are both Top Hat Electrostatic analysers and are identical in their electron optical design, except for the input aperture and collimator (LEEA has a reduced entrance collimator field of view and the size of the input aperture is also

reduced). While both sensors can cover the full energy range, the difference in their optical systems means LEEA has a lower geometric factor[1] than HEEA (by a factor of four). This lower geometric factor provides the sensor with a greater performance for the measurement of lower energy electrons (detecting electrons with energies between 0.59eV and 9.45eV). Conversely, HEEA's larger geometric factor extends the PEACE instrument's dynamic range. These top hat analysers have an angular field of view of 180°, meaning they can be positioned back-to-back directed radially outward from the spacecraft. This set-up allows the analyser to cover the complete angular range every half spin of the spacecraft.

In order to obtain a full three-dimensional particle distribution, both energy and direction of arrival must be measured. The LEEA and HEEA sensors create a full 360° field of view in the polar direction with both sensors having a 180° field of view each. They also have an azimuthal field of view of 2.79°± 0.14° and 5.27°± 0.20° respectively. Due to this setup, PEACE obtains a complete view of the sky once per spin, about every four seconds. Polar angles are measured with respect to the spacecraft's spin axis and the azimuthal angles measured in the spin plane. The instrument mounting and fields of view are depicted in Figure 3.3.

The polar resolution of each PEACE sensor is determined by the position-sensitive detector. Both LEEA and HEEA sensors are split up into 12 anodes, each with a 15° field of view, thus they both have a polar resolution of 15°. Each zone is subdivided into four fine zones of 3.75° in order to provide a more detailed resolution.

The PEACE sensor's azimuthal resolution is determined by the number of complete energy sweeps made per spacecraft spin. In general, the more energy samples collected, the longer the sweep takes to complete. The sweeps are adjusted so that high energy electrons are detected when the instrument entrance aperture is directed towards the sun. This is carried out to minimise the number of photons entering the system during low energy detection, as the potential photoelectrons created through photon interaction can affect low energy measurements. There are four sweeps modes available:

- High Angular Resolution (HAR):
  The instrument sweeps collect 30 energy levels with 64 sweeps per spin. As a result the azimuthal resolution is 5.625°.

[1]The geometric factor of a sensor is a combination of two main factors: the geometrical response of the analyser with the collimator, which is controlled by the mechanical structure of the analyser; and the efficiency of the micro channel plate, which is dependant on the surface of the plate and can change with use (*Johnstone et al.*, 1997).

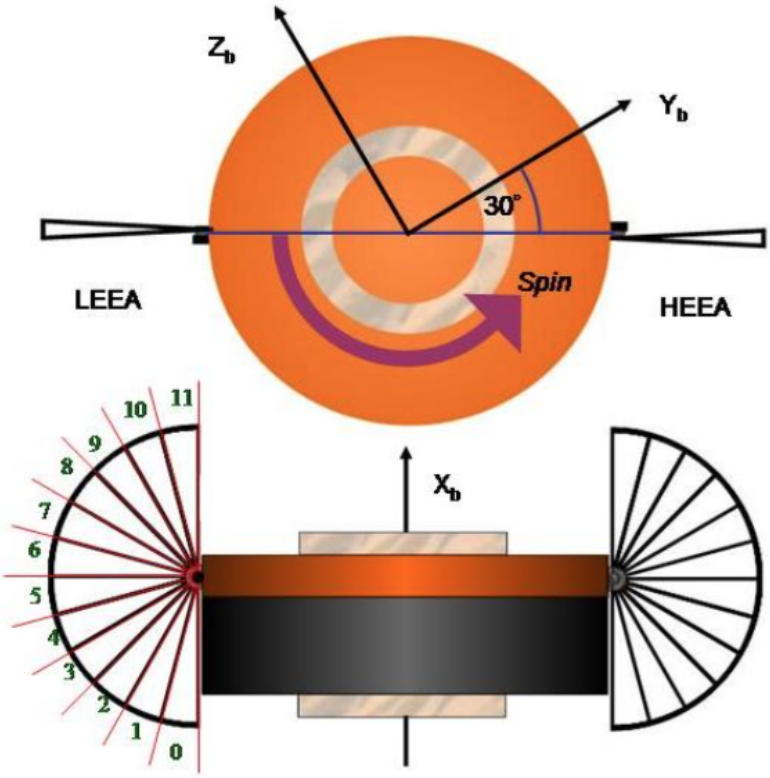

FIGURE 3.3: The sensor mounting on the spacecraft. The sensor numbering with respect to the spin axis is indicated, e.g., zone 0 looks towards Xb. In orbit the spacecraft spin axes are maintained roughly anti-parallel to the GSE Z axis (*Fazakerley et al.*, 2013).

- Medium Angular Resolution (MAR):
  The instrument sweeps through 60 energy levels at 32 sweeps per spin, giving an azimuthal resolution of 11.25°.
- Low Angular Resolution (LAR):
  The instrument's sweep includes 60 energy levels and 16 sweeps per spin and has an azimuthal resolution of 22.5°.
- Fixed Energy (FE):
  Used for operations and ground testing. A high time resolution can be obtained during a constant energy of up to 1800eV.

3.3.2.1 Data Distributions and Moments

Particle distributions functions and moments have been previously mentioned, but not discussed in any detail. This section will delve into this a little deeper to describe how the data products used within this thesis were obtained.

A particle distribution function essentially quantitatively describes how values of a property are distributed amongst its entire population. For example, when using particle detectors on the Cluster spacecraft, a full distribution of data is collected once per spacecraft rotation, and the moments of the distribution can be calculated from this. The practicality of using the moments calculated is questionable since they essentially reduce detailed information about a population down to just a few numbers, however distribution functions contain such a huge amount of data providing a level of detail that is just not needed in this study of plasma convection, and as such they are more useful that the full distribution function in the study presented in this thesis. Moments are a physical quantity which is related to the probability distribution. In general, the distribution function depends on velocity, space and time, whereas physical properties such as density, bulk flow velocity and temperature only depend on space and time. In order to obtain a quantity that does not depend on velocity, an integration over all velocities contributing to the quantity must be carried out. In order to obtain the i-th moment of the distribution function, the following integral must be calculated:

$$M_n = \int f(\mathbf{v})\mathbf{v}^n d^3v \tag{3.1}$$

where f($\mathbf{v}$) is the distribution function for the distribution of particles with velocity $\mathbf{v}^n$ denotes the n-fold diadic product (a tensor of rank n). The number of moments which can be calculated from this distribution function is infinite, however the first few are the only ones of real interest here. The first four moments are are; the the number density, N, the number flux density vector, N$\mathbf{V}$, the momentum flux density tensor, Π, and the energy flux density vector, $\mathbf{Q}$:

$$N = \int f(v)d^3v \tag{3.2}$$

$$N\mathbf{V} = \int f(\mathbf{v})\mathbf{v}d^3v \tag{3.3}$$

$$\Pi = m\int f(\mathbf{v})\mathbf{v}\mathbf{v}d^3v \tag{3.4}$$

$$\mathbf{Q} = \frac{m}{2}\int f(\mathbf{v})v^2\mathbf{v}d^3v \tag{3.5}$$

Where m is the mass and v is the average ion velocity.

Multiplying N and N$\mathbf{V}$ with the particle mass m, it is possible to obtain the mass density, , and the mass flux density vector, $\mathbf{V}$. From the zeroth and first-order moments it is possible to compute the average velocity, $\mathbf{V}$, of the particles, referred to as the bulk velocity:

$$\mathbf{V} = (N\mathbf{V})/N \tag{3.6}$$

Converting the momentum flux tensor and the energy flux vector to the frame where the average velocity is zero, it is possible to obtain the pressure tensor, P, and the heat flux vector, $\mathbf{H}$:

$$\mathbf{P} = \Pi - \rho\mathbf{V}\mathbf{V} \tag{3.7}$$

$$\mathbf{H} = \mathbf{Q} - \mathbf{V} \cdot \mathbf{P} - \frac{1}{2}\mathbf{V}Tr(P) \tag{3.8}$$

In general, there are two kinds of moment (a quantitative measurement returning a single value to represent a spread of data points) data returned by the spacecraft, ground-based and on-board moments. The first are created on Earth after selected distribution functions are transmitted to the ground during a dedicated information transmission period. The second type is when multiple spacecraft instruments are in operation and thus limiting bandwidth available to transmit data back to Earth. This is the most common scenario and due to the reduced transmission bandwidth, the whole raw data set cannot be returned to Earth so the moment must be calculated on the spacecraft.

This section has so far only discussed the calculation of a single particle species; however later on in Chapter 6, electron moments are used and thus it is necessary to take a look at how they are derived. Separate sets of moments can be calculated for each particle species and from these individual sets of moments, single-fluid quantities can be derived.

Using electrons and protons as an example, the equations are easily generalised to more than two species:

$$\rho = N_e m_e + N_i m_i = \rho_e + \rho_i \tag{3.9}$$

$$N = N_e + N_i \tag{3.10}$$

$$\mathbf{V} = \frac{(\rho_e \mathbf{V}_e + \rho_i \mathbf{V}_i)}{\rho_e + \rho_i} \tag{3.11}$$

$$P = P_e^{CM} + P_i^{CM} \tag{3.12}$$

It must be noted that in general the total pressure is not the sum of the partial pressures if the latter are computed in the bulk-velocity frames of the individual species. Instead the individual pressures must be computed in their joint centre-of-mass frame, which are superscripted with CM.

3.3.2.2 Spacecraft Charging, Secondary Electrons and Photoelectron Contamination

Secondary electrons created within the instrument can cause inaccurate measurements as they generate an undesirable background signal. As a result, the probability of them being created in the first place must be reduced and they must also be accounted for. There are two sources of these particles, both of which populate the 1eV to 10eV energy range. The first originate from incident electrons with an energy higher than the instrument is set up to measure. They have too much energy and therefore are not deflected sufficiently by the electric field along the instrument track. Consequently, they impact with the outer hemispherical plate near the entrance aperture, creating the low energy secondary electrons. The second source is due to the influx of solar ultraviolet radiation, generating secondary photoelectrons, however, they can only be created when the Sun is within the analyser's field of view.

The effect of sunlight on the sensor must be reduced in order to minimise any contamination which may occur. In order to do this, baffles are incorporated in the input collimator, along with highly absorbent, diffusely reflecting surfaces within. This method reduces the possibility in which the detector can be stimulated via internal reflections or direct illumination via the action of ultraviolet light. In addition, the background signal created by the internally generated secondaries and other penetrating radiation must be quantified in order to be accounted for. This can done by biassing a grid placed in front of the microchannel plates by -8V, repelling incident electrons and setting the plate voltage to the minimum of 0.59eV. No electrons can reach the detector through the instrument's track once these settings are in place and therefore any signals detected

must be generated by penetrating radiation or scattered secondary particles (*Johnstone et al.*, 1997). This phenomenon is often called internal spacecraft charging.

Charge can also accumulate on the surface of a spacecraft. The main contributors to this effect are: plasma interactions, incident charged particles, solar radiation and the Earth's magnetic field.

Plasma affects the spacecraft by inducing charges on its surfaces due to the flux of electrons and positive ions. The motion of the spacecraft through the plasma environment can also lead to the creation of a local environment (spacecraft wake) which can also create additional spacecraft charging. The presence of charged particles in the local vicinity of the spacecraft plays a large part in its charging. Generally electrons are more mobile than ions due to their smaller mass, giving them a higher thermal speed, hence electrons flux tends to dominate. This means that overall, negative electron current is larger than positive ion current. From this, a spacecraft's surface tends to charge negatively to a potential of the order of the electron temperature. However, when the spacecraft if illuminated by the Sun, Solar radiation acts to oppose this charging effect. As photons emitted from the Sun impact with the spacecraft, they interact via the photoelectric effect and as a result the spacecraft emits photoelectrons. These constitute as a current flowing into the spacecraft and therefore can reduce the effect of negative surface charging. When this occurs for an extended period, it is possible for the spacecraft to become positively charged as the rate of photo-emission can dominate.

Finally the Earth's magnetic field determines the regions of space where spacecraft charging can occur as well as affecting the escape of photoelectrons from the craft (*Mikaelian*, 2009).

When the spacecraft becomes charged, it interacts with the ambient charged particles surrounding it, altering the incoming and outgoing particle flux, giving rise to the magnitude of the spacecraft potential. Its value varies in different regions; for example, in areas of high density such as within the tail plasma sheet, the spacecraft experiences a much lower potential, of the order of tens of volts, whereas in low density regions, such as tail lobes, the potential can reach up to 100V. Cluster has the Active Spacecraft POtential Control (ASPOC) system installed which emits a beam of positive ions away from the craft, helping to reduce the spacecraft potential and maintain it below 2V. This minimises the number of electrons returning back to the spacecraft (*Szita et al.*, 2001).

The acceleration of ambient charged particles due to spacecraft charging changes the distribution in which they would ordinarily be observed. It adjusts their energy and direction of motion and therefore a measurement of the spacecraft potential must be taken so it can be accounted for in the results. This is particularly important while

measuring low-energy electrons as the energy band in which they sit can often be very close to that of the spacecraft potential. Photoelectrons are also detected by the PEACE instrument and thus the measured particle distribution can differ from the natural distribution. The contribution of both photoelectron and ambient-electron contamination is mitigated from both the ground-based and onboard moments.

Onboard moment calculations follow the assumption that raw data with energies below 10 eV must be contaminated and thus all raw data in this energy range are removed before any moment calculations are made. The ground moments are somewhat different as they use the measured spacecraft potential, and in addition, the user can also add a further offset if they have grounds to believe that the measured spacecraft potential (which is the potential difference between the spacecraft and the ends of the booms) is not representative of the real spacecraft potential (between the spacecraft and infinity). This is another reason as to why the latter are more accurate.

3.3.2.3 Instrument Calibration and The V_z Problem

Each Cluster spacecraft's spin plane is approximately aligned with the XY plane in the GSE coordinate system. Vector quantities collected by PEACE in the XY plane usually depend on electron fluxes measured by the same anode at different times during the craft's spin. Essentially, V_x is calculated using electron flux measurements collected by PEACE anodes with a component of their field of view in the direction of the spin plane, taking the difference between the Earthward and tailward measurements. Vectors taken out of the spin plane of the Cluster craft (V_z) are based on measurements combined across a number of different anodes. The final vector quantity can be affected by calibration uncertainties between the anodes, leading to a systematic offset from zero of the Z component of electron velocity (GSE). Inter-anode calibration has been carried out to all but eliminate this problem, although the anodes need to be recalibrated frequently as the sensors deteriorate over time (*Walsh*, 2009). The calibration makes use of a time dependent correction factor which is essentially a time history of anode sensitivity variations. A second correction factor is applied in order to satisfy the requirement that when measuring gyrotropic pitch angle distributions which are invariant over short time-scales, the same pitch angle may be observed by multiple anodes such that all of these anodes should yield that same electron flux measurements.

Version	Alpha	Inter-anode	Calibration Details	Validity Details
v5.1	yes	yes	Alpha factors derived using weekly MCP test method. Inter-anode calibration included.	C1,2(L&H) Jan01-May07 C3,4(H) Jan01-May07 C3(L) Jan01-10Apr07 C4(L) Jan01-16May06

TABLE 3.3: The dates over which the inter-anode calibration was carried out (*Fazakerley et al.*, 2013).

3.4 Cluster's Magnetic Field Detection Instrument

3.4.1 The Fluxgate Magnetometer (FGM)

The fluxgate magnetometer is based on the theory of H. Aschenbrenner and G. Goubau, developed in 1936. It has been widely used to carry out magnetic field measurements in space from as early as 1958 on the Sputnik 3 satellite (*Musmann*, 2010). It provides information about the strength and direction of three components of the ambient magnetic field around the satellite using triaxial orthogonal arrangements of single axis sensors.

The fluxgate sensor is made up of a permeable ferromagnetic core wrapped in a sensing coil. It operates by gating the ambient magnetic flux threading the coil, this occurs by periodically saturating the magnetic core in opposite directions with an excitation signal. This method of gating the ambient field gives rise to a time varying magnetic field which in turn induces a voltage in the sensing coil proportional to the strength and direction of the magnetic field (*Acuña*, 2002; *Grosz et al.*, 2016).

The FGM instrument (*Balogh et al.*, 1997, 2001) on each of the four Cluster spacecraft measure the magnetic field in the plasma environment surrounding them. They are made up of a data processing unit (DPU) and two tri-axial fluxgate magnetometers (magnetic field sensors) positioned on one of the spacecrafts 5.2m radial booms. The primary sensor is placed at the end of the boom with the secondary sensor 1.5m from the end, although either can be designated as the primary sensor via a telemetered command. The instrument is set up in this way to minimise contamination from the residual magnetic field of the spacecraft. Both sensors measure magnetic field in three dimensions and while the magnetometers are capable of operating across eight different field strength ranges, only five are utilised on Cluster, shown in Table 3.4. All three magnetic field components are measured using the same range and resolution at any given time. The instrument range and resolution can either be selected by telemetered commands or automatically chosen by the DPU. If the latter method of selection is used, the DPU constantly monitors the magnetic field components and if one exceeds 90% of the maximum values measurable in the current data range, the DPU increases the range.

Range Number	Range	Resolution
2	-64 nT to +63.97 nT	7.8×10^{-3} nT
3	-256 nT to +255.87 nT	3.1×10^{-2} nT
4	-1024 nT to +1023.5 nT	0.125 nT
5	-4096 nT to +4094 nT	0.5 nT
7	-65536 nT to +65504 nT	8 nT

TABLE 3.4: FGM data range and resolution modes (*Balogh et al.*, 2001). Ranges 2 to 5 are used on Cluster, range 7 is only used during ground testing.

Likewise, if all three of the field components are less than 10% of the minimum value measurable (for more than one spin period), then the range is decreased. These ranges were selected to give a good resolution in regions with the lowest expected magnetic field magnitudes, such as in the solar wind (between 3 and 30 nT), right up to the highest field values expected in the magnetosphere (up to about 1000 nT).

3.5 Magnetospheric Lobe Identification

The magnetospheric lobes are regions of very low plasma density (around $10\,m^{-3}$) and are populated with open magnetic field lines (*Kivelson and Russell*, 1995). When PEACE electron data are used, it is important that any data collected at the lobes are removed from the dataset as it is fraught with inconsistencies and errors. There are two main reasons for this; the first being that the PEACE instrument's lower sensitivity boundary is about $50\,m^{-3}$ (*Johnstone et al.*, 1997), which is somewhat higher than the average plasma density in the lobes. The second reason is that when the Cluster satellites are orbiting in regions of such low plasma density, the spacecraft potential can become dominant (discussed in section 3.3.2.2), which can lead to the deflection and acceleration of the incident particles, returning incorrect values.

In order to exclude magnetospheric lobe data from the analysis carried out in this thesis, two methods of magnetospheric lobe identification were used throughout; the European Cluster Assimilation Technology (ECLAT) dataset and the Coxon terrestrial lobe identification method (the Coxon method) and are discussed below.

3.5.1 ECLAT Dataset

The European Cluster Assimilation Technology (ECLAT) project produced a magnetotail plasma-region dataset. It is a comprehensive list of the plasma regions encountered by the Cluster spacecraft on the nightside of the Earth between 2001 and 2009. The

Plasma Region
Northern hemisphere tail lobe region
Southern hemisphere tail lobe region
Northern hemisphere boundary region
Southern hemisphere boundary region
Northern hemisphere outer plasma sheet
Southern hemisphere outer plasma sheet
Northern hemisphere inner plasma sheet
Southern hemisphere inner plasma sheet
North-south crossing of the neutral sheet
South-north crossing of the neutral sheet

TABLE 3.5: The plasma regions defined by the ECLAT dataset.

five regions identified are the most important and interesting plasma regions where the major energy-transport occurs, and are shown in Table 3.5.

The apogee of each Cluster spacecraft's orbit is situated on the nightside of the Earth for four months of the year, from the start of July to the end of October, the tail-season. Statistical studies were carried out on the tail-season for each year between 2001 and 2009 to identify the plasma regions. A tail-region box was initialised in order to avoid mis-identification of plasma sheet regions when the spacecraft cross into non-tail regions such as the magnetosheath. This box was set up with dimensions of X < -8R_E and $|Y| < 15R_E$ using GSM coordinates.

The ECLAT team expanded on the traditional use of plasma beta (the ratio of the plasma dynamic and magnetic pressure, giving an indication of what is controlling the plasma motion at a given time (*Tascione*, 1994)) to define different tail plasma regions taking advantage of Cluster's tetrahedral configuration. The plasma regions were defined by deriving new thresholds in plasma beta and magnetic field based on the statistical profile on tail current-density. These current densities are found from magnetic field gradients across the four Cluster spacecraft; essentially the net current through the spacecraft tetrahedron is determined. The plasma parameters are determined for each tail-season separately and the region conditions are shown in Figure 3.6 (*Boakes et al.*, 2014).

The magnetotail lobes were described as the high latitude region of low plasma density corresponding to the region of open magnetic field lines.

The undefined region (UR) contains intervals where regions could not be determined. Any data collected outside of the tail-region box are classed as undefined. This is because outside of this box, the plasma environment can change frequently due to the dynamic variability of the outer regions which often leads to identification of non-tail regions, which was to be avoided. Another method of undefined-region classification was if two consecutive data points were greater than 32 seconds apart, it was deemed too long an

Region	SC	Instrument and condition								
		2001	2002	2003	2004	2005	2006	2007	2008	2009
LOBE	C1	CODIF H1	CODIF H1	CODIF H1	HIA beta	HIA beta	HIA beta	HIA beta	HIA beta	HIA beta
		beta	beta	beta	<0.009	<0.01	<0.01	<0.022	<0.02	<0.025
		<0.02	<0.025	<0.015						
	C2	PEACE beta	PEACE beta	PEACE beta	PEACE beta	PEACE beta	PEACE beta	PEACE beta	PEACE beta	PEACE beta
		<0.005	<0.008	<0.0025	<0.0055	<0.0055	<0.0065	<0.0065	<0.01	<0.013
	C3	CODIF H1	CODIF H1	HIA beta	HIA beta	HIA beta	HIA beta	HIA beta	HIA beta	HIA beta
		beta	beta	<0.009	<0.009	<0.01	<0.01	<0.022	<0.02	<0.025
		<0.02	<0.025							
	C4	CODIF H1	CODIF H1	CODIF H1	CODIF H1	CODIF H1	CODIF H1	CODIF H1	CODIF H1	CODIF H1
		beta	beta	beta	beta	beta	beta	beta	beta	beta
		<0.02	<0.025	<0.015	<0.015	<0.01	<0.017	<0.017	<0.015	<0.02
BR	C1	CODIF H1	CODIF H1	CODIF H1	HIA beta	HIA beta	HIA beta	HIA beta	HIA beta	HIA beta
		beta	beta	beta	0.009–0.07	0.01–0.08	0.01–0.08	0.022–0.09	0.02–0.1	0.025–0.16
		0.02–0.12	0.025–0.16	0.015–0.12						
	C2	PEACE beta	PEACE beta	PEACE beta	PEACE beta	PEACE beta	PEACE beta	PEACE beta	PEACE beta	PEACE beta
		0.005–0.05	0.008–0.05	0.0025–0.03	0.0055–0.025	0.0055–0.06	0.0065–0.02	0.0065–0.056	0.01–0.04	0.013–0.035
	C3	CODIF H1	CODIF H1	HIA beta	HIA beta	HIA beta	HIA beta	HIA beta	HIA beta	HIA beta
		beta	beta	0.009–0.05	0.009–0.07	0.01–0.08	0.01–0.08	0.022–0.09	0.02–0.1	0.025–0.16
		0.02–0.12	0.025–0.16							
	C4	CODIF H1	CODIF H1	CODIF H1	CODIF H1	CODIF H1	CODIF H1	CODIF H1	CODIF H1	CODIF H1
		beta	beta	beta	beta	beta	beta	beta	beta	beta
		0.02–0.12	0.025–0.16	0.015–0.12	0.015–0.16	0.01–0.17	0.017–0.08	0.017–0.13	0.015–0.3	0.02–0.13
OPS	C1	CODIF H1	CODIF H1	CODIF H1	HIA beta	HIA beta	HIA beta	HIA beta	HIA beta	HIA beta
		beta	beta	beta	>0.07	>0.08	>0.08	>0.09	>0.1	>0.16
		>0.12	>0.16	>0.12	$B_{xy} > 14$	$B_{xy} > 15$	$B_{xy} > 15$	$B_{xy} > 13$	$B_{xy} > 13$	$B_{xy} > 11.5$
		$B_{xy} > 13$	$B_{xy} > 15$	$B_{xy} > 14$						
	C2	PEACE beta	PEACE beta	PEACE beta	PEACE beta	PEACE beta	PEACE beta	PEACE beta	PEACE beta	PEACE beta
		>0.05	>0.05	>0.0025	>0.0055	>0.0055	>0.0065	>0.0065	>0.01	>0.013
		$B_{xy} > 13$	$B_{xy} > 15$	$B_{xy} > 14$	$B_{xy} > 14$	$B_{xy} > 15$	$B_{xy} > 15$	$B_{xy} > 13$	$B_{xy} > 13$	$B_{xy} > 11.5$
		CODIF H1	CODIF H1	HIA beta	HIA beta	HIA beta	HIA beta	HIA beta	HIA beta	HIA beta
	C3	beta	beta	>0.05	>0.07	>0.08	>0.08	>0.09	>0.1	>0.16
		>0.12	>0.16	$B_{xy} > 14$	$B_{xy} > 14$	$B_{xy} > 15$	$B_{xy} > 15$	$B_{xy} > 13$	$B_{xy} > 13$	$B_{xy} > 11.5$
		$B_{xy} > 13$	$B_{xy} > 15$							
	C4	CODIF H1	CODIF H1	CODIF H1	CODIF H1	CODIF H1	CODIF H1	CODIF H1	CODIF H1	CODIF H1
		beta	beta	beta	beta	beta	beta	beta	beta	beta
		>0.12	>0.16	>0.1	>0.16	>0.17	>0.08	>0.13	>0.3	>0.13
		$B_{xy} > 13$	$B_{xy} > 15$	$B_{xy} > 14$	$B_{xy} > 14$	$B_{xy} > 15$	$B_{xy} > 15$	$B_{xy} > 13$	$B_{xy} > 13$	$B_{xy} > 11.5$
IPS	C1									
	C2	$B_{xy} < 13$	$B_{xy} < 15$	$B_{xy} < 14$	$B_{xy} < 14$	$B_{xy} < 15$	$B_{xy} < 15$	$B_{xy} < 13$	$B_{xy} < 13$	$B_{xy} < 11.5$
	C3									
	C4									
NSR	All SC	The region bracketing $B_x = 0$ crossing or $B_x = 0$ data point								

TABLE 3.6: Region identifcation, boundary conditions, and instruments used (*Boakes et al.*, 2014).

interval for the spacecraft to have remained in the same plasma region, and therefore the region was split into two with the two new regions separated with an undefined region. One final example of UR classification was during periods of high solar wind ram pressure. This phenomenon causes increased magnetospheric compression and in these periods, the spacecraft can occasionally cross through into the magnetosheath. In order to remove this non-tail region, any data in the $|YZ| > 10\mathrm{R}_E$ region (where $|\mathrm{YZ}| = \sqrt{Y^2 + Z^2}$ Y is the spacecraft's y-position and Z is the spacecraft's z-position using GSE coordinates) with a tailward flow-speed greater than 300 km s^{-1} and plasma density of more than 1 particle per cm^3 are redefined as being in an undefined region.

The main regions focussed on during the use of the ECLAT data set were the northern and southern hemisphere lobes and the undefined regions. The other regions identified by ECLAT were not treated separately during the data analysis because it was decided that doing this was unnecessary (*Boakes et al.*, 2014).

3.6 Coxon Lobe Identification

The Coxon model is described in *Coxon et al.* (2016). The method builds up on ideas presented by Jackman and Arridge in a study on Kronian lobe identification (*Jackman and Arridge*, 2011). They identify that the spacecraft is in the Kronian lobe during periods of time where there is low plasma density (in comparison to the plasma sheet) in conjunction with a fairly strong and steady magnetic field. Coxon's method uses the same concept, but neglects looking for times of low plasma density in order to exclusively use FGM magnetometer data. The following list highlights the selection criteria they used.

1. $\mathrm{X}_{GSE} > 0\mathrm{R}_E$
2. Radial distance to Earth $\mathrm{R} \geq 8\mathrm{R}_E$
3. $\sigma \leq \sigma_0$
4. $|\mathrm{B}_X| \geq \mathrm{B}_0$

X_{GSE} is the sunward component of the spacecraft position in Geocentric Solar Ecliptic (GSE) coordinates, σ is the standard deviation of the magnitude of the magnetic field for 20 minutes on either side of each data point (a 40 minute sliding window), and $|\mathrm{B}_X|$ is the magnitude of the sunward component of the magnetic field in GSE coordinates. $|\mathrm{B}_0|$ and σ_0 are threshold values for the magnetic field and its standard deviation used to determine the magnetospheric lobe position, as determined by *Coxon et al.* (2016).

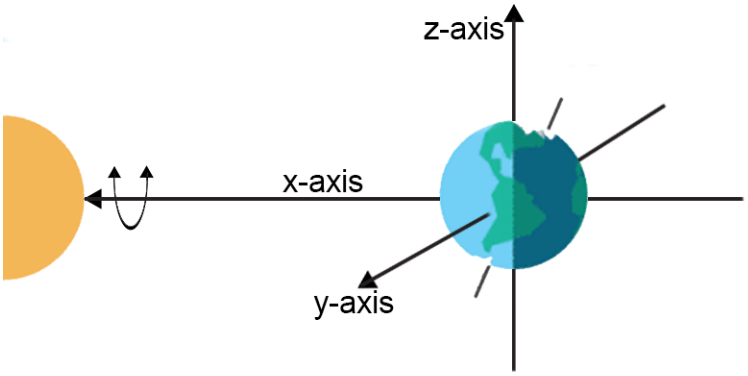

FIGURE 3.4: Illustration of GSE coordinate system.

Unlike ECLAT, a dataset containing lobe and undefined region flags needed to be created. In order to recreate Coxon's lobe identification dataset, a test dataset was created in compliance with Coxon's procedure in order to confirm that the new data set agreed with Coxon's, and thus producing the correct output data. The procedure was run for the tail-season months of 2003 using FGM data from Cluster 1 and used $\sigma_0 = 3.5$nT and $B_0 = 30$nT (taken from Table 4 in *Coxon et al.* (2016)). Results were created for both the whole year of 2003 and the tail season of the same year and were within 0.5% and 2% of Coxon's results respectively. One potential reason for how the two datasets differ could be from revisions carried out the the Cluster data-files between our respective download times. A second reason could be that perhaps different interpolation schemes were utilised across both investigations, perhaps leading to the use of different resolution data, or producing slightly different results between data points (*Coxon et al.*, 2016).

3.7 Coordinate Systems

The work presented in this thesis is based around two coordinate systems, the **Geocentric Solar Ecliptic** (GSE) and and the **Geocentric Solar Magnetospheric** (GSM) coordinate systems. The following section will briefly describe them both.

3.7.1 GSE Coordinate System

The GSE coordinate system is the fundamental system used for mapping spacecraft position relative to the centre of the Earth. As a result, it is at the core of terrestrial space science research.

The coordinate system has the Earth at its centre where the x-axis points towards the Sun along the Earth-Sun line, the y-axis is directed towards the dusk in the opposite direction to the Earth's orbit around the Sun, the z-axis lays perpendicular to both the x and y-axis to form a right-handed set. In this coordinate system, the Earth's spin axis gyrates around the z-axis once per year, and the magnetic pole gyrates in all components with a daily periodicity.

3.7.2 GSM Coordinate System

The GSM coordinate system is coordinate system based on the Earth-Sun line. It is an extension of the GSE system, with the x-axis directed towards the sun and an additional rotation about it. It is a geocentric system which rocks about the x-axis by up to $\pm$ 11.2° on yearly and daily cycles and this motion keeps the y-axis aligned with the magnetic equator and it ensures the projection of the Earth's magnetic pole is constrained to the x-z plane, giving it a two-dimensional path of motion. This coordinate system is particularly useful when working with magnetospheric magnetic fields as it reduces the positional variation of the magnetotail to the z-plane. This means that the tail only oscillates in the north-south plane (the z-plane) rather than oscillating in this direction as well as across the y-plane in the dawn-dusk direction, thus reducing the motion to two dimensions rather than three (*Bhavnani et al.*, 1991).

3.7.3 Aberrated GSM Coordinate System

The aberrated GSM coordinate system (AGSM) takes aberrations into account by rotating the GSM coordinate system by about 4 degrees rotation about the Z-axis (*Haaland et al.*, 2017).

Chapter 4

Ion Flow in the Terrestrial Magnetotail

4.1 Introduction

This chapter begins with a literature review of magnetospheric convection within the terrestrial magnetosphere, giving an overview of the research area and discussing more recent studies carried out. It then continues on the topic, discussing the research this thesis is based on, the mapping of magnetospheric convection in the Earth's magnetotail using Cluster spacecraft in the equatorial and noon-midnight meridian planes.

The solar wind, magnetosphere and ionosphere are coupled via magnetic reconnection, which *Vasyliunas* (1975) described as the process of plasma flowing across a surface which separates topologically different magnetic field lines. *Petschek* (1964) was the first to apply the idea of magnetic reconnection at the dayside magnetopause as a mechanism for converting magnetic energy into plasma energy. It took another 15 years for this phenomena to be observed with data from the ISEE 1 and 2 spacecraft to show high-speed plasma flow at the magnetopause (*Paschmann et al.*, 1979).

An explanation of magnetospheric convection, the twin cell convection observed at high latitudes (e.g. *Heppner and Maynard* (1987)) and the asymmetry of the magnetosphere (*Ness*, 1965) remained unclear for some time, with a number of different explanations being put forward [e.g. *Axford and Hines* (1961); *Dungey* (1961)]. While studying magnetic field data from the Explorer 12 satellite in conjunction with ground-based magnetometer data, *Fairfield and Cahill* (1966) found that a southerly directed IMF tended to be associated with disturbances at the ground, whereas northward directed IMF was found to be associated with quiet conditions, giving strong evidence in support

of Dungey's model. Similar results were later found by *Arnoldy* (1971), who found a linear correlation between the summation of B south over one hour periods (collected by the Explorer 33 spacecraft) and the AE index hourly average (derived from auroral zone magnetic observatories), providing further evidence in support of the Dungey cycle. Studies of the dayside location of the Earth's magnetopause show evidence of erosion of the dayside magnetosphere caused by dayside magnetic reconnection during periods of southward IMF without instantaneous replenishment of newly-closed flux from nightside reconnection (e.g. *Aubry et al.* (1970); *Haerendel et al.* (1978); *Milan et al.* (2007)). This dayside-nightside process decoupling provides evidence of how the Dungey cycle is driven. An example of further support for the Dungey cycle came somewhat later from *Zhu* (1993), who observed that most of the dayside flow vectors collected by the Fast Plasma Experiment (FPE) were directed toward the noon-meridian, leading to the notion that the 'mechanism proposed by Dungey' appears to be the principle cause of magnetospheric convection during active times. A more recent study by *Zhang et al.* (2015c) carried out observations of the full Dungey cycle during southward IMF by tracking the formation and full evolution of polar cap ionisation patches in the polar ionosphere.

Dungey (1961, 1963) proposed an open magnetic field model in his explanation of the magnetospheric system, commonly known as the Dungey cycle (previously discussed in detail in section 2.5.1). Since its inception, the Dungey cycle has become a useful paradigm to describe terrestrial magnetospheric phenomena, although it has not always been wholly accepted. In particular, Axford and Hines thought that the Dungey cycle was not able to explain the magnetospheric asymmetry as well as a closed magnetospheric system which is only driven by viscous interactions. They did however agree on the importance of convection within the magnetosphere (*Axford and Hines*, 1961; *Hines*, 1986).

Since the initial hypothesis, there have been a number of statistical studies carried out using ion moments investigating the general characteristics of magnetospheric convection. The research tends to fall into categories, that based on slow or fast plasma flow and is usually restricted to the nightside region.

On average, ion flow bulk velocity in the central plasma sheet (CPS) has been found to be of low speed, ($\sim$50 $\mathrm{km\,s^{-1}}$) (e.g. *Huang and Frank* (1986); *Baumjohann et al.* (1989)). *Angelopolous et al.* (1993) conducted a study of the quiet state of the inner plasma sheet (IPS), looking at periods of slow plasma flow in the equatorial plane. Angelopoulos and his colleagues found that at local midnight, the plasma flow was predominantly directed duskward and was caused by diamagnetic drift due to an inward pressure gradient. Closer to the flanks, flow was mostly Earthward due to the cross-tail

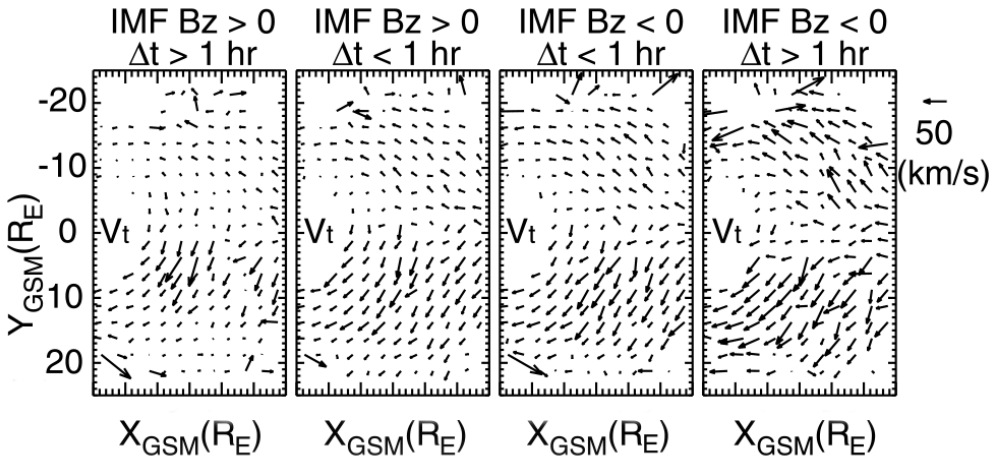

FIGURE 4.1: Perpendicular plasma flow in the equatorial plane where northward IMF is greater than one hour for different IMF B_z conditions. Only $|V_\perp| \leq 200\,\mathrm{km\,s^{-1}}$ was included in the study. The figure illustrates dawn-dusk asymmetry of perpendicular plasma flow in the Earth's magnetotail. From *Wang et al.* (2006).

electric field. Meanwhile *Zhu* (1993), using the FPE spacecraft, found that convection occurred strongly in the outer magnetosphere with a velocity of ~20-50 km s^{-1}. A third example of the study of slow plasma flow comes from *Wang et al.* (2006). Using Geotail spacecraft data, Wang reported a dawn-dusk asymmetry of perpendicular (to the magnetic field) plasma flow with the increased ion flow at the dusk side. This phenomena can be seen in Figure 4.1, where Wang plotted perpendicular plasma flow velocity vectors spatially about the Earth using the GSM coordinate system. He separated the data out according to IMF B_z conditions. It is very clear that a dawn-dusk asymmetry of plasma flow is present as higher velocities and greater deflections can clearly be seen in the dusk hemisphere (Y>0). It was suggested by Wang that this asymmetry is caused by westward diamagnetic drift (see section 2.3.6).

Dawn-dusk asymmetries are ubiquitous across the Earth's magnetosphere, from differences such as ion density and temperature in the dayside magnetosheath (*Walters*, 1964; *Walsh et al.*, 2012), to ion distribution in the inner magnetosphere (*Fok et al.*, 2003). The magnetotail is no different and while there are asymmetries across the spectrum of data products, the focus will be on plasma flows in this section. *Nishino et al.* (2007) used Geotail data to show that hot and cold ions (high and low energies respectively) flow towards midnight in the equatorial plane. Nishino argued that since two-component protons (a group of protons with separate hot and cold components though to originate from within the magnetosphere and the solar wind respectively (e.g. *Nishino et al.* (2007) and references therein)) are rarely observed in the dawn sector but frequently observed in the dusk sector, the likely source of ions at the midnight plasma sheet is the dusk flank under strong northward IMF. Another candidate for flow from the dusk

sector is turbulent flow from vortical structures of Kelvin-Helmholtz instability that develop around the dusk low-latitude boundary. Nishino also proposes that transport from the dawnside stems from viscous interactions between the high-latitude section of the plasma sheet and the magnetospheric lobes. As previously mentioned, the average quiet time plasma flow also exhibits a dawn-dusk asymmetry (*Angelopolous et al.*, 1993; *Wang et al.*, 2006) when observing slow plasma flow, but *Hori et al.* (2000) found that even when averaging all flow velocities, there is still a significant asymmetry about the noon-midnight meridian. Up until this point, only ion flow has been discussed, however there are a number of studies which have been carried out using electron velocity data by *Wang et al.* (2007) and *Walsh et al.* (2013b), using Geotail and THEMIS data respectively and both of which report electron dawn-dusk asymmetries in the plasma sheet.

The study of fast flow plasma in magnetosphere is just as extensive as that of slow plasma flow. Fast flows are often associated with substorm activity, in fact *Cao et al.* (2006) showed that almost all substorm events are associated with fast flows, with only between 2.2% and 4.5% (depending on whether single-spacecraft or multi-craft measurements are considered) being observed without them. Fast flows tend to occur in short sub-minute bursts and are likely created by impulsive magnetic reconnection. These short flow bursts are often grouped into ten-minute events called **bursty bulk flows** (BBFs) (*Angelopoulos et al.*, 1992, 1996). The BBF concept revolutionised the earlier notion of the relatively stable, large-scale phenomena of the NENL model. The observation of the intermittent bursty fast flows suggested that reconnection at the NENL was also an intermittent and bursty process, perhaps occurring at a localised X-line. The comparison of fast flow studies is relatively difficult as they often use quite different selection criteria and as a result, often offer varied results. For example, studies based on selection criteria of either $(B_x^2 + B_y^2)^{\frac{1}{2}} < 15$ nT or $\beta > 0.5$ to select plasma sheet data and $|V_x| > 400$ km s^{-1} to select BBF events did not reveal any distinct directional dependence (*Baumjohann et al.* (1990); *Angelopoulos et al.* (1994)). On the other hand, studies carried out using data from Geotail, THEMIS and WIND utilised selection criteria differentiating convective flows and field aligned flows. These studies yielded asymmetrical flow patterns for the convective flows and symmetrical flow distributions for the field aligned flows (*Nagai et al.* (1998); *Raj et al.* (2002); *McPherron et al.* (2011)).

A large-scale statistical study, incorporating data from Geotail, Cluster and THEMIS was carried out by *Juusola et al.* (2011). Figure 4.2 was taken from the paper and shows magnetospheric plasma flow speeds where the plasma beta is greater than 0.5. The length of each vector and colour of each bin shows the average speed (V_{xy}) and direction of plasma flow; with the plot on the left/right representing earthward/tailward

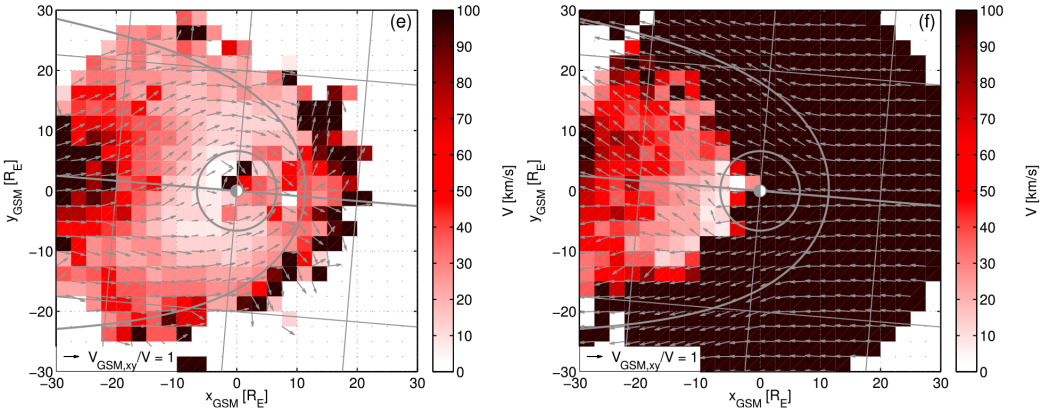

FIGURE 4.2: Magnetospheric plasma flow speed where $\beta > 0.5$ from *Juusola et al.* (2011). Vector length show speed and direction and colour also indicates the mean plasma speed (V_{xy}). (e) $V_x > 0$, (f) $V_x < 0$.

flows respectively. Juusola found on average there to be little asymmetry tailward of x = -15 R_E when using $\beta > 0.5$ to select plasma sheet data and the aberrated GSM coordinate system (AGSM), figure 4.2(e). Juusola also found that closer to Earth, when considering velocities smaller than 200 km s^{-1}, there was evidence of dawn-dusk asymmetry, although at higher velocities, they remained predominantly symmetric about midnight.

Pulkkinen et al. (2013) carried out a more recent study and although it focused on steady magnetospheric convection (SMC) events, the reference data set she created simulated average plasma conditions. The reference data set was made up of a selection of random THEMIS magnetospheric data taken three days before each steady magnetospheric convection event selected and lasting the same duration as each event, thus simulating average plasma conditions. Pulkkinen created a series of plots, seen in Figure 4.3 showing plasma flow speed in the equatorial plane using the GSM coordinate system where V is the bulk velocity ($V = \sqrt{V_X^2 + V_Y^2}$). The left plot shows the SMC data set collected, the central plot is the reference dataset Pulkkinen created and the right plot shows the difference between the two. Within each plot, the arrows and colour represent the average plasma flow direction and magnitude. The darker the coloured bin, the faster the plasma flow with red for earthward and green for tailward flows. Across 228 events, looking at Figure 4.3, there appears to be an asymmetric distribution of plasma flow with somewhat faster flows in the pre-midnight (dusk) sector. Pulkkinen used V_{xy} as part of her selection criteria and thus provides a curious result, as it contradicts some of the previous studies (e.g. *Runov et al.* (2005)) using the same velocity criteria.

Tailward or anti-sunward plasma flows have been observed in the plasma sheet across a number of studies (e.g. *Schödel et al.* (2001); *Ohtani et al.* (2009)) although its existence is often neglected when looking at average plasma conditions as earthward flow

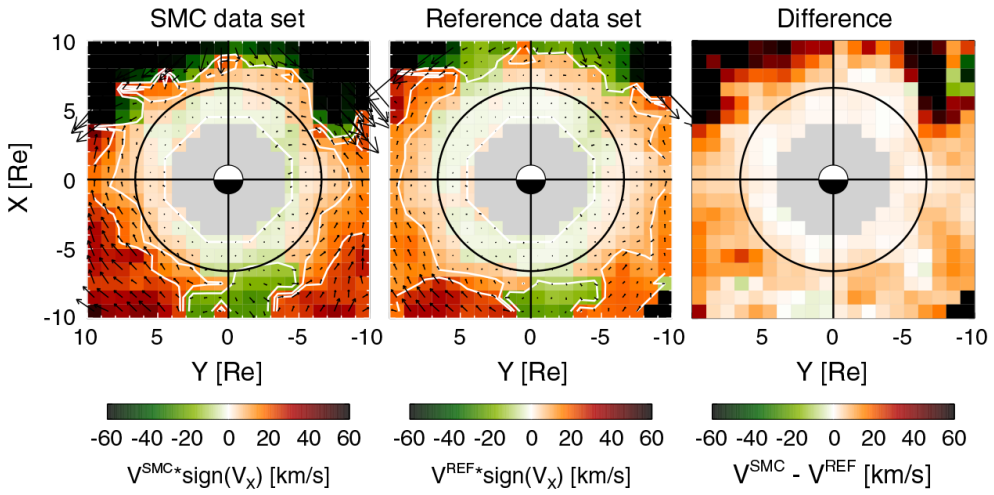

FIGURE 4.3: Plasma flow speed in the equatorial plane (GSM) where $V = \sqrt{V_X^2 + V_Y^2}$. Arrows and colour represent the average flow direction and magnitude. Red is for earthward flow and green is for tailward flow. The central figure illustrates average plasma flow from 228 events, *Pulkkinen et al.* (2013).

dominates the nightside magnetosphere. As a result, very little is actually known about these flows and they cannot be explained by traditional convection models (e.g. *Dungey* (1961); *Axford and Hines* (1961)), which focus on the earthward flow of plasma generated by magnetic reconnection of the Dungey cycle, a mechanism which cannot propel magnetospheric plasma tailward when looking earthward of the x-line. Only a handful of studies have focused on tailward flows. *Juusola et al.* (2011) noted that there was a significant amount of tailward (anti-sunward) flows in the nightside magnetosphere as seen in figure 4.2(f). It was suggested that they could be attributed to the passage of plasmoids (e.g. *Slavin et al.* (2003)) or when they are observed on closed magnetic field lines, they could be anti-sunward return flow on the outer edges of sunward fast flow channels (*Amm and Kauristie*, 2002).

Zhang et al. (2015a) carried out a more recent study looking at anti-sunward flows in the plasma sheet, using HIA ion data from the CIS instrument on the Cluster 3 spacecraft between 2001 and 2006. Zhang used a number of data selection criteria to isolate the plasma sheet and to ensure the earthward and tailward flows were separated. These use $\beta > 0.1$ and spatial parameters of -19 R_E < X < -10 R_E, 10 R_E < Y < 10 R_E and 4 R_E < Z < 4 R_E to define the effective plasma sheet. An additional criteria of $B_z > 0$ is used to remove data associated with anti-sunward plasmoid transport as they are not connected to the plasma sheet. Finally Zhang included a requirement to eliminate flow fluctuations in which the duration of plasma flow in one direction must exceed three minutes. Figure 4.4 shows one of the plots Zhang created during the study. It depicts earthward plasma flow in the equatorial plane as viewed from below (panel A), where the dawn flank is positioned at the bottom of the plot. Panel B shows earthward plasma

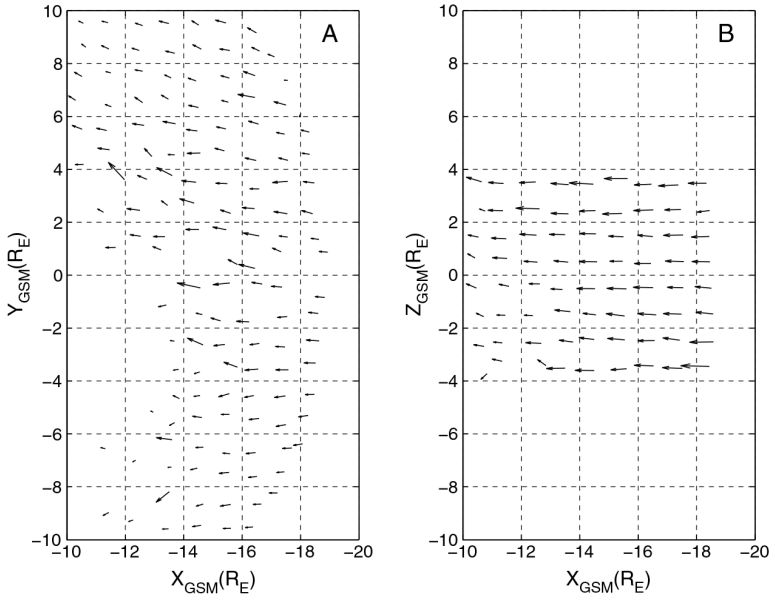

FIGURE 4.4: Earthward plasma flow in (A) the equatorial plane viewed from below, meaning the dawn flank is positioned at the bottom of the plot. (B) Plasma flow in the noon-midnight meridian plane from *Zhang et al.* (2015a).

flow in the noon-midnight meridian plane. Overall, Zhang found that in the equatorial plane, earthward and tailward flows show considerable deflection and deceleration as they near the Earth. These results can be clearly seen in Figure 4.4. Zhang suggested that enhanced magnetic and plasma pressure in the near-Earth region could have caused this behaviour (*Angelopolous et al.*, 1993). Zhang also concludes that while observing the equatorial plane, the most prominent deflections of earthward plasma flows were observed on the dawn side, however, at closer inspection of Figure 4.4A, which positions the dawn flank at the bottom of the figure, these conclusions could be questioned.

After careful consideration, we propose an alternative interpretation. Looking at Figure 4.4A, the results clearly show the more commonly noted duskward dominating plasma deflection direction since there is greater deflection towards the top of the figure. This confusion could be due to a typographical error as Zhang later states that these results are likened to the average quiet-time plasma flow which exhibits a dawn-dusk asymmetry (*Angelopolous et al.*, 1993). Zhang makes similar conclusions about the tailward flow in the equatorial plane, saying that the plasma deflection is greater in the dawn-side; again, there is disagreement as his plot clearly shows duskward dominance as before. Interestingly, there seems to be greater tailward flow deflections that earthward ones, which can be seen in *Zhang et al.* (2015a)'s third figure. Zhang also studied the noon-midnight meridian plane (Figure 4.4B), looking at a narrow 8 R_E channel through the plasma sheet within which very little deviation from sunward flow was observed.

Zhang has since continued the research he began in *Zhang et al.* (2015a), focussing on the

flow characteristics of the central plasma sheet (CPS) with $\beta > 1$ and the outer plasma sheet (OPS) with $0.1 < \beta < 1$ (*Zhang et al.*, 2015b). The study uses the same data selection method as *Zhang et al.* (2015a), concentrating on earthward and tailward flows. Zhang notes that earthward flows are found in both the CPS and OPS while tailward flows mainly occur in the OPS. Both flows are mostly convective in the CPS and are of similar velocities, where the tailward flows are thought to produced by the reflecting and rebounding of BBFs near the braking region[1] (e.g. *Ohtani et al.* (2009); *Panov et al.* (2010a,b)) and flow shear or vortices around plasma-depleted flux tubes (bubbles) (e.g. *Sergeev et al.* (1996); *Birn et al.* (2004); *Keika et al.* (2009)). Both earthward and tailward flows are predominantly parallel in the OPS and earthward flows appear to have higher velocities than the tailward flows. Zhang concludes that for both flow directions, their properties are consistent with reflection at near-Earth magnetic mirror points.

In general, the studies of magnetospheric convection and fast flow plasma described above do not provide conclusive evidence of dawn-dusk asymmetry, in fact the results are highly dependent on the data selection criteria used. For example studies focussing on perpendicular plasma velocity tend to find asymmetrical flow, but studies based upon $|B_{xy}|$ and β usually present rather symmetric flow patterns. There are still only a few studies on tailward flow in the magnetotail and offer limited explanations as to how they are formed, from plasmoid transportation to reflection and rebounding at BBF braking regions. The work presented in this thesis focuses on using more data than previous studies from the Cluster mission to investigate earthward and tailward ion flow in the terrestrial magnetotail in both the equatorial plane, and looking at previously unexplored regions in planes parallel to the noon-midnight meridian.

4.2 Data Selection, Organisation

4.2.1 Data Selection

There are several instruments onboard the Cluster spacecraft which carry out measurements relevant to the study of convection of the Earth's magnetic field. The main two instruments utilised by the investigation presented in this thesis are the PEACE electron spectrometer and the CIS ion spectrometer, which were discussed in Chapter 2.

[1]The BBF braking region is the area in which fast earthward flows are sufficiently decelerated by the strengthening background magnetic field (e.g. *Shiokawa et al.* (1997)) such that a flux tube being carried by fast earthward flows comes into equilibrium with the surrounding flux tubes (e.g. *Pontius and Wolf* (1990)). Often fast earthward flows can overshoot this equilibrium point and when this happens, the flux tube is pushed back, creating tailward flows (*Chen and Wolf* (1999)) and can be envisioned as a bouncing back of fast earthward flows.

The CIS-HIA onboard ion moment dataset was chosen as the primary data source because the majority of previous magnetospheric convection studies (e.g. *Kissinger et al.* (2012); *Juusola et al.* (2011); *Pulkkinen et al.* (2013); *Zhang et al.* (2015a)) utilise the ion moment data across a number of missions including GEOTAIL, THEMIS and Cluster. Therefore using the same data product enables direct comparison between the results presented in this thesis and the previous studies. In addition, velocity moments generated from electron data are generally less reliable because they are much more difficult to detect due to their small mass and the ratio between their thermal and bulk speed. Finally, when working with electrons, it can be difficult to discern between results generated from incident ambient electrons and photoelectrons as they both interact with the detector in the same way.

The moment data used were selected between the years of 2001 and 2006 and chosen in accordance with the calibration of the PEACE instrument (see Table 3.3) to ensure maximum accuracy of the results. This time-frame was used for both PEACE and CIS data, and was selected to maximise data overlap between the two instruments in order to optimise reliability when comparing their results.

4.2.1.1 Velocity Moment Selection

It was decided that while the CIS moment data provided by the Cluster Science Archive only contained ion bulk velocity, it was necessary to carry out a vector transformation, using boundary normal coordinates to remove the parallel component of ion velocity in order to obtain the perpendicular component of ion velocity to the Earth's magnetic field. The former provides information on how the magnetic field topology evolves with time, whereas the latter primarily provides information on the ion's motion as they moved along the field lines. For this study, it is clear that the perpendicular component would be most useful and thus was used. The transformations performed on the original ion bulk velocity moments, using the GSE coordinate system, is described below.

Boundary normal coordinates must be used when dealing with some natural boundary, in this case it is the Earth's magnetic field. These are denoted as lmn. n is a unit vector that is defined as being parallel to the local magnetic field, m is defined as being perpendicular to both n and the Z_{gse} axis and is thus defined as n $\times$ Zgse, and l is defined as m $\times$ n.

The l, m and n boundary vector components produce the transformation matrix, T_{lmn}, needed to convert ion bulk velocity moment data to ion perpendicular velocity moments. This matrix is then used to obtain the ion velocity vector in terms of the field-aligned coordinate system:

$$v_{lmn} = T.v_{gse} \tag{4.1}$$

Finally, to obtain the field perpendicular ion velocity, the field-aligned component must be set to zero ($v_{n,lmn} = 0$) and then the field-aligned vectors transformed back into the GSE coordinate system (*Hapgood*, 1992).

Following on from this, any mention of 'velocity' throughout Chapter 4 refers to the perpendicular component the ion velocity.

4.2.2 Data Organisation

This section will discuss how the raw data are organised to create the initial raw data files and alternative data binning methods to the conventional mean-averaging method. Each binning technique will be explored in relative detail so as to establish which is most suited to maximise the amount of data available for analysis while producing reliable and meaningful results.

4.2.2.1 Initial Raw Data file Creation

The initial datasets to be used during the research discussed in this thesis are the CIS moment and auxiliary (aux) datasets. The moment dataset provides the ion velocity vectors and time-stamp while the auxiliary dataset provides the position of each Cluster spacecraft at any given time in GSE coordinates, as well as another time-stamp. The data contained within the two datasets are sampled at different time-resolutions, the moment data at spin-resolution (four seconds) and the aux data at one-minute resolution. In order to ensure no data is lost at this early stage, an interpolation is carried out between consecutive position data-points, creating an intermediate position value which can then be assigned to the appropriate velocity vector. This preserves the four-second resolution rather than reducing it down to one minute.

Once all six years of data have been interpolated and the new position vectors generated, merged data files are created to store not only the velocity and position vectors, but also other useful information such as temperature and density values as well as the various data quality flags.

4.2.2.2 Spatial Binning

The raw data are averaged into discreet 3 R_E× 3 R_E× 3 R_E spatial bins. The main reason for this bin size is that it was used by *Kissinger et al.* (2012)'s study of plasma flow in the magnetotail during SMC and substorm times. Using the same bin size allows for direct comparison between Kissinger's investigation and the results presented in this thesis. It also allows for visual clarity when plotted as there are few overlapping vectors as a result. This binning criteria was used throughout the research presented in this thesis.

The data was also experimentally organised into 1 R_E× 1 R_E× 1 R_E bins in an attempt to improve the spatial resolution. This was quickly decided against as it was difficult to present the data in a clean and organised manner with so many vectors and counts being printed on the various figures. In addition, using smaller bins drastically reduced the amount of data available per bin, roughly reducing the counts to one-ninth of the larger bins. This meant that the counts often fell below the nominated 100 count cutoff value.

Using this method of binning, as with any other does have its drawbacks. For example it does not show precisely when the data was collected during the experimental window, whether it was taken over multiple years or on one single orbit. It is also not dwell-time normalised so does not show how much useful data was actually collected in comparison to the amount of time the spacecraft spends in the corresponding bin. While these parameters are useful in determining the fine details about when the data were collected and how they correspond to specific events, ultimately this investigation was about the average flow characteristics and thus it was decided that going into this level of detail was not necessary at this time.

4.2.2.3 Angle Average Binning

For this binning method, the velocity vectors contained within each spatial bin are subdivided into 8 discreet bins which in total cover an angle of 360°, as seen in Figure 4.5. Each angle bin covers a 45° direction with the zeroth bin centred in the positive x-direction and each consequential bin numbered moving in a clockwise direction such that the positive y-direction is in bin two. The velocity vectors are subsequently placed in one of the eight angle bins according to the angle at which it makes with the positive x-axis.

This method essentially reduces the amount of data cancellation that occurs when averaging vectors with components orientated in opposite directions. By using discreet

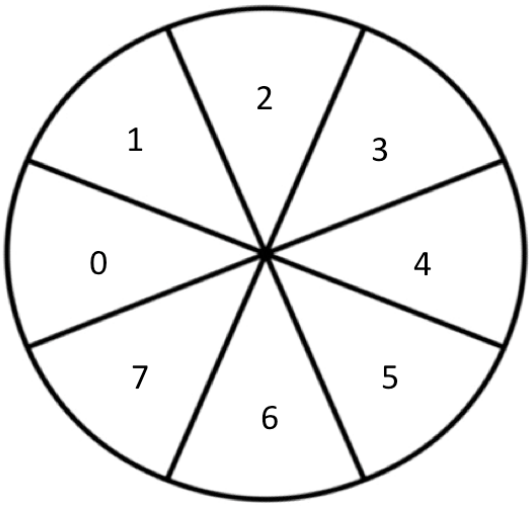

FIGURE 4.5: Angle averaging bin orientation with positive x directed towards the left of the page.

angle bins, the method preserves the magnitude of plasma flow velocity in each of the 45° bins and avoids the possibility of it cancelling down to zero, which would not give a good representation of the average plasma flow behaviour.

The main limitation of the angle averaging method is that it restricts the angular resolution to 45° (smaller bins could be used, but it would lead to the reduction of data available for the study) This can be improved by introducing a larger number of narrower angular bins, but this has the potential to lead to the skewing of results if an anomalously large velocity vector is present and the data-count per bin in too low. The other difficultly with this method is the selection of which of the eight angular bins best represents the data spread in each spatial bin. The options were to select via the greatest velocity or the largest number of counts per angular bin. The latter was chosen to avoid the skewing previously mentioned and using count number essentially makes the selection according to which is the most common direction in which plasma flow occurs, giving the best representation of the overall behaviour of the system. This method was not used in the final study. The following section describes the data binning method used through the research conducted in this thesis.

4.2.2.4 Hemispherical Data Overlap

The offset of the Earth's rotation axis from the z-axis of the GSE coordinate system gives rise to some effects which need to be assessed. As the Earth rotates, an apparent rocking motion of the Earth's magnetotail occurs as a result of fixing the x-axis of the GSE and GSM coordinate systems along the Earth-Sun line. This motion can be seen

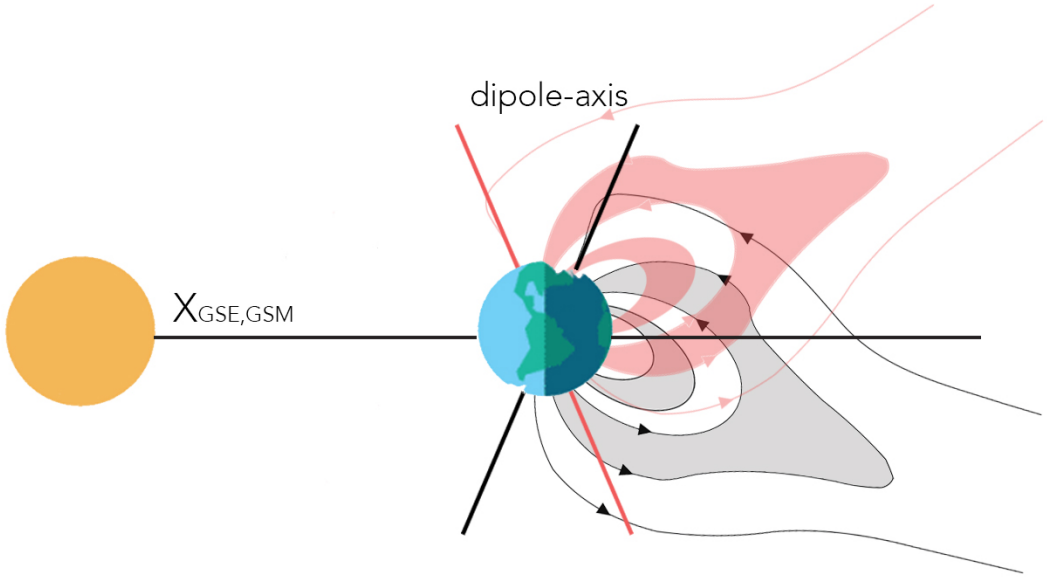

FIGURE 4.6: Effect on Earth's magnetotail orientation caused by it's daily rotation. The red and black dipole-axis and magnetic field lines show an example of how the magnetotail could appear at 12 hour intervals. Adapted from two images, *timeanddate.com* (1995-2017) and *Narinder* (2016).

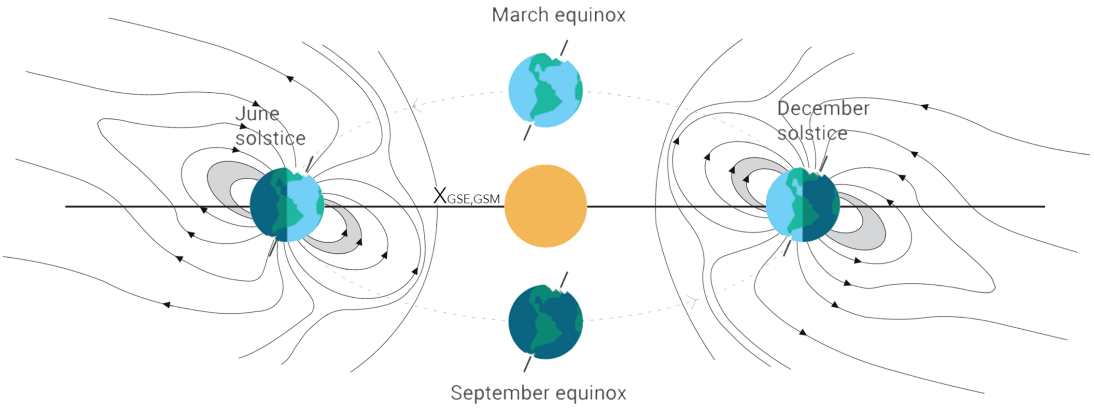

FIGURE 4.7: Seasonal effect on the Earth's magnetotail caused by the tilt of it's polar axis and it's relative position to the Sun. Adapted from two images, *timeanddate.com* (1995-2017) and *Narinder* (2016).

in figure 4.6. The red polar-axis and magnetic field lines illustrate how the magnetotail could be orientated about either of the coordinate system's x-axis. The black dipole-axis and magnetic field lines illustrate how the system could be orientated 12 hours later. It is clear there can be quite a dramatic difference.

This daily effect can also be seen on a larger scale as a seasonal effect as the Earth orbits then Sun and can be seen in figure 4.7. It is clear from the figure that depending on where the Earth is relative to the Sun, the magnetotail can appear to be situated on either side of the Earth-Sun line.

The apparent rocking motion of the magnetotail can attribute to cross-contamination of plasma flows in the northern and southern hemispheres if the selection criteria is based solely on GSE/GSM coordinates. This could lead to a skewed average direction results if the vectors are placed in the incorrect bins on account of this effect. Therefore another method of binning the data could be to organise it according to the moment vectors' associated B_x value. If a vector's B_x value is less than zero, it is situated in the southern hemisphere and if B_x is positive, it is in the northern hemisphere. Combining this binning technique with the angle averaging technique would both maintain the magnitude of the velocity and reduce the hemispherical contamination of the vectors allowing for a clearer representation of the average plasma flow in the Earth's magnetotail. This method was also not used in the final study because a better averaging method was found, as described below.

4.2.2.5 Earthward and Tailward Plasma Flow

An alternative method of data binning which could be utilised is to bin the data according to the prevailing x-direction the plasma flows in. Vectors are classed as earthward if they have an associated positive V_x value and tailward if they have a negative V_x value. The dataset would be organised according to the sign of the vectors V_x within each spatial bin, and then mean-averaged together. The mean-averaging is carried out by calculating the sum of the vector components in each of the x, y and z-directions separately, and then dividing each value by the total number of data-points contributing to each returned value. Finally the three averaged values are combined trigonometrically to provide the prevailing vector magnitude and direction for both earthward and tailward flows for every spatial bin. This method does not require the use of average-angle-binning (section 4.2.2.3) as there is no risk of cancelling out the moment vectors to zero.

Binning moment data according to V_x was chosen to be the main averaging technique throughout the research presented in this thesis because it avoids the cancellation of oppositely directed vectors. This is because they are not placed into discrete angular bins and as such, this method possesses a much higher degree of directional precision than the average-angle-binning technique. The main drawback to the V_x method is that it is not used in conjunction with the hemispherical binning method. While it is possible to combine both binning methods, in practice it is somewhat impractical as it would double the amount plots created and reduce the amount of data available in many of the bins. The reduced amount of data per bin would become more significant when analysing substorm data as there is not a huge amount available to begin with. As a result while there will be some northern and southern hemispherical cross-contamination of moment

vectors, it was decided that preserving the number of data points within each spatial bin was of higher priority. Overall, it was decided this data binning the data according to earthward or tailward plasma flow direction would yield the best representation of the moment datasets.

4.3 Data Visualisation and Presentation

4.3.1 General Data Restrictions

Before the data are plotted, it is important to remove unnecessary raw data. The first cutoff removes all data with a positive x position as the dayside region is not being investigated as part of this study. A number of general data cutoffs are also applied to the raw dataset and are used to remove 'bad data' or data that can skew and contaminate the set, leading to a misrepresentation of the results. The CIS-HIA quality flag was therefore applied. This operates using the CAA (Cluster Active Archive) standard and only data with an index of three and four were used:

- 0: Not applicable (used by CIS to flag no science data tacking periods).
- 1: Major problems, check caveats.
- 2: Minor problems, check caveats.
- 3: Good data (default CIS data quality index value, unless a data quality issue is identified).
- 4: Excellent data which has received special treatment.

4.3.2 Magnetosheath Contamination

It has been noted that very high velocity plasma flow vectors are present in the raw data set, especially at distances greater where $\sqrt{Y_{GSM}^2 + Z_{GSM}^2} > 12$ R_E. After some consideration, it was decided that these vectors were likely due to the spacecraft entering and perhaps passing through the magnetosheath and into the solar wind. A series of data cutoffs were established in order to remove the contaminant data. In order to specify which cutoff were needed to only remove sheath data while preserving as much useful data as possible, the Cluster Science Archive quick-look plots were utilised to establish the plasma behaviour within the various magnetospheric regions.

It can be seen in first pane of Figure 4.8 that the magnetic field strength is fairly low. In the top corner of the same figure, it is clear that the spacecraft are situated close to

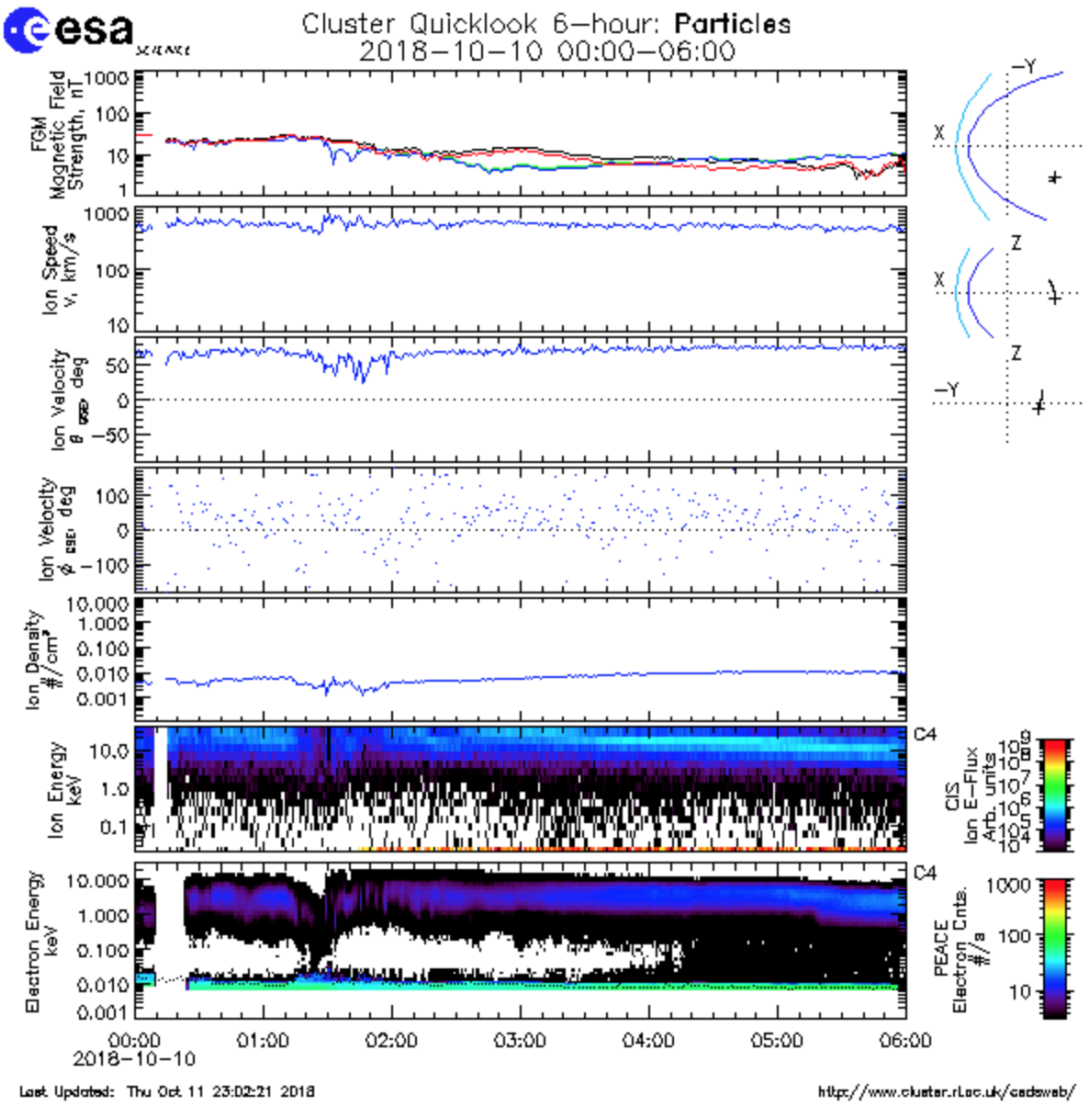

FIGURE 4.8: A quick-look plot from the Cluster Science Archive showing a period for which the Cluster Spacecraft are situated in the terrestrial plasma sheet.

the middle of the X-Z plane. In the second pane of Figure 4.8, it can be seen that the bulk velocity of the ions is fast, around 500 km s^{-1}, and they are also hot, looking at the penultimate panel of Figure 4.8, it can be seen that the average ion energy (related to temperature) is above 10 keV. The electrons in this region are also hot (seventh pane), showing temperature between 1 - 10 keV (*Walsh et al.*, 2011a). From this analysis, it was decided that these properties best represent the plasma sheet (*Baumjohann et al.*, 1989).

It can be seen in plane 6 of Figure 4.9 that the ion temperatures are roughly alternating between 1 keV and 10 keV at the same time as alternating 100 eV and 1 keV electrons (pane 7). This motion suggests that the spacecraft is alternating between being situated in the sheath and the magnetosphere (*Kletzing et al.*, 2003; *Walsh et al.*, 2011a). The

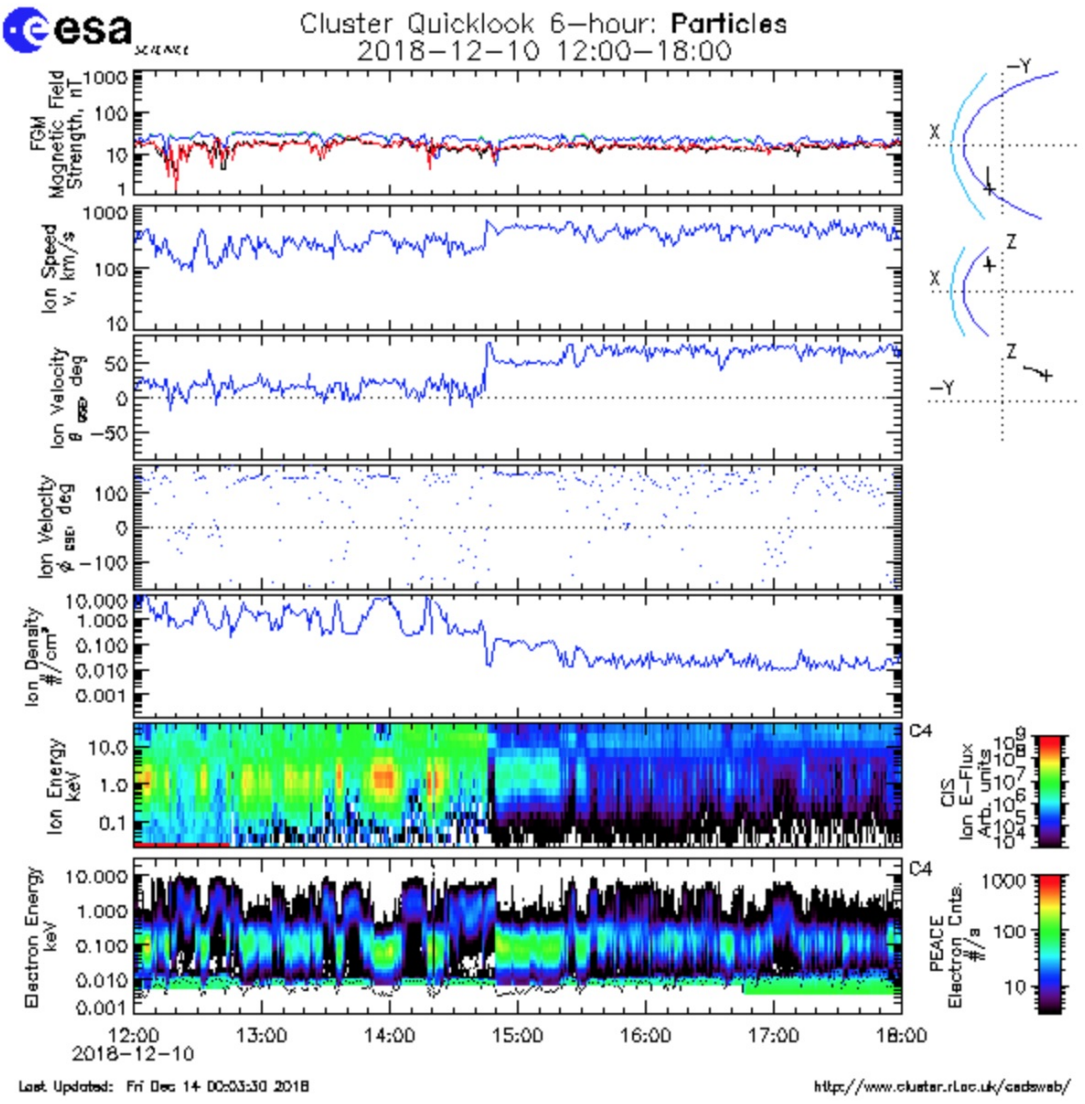

FIGURE 4.9: A quick-look plot from the Cluster Science Archive showing a period for which the Cluster Spacecraft are alternating between being situated in the magnetosheath and magnetosphere.

ion density in pane 5 supports this idea as it is high during periods of low temperature regimes, showing the spacecraft is in the sheath (*Baumjohann et al.*, 1989).

In can be seen in the last plane of Figure 4.10 that between 18:00 and 20:40, sub 100 eV electrons are present at the same time as a fast narrow ion beam (plane 6). This is evidence of the spacecraft being situated in the solar wind. Looking at the latter part of the same two panes, it can be seen that the electron temperatures are a little higher at around 100 eV and the ion distribution is much wider. Couple this with spatial positioning as seen in the top right corner, it is clear that the spacecraft is switching from being in the solar wind to the sheath.

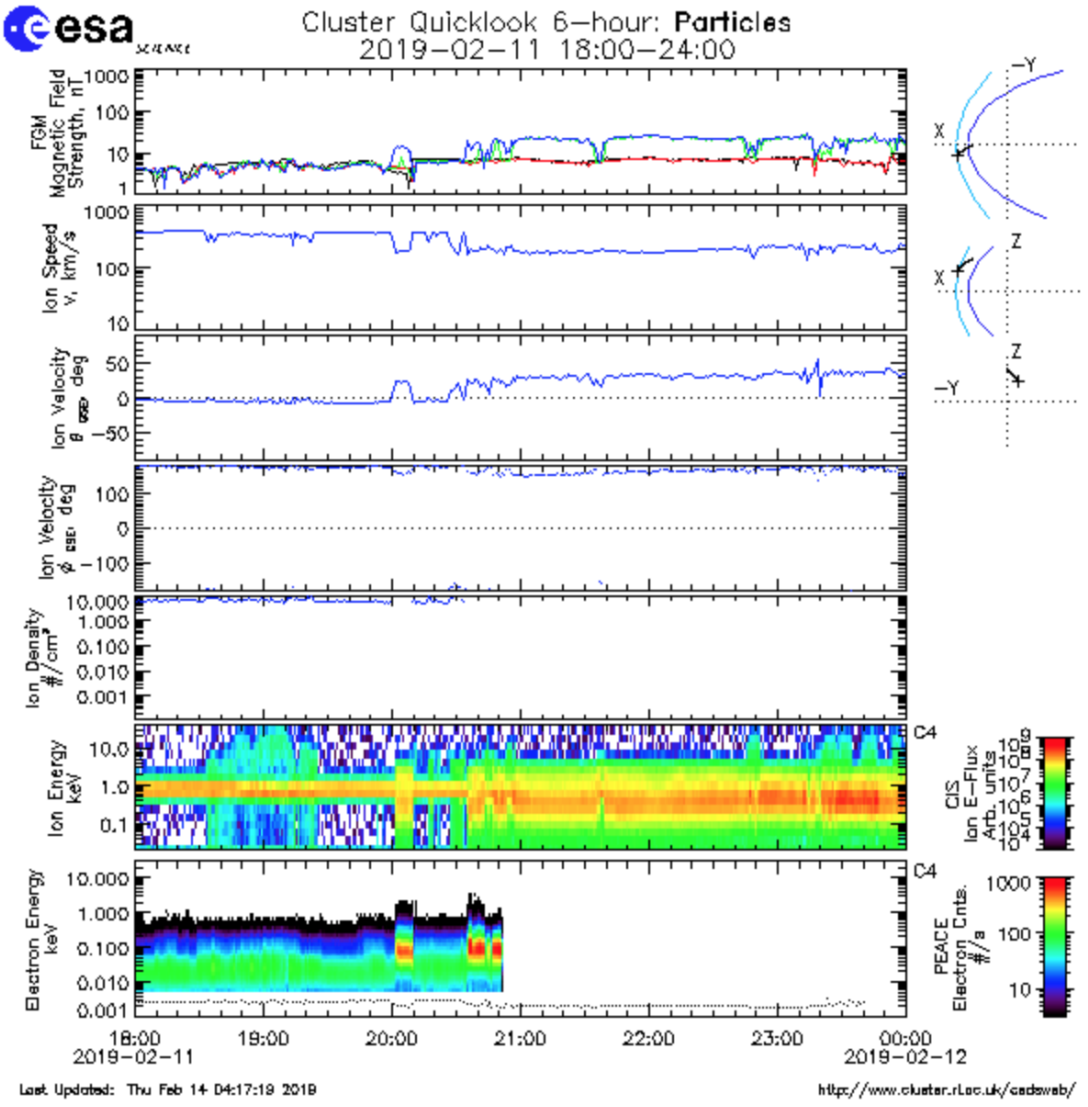

FIGURE 4.10: A quick-look plot from the Cluster Science Archive showing a period for which the Cluster Spacecraft are alternating between being situated in the magnetosheath and the solar wind.

From this investigation, the cutoffs to remove the contaminant sheath and solar wind data were selected, all of which must be satisfied:

- Ion density > 0.5 particles cm^{-1}
- Ion temperature < 0.5 keV
- $\sqrt{Y_{GSM}^2 + Z_{GSM}^2} > 12$ R$_E$

It can be seen in Figure 4.11, panes A, B, E and F, that the overall ion counts in the plane centred about Z = 3 R$_E$ for both the tailward (from panes A - E) and the earthward (from panes B - F) are reduced. The average tailward ion velocity has also decreased

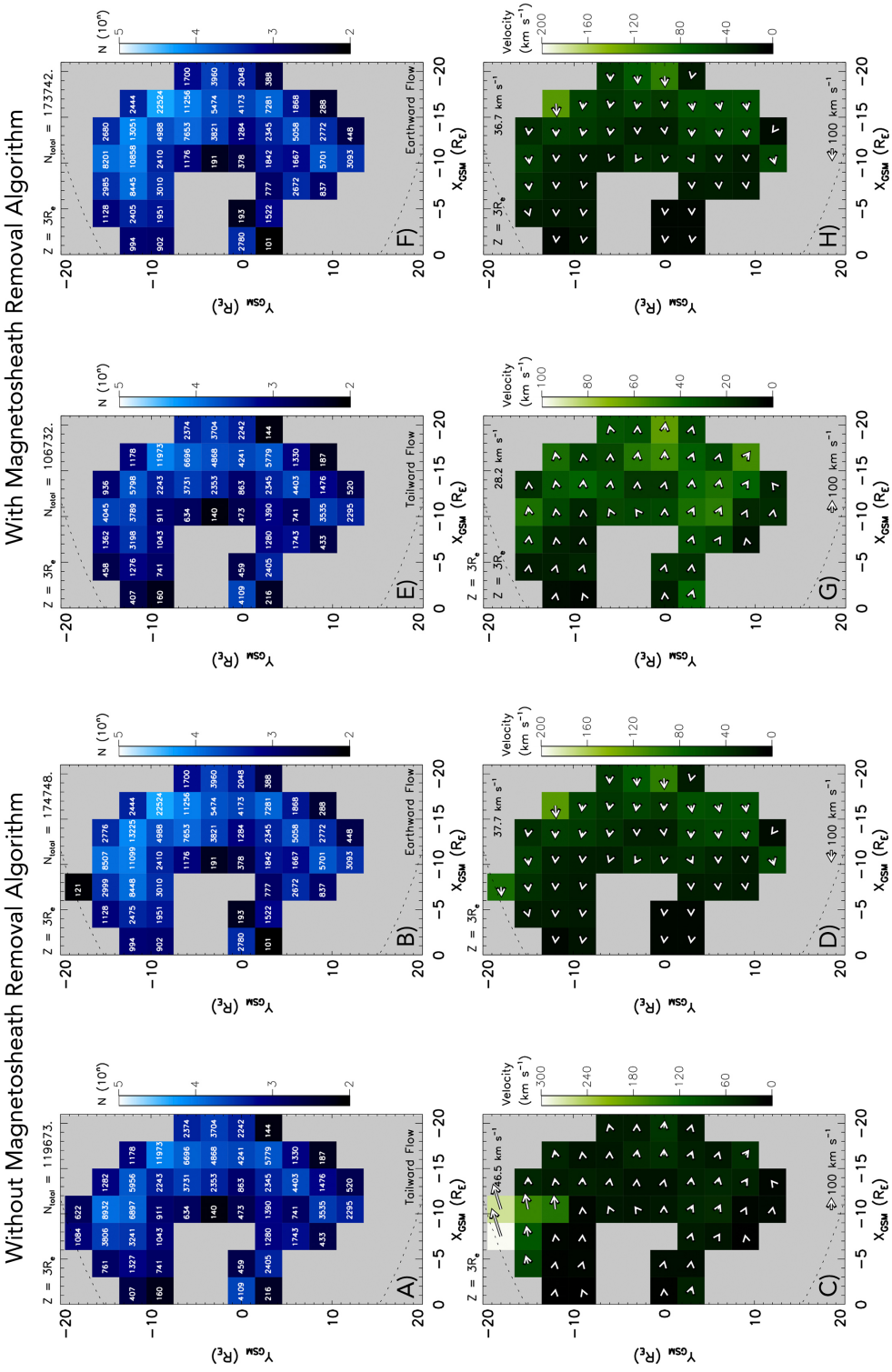

FIGURE 4.11: A series of plots for plane Z = 3 R_E showing the how applying the magnetosheath removal algorithm affects the results. Panes A-B: Show the tailward and earthward counts respectively calculated before the algorithm is implemented. Panes E-F: Show the tailward and earthward counts respectively calculated after the algorithm is implemented. Panes C-D: Show the tailward and earthward ion velocity vectors respectively calculated before the algorithm is implemented. Panes G-H: Show the tailward and earthward ion velocity vectors respectively calculated after the algorithm is implemented.

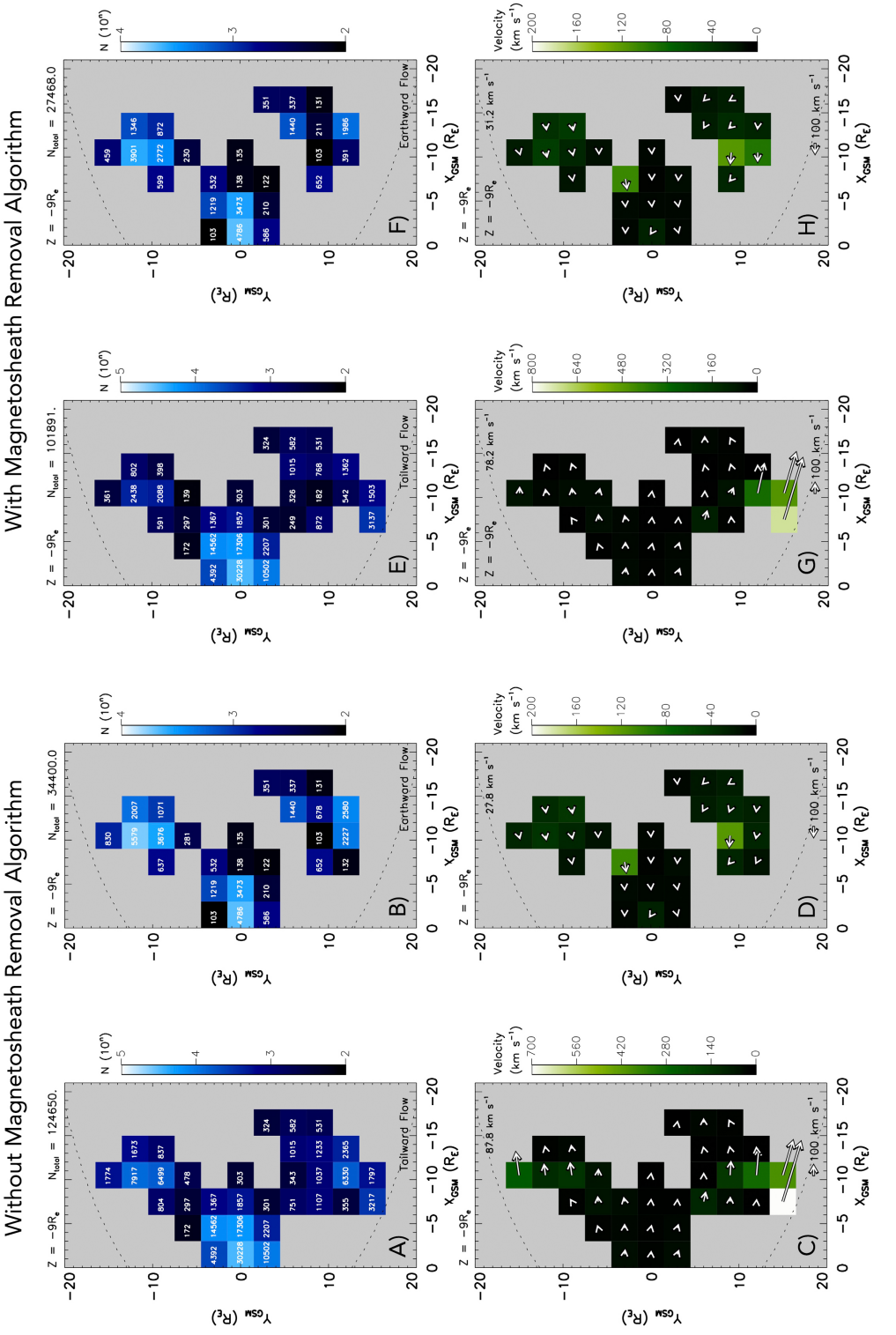

FIGURE 4.12: A series of plots for plane Z = -9 R_E showing the how applying the magnetosheath removal algorithm affects the results. Panes A-B: Show the tailward and earthward counts respectively calculated before the algorithm is implemented. Panes E-F: Show the tailward and earthward counts respectively calculated after the algorithm is implemented. Panes C-D: Show the tailward and earthward ion velocity vectors respectively calculated before the algorithm is implemented. Panes G-H: Show the tailward and earthward ion velocity vectors respectively calculated after the algorithm is implemented.

from 46.5 km s^{-1} (pane C) to 28.2 km s^{-1} (pane G). Many of the faster flank ion velocity vectors have also been removed too, reducing the maximum bin-average velocity from close to 300 km s^{-1} to below 100 km s^{-1}. Looking at the earthward ion velocity vectors,

it is clear that the fact the two earthward averages are similar (plane-average velocity of 37.7 km s^{-1} in pane D and 36.7 km s^{-1} in pane H), indicates that the method has overwhelmingly worked in this plane, though the slight difference between these two figures indicates that a small number of earthward flows (which will not be magnetosheath) have erroneously been removed. The algorithm however is not perfectly accurate, as can be seen in Figure 4.12. Looking at panes C and G is is clear that the very large velocity vectors have not been removed. This was most likely due to the spatial parameter as these extremely fast flows occurred within the parameter and as such would not trigger its removal. Decreasing the distance of the spatial parameter was considered, but since this was the only plane for which particularly large vectors were not removed, it was decided it was not worth risking the removal of potentially good data closer in to the Earth. Looking at panes D and H of Figure 4.12, a slight increase in the plane-average ion velocity was also found. It is also worth noting that the maximum velocity in pane G actually increases. This is because there was a 2000 km s^{-1} velocity cutoff originally implemented which was deemed irrelevant once the new magnetosheath removal algorithm was implemented. Overall, the it was deemed successful and as such was used throughout the study.

4.3.3 Magnetospheric Lobe Contamination

One additional data constraint was applied to facilitate the removal of any data collected while the Cluster spacecraft were in the magnetospheric lobes. The reasoning behind this was described in section 3.5, but essentially it boiled down to the fact that moment measurements were too unreliable in the lobe regions. There are a number of methods in which data selection can be carried out to ensure no lobe data is used during analysis. The first and easiest way is to establish a set of spatial parameters to isolate the data collected within the plasma sheet. While this method is simple, it is somewhat conservative as the parameters would need to be underestimated to reduce the risk of lobe data accidentally being included. With this method there is a possibility that a good deal of plasma sheet data could be neglected if it lies outside of the accepted-data spatial region. The other method is to use an identification procedure specifically designed to find when data has been collected in the magnetospheric lobes. Two of these procedures exist; the first to be created was ECLAT (described in section 3.5.1) with the Coxon method (described in section 3.6) created later. This method of selection is somewhat more complicated as it relies on the use of multiple instruments operating at the same

time and the procedures are somewhat more complicated to implement than a simple spatial cutoff.

4.3.3.1 Magnetospheric Lobe Identification: Method Selection

Both ECLAT (*Boakes et al.*, 2014) and the Coxon method (*Coxon et al.*, 2016) have been described in detail in Chapter 3 and as such, the details will not be repeated in this chapter; however, a discussion must be had in order to decide which lobe identification method is best suited to this study.

The ECLAT data set is a comprehensive list of plasma regions in the magnetotail during the tail seasons of 2001 to 2009. The lobe identification method expands on the traditional use of plasma beta to determine plasma regions and essentially calculates the net current through the Cluster tetrahedron. There are two important limitations of the ECLAT data set; the first is its use of the tail-region box, whereby the selection method only considers data within X < -8 R_E and |Y| < 15 R_E. The tail box is applied to try and avoid misidentification of the plasma sheet during non-tail times, such as when the spacecraft crosses into the magnetosheath. While this is a quick and simple method of mitigating these misidentifications, as previously mentioned, there is a chance that some useful plasma sheet data could also be lost when using such a strict cutoff. The second limitation is that the ECLAT data set is reliant on the use of multiple instruments operating at the same time in order to make a positive identification. Throughout the mission there will be many occasions where this will not occur and so as a result, no identifications can be made; in effect throwing away a good proportion of the available data.

The second magnetotail region identification model, the Coxon method, uses the model introduced by *Jackman and Arridge* (2011) on Kronian lobe identification. Coxon modified this method to make it suitable for use with the terrestrial magnetosphere, neglecting times of low plasma density in order to exclusively use FGM magnetometer data. Coxon created a list of selection criteria and if all are satisfied, then a lobe is successfully identified.

1. $X_{GSE} > 0R_E$
2. Radial distance to Earth $R \geq 8R_E$
3. $\sigma \leq \sigma_0$
4. $|B_X| \geq B_0$

X_{GSE} is the sunward component of the spacecraft position in geocentric solar ecliptic (GSE) coordinates, σ is the standard deviation of the magnitude of the magnetic field for 20 minutes on either side of each data point (a 40 minute sliding window), and $|B_X|$ is the magnitude of the sunward component of the magnetic field in GSE coordinates.

Coxon reported that the method has a detection accuracy of 66% and an 11% probability of false detection (a false positive result), however false negative results are not discussed, thus it is unclear how much of the plasma sheet may have been accidentally removed when using this method. It was also shown that the amount of data identified as magnetotail lobe by this method during 2001-2009 was 140% the number identified by the ECLAT method. Following on from this comparison, it was decided that the Coxon method was to be used in this study.

4.3.4 Bin Size Selection

Once the unwanted data had been removed, the raw data needed to be organised into discreet spatial bins. It was decided that the bin-size options were: 3 x 3 x 3 R_E bins, 2 x 2 x 2 R_E bins and 1 x 1 x 1 R_E bins. Figure 4.13 shows examples of plots at the equatorial plane utilising each of the bin sizes. The main factors which were analysed when deciding which bin-size to use were: spatial coverage, amount of data available per bin and how well the data can be presented.

Looking at the amount of data available per bin in Figure 4.13, it can be seen that the 3^3 R_E possess the largest amount of data per bin with the 1^3 R_E having the least, as expected. A larger data volume tends to mean more reliable results, but it also leads to the smoothing out of the finer details. However using smaller bins clearly reduces the amount of data available per bin, which could lead to not having enough data to provide meaningful results. It was decided that a bin must have more than 100 counts in it to be classes as meaningful and any bin with less than this was not presented. In Figure 4.13, the top row of plots use the 100 count cutoff while the bottom row does not. It can clearly be seen that when using the 100 count cutoff, only one bin was disregarded with the 3^3 R_E regime, while 7 and 40 were lost from the 2^3 R_E and 1^3 R_E bin regimes

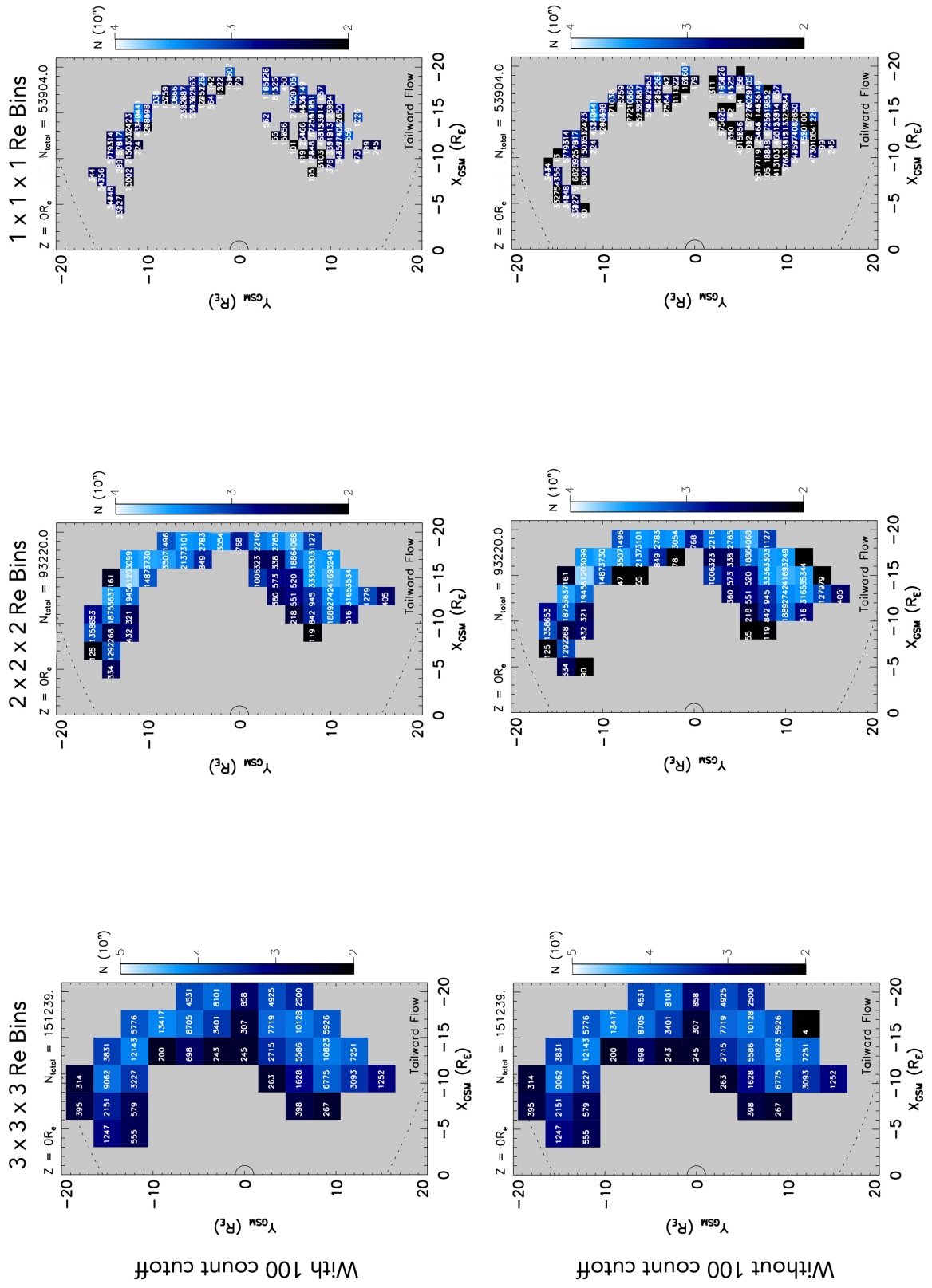

FIGURE 4.13: A series of data count plots centred about the equatorial plane. The top row of plots have the 100 data count cutoff applied to them, the bottom row do not. The left column uses 3^3 R_E bins, the central column uses 2^3 R_E bins and the left column uses 1^3 R_E bins.

respectively. Taking these factors into consideration, again it was decided that losing as little data as possible was a priority and as such the 3^3 R_E bin regime was preferable.

Finally data presentation was investigated. Figure 4.14 shows a selection of ion velocity vector plots, again with the top row using the 100 count cutoff while the bottom row does not. The 1^3 R_E bin plots (plots on the left) do provide the most detailed view of the ion flow direction, however it does look cluttered, with many of the vectors overlapping each other. This actually makes the figures quite difficult to read and analysis as a result could be slightly more difficult to carry out. The 2^3 R_E bin plots look much more ordered yet still provide a little more directional detail that the 3^3 R_E bins.

4.3.4.1 Dwell Time Normalisation

The penultimate study carried out was to normalise the dataset to the total spacecraft dwell-time in each 3 R_E deep plane in the Z direction. To do this, the total counts of data available per spatial bin were divided by the total spacecraft dwell-time in the associated plane, and the result then multiplied by 100 to obtain a percentage value. This analysis method was used to understand more clearly how much useful data was collected in comparison to the total spacecraft flight-time. Normalising the data allowed a more direct comparison both across the bins of any size and in any given plane. Figure 4.15 shows a series of dwell-time normalisation plots for 3^3 R_E (left), 2^3 R_E (middle) and 1^3 R_E (right) bins. Each set of bins are divided by the total C1 and C3 spacecraft dwell-time collected in the plane -1.5 R_E < Z < 1.5 R_E, thus are directly comparable.

First of all it is clear that when scaled to the plane spacecraft dwell time, there are very few bins which spend more than 0.5% of the spacecraft's dwell time collecting usable data for this study. It is unsurprising that the largest bins, the 3^3 R_E bins, do contain the highest proportion of useful data, with the 2^3 R_E bins holding notably less and the 1^3 R_E bins containing an incredibly small amount. It can also be seen that where the spacecraft visits most frequently, the central region about the radial distance of about 10 R_E also contains the highest proportion of useful data. From this it is also possible to get an idea of the regions where results could be biased due to spare coverage. Overall this investigation further supports the idea that the 3^3 R_E binning regime is most suitable for the study carried out in this thesis.

4.3.4.2 Orbital Sampling

A final study was carried out on the data set to further understand how the data is distributed throughout the nightside magnetosphere and how spacecraft location and

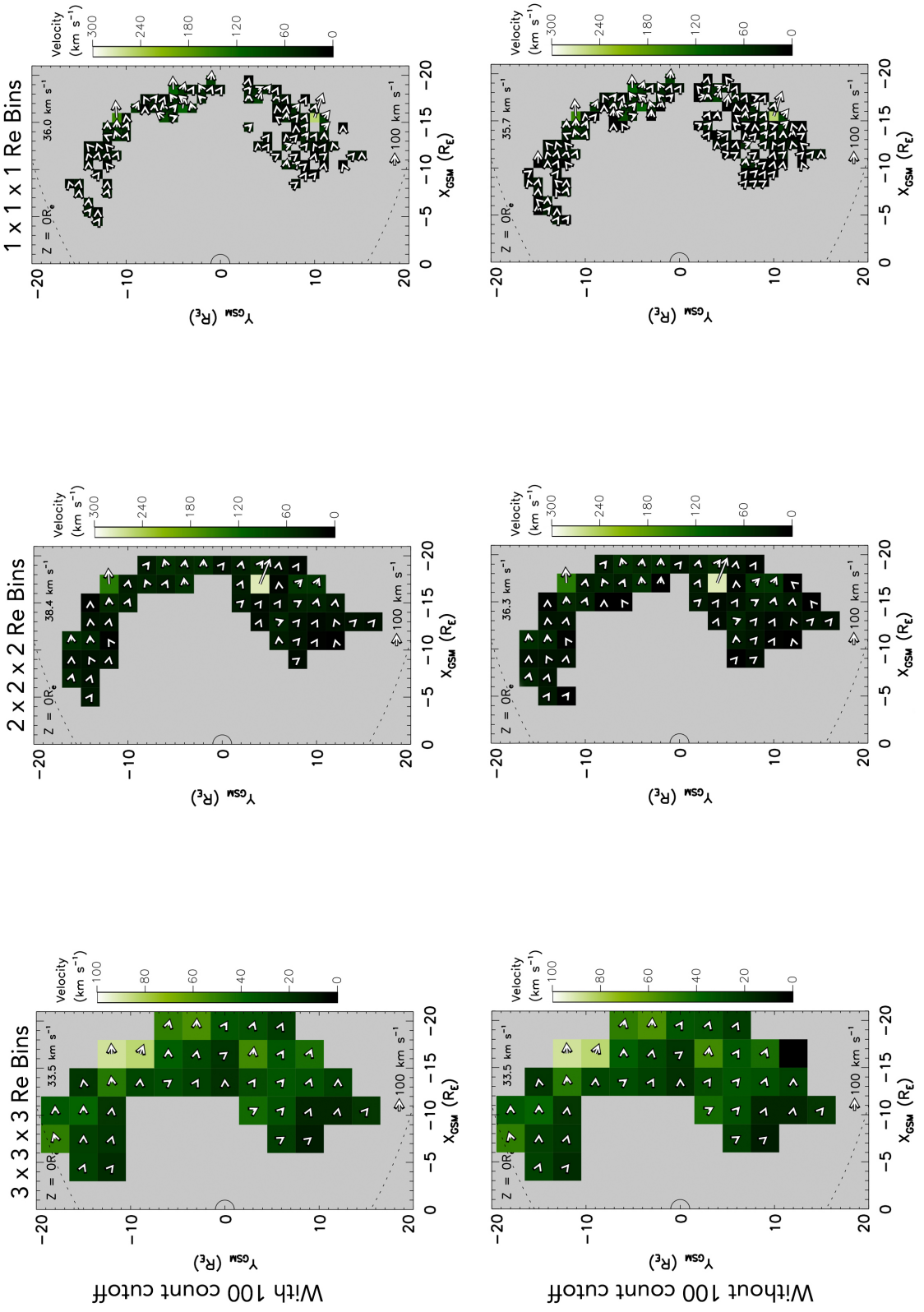

FIGURE 4.14: A series of velocity vector plots centred about the equatorial plane. The top row of plots have the 100 data count cutoff applied to them, the bottom row do not. The left column uses 3^3 R_E bins, the central column uses 2^3 R_E bins and the left column uses 1^3 R_E bins.

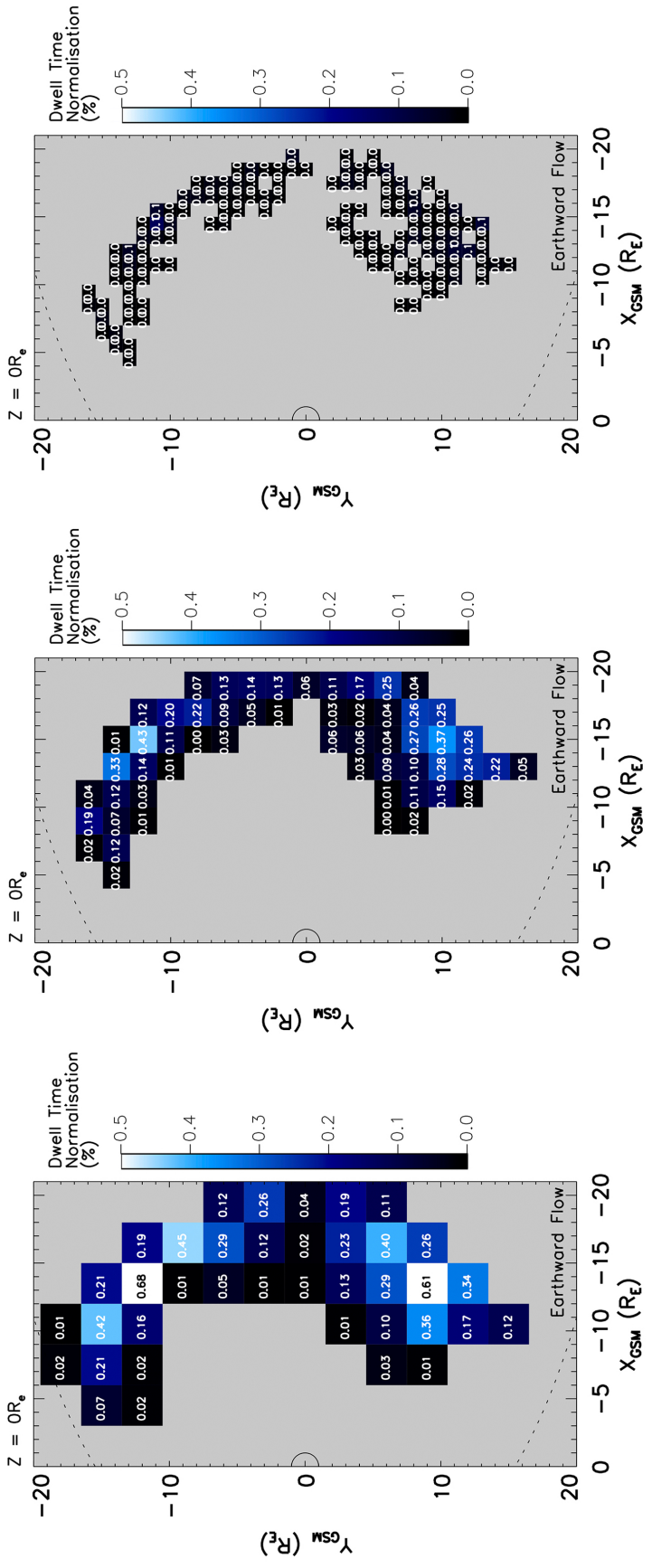

FIGURE 4.15: A series of dwell-time normalisation plots for 3^3 R_E (left), 2^3 R_E (middle) and 1^3 R_E (right) bins. Results presented as a percentage of amount of good data collected against time the C1 and C3 spacecraft spend in the -1.5 R_E < Z < 1.5 R_E plane.

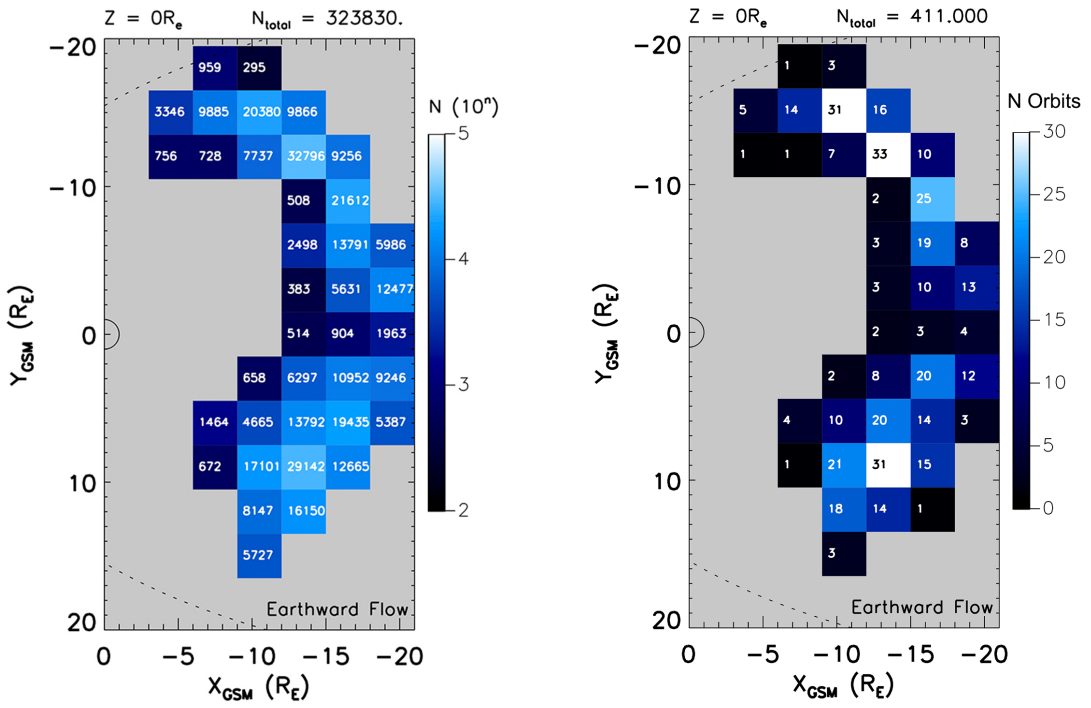

FIGURE 4.16: Left: Total number of data counts per $(3\ R_E)^3$ bin for nightside earthward ion flows where $Z = 0 \pm 1.5\ R_E$. Right: Number of orbits the data is sampled from per $(3\ R_E)^3$ bin for nightside earthward ion flows where $Z = 0 \pm 1.5\ R_E$.

sampling rate affects the results. Figure 4.16 shows a comparison between the total data count available per $(3\ R_E)^3$ bin for earthward ions flows in the $Z = 0 \pm 1.5\ R_E$ plane (left) and the number of orbits the data was sampled from per spatial bin (right). It is clear that there is a direct correlation between the amount of data collected and the number of orbits the data was sampled from; the more data collected in a bin, the more orbits passed through it. In order to establish reliable results, it is best practice to use a binning method which provides the highest number of sampled orbits per bin. If more spacecraft orbits contribute to the overall data available for analysis, it provides a healthier spread of data and thus a better picture of the average plasma flow in each binned region.

Orbit count plots were created for the $(2\ R_E)^3$ and $(1\ R_E)^3$ bin plots to observe how they compare with the $(3\ R_E)^3$ in order to establish which binning system would best suit my study. Figure 4.17 shows a comparison between the total data count available per $(2\ R_E)^3$ bin (top), the total data count available per $(1\ R_E)^3$ bin (bottom), the number of orbits the data was sampled from per $(2\ R_E)^3$ bin (top right) and the number of orbits the data was sampled from per $(1\ R_E)^3$ bin (bottom right), all for earthward ions flows in the $Z = 0 \pm 1.5\ R_E$ plane. It is clear that the number of orbits per bin is reduced when the bins are decreased in size to $(2\ R_E)^3$ with 13 bins now only possessing data collected from one orbit (Figure 4.17, top right). When the bins are decreased in

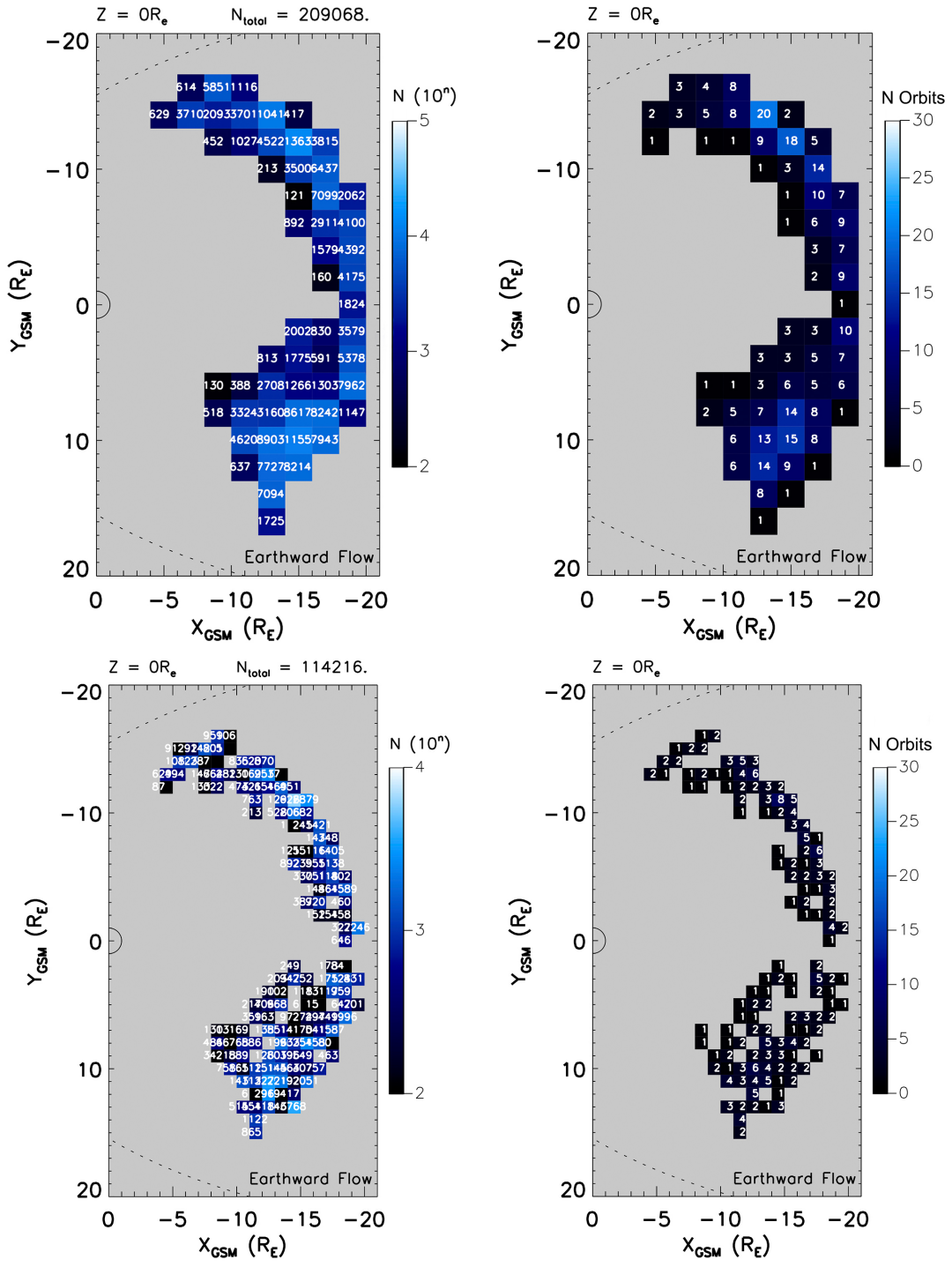

FIGURE 4.17: Top left: Total number of data counts per $(2\ R_E)^3$ bin for nightside earthward ion flows where Z = 0 ± 1.5 R_E. Top right: Number of orbits the data is sampled from per $(2\ R_E)^3$ bin for nightside earthward ion flows where Z = 0 ± 1.5 R_E. Bottom left: Total number of data counts per $(1\ R_E)^3$ bin for nightside earthward ion flows where Z = 0 ± 1.5 R_E. Bottom right: Number of orbits the data is sampled per $(1\ R_E)^3$ bin from for nightside earthward ion flows where Z = 0 ± 1.5 R_E.

size again to $(1\ R_E)^3$, no bins possess data collected from more that 10 spacecraft orbits, with the majority of the bins only being subject to three or less spacecraft passes. It is clear that the $(1\ R_E)^3$ bins do not contain enough data spread across the entire 6 year study period to be useful. While the $(2\ R_E)^3$ bins do see an improvement on the smaller bins, they still considerably few spacecraft passes than the $(3\ R_E)^3$ bins (Figure 4.16) and thus again the $(3\ R_E)^3$ binning procedure comes out is favoured.

Overall, after considering the investigations carried out to establish which binning regime was used in the study presented in this thesis, it was decided to use $3^3\ R_E$ bin method. This was because it provided the best spatial coverage, lost the least amount of data due to the 100 count cutoff and yet still provided adequate spatial resolution for the ion flow directions.

4.3.4.3 Data Presentation

Once all of the data selection criteria are applied, the raw data are organised into discreet 3 R_E^3 spatial bins and plots are created to display the particle distribution of plasma convection in both the equatorial and noon-midnight meridian planes. Two versions of each plot are created, one displaying tailward-directed plasma flow and the other showing earthward-directed plasma flow are orientated such that the Sun is to the left, dusk to the bottom and dawn to the top. In addition, the Shue magnetopause model (*Shue et al.*, 1997) (which obtains a quantitative relation between the size and shape of the Earth's magnetopause, the solar wind dynamic pressure, P_d and IMF B_z), was used to trace an idealised magnetopause position onto all of the plots in order to help emphasise the region being observed. Figure 4.18 illustrates the position of the magnetopause' surface at varying distances between $z = 0\,R_E$ and $z = 20\,R_E$. Due to the conical shape of the magnetopause, the further the cut is from the equatorial plane (greater z value), the further anti-sunward the magnetopause boundary appears. The model is also cylindrically symmetric about x, meaning that the magnetopause contours are the same in the positive and negative z directions, and the pattern is the same in the positive and negative y direction when observing the noon-midnight meridian.

The first two plots created depict the number of velocity vectors (N) per spatial bin, figure 4.19. The value in each bin details the number of counts within it and the colour, based on a logarithmic scale, helps to quickly determine the spatial and count distribution of the data. The total count value displayed at the top of each plot enables quick comparison between earthward and tailward-flow plots, showing which plasma flow direction is dominant, so which flow direction occurs more frequently. It also allows easy comparison between planes above and below the central equatorial and non-midnight

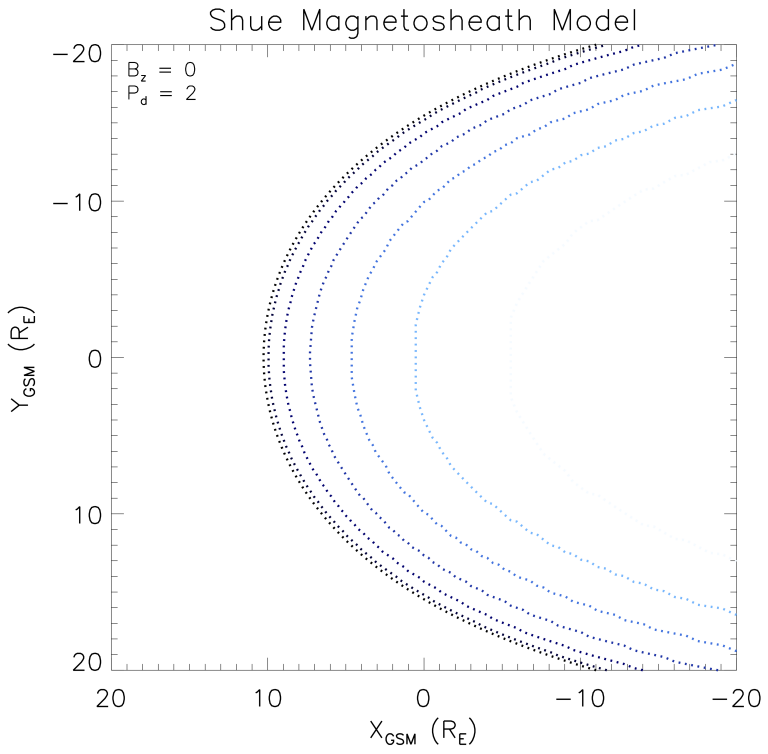

FIGURE 4.18: Cuts of the magnetopause at varying altitudes using the Shue Magnetopause Model (*Shue et al.*, 1997). The most leftward trace is at z = 0 R_E and the most rightward at z = 20 R_E.

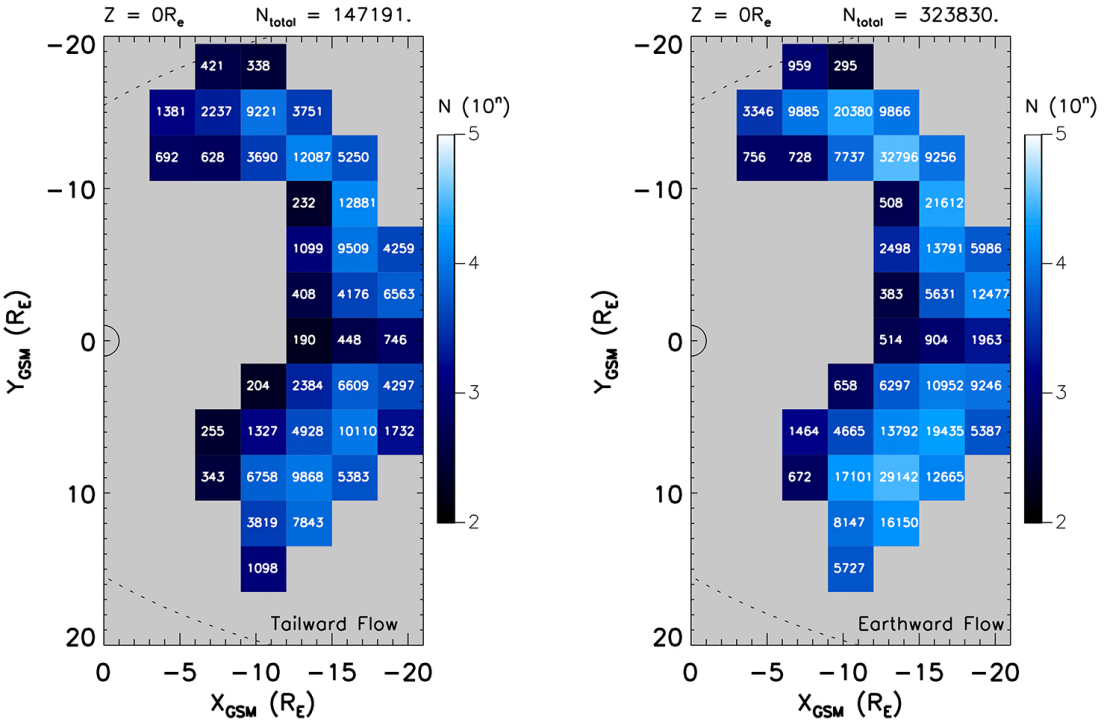

FIGURE 4.19: Example of sample count plots displaying tailward(left) and earthward(right) plasma flow.

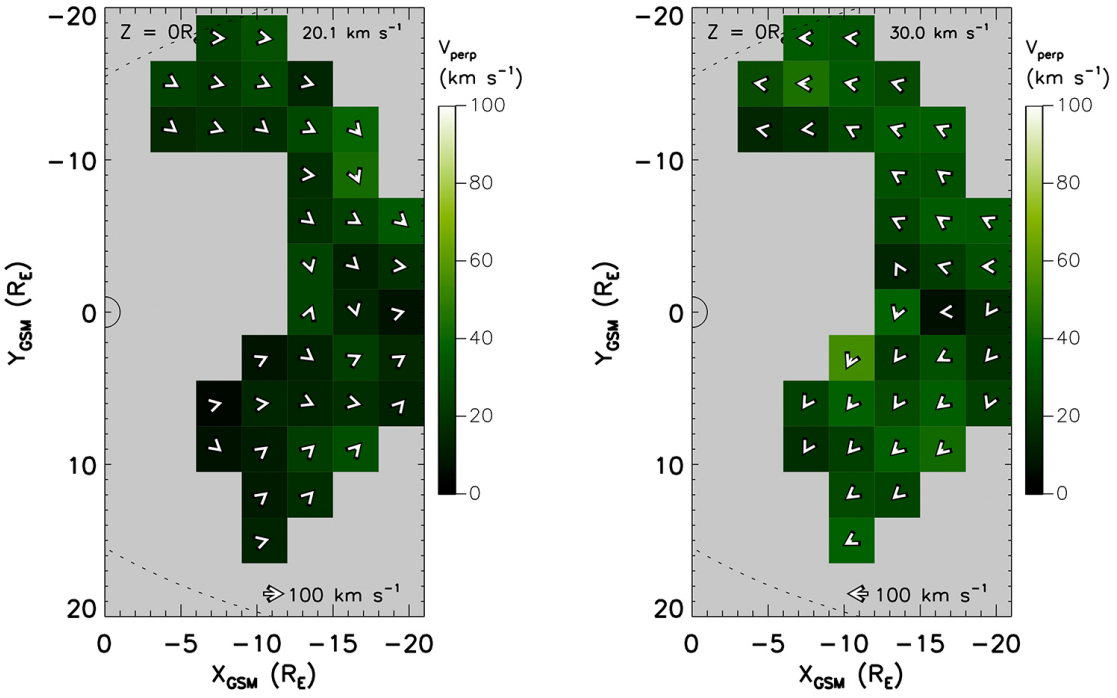

FIGURE 4.20: Example of a velocity vector plot displaying tailward(left) and earthward(right) plasma flow.

meridian planes, providing a three-dimensional picture of the vector distribution. An upper limit of 10^5 counts per bin was set for the colour bar. It allowed for a good compromise between including as many bins as possible within the colour range and avoiding the colour saturation of bins where possible. For example, if an upper limit of 10^6 counts was used, while it would include the bins with the highest count values in the colour range, it would compress the colour of the bins with much lower counts together. This would mean that the colours of adjacent bins would become very similar even if their counts were not so similar, making it difficult to quickly determine the count distribution across the plane. Note that a white bin highlights that it contains more counts than the upper limit, saturating the colour scale used.

The second pair of plots created display the magnitude and direction of the average velocity per bin in the XY plane (V_{xy}), figure 4.20. The vector in each bin displays the mean averaged direction of either earthward or tailward flow in that bin with its length showing the average velocity scaled to 100 km s^{-1}. The linear colour scale represents the magnitude of the average velocity per bin and helps to quickly determine the velocity distribution in each particular plane.

The final pair of plots display the normalised magnitude and direction of the average velocity per bin in the XY plane ($\hat{V}$), figure 4.21. $\hat{V}$ is calculated by dividing $|V_{xy}|$ by $|V_{xyz}|$. The resultant vector length describes the degree to which the average ion

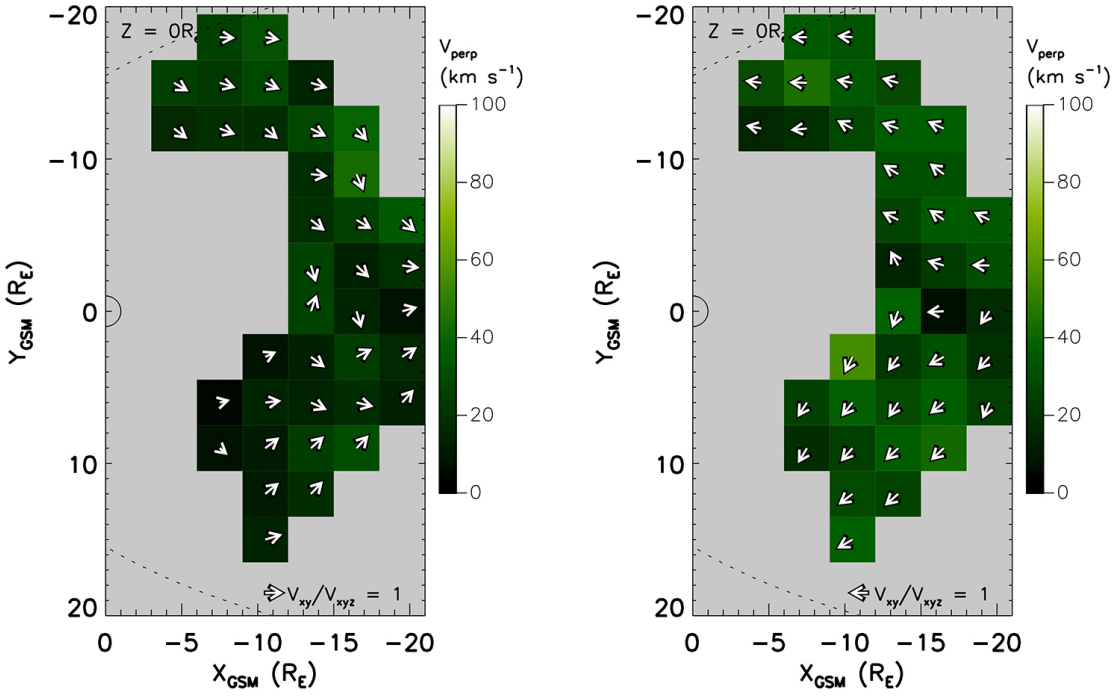

FIGURE 4.21: An example of velocity vector plots displaying unit vector arrows plotted over total tailward (left) and earthward (right) plasma flow magnitude in the XY plane.

velocity vector is directed in the plane being investigated. If the vector length is equal to 1 (depicted in the key of figure 4.21), then the direction of flow is entirely in the current plane. If its length is less than unity, then the plasma flow has a component directed out of the plane. These plots provide a three dimensional view of the plasma flow direction. All of the figures from this chapter can be seen in Appendix A.

4.3.4.4 Uncertainty Management

In order the assess the robustness of the analysis in the presence of uncertainties within the ion velocity moment vectors, some additional testing was carried out to ensure that any uncertainties present within the data do not unduly affect the results. Uncertainties are most likely to arise within the ion direction calculation as the spacecraft can only measure a finite area of space about it at any given moment. This means that the ion direction of motion can only have a finite accuracy, a figure which is not provided within the dataset. In order to account for this and to ensure it does not have an adverse affect, a random perturbation was applied to the angular direction of every input vector following a normal distribution with a standard deviation of 10°. This meant that the perturbation could be as large as 40°, although due to the distribution function, the majority of the perturbations we between -10° and 10°.

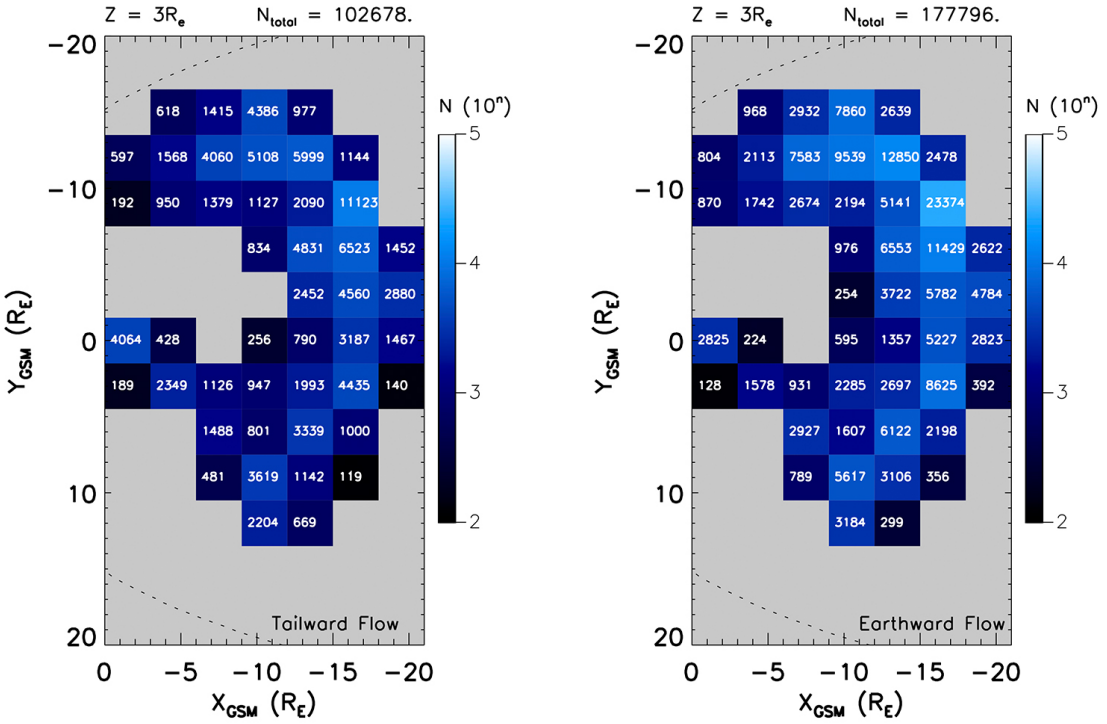

FIGURE 4.22: Sample count plots displaying tailward (left) and earthward (right) plasma flow in the XY plane where Z = 3±1.5 R_E.

This random perturbation was applied 10 times to the data set to establish a good average perturbation for the random uncertainty. Also note that this was not applied to any bins with less that 100 counts since these bins were rejected from the final analysis. Overall it was found that across the 10 iterations, the average angular variation of earthward flows and tailward flows from the final data set was -0.154° and -1.72° respectively. Clearly this is a very small deviation from the final data set and thus signifies that the analysis presented in the thesis is robust enough to deal with any uncertainties contained within the ion velocity moment data.

4.4 Plasma Flow in the XY Plane

4.4.1 Sample Counts

First consider all thirteen XY-planes (all sample count plots which are not explicitly discussed in this section can be seen in Appendix A. The northern hemisphere (+Z planes) contains more data than the southern hemisphere (-Z planes) with 591207 counts to 468134 counts and therefore has the greatest data coverage. Due to the orbital inclination of the Cluster spacecraft and the southerly progression of the orbit throughout the mission, it would be expected that there would in fact be more data in the southern

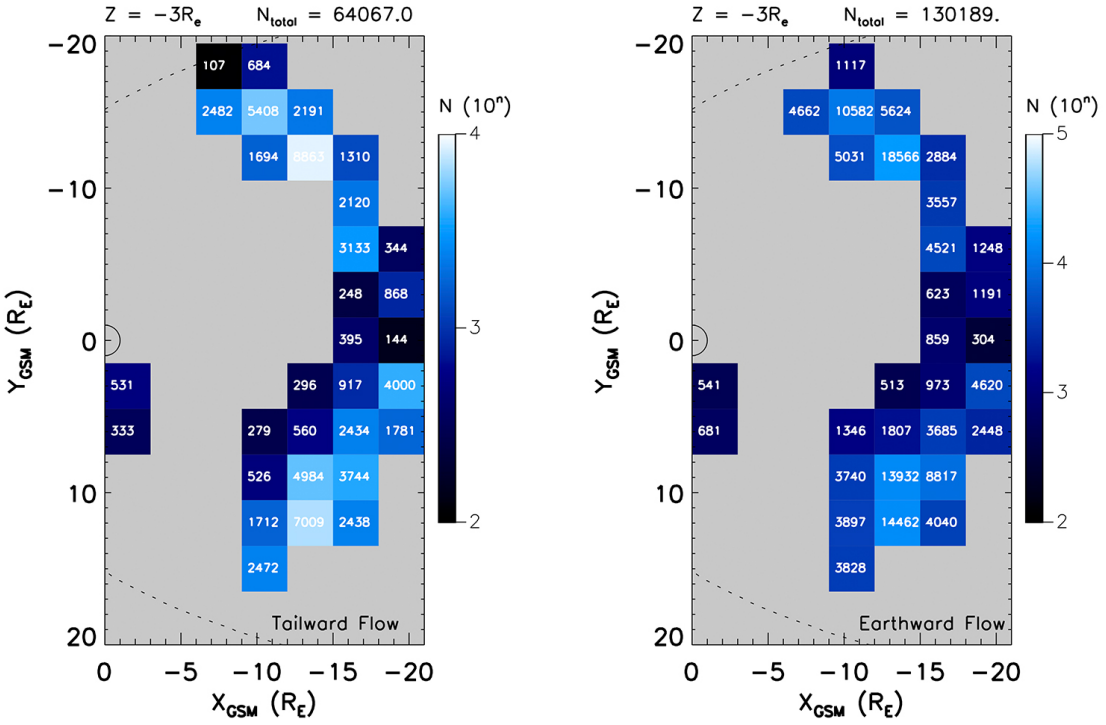

FIGURE 4.23: Sample count plots displaying tailward (left) and earthward (right) plasma flow in the XY plane where Z = -3±1.5 R_E.

hemisphere. However, much of the most southerly data was removed due to contamination with data collected in the magnetosheath.

In addition, the spatial distribution of the data collected is more comprehensive in the northern than the southern hemisphere. For example, at lower latitudes there are a good deal more bins occupied in the northern hemisphere than the southern. For the plane covering z = 3 ± 1.5 R_E (Figure 4.22), 46 bins (tailward) contain data, whereas for the plane covering z = -3 ± 1.5 R_E (Figure 4.23), just 31 bins (tailward) are filled. The same trend is evident at higher latitudes, where the plane covering z = 6 ± 1.5 R_E (Figure 4.24), 34 tailward bins contain data, whereas the plane covering z = -6 ± 1.5 R_E (Figure 4.25) only has 19 tailward bins filled. This distribution is likely to have occurred due to the elliptical orbit and its inclination. This means the perigee of Cluster's orbit occurs most frequently in the region about the equatorial plane, so the spacecraft spend more time at closer distances to the Earth in this region. The apogee of Cluster's orbit occurs most frequently in the region below the Earth's equatorial plane, hence the spacecraft spends more time at larger distances in this region.

In the northern hemisphere there is an asymmetrical data distribution with a greater coverage in the dawn side (negative Y region) than in the dusk (positive Y region) across all the northern planes. The distribution across each plane in the southern hemisphere is generally more sparse than the northern region with the majority of data concentrated

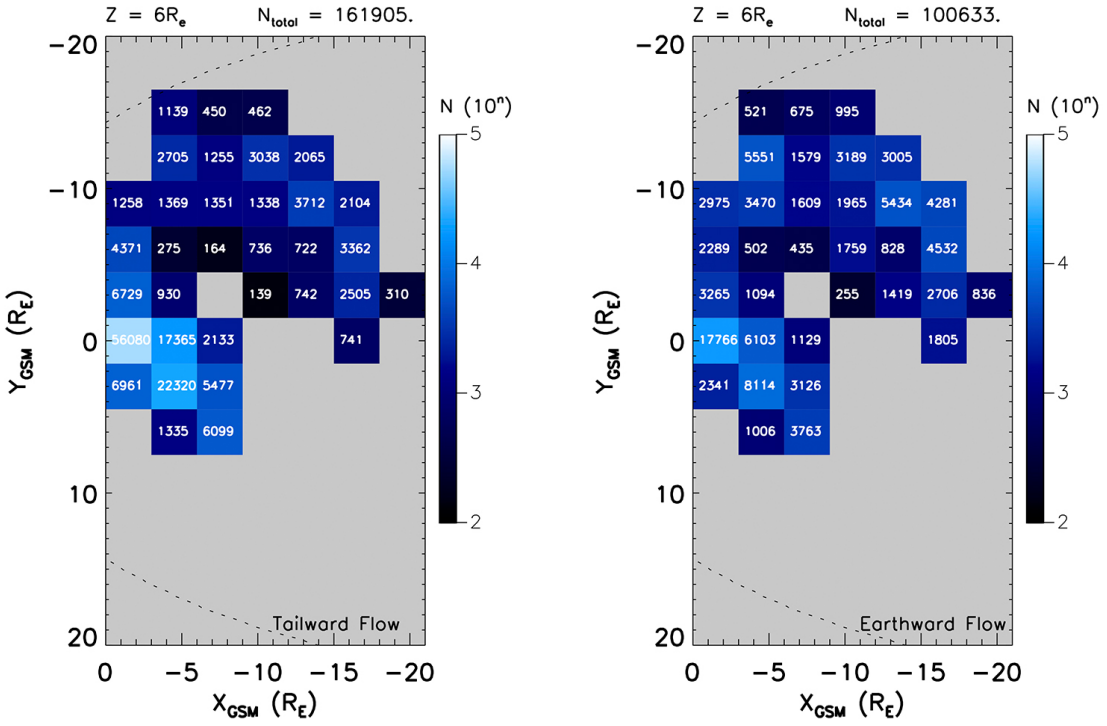

FIGURE 4.24: Sample count plots displaying tailward (left) and earthward (right) plasma flow in the XY plane where Z = 6±1.5 R_E.

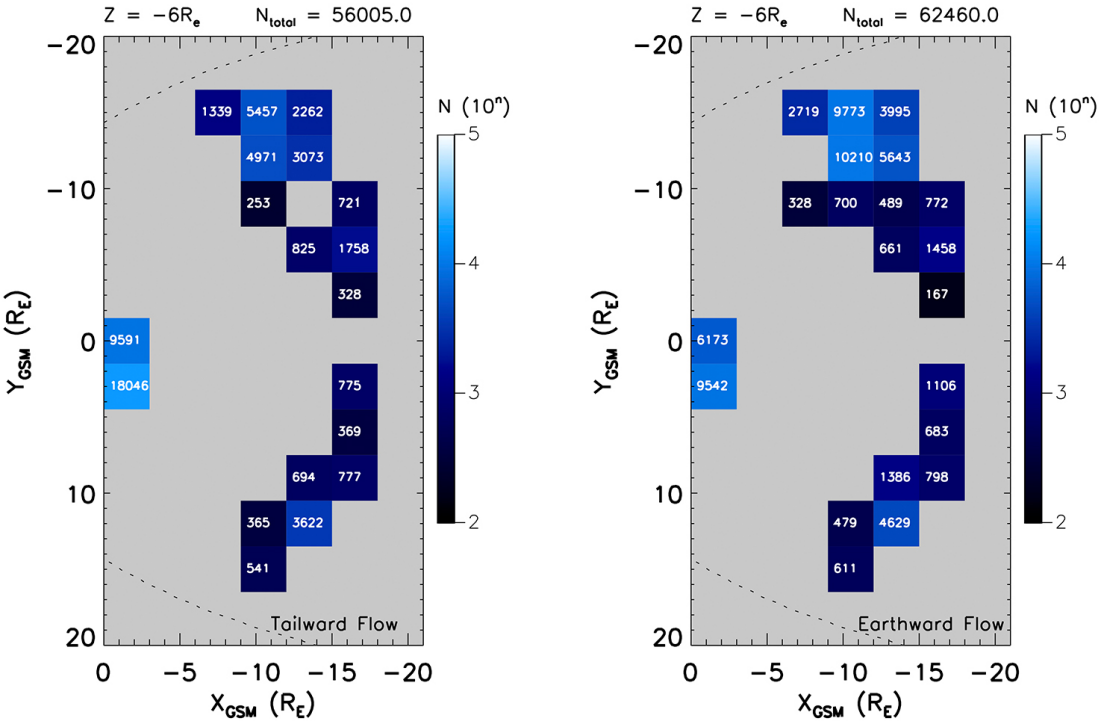

FIGURE 4.25: Sample count plots displaying tailward (left) and earthward (right) plasma flow in the XY plane where Z = -6±1.5 R_E.

at mid-to-distant tail regions, X < -9 R_E (Figure 4.23). However coverage does shift

to greater X positions at larger distances from the equatorial plane (Figure 4.26). The distribution is more symmetric about midnight in the southern hemisphere than the northern region, although in general there is more data in the dusk sector, and the data becomes distributed progressively more earthward and duskward with greater distance from the equatorial plane.

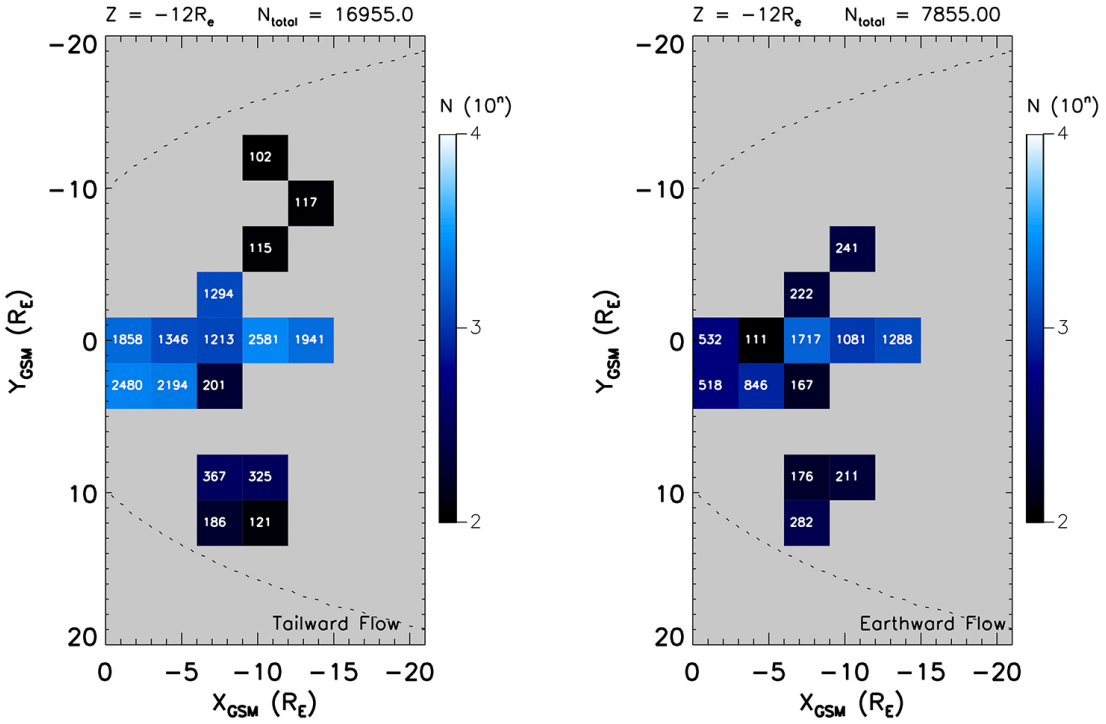

FIGURE 4.26: Sample count plots displaying tailward (left) and earthward (right) plasma flow in the XY plane where Z = -12±1.5 R_E.

For the plane centred about Z = 0 R_E, the inner edge of the data distribution is the more sparsely populated, with the most densely occupied bins lying at radial distances greater than about 10 R_E, with a couple of lower density bins at midnight and at the periphery of the dataset. These spatial distribution patterns and the count gradient are both artefacts of the Cluster spacecraft trajectories, with the spacecraft generally visiting the regions centred about a radial distance of 10 R_E more frequently. There is also a dawn-dusk asymmetric spatial data-distribution with greater coverage on the dawn side with 19 bins occupied as opposed to 16 bins in the dusk side.

Looking across all thirteen XY planes in the z-direction (all sample count plots which are not explicitly discussed in this section can be seen in Appendix A, it is clear that overall there is more earthward directed plasma flow than tailward flow, except in the regions of -16.5 R_E < Z < -7.5 R_E and 4.5 R_E < Z < 13.5 R_E where tailward flow dominates, table 4.1. This is unsurprising when considering previous studies. *Zhang et al.*

Plane (Z=nR_E)	$N_{earthward}$	$N_{tailward}$	N_{total}	% Earthward	% Tailward
18	0	0	0	-	-
15	0	0	0	-	-
12	229	411	640	35.8	64.2
9	12777	34778	47555	26.9	73.1
6	100633	161905	262538	38.3	61.7
3	177796	102678	280474	63.4	36.6
0	323830	147191	471021	68.8	31.2
-3	130189	64067	194256	67.0	33.0
-6	62460	56005	118465	52.7	47.3
-9	41254	88105	129359	31.9	68.1
-12	7855	16955	24810	31.7	68.3
-15	509	735	1244	40.9	59.1
-18	0	0	0	0	0
Totals	857532	672830	1530362	56.0	44.0

TABLE 4.1: Sample count distribution for the XY plane across 13 cuts in the z-direction. The Z value given is the position on which the plane is centred on.

(2015a,b) use spatial parameters to only select data from the plasma sheet, encompassing -4 R_E < Z < 4 R_E. In these studies, as previously mentioned, Zhang presents that Earthward flow is dominant in the region, so the results presented here are consistent with Zhang's results. Extrapolating out the reasoning for Zhang's spatial parameters suggests that he believes that the plasma sheet does not extend out beyond |Z| = 4 R_E, and as such this must be close to the plasma sheet boundary layer, the region in which the magnetospheric lobes meet the plasma sheet. The results presented in this chapter are again consistent with this since the outer regions beyond Z = 4.5 R_E and Z = -7.5 R_E are dominated by tailward plasma flow. They are also in agreement with *Ohtani et al.* (2009) who showed that in the region -8 R_E > X ≥ -15 R_E and |Y|< 5 R_E (although it is unclear how wide the data sample is in the z-direction), 37% of plasma flow was tailward. In comparison, looking at Table 4.1, it can be seen that if just the central equatorial plane is considered with a thickness of 3 R_E in the z-direction, 31.2% of the plasma flow is tailward. If considering the central three planes with a thickness of 9 R_E in the z-direction spanning |Z|< 4.5 R_E, the plasma flow is tailward 33.6% of the time. From this, it is clear that this study presents a strong correlation with Ohtani's results.

Following the classic convection model of *Dungey* (1961) (as discussed in section 4.1), it is expected that over large time-scales, the rate of magnetic reconnection at the dayside and nightside should be equal. If the dayside rate is higher, then it adds more open flux to the nightside and erodes flux on the dayside, making this side of the magnetosphere thinner. If the nightside rate is higher then it closes all the open flux eventually leaving a closed magnetosphere. As presented in this section, it is shown that on average between 2001

and 2006, 55.8% of the time tailward flow is dominant. However, the rate of reconnection on both the dayside and the nightside is not inherently connected with the direction of plasma flow. Following nightside reconnection, the Dungey cycle continues transporting plasma contained on newly closed field lines, however, tailward of the reconnection x-line, the fully disconnected field lines which have been returned to the solar wind, still possess negative V_x and are still documented by the Cluster spacecraft. As this additional tailward data follows the nightside reconnection event, it is outside of the balanced-reconnection rate parameters and as such, leads to the imbalance of plasma flow rates. Another possible explanation for tailward flows being recorded more than half of the time could be due to the bursty nature of magnetospheric reconnection. For example, if dayside reconnection is occurring at a slow and steady rate, but tail reconnection occurs impulsively in bursts, you could expect to see more periods of tailward flow. This is because even though the reconnection rates balance out on average, it is the amount of time plasma is seen flowing earthward/tailward being measured rather than the amount of flux seen convecting earthward/tailward. A third contributing factor to the imbalance of flow rates could be due to the sampling position of the spacecraft at any given time in comparison to the NENL during substorm events (which are included in this section of the research). During the steady flow of the normal Dungey cycle, the magnetospheric reconnection line is usually situated at a great distance tailward of the Earth, thus the spacecraft are always Earthward of this boundary, where Earthward flow almost certainly dominate. However, when a NENL is triggered during substorm activity (which does occur many times a day), this new reconnection line may well now sit Earthward of the spacecraft and as such, tailward flows would certainly dominate during this period. So from this it is clear that while broadly speaking the flow rates should be balance, spacecraft sampling position could play a role in displacing this.

4.4.2 Ion Velocity: Magnitude and Direction

When considering both earthward and tailward flows together in the XY plane, it is interesting to note that on average, across all thirteen planes (all ion velocity figures which are not directly discussed in this section can be seen in Appendix A.), earthward ion flows occur more frequently (Table 4.1), although tailward velocities are slightly faster (Table 4.2). This result generally agrees with previous studies which have also shown that earthward flows occur more frequently than tailward flows within the Earth's magnetotail (e.g. *McPherron et al.* (2011); *Zhang et al.* (2015a)). It can be seen in

Plane (Z=n±1.5 R_E)	V_{xy} Earthward [km s^{-1}]	V_{xy} Tailward [km s^{-1}]	Weighted Mean V_{xy} [km s^{-1}]	Weighted Mean $\|V_{xy}\|$ [km s^{-1}]
18	-	-	-	-
15	-	-	-	-
12	25.3	16.4	1.5	19.6
9	11.3	17.9	-10.0	16.1
6	17.9	19.0	-4.9	18.6
3	22.0	14.9	8.5	19.4
0	30.0	20.1	14.4	26.9
-3	28.6	21.3	12.1	26.1
-6	17.0	25.1	-2.9	20.8
-9	13.9	49.3	-29.1	38.0
-12	12.6	27.3	-14.7	22.6
-15	12.2	74.4	-39.0	49.0
-18	-	-	-	-
Average	19.1	28.6	-6.4	25.7

TABLE 4.2: Average V_{xy} for the XY plane across 13 cuts in the z-direction. The Z value given is the position on which the plane is centred on. Earthward V_{xy} refers to the average positive V_x and V_y value for the plane. Tailward V_{xy} refers to the average negative V_x and V_y value for the plane. Weighted mean average V_{xy} refers to the average earthward and tailward V_{xy} taking into consideration flow direction for each plane. Weighted mean average $|V_{xy}|$ refers to the average magnitude of earthward and tailward flow velocity, neglecting flow direction. Average includes data from all planes for each column.

Table 4.2 that the weighted mean[2] V_{xy} across all planes in both flow directions is -6.4 km s^{-1}. This result can be explained, as at greater distances from the equatorial plane, there is a good chance that the Cluster spacecraft have passed into the magnetospheric lobes and perhaps right through to the magnetosheath. In these regions tailward flow dominates. Their influence should be minimised due to the magnetosheath and lobe data removal procedures incorporated into the analysis, although of course they are not perfect and thus it can be expected that some data slipped through, especially within the outer planes. Flow domination in these regions occurs due to the Dungey cycle. The magnetospheric lobes are populated by open magnetic field line connecting the terrestrial magnetic field to the solar wind. The momentum from anti-sunward flow of the solar wind draws the open magnetic field lines tailward, thus this flow direction dominates this region. When looking at the central three planes where earthward flows have a higher occurrence rate, the average earthward V_{xy} dominates with V_{xy} = 11.7 km s^{-1}. This result in is general agreement with Zhang's (*Zhang et al.*, 2015a) study.

[2]The weighted mean essentially takes into account the occurrence rate of both earthward and tailward flows and scales the average ion flow velocity accordingly. For example, if the earthward flow rate in a particular plane is 60% earthward and 40% tailward, with respective velocities of 25 km s^{-1} and 12 km s^{-1}, then the earthward flow velocity contributes to 60% of mean ion flow velocity. This was done to ensure any planes with particularly different earthward and tailward flow occurrence rates did not give bias to the results.

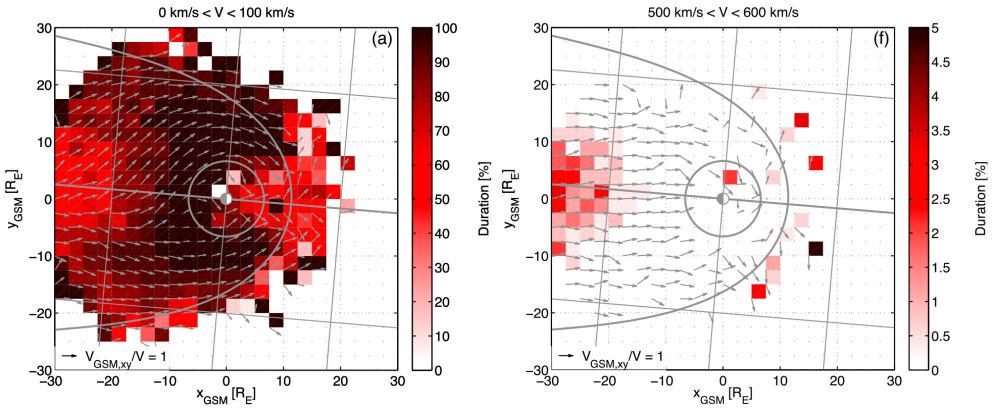

FIGURE 4.27: Earthward plasma flow in the Earth's plasma sheet velocity comparison. Left: Plasma flow for $0\,\mathrm{km\,s^{-1}} < \mathrm{v} < 100\,\mathrm{km\,s^{-1}}$. Right: Plasma flow for $500\,\mathrm{km\,s^{-1}} < \mathrm{v} < 600\,\mathrm{km\,s^{-1}}$. From *Juusola et al.* (2011).

Overall, while these results are useful in identifying the direction in which the flow velocity is greatest, it is somewhat deceptive as plasma flow does not occur in both the tailward and earthward flow at precisely the same moment, and therefore do not act to cancel each other out. Following this notion, it seems prudent to look at the average velocities in a different manner. One method is to treat earthward and tailward flows entirely separately, assuming the are completely disconnected and in doing so, allowing the numerical comparison between flow directions without combining the results. A second method is to consider the magnitude of the weighted average plasma flow velocity irrespective of direction, combining the earthward and tailward results to describes how fast the plasma is moving within the magnetosphere.

Using the first additional analysis criteria, it can be seen in Table 4.2 that the average earthward plasma flow velocity is 19.1 $\mathrm{km\,s^{-1}}$, with V_{xy} never exceeding an average of 30 $\mathrm{km\,s^{-1}}$ in any one plane. In the tailward direction, the average ion flow velocity is higher at 28.6 $\mathrm{km\,s^{-1}}$, and reaches 74.4 $\mathrm{km\,s^{-1}}$ in the outermost occupied plane in the z-direction. In the central three planes, earthward flow is faster, on average 26.9 $\mathrm{km\,s^{-1}}$ compared to the average tailward flow of 18.8 $\mathrm{km\,s^{-1}}$. These results agree with *McPherron et al.* (2011) who found that earthward flow was generally faster than tailward flow when observing plasma flows at the inner edge of the plasma sheet with $|\mathrm{v}_\perp| > 150\,\mathrm{km\,s^{-1}}$.

The second criteria yields an overall average plasma flow velocity magnitude of 25.7 $\mathrm{km\,s^{-1}}$ across all thirteen planes and 24.1 $\mathrm{km\,s^{-1}}$ across the central three. These results are somewhat lower than the average velocities presented by *Baumjohann et al.* (1989) who found the average ion flow velocity to be about $50\,\mathrm{km\,s^{-1}}$ in the central plasma sheet.

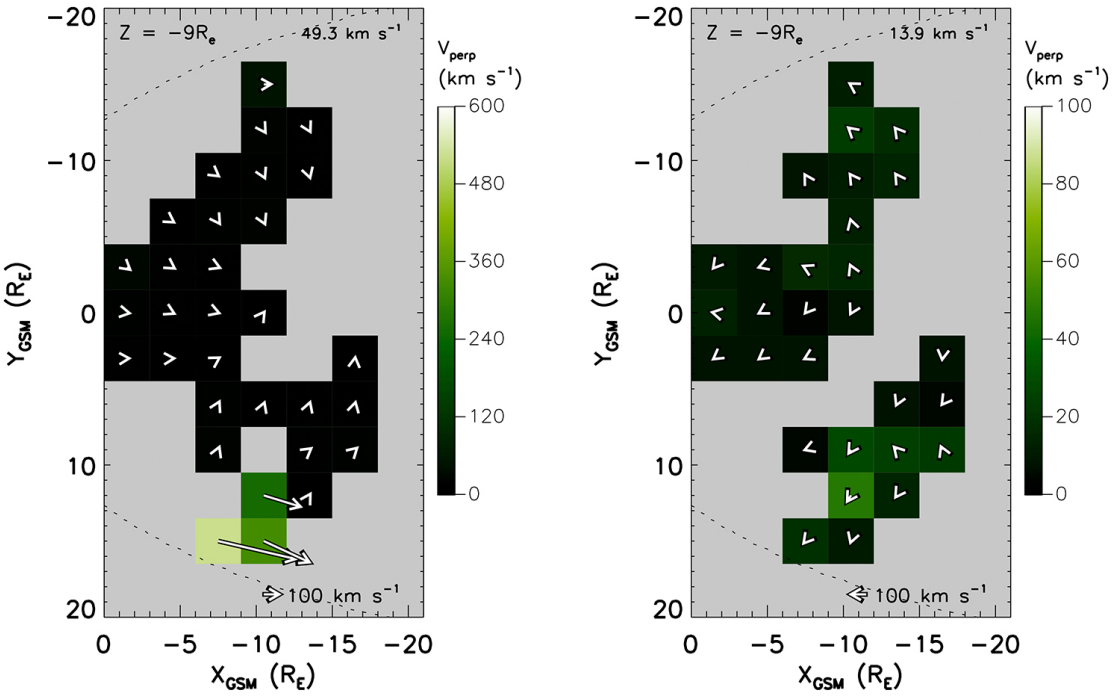

FIGURE 4.28: Ion Velocity plots displaying tailward (left) and earthward (right) plasma flow in the XY plane where Z = -9±1.5 R_E.

Juusola et al. (2011)'s study explored in more detail the bulk-velocity distribution of plasma sheet convection. While it predominantly focused on earthward flow, tailward flow was also discussed albeit in less detail. Juusola observed that the majority of plasma sheet convection were slow flows, in fact 95% of the plasma flows measured had v < 100 km s^{-1}. This result agrees with the study presented in this chapter, with 94.9% of plasma flow measured having v < 100 km s^{-1}. Juusola also found that in the earthward direction, the higher the flow velocity, the more sunward the flows were directed, as seen in right plot of Figure 4.27 where it is clear the higher velocity vectors are much less deflected than those of slower velocity in the leftward plot. When looking at tailward flows, Juusola finds a similar, but less distinct trend between velocity and the degree of flow deflection. Unfortunately it was not possible to carry out a direct comparison between Juusola's results about this particular ion flow characteristic and this thesis' study results. This was because the data have not been split up according to velocity, and while Juusola used bulk ion velocity (including both parallel and perpendicular velocity components), this study exclusively worked with field-perpendicular flows.

The work carried out by *Ohtani et al.* (2009) is related to the study presented in this thesis as it focused on the distinction between earthward and tailward flows, however velocity distribution was only discussed in brief. Ohtani observed that the tailward flow velocity does exceed 200 km s^{-1}, a result which can only be seen repeated in left

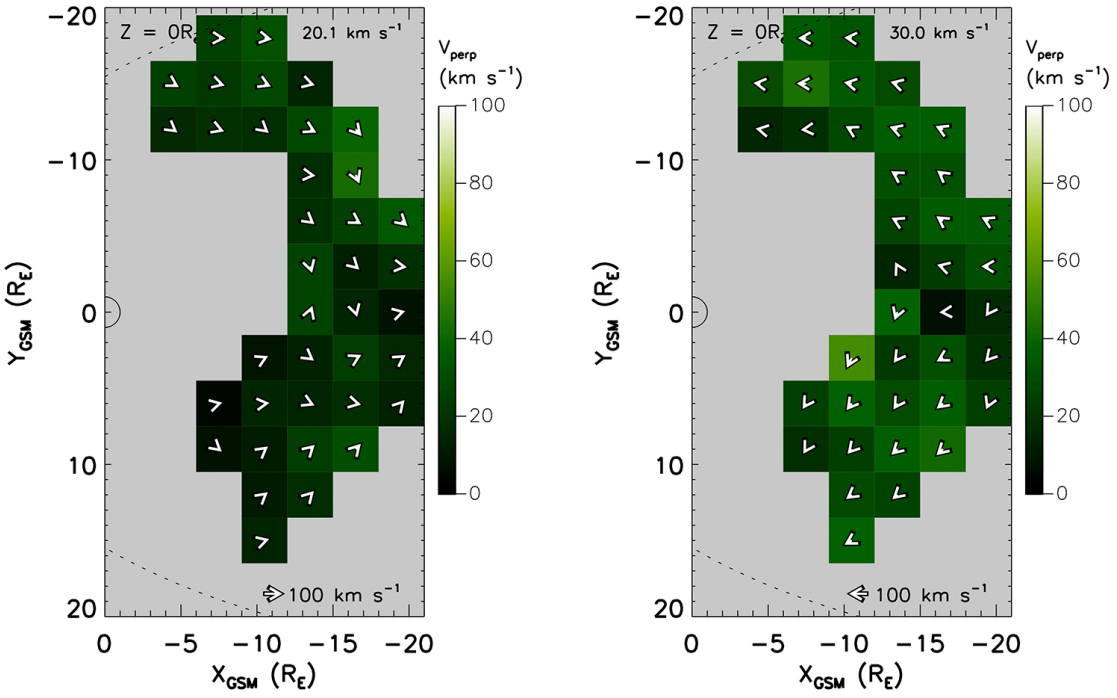

FIGURE 4.29: Ion Velocity plots displaying tailward (left) and earthward (right) plasma flow in the XY plane where Z = 0±1.5 R_E.

plot of Figure 4.28. As discussed in section 4.3.2, the fast flows are likely due to the spacecraft entering or passing very close to the magnetosheath and were not removed by the magnetosheath-contamination removal procedure due to their proximity to the Earth. This is also a likely explanation for Ohtani's results.

The average vector flow direction is the final observation to discuss. Considering the z = 0 ± 1.5R_E plane (the rightward plot of Figure 4.29), it is clear that there is a dawn-dusk asymmetric flow pattern for earthward flows. In the dawn beyond y = -10R_E, the flow is almost entirely sunward, while closer to local midnight, deflections are observed towards the dawn flank. On the dusk side, duskward deflection is more widespread across the region and contributes more significantly to the flow direction that the dusk-side deflection. Close to the local midnight, duskward-directed cross-tail flow is present. The earthward flow patterns observed in this study appear to be in agreement with a number of similar studies previously carried out when looking at their figures and discussions (e.g. *Angelopolous et al.* (1993); *Hori et al.* (2000); *Raj et al.* (2002); *Nakamura et al.* (1994); *Runov et al.* (2005); *Wang et al.* (2006); *Juusola et al.* (2011); *Zhang et al.* (2015a)). There is little evidence of plasma deceleration about local midnight (e.g. *Zhu* (1993); *Zhang et al.* (2015a); *McPherron et al.* (2011)) although minimal deceleration is apparent at y < -9R_E closer to the flanks. It is also interesting to examine the proportion of plasma flow directed out of the XY plane. This can be

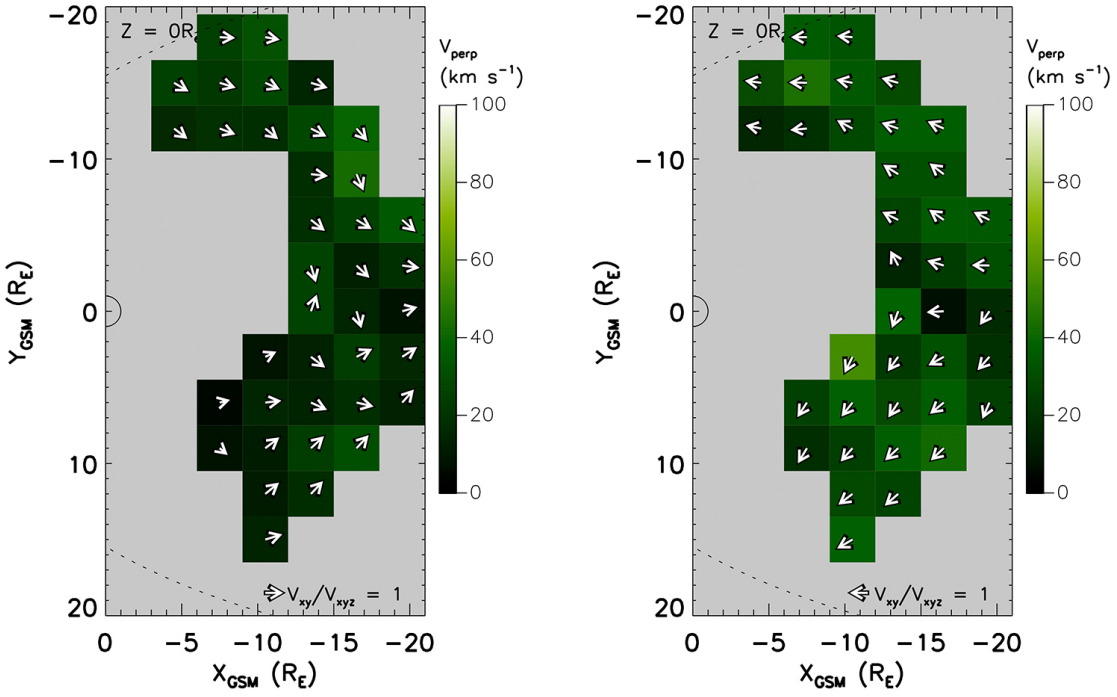

FIGURE 4.30: Velocity vector plots displaying unit vector arrows plotted over total tailward (left) and earthward (right) plasma flow magnitude in the XY plane for Z = 0±1.5 R_E.

done by dividing the V_{xy} vectors by V_{xyz} as seen in Figure 4.30. It is clear from this figure that all of the vectors are very close to unity length (as indicated in the key), meaning that there is very little contribution to the field-perpendicular flow direction from the z-component earthward velocity vector.

Looking at tailward flows in the same plane (Figure 4.29), it is clear there is also evidence of asymmetric flow. In the dawn sector, beyond y = -7.5 R_E, the plasma flow is predominantly anti-sunward with a a small cross-tail flow component directed towards local midnight. At greater radial distances and beyond x = -12 R_E, stronger deflections towards midnight are present. Within y = -7.5 R_E, closer to local midnight, the tailward flow exhibits slightly stronger deflections towards local midnight. This could be evidence of earthward flows being reflected back outward away from the Earth (*McPherron et al.*, 2011). At local midnight, the majority of the flow vectors are strongly deflected within x = -15 R_E which suggests they could be the result of the magnetosphere peeling back sunward following reconnection. Crossing the local midnight into the dusk sector, the tailward flows experience greater deflection towards midnight with increasing y-position throughout the region. The observed tailward flow pattern is in general agreement with previous studies (i.e. *McPherron et al.* (2011); *Juusola et al.* (2011); *Zhang et al.* (2015a)). Looking at the normalised vector plots for this plane, Figure 4.30, again it is

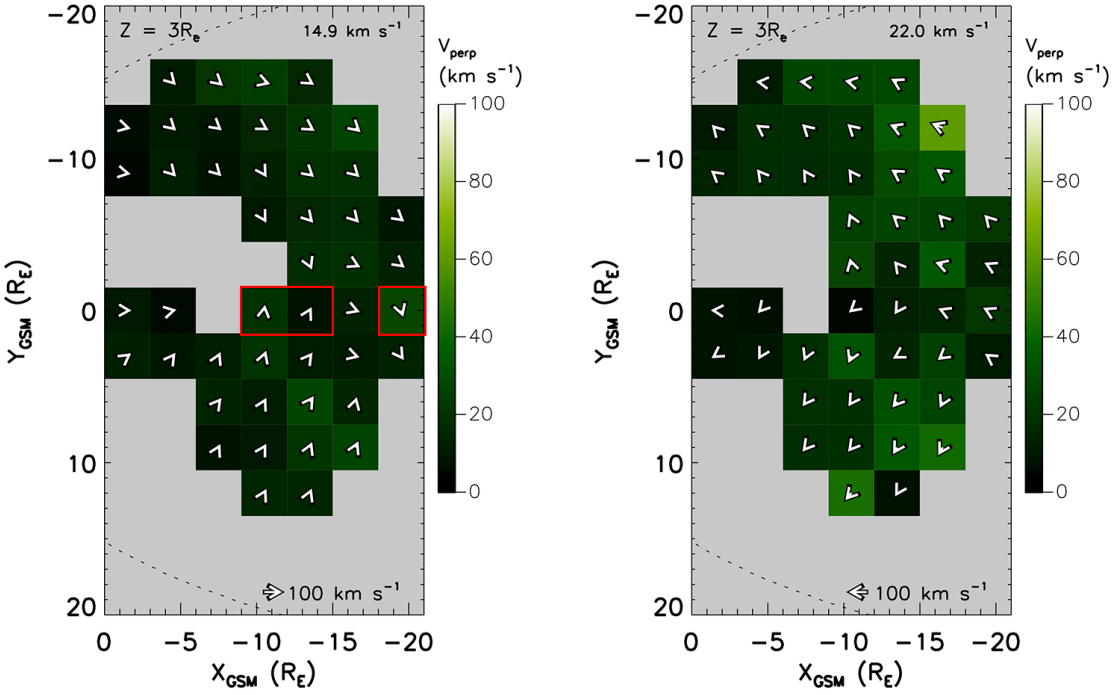

FIGURE 4.31: Ion velocity plots displaying tailward (left) and earthward (right) plasma flow in the XY plane where Z = 3±1.5 R_E.

clear that the majority of the vectors are near unity length and so there is very little contribution to the overall flow direction from the tailward velocity vector z-component.

Away from the central plane, some dawn-dusk asymmetry can still be observed. Looking at earthward flow in the z = $3 \pm 1.5 R_E$ plane (seen in the rightward plot of Figure 4.31), sunward flow is prevalent beyond y = -13.5 R_E, but within this distance, fairly strong deflections can be seen directed towards the dawn flank. At local midnight, the flow is directed slightly more earthward with some duskward deflections within x = -15 R_E and dawnward beyond. The flow in the dusk sector is more strongly deflected in the duskward direction, with the strongest deflections beyond y = 3.5 R_E. Throughout the plane, there is slightly more evidence of flow deceleration with the bins at a radial distance greater than about $10 R_E$ showing larger velocities than those within this boundary. Tailward flow in this plane (Figure 4.31) generally exhibit much stronger deflections towards midnight than the central z = $0 \pm 1.5 R_E$ plane. Throughout the dawn sector, deflections directed toward local midnight tend to be somewhat weaker than those in the dusk sector. The deflections weaken towards local midnight down to y = $\pm |1.5| R_E$. At local midnight itself, flow is either strongly anti-earthward or strongly deflected (red boxes in Figure 4.31). Again this is likely to be evidence of Dungey Cycle motion as the field lines peel outwards and back towards the dayside.

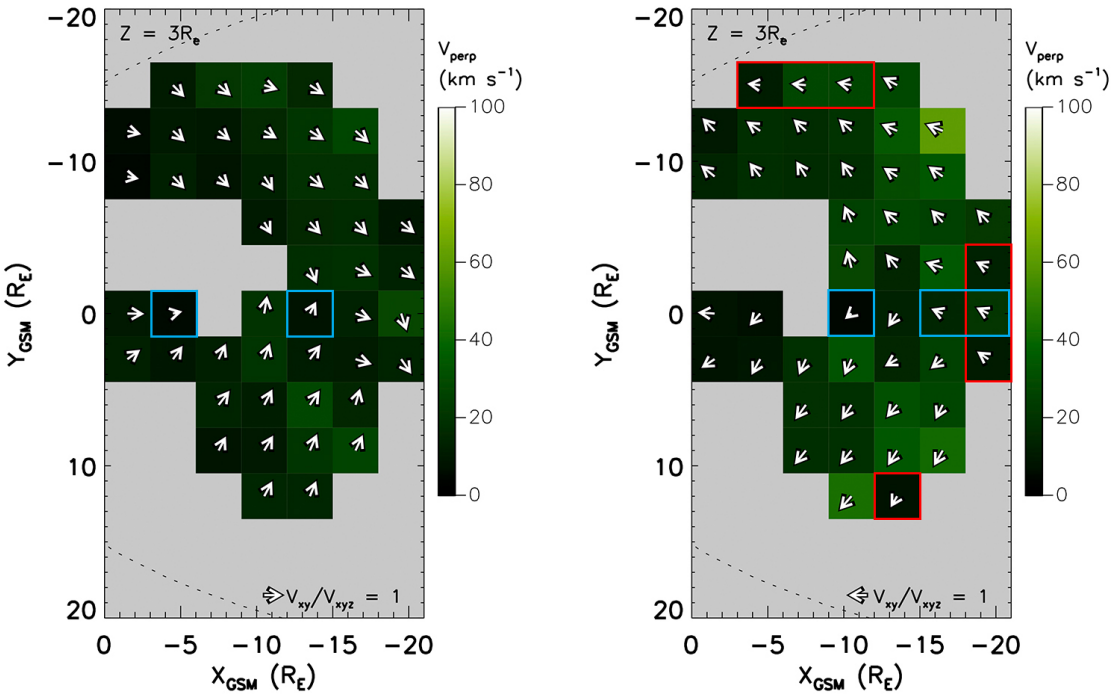

FIGURE 4.32: Velocity vector plots displaying unit vector arrows plotted over total tailward (left) and earthward (right) plasma flow magnitude in the XY plane for Z = 3±1.5 R_E.

Considering the plasma flow direction out of the plane in the z = 3 ± 1.5R_E using Figure 4.32. For earthward flow (right plot), many of the vectors are somewhat shorter than unitary length and thus there is some influence from the z-direction ion velocity flow component. This effect is strongest at the most distant radial distances from Earth (red boxes) as well as at local midnight (blue boxes). This shows that there is more influence from the z-direction velocity component something that there is some stronger plasma convection in the vertical direction (relative to the GSM coordinate system) present in these regions. The same general behaviour can be seen for the tailward flows (left plot of Figure 4.32), with the strongest deflections present at local midnight (blue boxes).

Further out into the magnetosphere, the asymmetry of flow begins to break down. While the tailward flow occurrence rate becomes dominant, strong flow deflections towards local midnight are still very much present, seen in Figure 4.33. The asymmetry of earthward flow also appear to break down, although data coverage is reduced at greater z-distances and thus these conclusions become more difficult to verify (Figure 4.34). Deflections of earthward flows are clearly apparent throughout the planes, being directed quite evenly around the Earth.

Looking at the proportion of plasma flowing out of the plane (Figure 4.35), it appears that many of the vectors are somewhat below unity length for tailward flow, suggesting

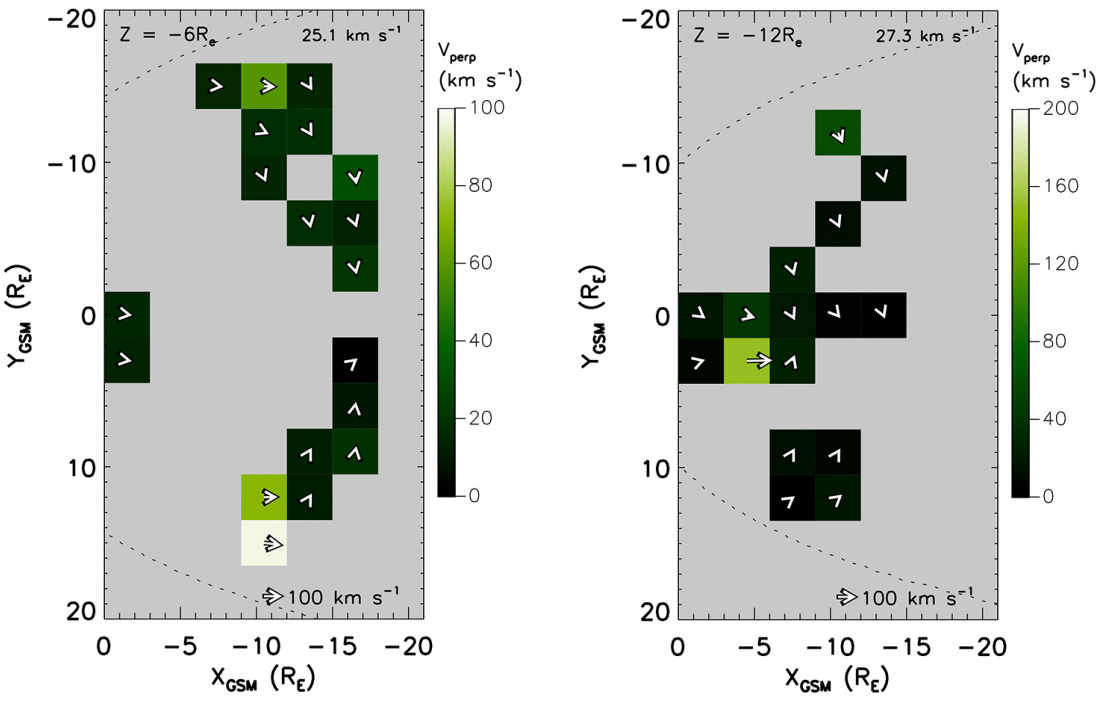

FIGURE 4.33: Ion velocity plots displaying tailward plasma flows for the planes Z = -6±1.5 R_E (left) and z = -12 R_E (right).

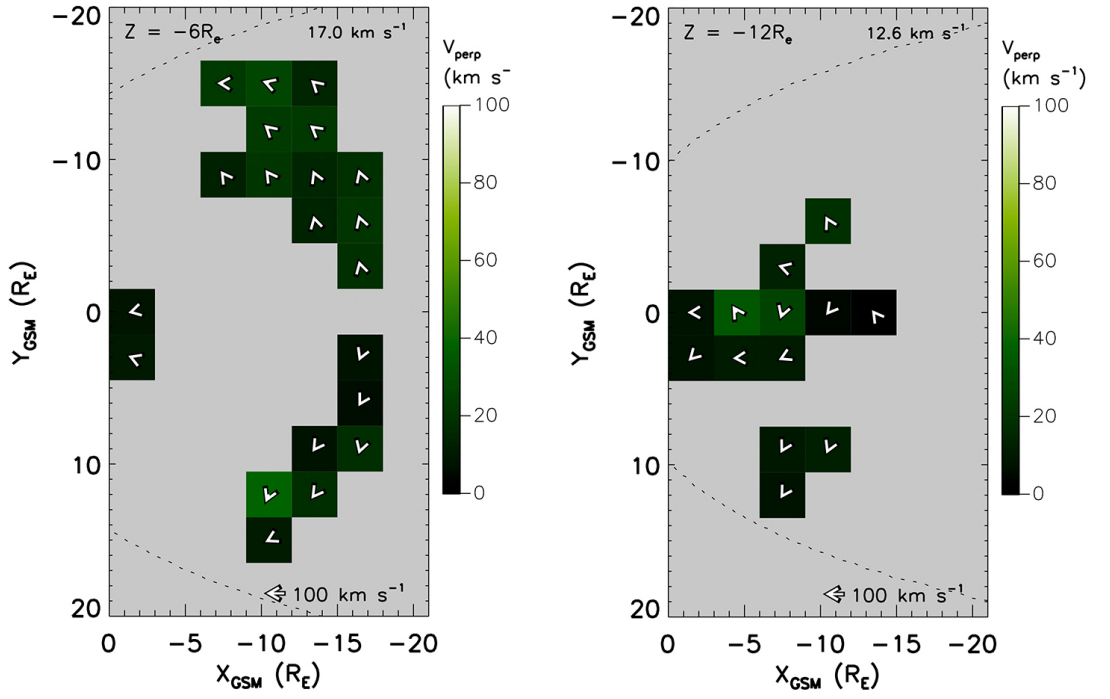

FIGURE 4.34: Ion velocity plots displaying earthward plasma flows for the planes Z = -6±1.5 R_E (left) and z = -12 R_E (right).

that there is still a consistent influence from the z-direction ion velocity component.

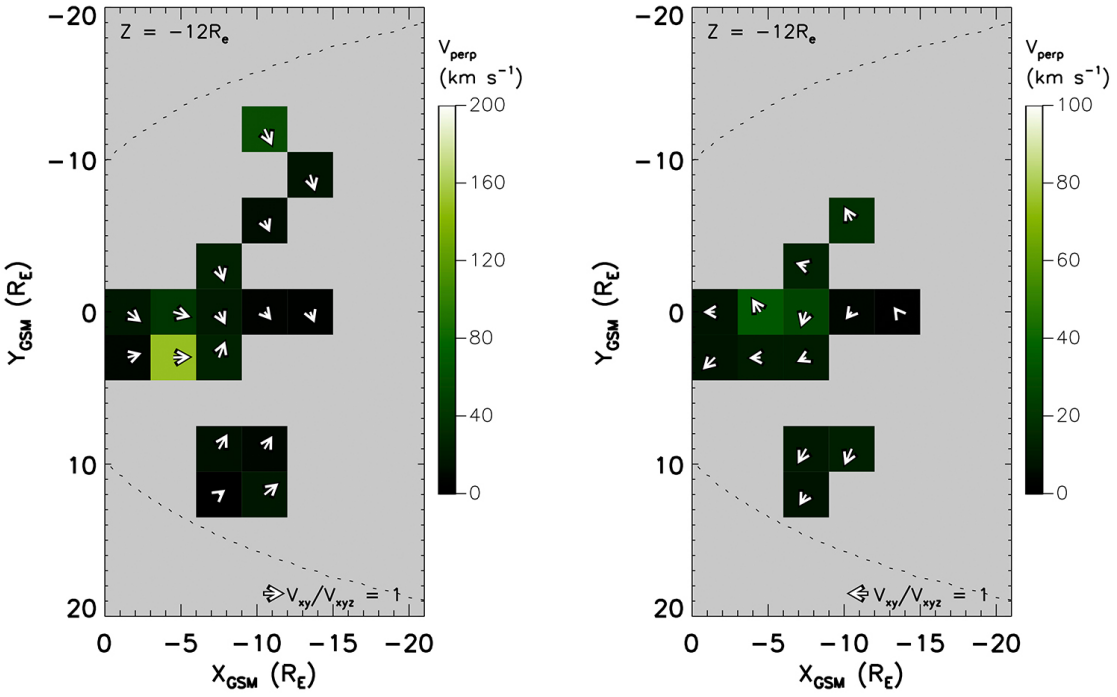

FIGURE 4.35: Velocity vector plots displaying unit vector arrows plotted over total tailward (left) and earthward (right) plasma flow magnitude in the XY plane for Z = -12±1.5 R_E.

Again it seems the strongest defections are at the local midnight with more z-directed deflections present at greater x-positions (left plot, blue boxes on Figure 4.35). The general trend is similar for earthward flow (right plot) whereby there are deflections in the z-direction throughout the plane with the most significant effect present in the region surrounding local midnight.

4.4.3 Summary

4.4.3.1 Sample Counts

When taking observations in the XY plane, it was found that there are much more ion velocity data available in the northern hemisphere than the southern hemisphere. Naively this appeared to be incorrect because from the orbital inclination of the Cluster spacecraft and the southerly progression of the orbit throughout the mission, it would be expected that there should be more data in the southern hemisphere. However, much of the most southerly data was removed due to contamination with data collected in the magnetosheath. The spatial coverage is also greater in the northern hemisphere, with more bins being filled with the available data than in the southern hemisphere. In the northern hemisphere, there is a somewhat asymmetric data distribution about the local

midnight, whereas this distribution is more symmetrical in the southern hemisphere, although there does tend to be more data available in the dusk sector. When looking at the most commonly studied plane, the central equatorial plane ($z = 0 \pm 1.5\,R_E$, Figure 4.36), it can be seen that the most densely populated bins are at radial distances greater than $10\,R_E$, a phenomena which is believed to be an artefact of the spacecraft orbit. The final key observation made when considering the sample count plots was that there was a greater occurrence of plasma flow in the earthward direction than there was in the tailward direction. Previous studies (*Juusola et al.*, 2011; *Zhang et al.*, 2015a) generally agree with this.

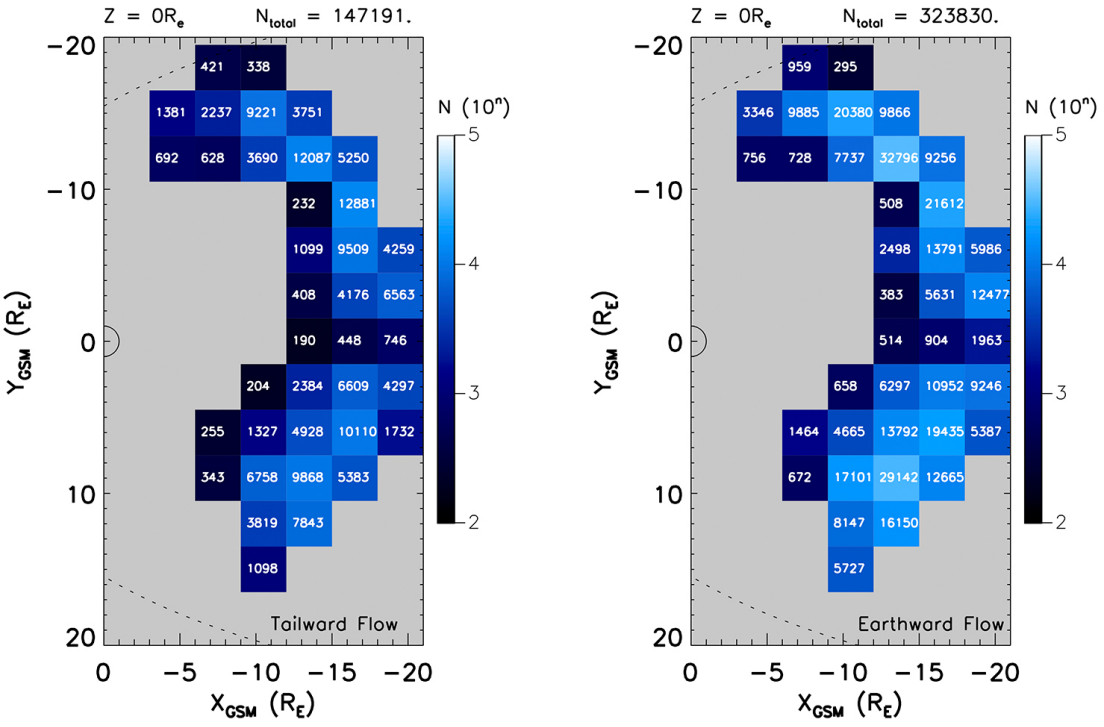

FIGURE 4.36: Sample count plots displaying tailward (left) and earthward (right) plasma flow in the XY plane where $Z = 0 \pm 1.5\,R_E$.

This study generally provides a unique set of results as not only does if focus on magnetospheric convection through the use of the perpendicular ion velocity component (the most similar previous studies by *Juusola et al.* (2011) and *Zhang et al.* (2015a) use bulk ion flow), it also includes all magnetotail data rather then using narrow bands of data in the XY and XZ plane as Zhang and Juusola do respectively. This allowed the analysis of a much larger magnetospheric area, providing a much better picture of the global behaviour of ion flows on the nightside of the Earth.

4.4.3.2 Ion Flows in the XY Plane

When investigating ion flow velocity and direction, it was found that the weighted-mean average perpendicular tailward ion flow velocity of V_{xy} = -6.4 km s^{-1} dominated across all planes. This is not altogether unsurprising as while much of the fast contaminant tailward lobe and magnetosheath data was removed, some did slip through the net, pushing the average tailward velocity higher.

Looking at the central three planes, earthward flow dominates with a weighted-average field-perpendicular ion flow velocity of $V_{xy} = 14.7$ km s^{-1}, an expected result since earthward plasma sheet flow clearly dominates this region. This velocity magnitude seems like a reasonable number when looking at Figure 2 of the *Zhang et al.* (2015a) study which appears to depict similarly slow velocities. When treating earthward and tailward flows separately, it was found that the average earthward and tailward field-perpendicular ion flow velocity was 19.1 km s^{-1} and 28.6 km s^{-1} respectively. Overall, 94.9% of all ion flows were found to have velocities lower than 100 km s^{-1}, a result which almost exactly agrees with the *Juusola et al.* (2011) study. There were a couple of bins with exceedingly large vectors (for example Figures 4.28) which had velocities in excess of 200 km s^{-1}. It was clear that these were causes by magnetosheath contaminant data which slipped by the data removal procedures. This was double checked and by looking at the quick-look plots in the Cluster Active archive, indeed the data contribution to these specific bins were collected early in the tail-season when the Cluster spacecraft spend a reasonable amount of time situated in and around the magnetosheath.

A dawn-dusk asymmetry of ion flow is prominent in the most central planes. While strong flow deflections are present at greater distances from the equatorial plane, the asymmetry breaks down. Tailward ion flows certainly dominate in the outer regions, just as one would expect. For planes above the equatorial plane with positive z-positions, the deflection of tailward flows appear greater than the earthward flows.

Finally, the normalised vector plots (Figures 4.32) were used to try to establish the amount of plasma flowing out of the XY plane. It was found that in general many of the vectors were less than unitary in length and thus experience some convective flow in the z-direction, although it appears to be weaker than deflections in the y-direction. The strongest deflections were found to be close to local midnight as well as at the peripheries of the data set. This was basically the same for both earthward and tailward flows.

The key results in this section were essentially supporting the results from previous studies (*Juusola et al.*, 2011; *Zhang et al.*, 2015a) and therefore at first glance do not appear to bring anything new to the table. However it must be remembered that the most similar previous studies used bulk-ion velocity moments, not perpendicular-velocity

moments and as such, the results are a new alternative outlook which come to the same conclusions. This study also reaches out in the much greater areas above and below the equatorial plane then previous studies and thus the flow behaviour here has not previously been reported on in any great detail.

4.5 Plasma Flow in the XZ Plane

4.5.1 Sample Count

This section presents the spatial distribution of the data in the XZ-planes. Looking across all thirteen XZ planes in the y-direction (all sample count plots which are not explicitly discussed in this section can be seen in Appendix B, the dawn hemisphere (-Y planes) contains more data than the dusk hemisphere (741544 counts to 547511 counts) and therefore has the greatest data coverage. The spatial distribution of the data collected is more comprehensive in the inner dusk hemisphere (between y = 1.5 R_E and y = 7.5 R_E, for example Figure 4.37) than the inner dawn sector (for example Figure 4.38), however at greater distances from Earth there are more bins occupied in the dawn hemisphere than the dusk hemisphere. For example, the plane covering y = 3 $\pm$ 1.5 R_E has 30 tailward bins with data in, whereas for plane covering y = -3 $\pm$ 1.5 R_E, 23 bins are filled. At higher latitudes the plane covering y = 15 $\pm$ 1.5 R_E, only has 5 tailward bins of data, whereas for the plane covering y = -15 $\pm$ 1.5 R_E has 18 tailward bins filled. This distribution provides evidence for the orbital shape and positioning of the Cluster spacecraft. It suggests that in the dusk hemisphere, the spacecraft follows a wider trajectory in the z-direction and a shallower trajectory in the y-direction. In the dawn hemisphere, the spacecraft appears to follow a shallower trajectory in the z-direction and a deeper trajectory in the y-direction. This idea is supported by the fact there was no data collected beyond y = 16.5 R_E whereas there were several thousand data points collected in the plane centred on y = -18$\pm$1.5 R_E. This orbital trajectory also goes some way in explaining why there is more data collected in the dusk hemisphere.

Looking across all y-planes, there is an asymmetrical data distribution in both the dawn and dusk hemispheres. In the dawn (-y planes), there tends to be more bins occupied in the northern hemisphere than the southern hemisphere with no data collected beyond z = -13.5 R_E (an example of this can be seen in Figure 4.38). This trend is reversed on the dusk side (+y planes) with no data beyond z = 10.5 R_E (an example of this can be seen in Figure 4.37). This difference in distribution can be explained by Cluster's orbital inclination in the YZ plane, whereby when the orbit is predominantly in the dawn hemisphere, the orbit is tilted in the positive z direction and when the orbit is mostly in the dusk sector, the orbit is tilted in the negative z direction. While the orbital plane is fixed in inertial space, because the GSM coordinate system is being used, the frme of reference is being rotated in inertial space. As such a seasonal effect occurs in the form of this orbital tilt, as shown in Figure 4.7.

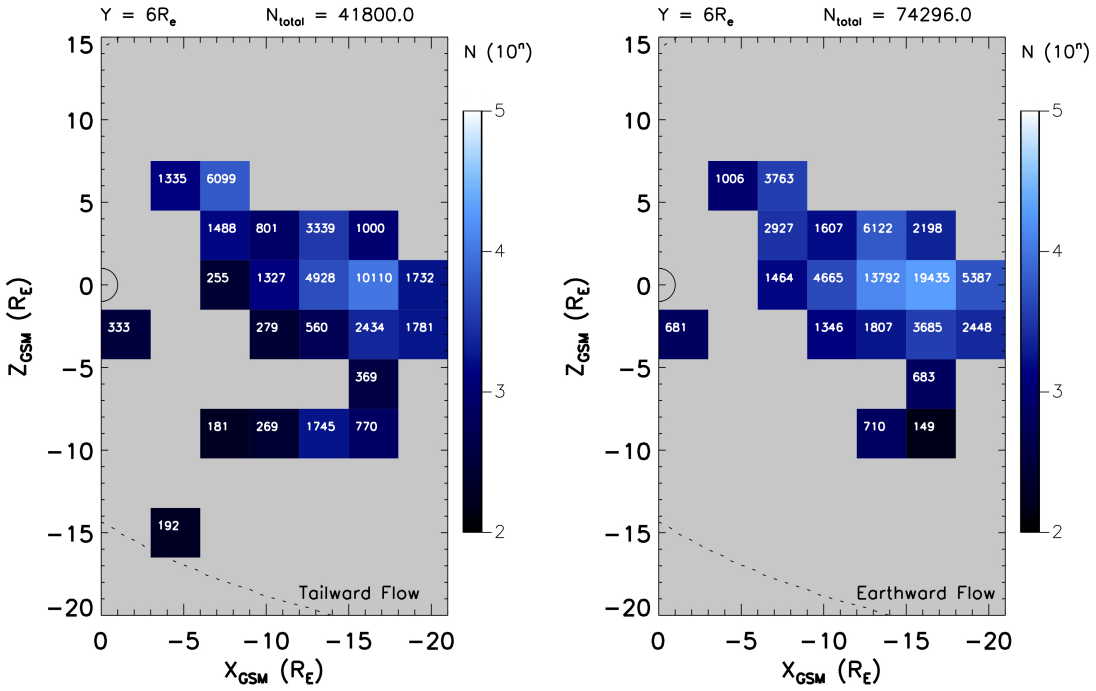

FIGURE 4.37: Sample count plot for XZ plane Y = 6 ± 1.5 R_e displaying tailward (left) and earthward (right) plasma flow.

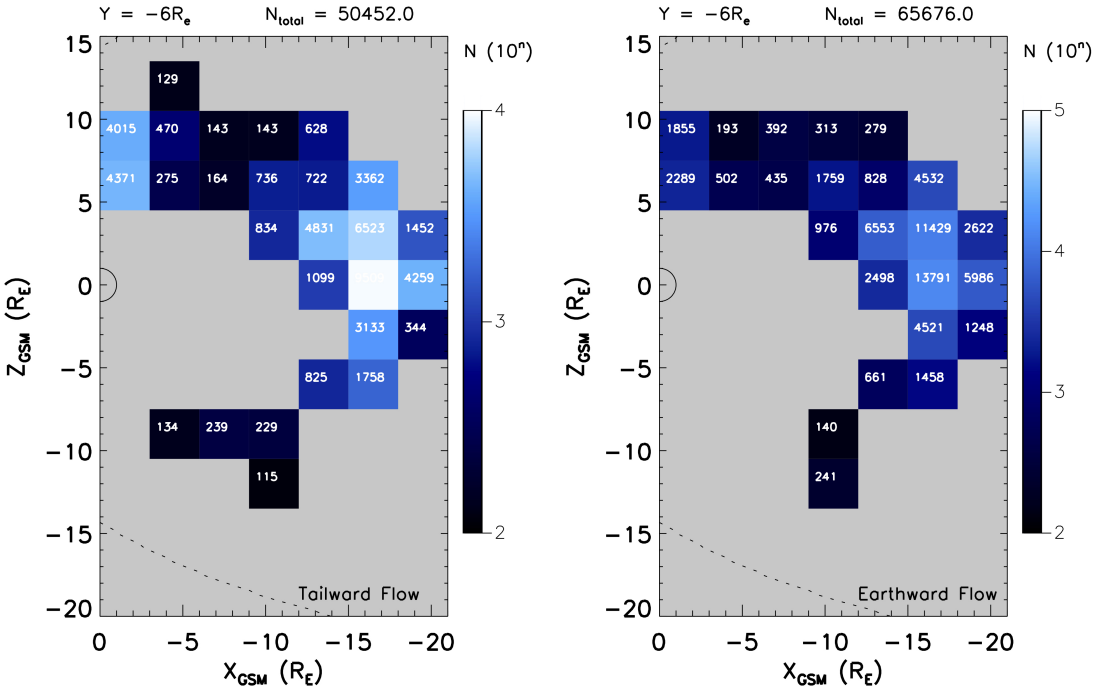

FIGURE 4.38: Sample count plot for XZ plane Y = -6 ± 1.5 R_e displaying tailward (left) and earthward (right) plasma flow.

As discussed in the previous section, there is more earthward flow than tailward flow across all of the data collected (Table 4.3). However, when observing the data distribution in XZ planes, the central three planes all have more tailward than earthward flow

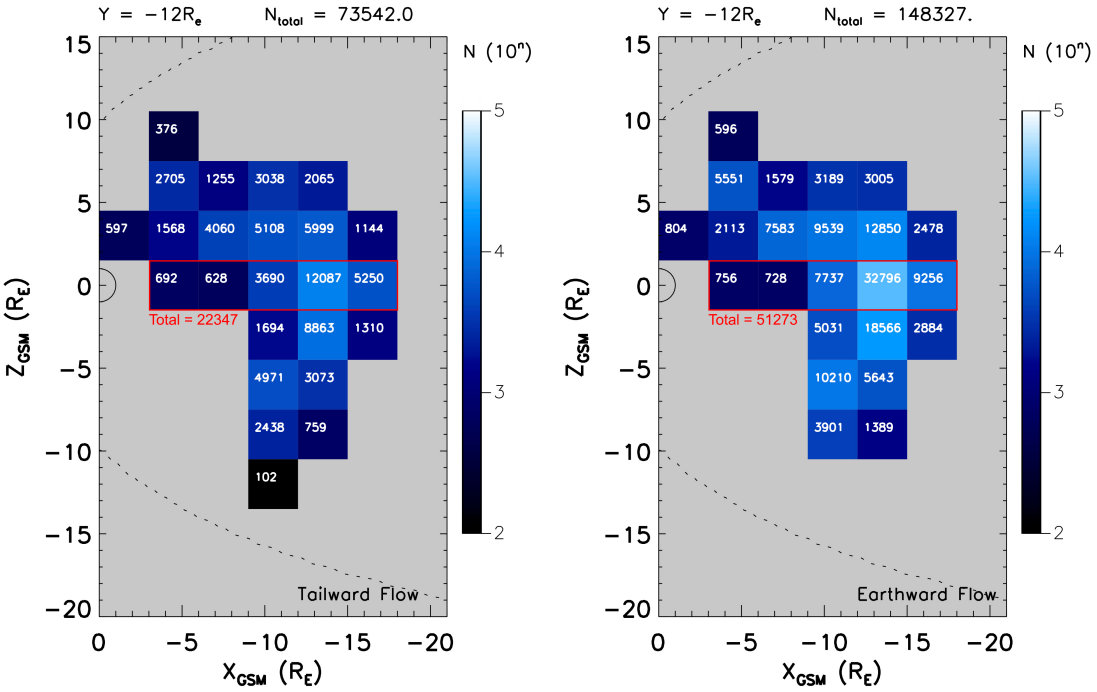

FIGURE 4.39: Sample count plot for XZ plane Y = -12 ± 1.5 R_e displaying tailward (left) and earthward (right) plasma flow.

occurrences. When using the *Zhang et al.* (2015a) plasma sheet spatial parameters as a rough guide, this result becomes more obvious. Zhang suggests that the plasma sheet spans 8 R_E in the z-direction and 20 R_E in the y-direction and therefore it is now clear that there is likely to be less plasma sheet data contained within the XZ plane and potentially proportionally more contaminant magnetosheath and tail-lobe data contained within each plane. The data distribution further out away from Earth is somewhat more perplexing as earthward flows become dominant beyond z = ± 4.5 R_E. Looking at this distribution more closely in Figure 4.39, it can be seen that in the row centred on z = 0 (red boxes), the number of earthward flows double the tailward flow occurrence rate (51,273 earthward counts equalling over two thirds that of all tailward flow for the plane). The large earthward flow occurrence rate found at greater y-positions along the equatorial plane in this study suggests that the plasma sheet does extend out beyond Zhang's conservative spatial parameter of -10 R_E < y <10 R_E. These results provide strong evidence that at times the plasma sheet can extend out as far as 19.5 R_E in y-direction and extrapolating this, it could be said that during these periods, the magnetosphere could stretch as wide as 39 R_E. Of course it is a dynamic such the plasma sheet boundaries are not static, expanding and contracting with varying magnetospheric conditions.

Plane (Y = nR$_E$)	N$_{earthward}$	N$_{tailward}$	N$_{total}$	% Earthward	% Tailward
18	-	-	-	-	-
15	10588	8417	19005	55.7	44.3
12	58090	31961	90051	64.5	35.5
9	99999	41687	141686	70.6	29.4
6	74296	41800	116096	64.0	36.0
3	80362	100311	180673	44.5	55.5
0	77424	163883	241307	32.0	68.0
-3	52658	64077	116735	45.1	54.9
-6	65676	50452	116128	56.6	43.4
-9	89739	49391	139130	64.5	35.5
-12	148327	73542	221869	66.9	33.1
-15	97904	45656	143560	68.2	31.8
-18	2469	1653	4122	59.9	40.1
Totals	857532	672830	1530362	56.0	44.0

TABLE 4.3: Sample count distribution for the XZ plane across 13 cuts in the y-direction. The Y value given is the position on which the plane is centred on.

4.5.2 Ion Flow: Magnitude and Direction

Considering earthward and tailward flows together, just as with the XY planes, on average across all thirteen XZ planes, as seen in Table 4.4, tailward velocity dominates with an average V$_{xz}$ of -4.1 km s^{-1}. This is an interesting result as when comparing it to the average ion flow velocity in the XY plane, there is only 2.3 km s^{-1} difference. While this is not a formally significant difference, it does shows that flow in the x-direction is the main contributor to the direction of ion flow in the magnetotail. The velocity difference could be affected by noise in the calculations from the rounding of results earlier on, however the more likely cause is the fact that in the XY plane, the x and y components of velocity are used, whereas in the XZ plane, the x and z components of velocity are used. In general, this result strengthens the idea that on average, over large time-scales, the magnetosphere is rather slow-moving system in comparison to say the solar wind. This is even more true for the midnight sector, as the average velocity of the inner three planes is just -3.4 km s^{-1}. As previously discussed, while this result is useful in identifying the direction in which the flow velocity is greatest, it does not give an accurate representation of general plasma flow conditions, whereby bursts of tailward or earthward flows occur separately, not simultaneously as this average suggests.

Treating earthward and tailward flows entirely separately, it can be seen that the weighted-average plasma flow velocity is generally rather low in the earthward direction (Table 4.4), with the average V$_{xz}$ never exceeding an average of 42.7 km s^{-1} in any plane. In the tailward direction, the flow velocity is quite similar to the earthward flow magnitude although does get a little higher in the outer planes. It even exceeds 190

Plane (Y=n±1.5 R_E)	V_{xz} Earthward [km s^{-1}]	V_{xz} Tailward [km s^{-1}]	Weighted Mean V_{xz} [km s^{-1}]	Weighted Mean $\|V_{xz}\|$ [km s^{-1}]
18	-	-	-	-
15	24.4	191.9	-71.4	98.6
12	19.4	32.6	0.9	24.1
9	16.1	11.4	8.0	14.7
6	15.1	20.0	2.5	16.9
3	11.6	17.2	-4.4	14.7
0	12.5	12.9	-4.8	12.8
-3	15.1	14.0	-0.9	14.5
-6	14.8	13.0	2.7	14.0
-9	14.7	14.4	4.4	14.6
-12	22.6	16.6	9.6	20.6
-15	29.7	27.4	11.5	29.0
-18	42.7	43.5	8.1	43.0
Average	19.9	34.6	-4.1	26.4

TABLE 4.4: Average V_{xz} for the XZ plane across 13 cuts in the y-direction. The Y value given is the position on which the plane is centred on. Earthward V_{xz} refers to the average positive V_x and V_z value for the plane. Tailward V_{xz} refers to the average negative V_x and V_z value for the plane. Weighted mean average V_{xz} refers to the average earthward and tailward V_{xz} taking into consideration flow direction for each plane. Weighted mean average $|V_{xz}|$ refers to the average magnitude of earthward and tailward flow velocity, neglecting flow direction. Average includes data from all planes for each column.

$km\,s^{-1}$ in the plane centred upon Y = 15 R_E, however looking at Figure 4.40, the exceedingly large vectors could be due to some magnetosheath data which slipped through the sheath-killer algorithm.

When averaged across all 13 planes, the average earthward and tailward plasma flow velocity is 19.9 $km\,s^{-1}$ and 34.6 $km\,s^{-1}$ respectively, clearly showing that plasma flow velocity is on average greater in the tailward direction. It also shows that the average z-component of ion velocity is slightly higher than that of the y-component as the average earthward velocity is 0.8 $km\,s^{-1}$ faster and the average tailward velocity is 6 $km\,s^{-1}$ faster in the XZ planes than the XY planes. In the central three planes, tailward flow is still a little faster, on average 14.3 $km\,s^{-1}$ compared to the average earthward flow of 13.1 $km\,s^{-1}$. These results are in contrast with *McPherron et al.* (2011) who found that earthward flow was generally faster than tailward flow when observing plasma flows at the inner edge of the plasma sheet with $|v_\perp| > 150\,km\,s^{-1}$. The reasons for this difference are as described before in section 4.4.2 with the addition of there being less plasma sheet data included in each XZ plane due to the spatial parameters of the region. The final method of the plasma velocity analysis is to consider the magnitude of the average plasma flow velocity irrespective of direction, combining the earthward and tailward results to describes how fast the plasma is generally moving within the magnetosphere. This criteria yields a weighted-average plasma flow velocity magnitude of 26.4 $km\,s^{-1}$

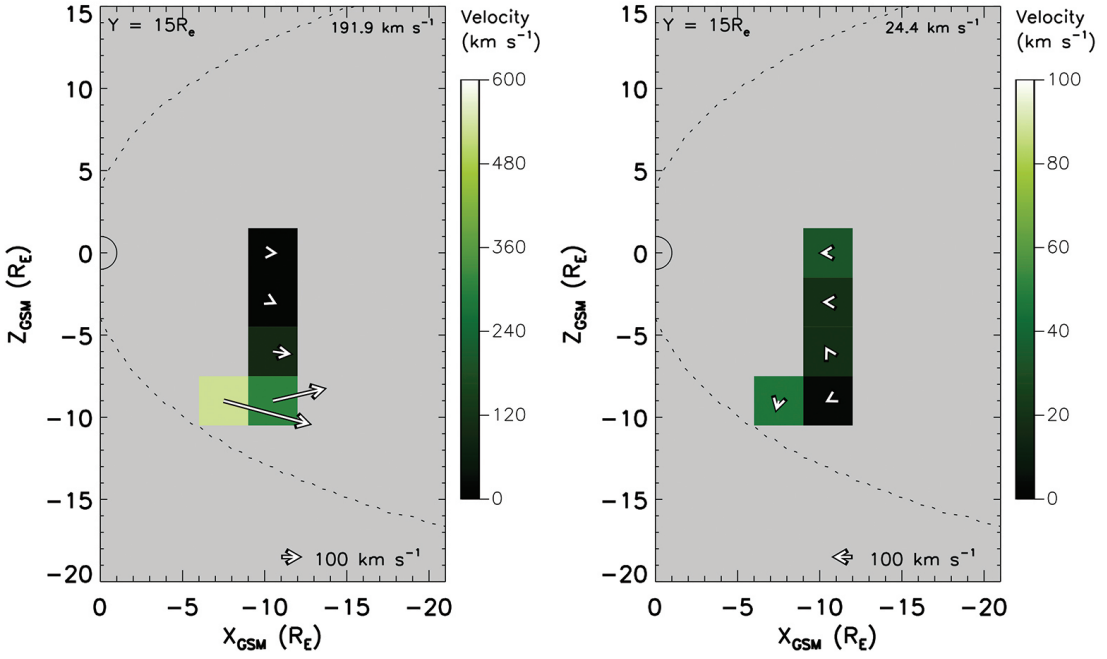

FIGURE 4.40: Sample count plots displaying tailward (left) and earthward (right) plasma flow in the XZ plane for Y = 15±1.5 R_E.

across all thirteen planes and 14 km s^{-1} across the central three planes. The general velocity result underestimates the results reported by *Baumjohann et al.* (1989), who found the average ion flow velocity to be about 50 km s^{-1} in the central plasma sheet, while the average of the central three planes underestimates Baumjohann's results by about 70%.

The average vector flow direction is the final observation to discuss. Considering the y = 0 ± 1.5 R_E plane (Figure 4.41), the earthward flow pattern (right plot) is fairly symmetrical about local midnight with reasonably strong deflections away from the equatorial plane in both the northern and southern hemispheres. At the equatorial plane the flows are predominantly sunward. It is difficult to make direct comparisons with previous studies as the majority of them carry out observations in the XY plane with the exception of *Zhang et al.* (2015a). However, the spatial parameters Zhang incorporated restricts the comparable regions to just the central three rows of bins (-4.5 R_E < z < 4.5 R_E) and for y < -10 R_E, Figure 4.42. The results contained with the yellow boxes of Figure 4.41 can be compared to the results in the *Zhang et al.* (2015a) study. He found that earthward flow deflections were minimal, meaning the flow was predominantly reasonably parallel to the x-axis of the GSM coordinate system. In comparison, the results collected in this chapter exhibit somewhat more deflected flow on either side of the noon-midnight meridian (NMM) within same same region Zhang studied. Along the NMM however, the earthward flows were found to be deflected much

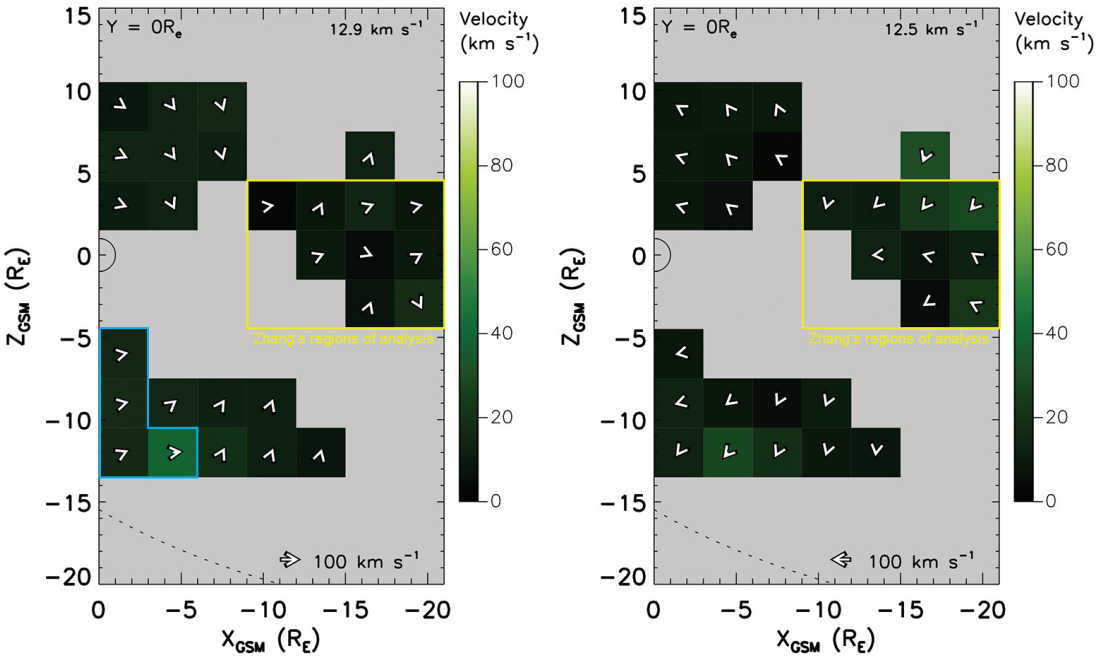

FIGURE 4.41: Ion perpendicular-velocity plots displaying tailward (left) and earthward (right) plasma flow in the XZ plane for Y = 0±1.5 R_E. The area surrounded by the yellow boxes corresponds to the area which is covered by the *Zhang et al.* (2015a) study.

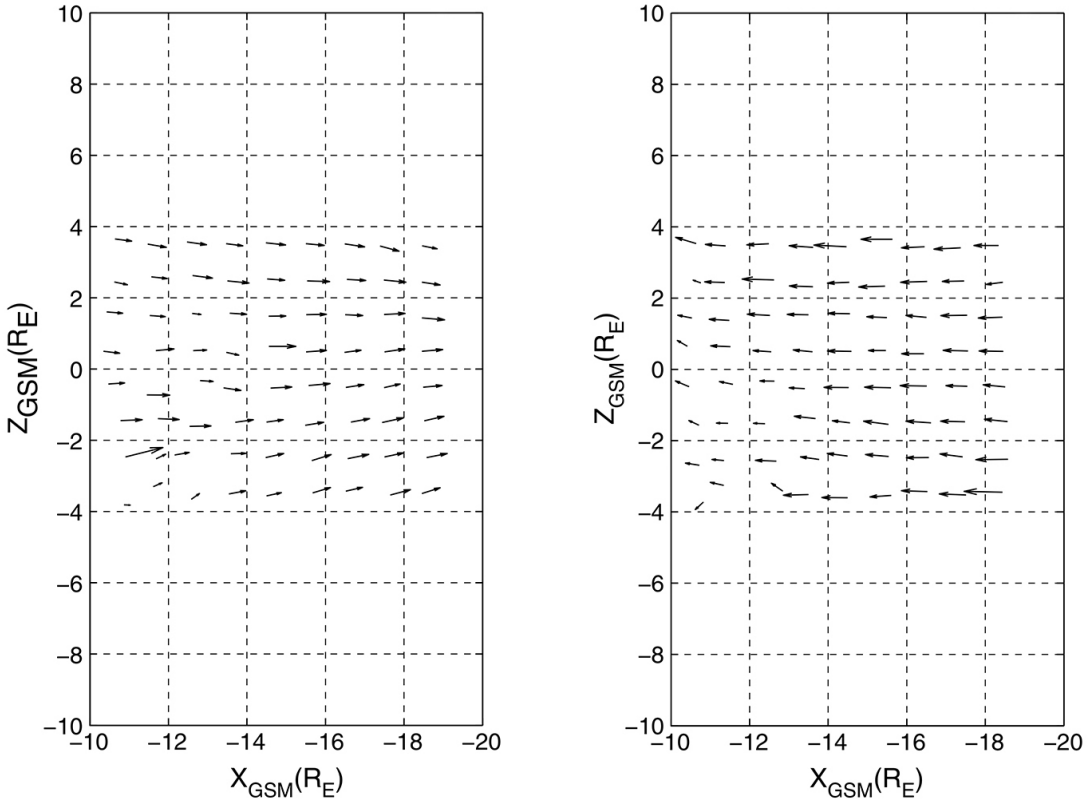

FIGURE 4.42: Zhang XZ plane tailward (left) and earthward (right) bulk ion-flow plots. The length of 1 R_E in the coordinate axis is equal to 100 km s^{-1}. Taken from *Zhang et al.* (2015a).s

less and directed more towards Earth (Figures 4.43 and 4.46). So both set of results are in somewhat agreement, and the likely reason for the difference at the outer reaches of the region studies is that Zhang used bulk-velocity moment data, whereas the study in the chapter utilised perpendicular-velocity moments, thus there will always be some differences between the two sets of results which depends on how strong the field-aligned velocity moment is at any given time. Zhang also found there to be some deceleration present in the earthward direction. Some evidence of this behaviour is also present in this study with the more distant bins (from the Earth) generally possessing higher velocities than the bins closer in to Earth. Looking away from the region studied by Zhang, strong deflections towards the northern and southern flanks can be observed, providing further evidence for the convective flow pattern of the Dungey cycle. This pattern likely shows either the remnant flow pattern of any magnetospheric lobe data which was missed by the Coxon lobe-removal algorithm, or perhaps the outer plasma sheet convecting downwards, or more likely a combination of both.

Looking at tailward flows in y = 0±1.5 R_E (Figure 4.41), there is evidence of north-south asymmetry, with the deflections towards the equatorial plane are somewhat stronger in the northern hemisphere than the southern hemisphere. This deflection pattern could be evidence of magnetic reconnection. As closed magnetic field lines are opened via magnetic reconnection (on the dayside magnetosphere), the magnetic tension of the field acts to straighten the newly opened lines. The momentum of the solar wind draws the open magnetic field lines tailward, and as more open field lines are drawn tailward, they are compressed towards local midnight. This motion is likely to be the cause of the deflection flow pattern observed in Figure 4.41. Within the region Zhang studies (contained in the yellow boxes) the tailward field-perpendicular ion flow is predominantly is somewhat more anti-sunward with stronger deviation in the bins centred upon z = 3±1.5 R_E. In this plane the prevalent anti-sunward flow could provide additional evidence in support of the idea that they could be the result of earthward flows reflected back outward (*McPherron et al.*, 2011). In the southern hemisphere out to x = -9 R_E, strong deflections towards the magnetic equator are observed with the weakest located by the southern terminator boundary(bins contained within the blue box) . Only a slight variation in ion velocity magnitude can be seen. Comparing these results with *Zhang et al.* (2015a), again more ion flow deflection was found in the study presented in this chapter.

Looking away from the noon-midnight meridian, asymmetries are present in both the dawn and dusk hemispheres. Considering the dawn hemisphere first (-y planes), earthward flows in the region surrounding the NMM in plane y = -3 ± 1.5 R_E (Figure 4.43) are minimally deflected. Ion flow deflections in the northern/southern hemispheres become more prominent in the northward/southward directions with greater distances from y

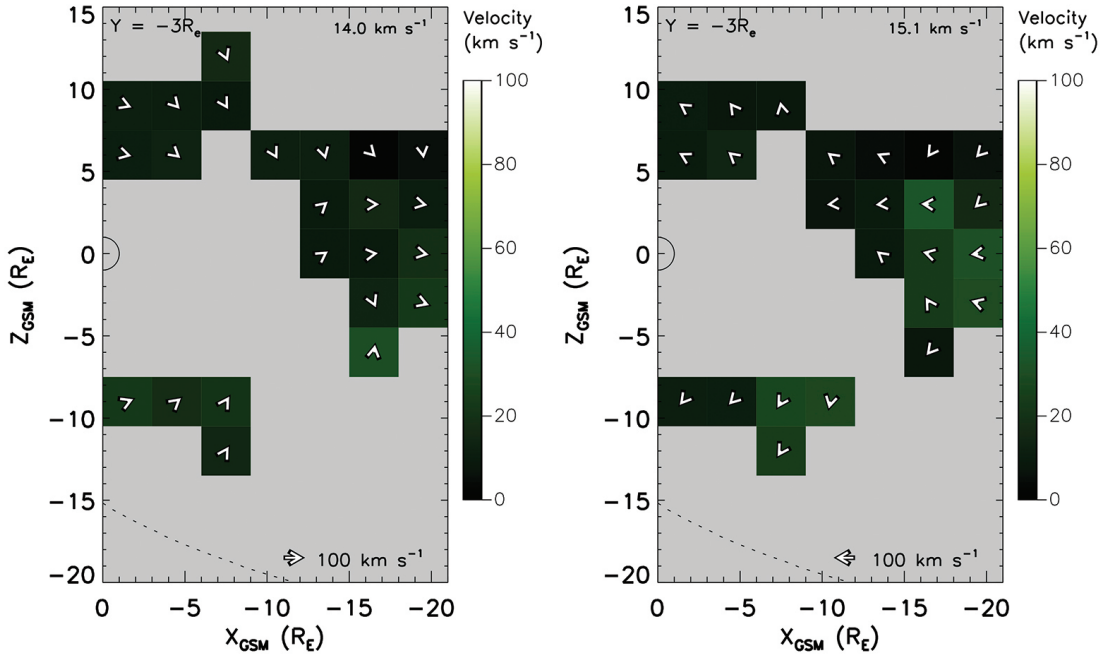

FIGURE 4.43: Ion perpendicular-velocity plots displaying tailward (left) and earthward (right) plasma flow in the XZ plane for Y = -3±1.5 R_E.

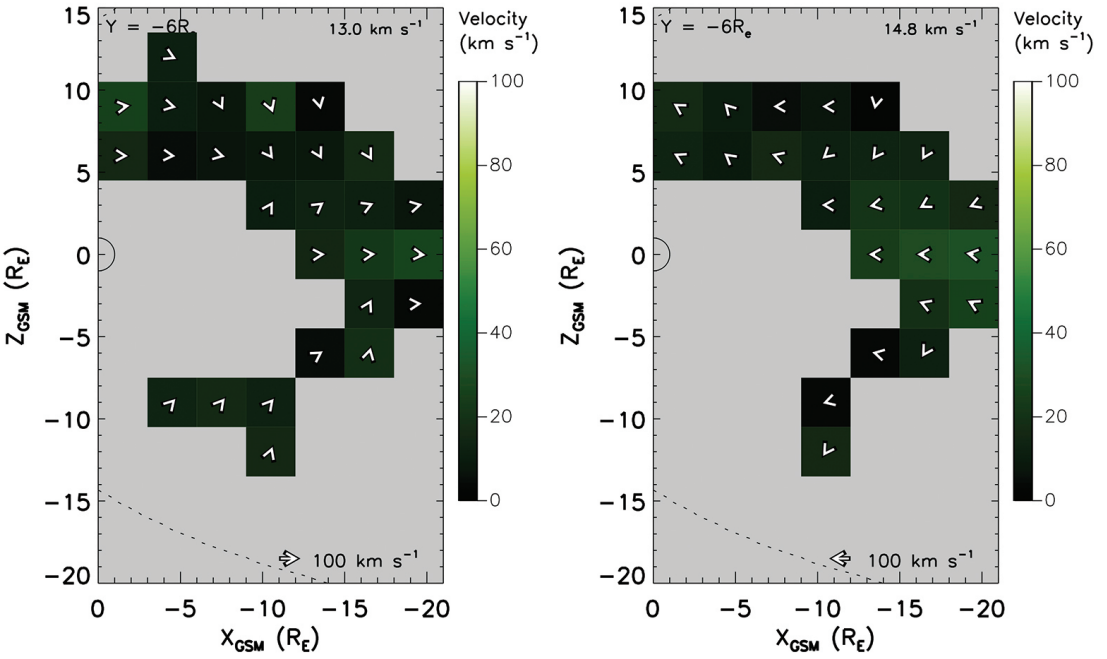

FIGURE 4.44: Ion perpendicular-velocity plots displaying tailward (left) and earthward (right) plasma flow in the XZ plane for Y = -6±1.5 R_E.

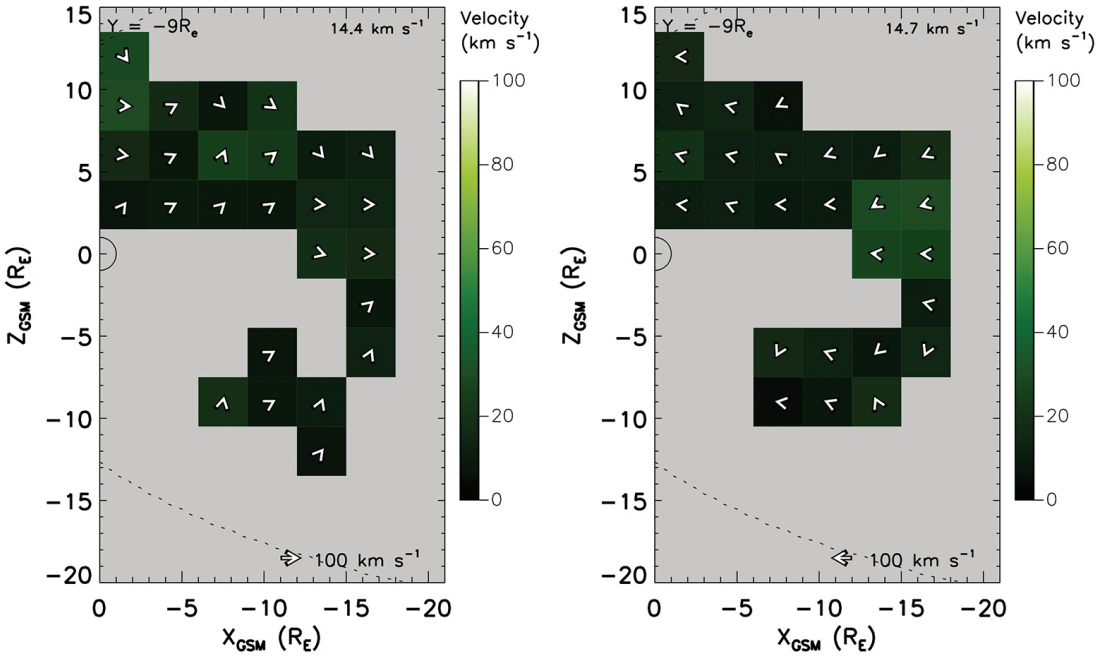

FIGURE 4.45: Ion perpendicular-velocity plots displaying tailward (left) and earthward (right) plasma flow in the XZ plane for Y = -9±1.5 R_E.

= 0 R_E, and strongest at the terminators (bins closest the x = 0 R_E) of the northern/southern hemispheres respectively. This flow pattern is repeated across the dawn hemisphere with a gradual reduction of ion flow deflection with distance from Earth. An example of this can be seen in Figure 4.44 where the ion flow vectors are orientated much more parallel to the x-axis. The tailward flow pattern is not too dissimilar to the earthward flows, although they are more symmetrical about the noon-midnight meridian. It can be seen in Figure 4.43 that while deflections towards the NMM are present, they are not overly strong, and the closer to the central, plane, the more anti-earthward (less deflected) the flow becomes. This tailward flow pattern is repeated out to about y = -7.5 R_E, beyond this distance, anti-sunward flow begins to dominate, although some curved tailward ion flow can be seen in the northern hemisphere of Figure 4.45. Looking further out into the dawn hemisphere, deflections are generally reduced beyond y = -10.5 R_E.

In the dusk hemisphere, earthward flows in the northern hemisphere of plane y = $3 \pm 1.5\,R_E$ are mostly sunward with minimal deflections (seen in Figure 4.46). The southern hemisphere presents stronger deflections towards the southern flank. Across the rest of the dusk hemisphere, the flow pattern is much the same with the deflections in the southern hemisphere generally reducing with distance from the NMM (an example of this can be seen in Figure 4.47 where the earthward flows exhibit minimal deflections). As with the dawn hemisphere, tailward flows in the dusk hemisphere exhibit a

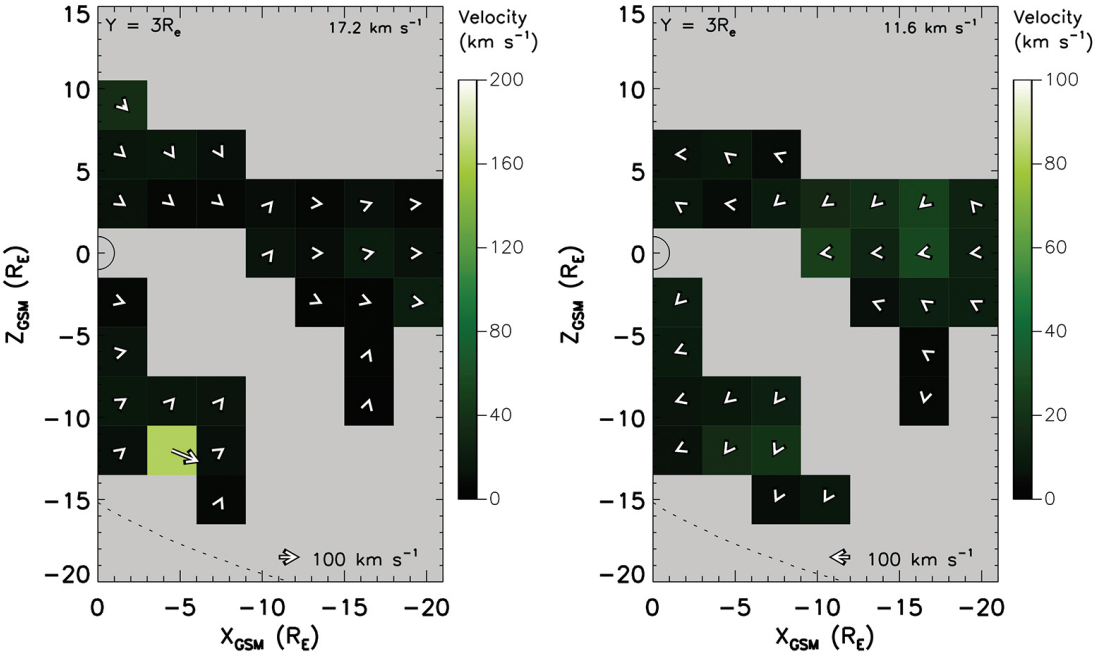

FIGURE 4.46: Ion perpendicular-velocity plots displaying tailward (left) and earthward (right) plasma flow in the XZ plane for Y = 3±1.5 R_E.

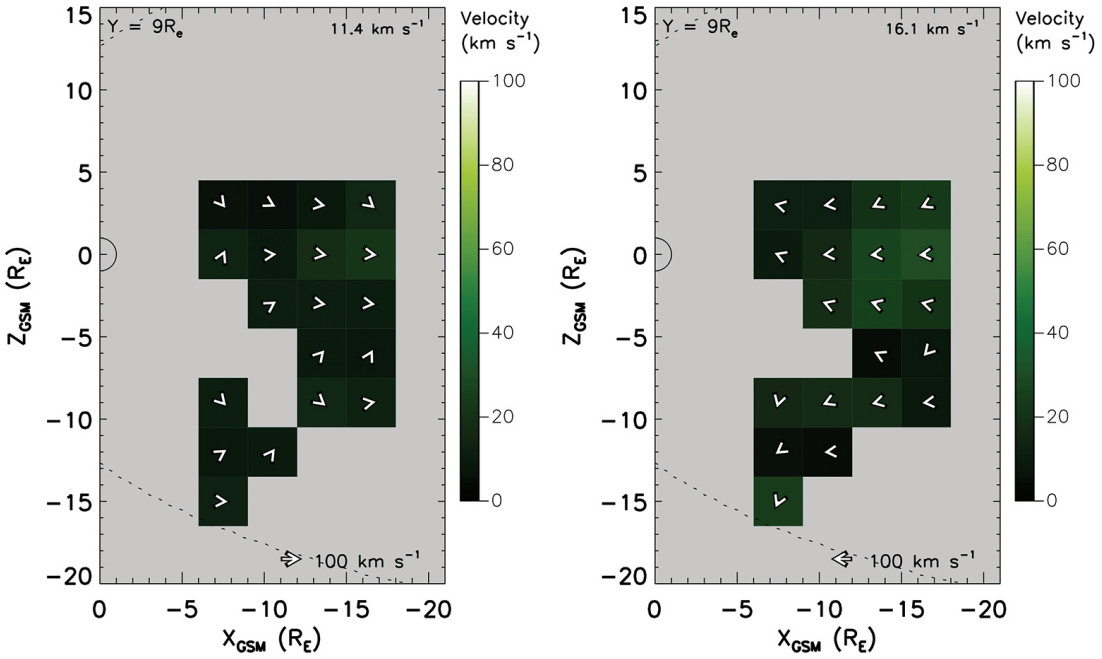

FIGURE 4.47: Ion perpendicular-velocity plots displaying tailward (left) and earthward (right) plasma flow in the XZ plane for Y = 9±1.5 R_E.

more symmetrical ion flow pattern about the NMM and directed towards it. Minimal deflections can be seen at the NMM plane (left plot of Figure 4.46). Further out into the

dusk hemisphere, the ion flow deflections quickly dissipate resulting in a predominantly anti-sunward flow pattern with few deflections still present at the periphery of the data set (see Figure 4.47).

4.5.3 Summary

When taking observations in the XZ plane, it was found that there are much more ion velocity data available in the dawn hemisphere than the dusk hemisphere. The spatial coverage is greater in the dusk hemisphere than the dawn hemisphere between y = 1.5 R_E and y = 7.5 R_E, however, at greater distances from Earth, this reverses so there is more coverage in the dawn hemisphere in this region. This provides evidence of the orbital characteristics and shape of the Cluster spacecraft. There is also an asymmetrical data distribution in the dusk and dawn hemispheres whereby in the dawn side, more bins are occupied in the north, whereas in the dusk side, more bins are occupied in the south. This data distribution is likely caused by the orbital inclination in the YZ plane, creating this seasonal effect. In general, there were found to be more earthward flows than tailward flows across all of the XY-planes. However in the central three planes tailward-directed ion flows occurred more frequently than earthward flows. This is likely due to there being less plasma sheet data contained within each XZ-plane in comparison to the XY-plane plots and potentially proportionally more contaminant magnetosheath and tail-lobe data being contained within each plane. Beyond z = $\pm$ 4.5 R_E earthward flow dominates. This result suggests that the *Zhang et al.* (2015a) underestimated the size of the plasma sheet in the y-direction and as such provides strong evidence that at times the plasma sheet can extend out as far as 19.5 $_E$ in y-direction and extrapolating this, it could be said that during these periods, the magnetosphere could stretch as wide as 39 $_E$. Of course it is a dynamic such the plasma sheet boundaries are not static, expanding and contracting with varying magnetospheric conditions.

When investigating ion flow velocity and direction it was found that tailward flow velocity dominates with an overall ion flow velocity of V_{xz} = -4.1 km s^{-1} across all planes. This is 2.3 km s^{-1} greater than the average velocity in the XY planes, such a small difference indicates that V_x is the dominant velocity component throughout the magnetotail. In general, this result strengthens the idea that on average, over large time-scales, the magnetosphere is rather slow-moving system.

When treating the tailward and earthward flows separately, it was found that the average tailward flow velocity (34.6 km s^{-1}) is a good deal higher than the average earthward flow velocity of 19.9 km s^{-1}. These velocities are higher than the equivalent velocities in the XY planes, and as such, it shows that overall, $V_z > V_y$. In the central three

planes, tailward flow is still a little faster, on average 14.3 $\mathrm{km\,s^{-1}}$ compared to the average earthward flow of 13.1 $\mathrm{km\,s^{-1}}$. These results are in contrast with a previous study by *McPherron et al.* (2011) who found the opposite occurred, however his data selection criteria was rather different and did not include slow-flow ion data as the study in this chapter did. Finally, when looking at the weighted-average ion flow velocity in the magnetotail when disregarding flow direction, the result was found to be $|\mathrm{V}_{xz}| = 26.4\,\mathrm{km\,s^{-1}}$. This result is much slower than the $50\,\mathrm{km\,s^{-1}}$ average found by *Baumjohann et al.* (1989)). These differences are almost certainly due to the data selection criteria used by Baumjohann. His study only incorporated four months worth of data, only focused on the region containing the central plasma sheet and used bulk-ion velocity moments. The study presented in this chapter used 6 years of perpendicular ion velocities moments collects across the entire magnetotail (after lobe and sheath data was removed).

The ion flow patterns throughout the XZ planes do display some north-south asymmetries, although in the noon-midnight meridian plane (centred on y = $0\,\mathrm{R}_E$), the earthward flow pattern is fairly symmetrical about local midnight with reasonably strong deflections away from the equatorial plane in both the northern and southern hemispheres. At the equatorial plane the flows are predominantly sunward. In comparison to the study carried out by *Zhang et al.* (2015a) who found earthward flows to be mostly close to parallel with the x-plane, the research in this chapter showed the earthward flows to be somewhat more disturbed and much less uniform in direction on either side of the NMM plane. Right along the equatorial plane however, the flows were much more uniform and in line with Zhang's findings. When observing the tailward flow, evidence was present for north-south asymmetries, with the deflections towards local midnight somewhat stronger in the northern hemisphere than the southern hemisphere. There is also further evidence for flow reflection in the equatorial plane with the anti-sunward plasma flow being present in the same plane as the sunward earthward flows. When comparing these results with *Zhang et al.* (2015a), tailward ion flow-deflections were found to be stronger and thus the new results show a much more disturbed system.

Looking away from the noon-midnight meridian plane into the dawn and dusk hemispheres, asymmetrical ion flow can be seen throughout. Considering the dawn hemisphere earthward flows in the region surrounding the equatorial plane where y = -3 $\pm$ 1.5 R_E are minimally deflected. At the northern and southern terminators, the deflections are more prominent in the northern and southern directions. The further away from the noon-midnight meridian observations are taken, the more reduced the deflections become. This flow pattern is repeated across the dawn hemisphere.

In the dusk hemisphere, earthward flows in the northern hemisphere of plane y = 3 $\pm$ 1.5 R_E are mostly sunward with minimal deflections and the southern hemisphere presents

stronger deflections towards the southern flank. Across the rest of the dusk hemisphere, the flow pattern is much the same with the deflections in the southern hemisphere generally reducing with distance from the NMM. As with the dawn hemisphere, tailward flows in the dusk hemisphere exhibit a more symmetrical ion flow pattern about the NMM and directed towards it. Further out into the dusk hemisphere, the ion flow deflections quickly dissipate resulting in a predominantly anti-sunward flow pattern.

4.5.3.1 Key Original Results

There were a number of key original results shown in the chapter. Firstly it was found that there were large earthward flow occurrence rates found at greater y-positions along the equatorial plane during the study of the XZ planes. These results provide strong evidence that at times the plasma sheet can extend out as far as 19.5 R_E in y-direction and extrapolating this, it could be said that during these periods, the magnetosphere could stretch as wide as 39 R_E. While it has been generally agreed that the plasma sheet covers the extent of the magnetosphere out to the magnetosheath, few studies have discussed the physical size of this region and all the most similar studies have focused on the use of bulk rather than perpendicular velocity moments.

The next key result is that on average, ion flows were much slower than those from in previous studies such as *Baumjohann et al.* (1989). When considering similar magnetotail volumes, the average ion flow velocity was found to be around 70% slower than Baumjohann. These differences are almost certainly due to the data selection criteria used by Baumjohann. His study only incorporated four months worth of data, only focused on the region containing the central plasma sheet and used bulk-ion velocity moments. The study presented in this chapter used 6 years of perpendicular ion velocities moments collects across the entire magnetotail (after lobe and sheath data was removed). In addition ion flows appeared to be more turbulent than those found in the *Zhang et al.* (2015a) study, who again used bulk ion velocity moments rather than perpendicular ion velocity moments.

Another key result is that when looking at the central region about the NMM, tailward flow is faster than earthward flows. These results contrast a previous study by *McPherron et al.* (2011) who found earthward flows were faster. However he did not include slow-flow ion data as the study in this chapter did. Thus a new result that tailward flows are on average marginally faster than earthward flows in the central region about NMM when considering all ion flow moment vectors was found.

The final key result presented in this chapter was the fact that asymmetrical ion flow patterns were found out away from the the NMM. This is new as there have been

no previous studies that have looked at the north-south planes this far out into the y-direction of the magnetosphere before.

Chapter 5

Magnetospheric Ion Flow During Substorm Phases

5.1 Introduction

During periods of southward IMF, magnetic flux is piled up in the magnetospheric tail region due to the enhanced rate of dayside reconnection. Eventually this stored energy is released in an explosive event and the newly closed magnetic field lines are convected back to the dayside ready to start the cycle again. This process is the magnetospheric substorm. The energetic events are split up into three phases, the growth, expansion and recovery phases (*McPherron*, 1979) and they are the focus of this study. This chapter investigates plasma flows in the terrestrial magnetosphere during these three substorm phases. The substorm phenomena and magnetospheric convection have been discussed previously in sections 2.6 and 4.1 respectively, and so this chapter begins with a literature review of the topic, providing an overview of the research and discussing recent findings. The chapter then goes on to discuss the mapping of magnetospheric convection in the Earth's magnetotail using Cluster spacecraft in the equatorial and noon-midnight meridian planes during the various substorm phases.

The study presented in this chapter focuses on the observation of the general state of plasma flow during the three phases of substorm events, and attempting to look at regions which previous studies either couldn't observe (due to the space mission's trajectory) or chose to examine. Surprisingly, there have been relatively few studies carried out on this research area, since the main focus has often been directed towards the investigation of mechanisms which trigger substorms to initiate, a hotly debated topic ever since the idea of the substorm was introduced (*Akasofu*, 1964). This is a huge field of study, too much to review in detail here, although further details can

be found in various review papers and textbooks (i.e. *Sergeev et al.* (2012); *Kivelson and Russell* (1995); *Baumjohann and Treumann* (1997)). A particular area of research relevant to the study presented in this chapter is the observation of plasma flows and investigating flow patterns and behaviour during substorm onset to establish whether they present any specific signatures during this period. *Nagai et al.* (2000) found that earthward ion flows (sometimes with velocities exceeding 500 $\mathrm{km\,s^{-1}}$) often appear as an initial signal in the near-Earth plasma sheet for substorm onsets in the onset sector (the region in which the substorm begins). It was found that ion flow usually has a duskward component of flow in the dusk hemisphere and dawnward component in the dawn hemisphere and Nagai suggested that this flow pattern indicates that the earthward region expands longitudinally both east and westward from the onset sector. Slow tailward flows, associated with field dipolarisation, were also observed near the equatorial plane. Nagai suggested that these tailward flows are likely to be an onset signature outside of the onset sector and thought to be related to vortical plasma flows. It was also suggested that perhaps these slower flows could explain the lack of high-speed flows in the midtail during substorm activity (*Lopez et al.*, 1994). Another interesting study by *Li et al.* (2014) compared fast flows in the central plasma sheet with auroral breakup signatures to establish whether there was any correlation between the two phenomena. Li observed 560 fast flows in the midnight central plasma sheet and it was found that the onset of short-duration fast flows in the dipolarisation region (x = -9 to -11 R_E) were almost simultaneous with the onset of auroral breakup. It was also found that there was no clear association between long-duration fast flows and auroral breakups. Li highlighted that these results provide support for several earlier studies (*Nishimura et al.*, 2010; *Mende et al.*, 2011; *Sergeev et al.*, 2012) suggesting auroral breakups could actually be caused by fast flow bursts in the central plasma sheet. Another study in support of this idea was by *McPherron et al.* (2011) who found that fast flows observed at about 11 R_E were closely correlated with substorm onsets based on the AL index. Finally, a pair of studies by *Ohtani et al.* (2002a,b) found that perhaps fast flows do not provide a direct contribution to substorm aurora, however they could create favourable conditions for development of substorm expansion onset.

The observation of fast flows within the magnetosphere is a popular area of research as it is well documented that flow bursts carry out the majority of transport throughout the system and as a result, the study of fast plasma flows in the magnetosphere during substorm times has become a topic of frequent interest. *Cao et al.* (2006) found that 95.5% of substorm events were associated with bursty bulk flows when using the data from three Cluster spacecraft and only 78% of substorms were associated with BBFs when using data from just one spacecraft. This interesting result highlights that fast plasma flows are to be expected during substorm events as well as showing that in

all likelihood, there is a good probability that many fast flow events are also missed during data collection. In addition to looking at substorm events as a single entity, plasma flow bursts have also been observed in the substorm growth phase associated with precursor activity (*Angelopoulos et al.*, 1997), in the expansion phase (*Angelopoulos et al.*, 1996) and also in the recovery phase (*Sergeev et al.*, 1996). Although fast flow bursts have been observed in all three substorm phases, the superposed epoch study carried out by *Angelopoulos et al.* (1996) found that these flows tend to occur more often in the substorm expansion phase. A more recent study on the velocity distribution of earthward flow bursts in the inner plasma sheet during the three substorm phases was carried out by *Ma et al.* (2009) using Cluster ion data in 2001 and 2002. It was found that the mean peak velocity was fastest in the expansion phase ($520\,\mathrm{km\,s^{-1}}$), followed by the growth phase ($490\,\mathrm{km\,s^{-1}}$), with the lowest peak velocity occurring in the recovery phase ($390\,\mathrm{km\,s^{-1}}$). *Ma et al.* (2009) goes on to highlight that there have also been a great deal of studies carried out linking fast flows to key processes such as reconnection, the aurora and the substorm current wedge (e.g. *Shiokawa et al.* (1997); *Baumjohann* (2002); *Kepko et al.* (2001); *Grocott et al.* (2004); *Cao et al.* (2008)).

A study by *Kissinger et al.* (2012) was carried out to examine the average plasma conditions and fast earthward flows during steady magnetospheric convection (SMC) events and compared them to other types of geomagnetic activity including the three phases of isolated substorms. The study used 14 years of data from the Geotail and THEMIS missions, focussing on earthward plasma flows with velocities greater than $200\,\mathrm{km\,s^{-1}}$. The substorm onset time was selected visually from auroral AL indices and the substorm phase intervals were selected according to a set of temporal parameters, both of which will be described in more detail in section 5.2.1. Kissinger found that the recovery phase had a 1.8% occurrence rate of earthward fast flows, meaning that of all of the earthward flows measured across the recovery phases of 8600 substorm events included in the study, 1.8% of them had velocity of over $200\,\mathrm{km\,s^{-1}}$. The occurrence rates for the expansion and growth phases were lower than that of the recovery phase, 1.5% and 1.1% respectively. Within $15\,\mathrm{R}_E$, their occurrence rate drops quite sharply, with fewer fast flows being observed in this region. The expansion phase has the largest occurrence rate of 0.5% with the growth and recovery phase only showing 0.22% and 0.2% earthward fast flows in this region. This gradient in fast flow distribution is highlighted through the calculation of the probability of observing earthward fast flows with radial distance from Earth. In general, it is clear that the probability increases with radial distance, although this is more variable for the expansion phase. The recovery phase has the largest probability of earthward fast flow observation with the growth phase having the lowest. Kissinger continued to investigate the deflection angle of earthward fast flows across the expansion and recovery substorm phases. It was found that at radial

distances between 15 and 20 R_E, the expansion phase exhibited a smaller degree of flow deflection than the recovery phase, and at radial distances less than 15 R_E, the recovery phase displays a lower degree of deflection, although the difference between the two phases was less than at greater distances. The growth phase was not discussed. When observing the flow patterns of earthward fast flows, Kissinger found that during the expansion phase, earthward fast flows were predominantly directed earthward, especially in the midnight region ($|Y| < 7\,R_E$). Some deflection away from midnight towards the flanks was observed, but no distinct pattern could be made out and therefore no clear asymmetry was seen. The plasma flow patterns for the recovery and growth phases were not discussed. Kissinger concluded that in general, fast earthward flows during substorm times were directed toward the inner magnetosphere and remained there in a 'pile-up region', as *Baumjohann et al.* (1999) discussed.

The final study to be discussed in this section is by *Juusola et al.* (2011). It used a combination of the Geotail, THEMIS and Cluster data, spanning 15 years, to examine the statistical distribution of earthward plasma sheet flows during substorm phases. The phases were determined from a time series of the AL index as well as the z-component of the interplanetary field. Overall Juusola found that 56% of earthward flows occurred during non-substorm times while 12% occurred in the growth phase, 11% in the expansion phase and 21% in the recovery phase. This result somewhat agreed with *Kissinger et al.* (2012), as while this study accounts for all velocity flows and not just fast flows, both studies show that the most earthward flows were found in the recovery phase. They don't quite agree with the other two phases, however it is likely that the difference is down to the different velocity selection criteria. Juusola went on to find, as the majority of previous studies have also found, that the plasma sheet is dominated by slow plasma flows. It was found that 97% of earthward flows were during non-substorm intervals $V < 100\,km\,s^{-1}$. This low velocity dominance was also found in the growth phase (96%), the expansion phase (89%) and the recovery phase (90%). Generally, the frequency of flows with $V \geq 100\,km\,s^{-1}$ was lowest during non-substorm intervals and the higher the velocity, the less frequently such flows were observed outside of substorm intervals. During the growth phase, Juusola found that the velocities were only marginally higher than those of the non-substorm time, with a tendency to increase towards the end of the interval. At onset, the beginning of the expansion phase, the frequency of higher-velocity flows sharply increased and remained elevated throughout both the expansion and recovery phases. The frequency of faster flows peaked at the end of the expansion phase and the beginning and the recovery phase. Towards the end of the latter, the frequency decreased. Juusola concluded that any effect flow may have on substorm onset triggering would be caused by medium velocity flows rather than very

fast flows. In addition, Juusola found that during the recovery phase, enhanced velocities were generally distributed symmetrically about an aberrated midnight axis. For the expansion phase, the average velocity was more enhanced on the duskside than the dawnside, and finally the average velocity in the growth phase was found to be slightly increased.

5.2 Data Visualisation and Selection

The methodology for this chapter's study, as well as the organisation and visualisation of the data, is predominantly the same as for the first study described in Chapter 4. As well as the figures described in Chapter 4, a set of alternatively binned plots were created and an additional substorm-time parameter was included to remove all data not collected during a substorm interval. The methods used to select the appropriate intervals and to create the new plots are described below.

5.2.1 Determining Substorm Phases

Substorm onset times were obtained from the SuperMAG substorm database (*Gjerloev*, 2012). The database is a comprehensive list of substorm onset times which have been derived using an automated algorithm used to identify substorm expansion phase onsets from the SML index, the SuperMAG equivalent of the AL index. There are a number of methods which can be used to select substorm onset times. *Kissinger et al.* (2012) selects onsets visually from auroral indices characterised by a sharp drop in the AL index (*Hsu and McPherron*, 2012). More recently, *Forsyth et al.* (2015) provides a quantitative method to determine the times and durations of substorm expansion and recovery phases, as well as possibly determining substorm growth phases too, based on percentiles of the rate of change of auroral electrojet indices.

Substorm event selection was carried out using several temporal parameters from the *Kissinger et al.* (2012) study. Only isolated substorms were selected, and so in order to ensure no overlapping events were selected, it was required that onset times could not be within ± 2.5 hours of another onset time. In the tail seasons between 2001 and 2006, there were found to be 656 isolated substorm events available for analysis. The three substorm phases could then be identified: growth, expansion and recovery. Their phase duration times were again taken from *Kissinger et al.* (2012). The growth phase interval was set to begin 30 minutes before onset and end of the interval as the onset time. The expansion phase intervals were set to begin at onset and end 30 minutes later.

The recovery phase interval was set to begin 45 minutes after onset and end 120 minutes after the onset time.

5.2.2 Data Selection

As previously mentioned, 656 isolated substorm events were selected for analysis during the six year data window the study planned to use. The relatively low number of events (in comparison to the 8600 substorm events *Kissinger et al.* (2012) used) combined with the short duration of each substorm phase meant that the amount data available was severely limited. For example, there was a total of 19680 minutes of substorm expansion phase covered by the study, just 0.62% of the total time available, and data could only be collected if they occurred during the four months of the tail season each year, further limiting its availability. From this, it was decided to expand the time frame being used from six years to fourteen years, spanning the entire data availability for the CIS instruments on the Cluster mission. Data for the Cluster 3 spacecraft was collected until the 11 November 2009 under normal operations and was switched off following this date. For the Cluster 1 spacecraft, data was collected under normal operations until April 2011 when it was restricted to only magnetospheric modes. From November 2012, the instrument was reduced to one hour segments of operation, with HIA moment and quality flag data being available until the end of 2014. The inclusion of these additional years of data in the study allowed 1430 substorm events to be analysed, almost three times the original count. Finally it must be noted that the study presented in this chapter is a statistical study and as such, the dataset does contain Bursty Bulk Flow events and other such perturbations.

Interestingly, when the new figures were created using the 14 years of data, the amount of data available for analysis in each plane did not increase proportionally, increasing at most by about 1000 counts, but most planes only saw a very small increase. An investigation was carried out to establish why this was the case, and it turned out that when reducing the data quality flag threshold by one (allowing any data through with a value of two or more) increased the amount of data available substantially, see Table 5.1. It was tempting to utilise the lower quality flag value in order to maximise the amount of data available, however, after reading more about the data flags in the Cluster Science Archive (*Dandouras and the CIS Team*, 2017), where data with a quality flag value of less than three was described to be of inadequate quality, it was decided to maintain the use of data with quality flag values of three or more. However, it was also decided to include the additional years of data into the study.

TABLE 5.1: The number of days with available data for each substorm phase, collected by Cluster 1 and 3 when varying the quality flag (QF) value.

Substorm Phase	C1. QF > 2	C1. QF > 1	C3. QF > 2	C3. QF > 1
Growth	81	1147	173	898
Expansion	87	1157	175	889
Recovery	97	1129	178	868
Total [days]	265	3433	526	2655

As with Chapter 4 the magnetosheath removal procedure was also applied to the analysis here in order to remove as much of the contamination from the Earth's magnetosheath as possible. This study utilises the same cutoff values for the ion density, temperature and distance from the Earth and as such all that is discussed in Section 4.3.2 is also relevant in this chapter.

5.2.3 Alternative Substorm Plots

The limited amount of data available for this study led to a substantial reduction in the spatial coverage available (when compared with the coverage available in Chapter 4), especially for the growth and expansion phases, which have a shorter duration than the recovery phase. This was likely due to a combination of each substorm phase only occurring for a short period of time as well as it being an artefact of the spacecraft orbital trajectory. In order to improve the data coverage show in each of the figures, the original $3^3\,R_E$ bins were averaged together in groups of three (z-direction for the XY plane and the y-direction for the XZ plane), creating a new set of bins with the dimensions $3\times\ 3\ \times\ 9\ R_E$. An alternative way to describe this method binning is a collapse of the plots in the z-direction to fill out gaps in the x-y distribution. Three sets of figures were created $|Z| \leq 13.5\,R_E$ and $|Y| \leq 13.5\,R_E$ for the XY and XZ planes respectively, with each figure spanning $9\,R_E$ in the relevant direction.

The new spatial parameters used for the alternative substorm plots allow for improved visual clarity, placing more bins within the figures, in essence compressing the region visually.

As the spatial coverage is so limited, many of the bin positions are only occupied in one of the three original planes, and as such the flow velocity and direction is not diluted, and so applying the larger spatial parameters acts to compress the region spatially, allowing for improved visual clarity. Of course there are some bin positions which are doubled up and in these cases, the multiple bins are averaged together. When this occurs, it can become difficult to infer average flow directions accurately since each bin covers such a large area ($9\,R_E$ out of the plane of view) and as such, the results in these cases should

Phase	Plane (Z = nR$_e$)	N$_{earthward}$	N$_{tailward}$	N$_{total}$	% EF	% TF
Growth	9	1731	3223	4954	34.9	65.1
	0	10681	5690	16371	65.2	34.8
	-9	1862	2048	3910	47.6	52.4
Total		14274	10961	25235	56.6	43.4
Expansion	9	1636	3799	5435	30.1	69.9
	0	12693	7564	20257	62.7	37.3
	-9	2343	2537	4880	48.0	52.0
Total		16672	13900	30572	54.5	45.5
Recovery	9	2307	5217	7524	30.7	69.3
	0	26441	11349	37790	70.0	30.0
	-9	4080	4496	8576	47.6	52.4
Total		32828	21062	53890	60.9	39.1

TABLE 5.2: Sample counts distribution for the XY plane across 3 cuts in the z-direction for each substorm phase. The Z value given is the position on which the plane is centred. EF represents earthward flow and TF represents tailward flow.

be treated with care, looking at the three constituent planes averaged together to create the alternative substorm plots.

5.3 Ion Flow During Substorm Events in the XY Planes

5.3.1 Sample counts

This section will discuss the distribution of data analysed during the three substorm phases in the XY plane. First consider the spatial distribution of the data. With the longest phase duration, it is no surprise that the recovery phase possesses the most data, doubling the amount of data available for either of the growth or expansion phases (Table 5.2). Overall there are more earthward ion flow occurrences than tailward flows, however looking at the outer Z-planes of each substorm phase it can be seen in Table 5.2 that there are more tailward and earthward ion flow occurrences. As discussed in Chapter 4, this flow behaviour has much to do with contamination from the magnetosheath and lobe data which was not removed by the sheath-removal and Coxon lobe removal procedures respectively. There is perhaps some dawn-dusk asymmetrical data distribution present across all three substorm phases. There is generally more spatial coverage in the dawn hemisphere of all three planes than in the dusk sector. As previously explained, this coverage asymmetry is likely caused by Cluster's orbital inclination in the YZ plane. However it must be noted that this is a tenuous result; due to the spatial coverage being so sparse, it is difficult to verify this with any great deal of accuracy.

Considering all three planes for each substorm phase in the XY direction, it is clear that overall there are more earthward directed plasma flow data than for tailward flow (Table

5.2). The expansion phase presents the smallest difference with earthward flow possessing 2772 more counts than earthward flow. The growth and recovery phases present a larger difference with tailward flows having about 3313 and 11766 more occurrences that tailward flows respectively. While the outer-most planes during each substorm phase present clear tailward flow dominance (Table 5.2), the plane centred on the equator is dominated by earthward flow. Here the most earthward flow data was collected during the recovery phase, followed by the expansion phase having 2.5% more earthward flow occurrences than the growth phase. When looking at previous studies, *Juusola et al.* (2011) found fast earthward flows occurred more often in the recovery phase, than both the growth and expansion phases, although there was only 1% more earthward flows in the growth phase than the expansion phase. Another similar study carried out by *Kissinger et al.* (2012) also found there to be more earthward fast flow occurrences in the recovery phase but found more fast flow occurrences in the expansion phase than the growth phase, a result which the study presented in this chapter agrees with. It must be noted that while this chapter's study agrees with Kissinger's, it does not agree with the earthward flow occurrences found in Juusola's study. Both the Kissinger and Juusola studies focussed on fast earthward flows rather than all velocity flows as with this chapter. The difference in results between the three studies could well be to do with how the data has been sampled and presented. Juusola's study used smaller spatial bins and an aberrated coordinate system, where both this chapter's study and Kissinger's did not.

When thinking about the relative proportions of earthward/tailward flows between the three substorm phases, it was initially thought that the expansion phase would have the greatest proportion of earthward flows because this is the most energetic phase which tailward reconnection being triggered and thus a great deal of charged particles are launched back towards the Earth. Similarly it was thought that tailward flows would be most prevalent in the growth phase because a heightened rate of dayside-reconnection causes the newly-opened magnetic field-lines to be dragged tailward via the solar wind's momentum. Finally it was thought that the recovery phase would be the most balanced because it is seen as the most relaxed of the three phases. However, after some additional background research, including reading *Lui* (2000), it is clear that the physical mechanisms are not quite as simple as they may first appear and as such the results found in this chapter paint a different picture.

Comparing the flow directions across the equatorial plane of the three substorm phases, various properties of each phase can be inferred from table 5.2. The recovery phase (Figure 5.1) has the lowest proportion of tailward flow and therefore the highest proportion of earthward flow. The expansion phase (Figure 5.2) is at the other end of the scale, with the largest proportion of tailward flow and thus the lowest proportion of

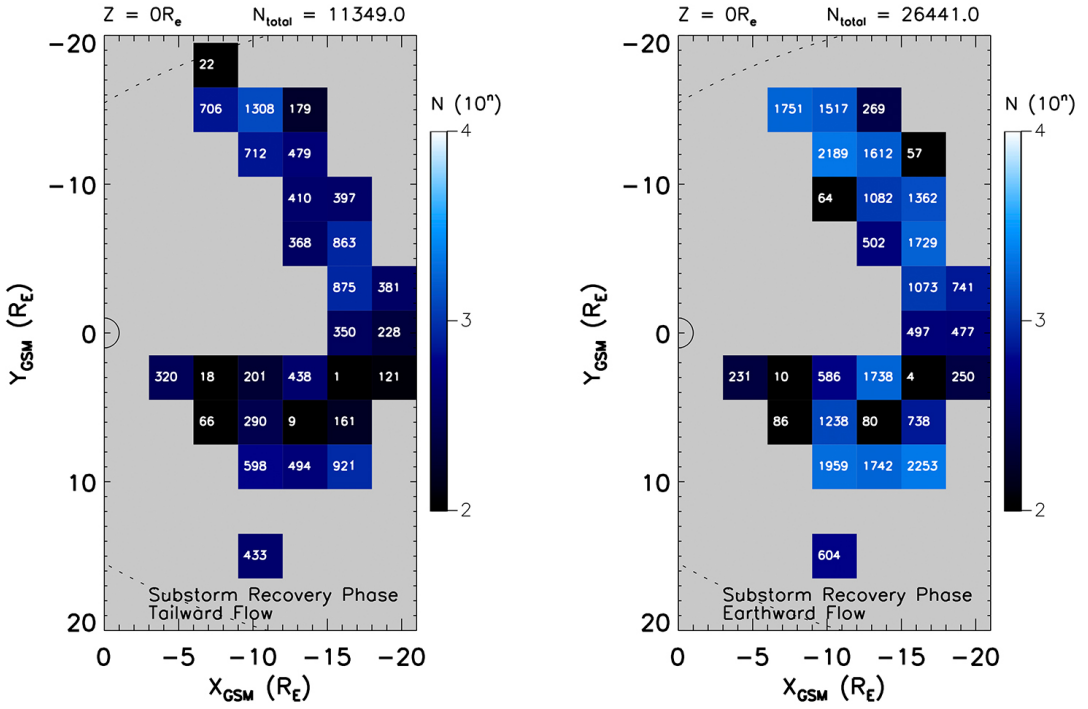

FIGURE 5.1: Sample count plot for the XY plane Z = 0 ± 4.5 R_E displaying tailward (left) and earthward (right) plasma flow during the substorm recovery phase.

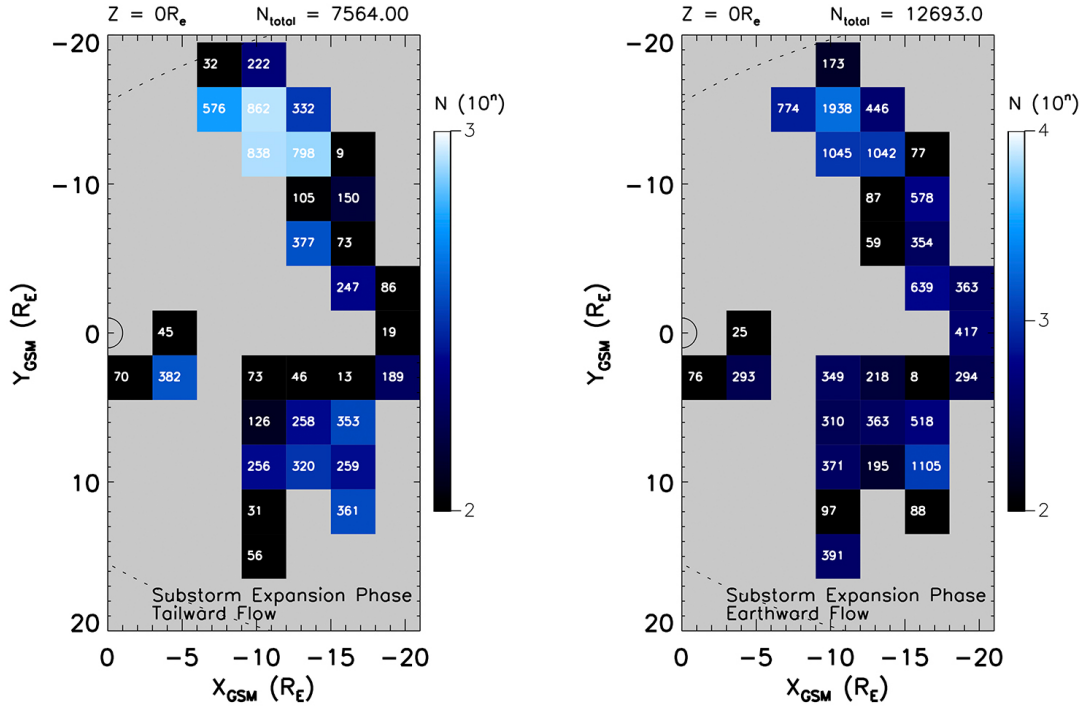

FIGURE 5.2: Sample count plot for the XY plane Z = 0 ± 4.5 R_E displaying tailward (left) and earthward (right) plasma flow during the substorm expansion phase.

earthward flow. While the growth phase (Figure 5.3) shows greater difference in the amount of earthward and tailward flow, it sits between the two other phases with both

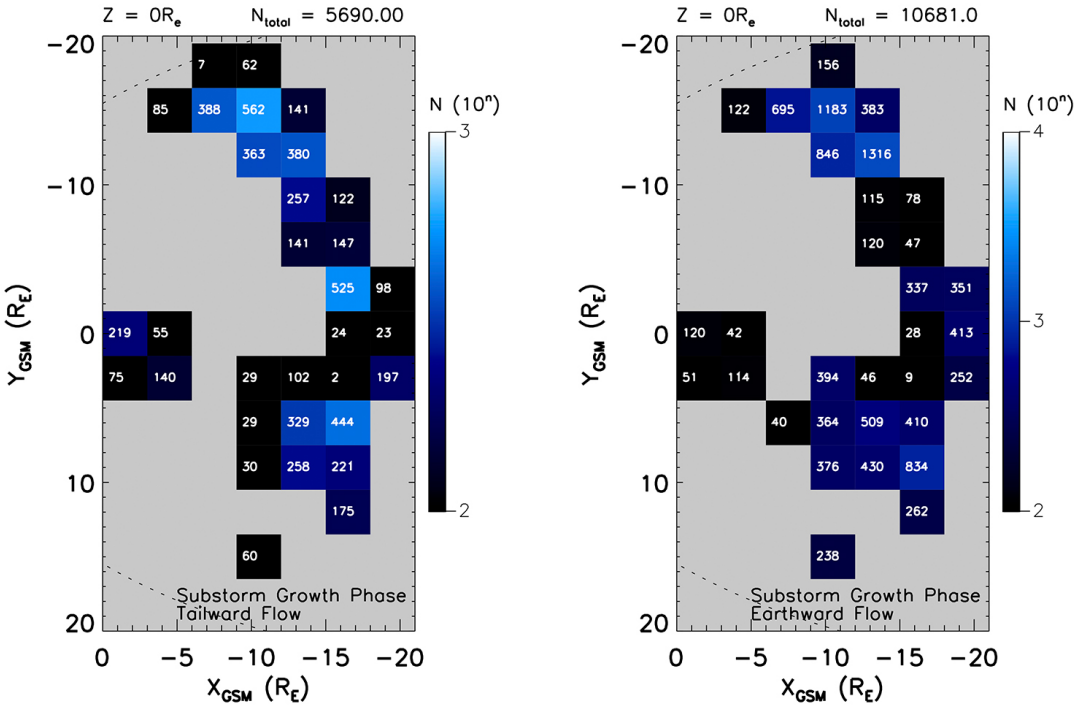

FIGURE 5.3: Sample count plot for the XY plane Z = 0 ± 4.5 R_E displaying tailward (left) and earthward (right) plasma flow during the substorm growth phase.

the amount of tailward and earthward flow. The growth phase shows a larger proportion of earthward flow than tailward flow occurrence. The growth phase is the time period whereby a heightened rate of dayside reconnection causes a pileup of magnetic flux in the near-earth magnetotail, during which time the cross-section of the magnetotail enlarges (*Lui*, 2000). This means that tailward flows are likely occurring at greater distances that those what are being considered in Figure 5.3, and as such leads to earthward flows dominating. Tailward flow is seen proportionally less frequently because the growth phase mechanism increases energy storage in the magnetotail and as such, it is without the increased amount of nightside reconnection needed to counteract the flux pileup and release the energy, hence tailward plasma flow appears to be proportionally reduced. The expansion phase is the most balanced with 54.5% of the contributing flows directed earthward and 45.5% tailward as it it is the closest to 50/50 flow direction distribution. Note this phase also has the largest proportion of tailward flows and as such, the lowest proportion of earthward flows compared with the other phases. As the substorm onset is triggered, the growth phase ends and the expansion begins. Following the NENL model (section 2.6.2.4), rapid nightside reconnection is initiated closer to the Earth than where it usually occurs during quiet times. The tailward flow rate is increased and more proportionately balanced with earthward directed flow in comparison to the other phases due to the increased level of nightside reconnection. The increased rate of reconnection causes more plasma to be launched tailward away from the Earth as it is reconnected

into the solar wind. Finally, the recovery phase has the largest proportion of earthward flow in comparison with the other two substorm phases. The likely reason for this result is that in this phase, the mid-tail region plasma sheet suddenly thickens with fast plasma flows at the plasma sheet boundary (*Lui*, 2000), a region which is almost certainly included in the wider bins utilised in this study.

One must consider the statistical significance of the balance between ion flow direction occurrence rates. In general, the number of earthward and tailward flows in each bin is governed by the spacecraft trajectory, the time coverage of the observations, the number of total samples in the bin and so on. If the same experiment was carried out again, with the new spacecraft following exactly the same trajectory, it is unlikely that precisely the same results would found due to the natural variability of the magnetosphere. The usual approach to overcome this is to take enough data in the hope to smooth it out and get a reasonable average. The reliability of the data analysis procedures utilised throughout this thesis has been discussed in depth in Chapter 4, and it was shown that overall the results were reliable. Looking specifically at this chapter, data was taken from 656 isolated substorm events, which is not an enormous time-frame. Clearly the results uncovered are very much dependent on the point at which substorm onset occurs and the position of the spacecraft at that given moment. Thus any inference of general flow patterns and spatial distribution must taken as a loose guide rather than the gospel truth.

5.3.2 Ion Velocity: Magnitude and Direction

Phase	Plane (Z=n±1.5 R_e)	V_{xy} Earthward [km s^{-1}]	V_{xy} Tailward [km s^{-1}]	Weighted Mean Av. V_{xy} [km s^{-1}]
Growth	-9	6.3	7.0	-2.4
	0	14.6	12.0	5.3
	9	5.2	5.1	-0.2
Average		8.7	8.0	1.5
Expansion	-9	7.4	7.3	-2.9
	0	16.0	16.5	3.9
	9	5.0	6.1	-0.8
Average		9.5	10.0	0.6
Recovery	-9	6.5	10.0	-4.9
	0	16.8	15.8	7.0
	9	5.2	5.4	-0.4
Average		9.5	10.4	1.7

TABLE 5.3: V_{xy} distribution for the XY plane across 3 cuts in the z-direction for each substorm phase. The Z value given is the position on which the plane is centred.

When considering both earthward and tailward perpendicular ion flows together in the XY plane, it is interesting to note that on average, across all planes observed and all substorm phases, earthward ion velocity (V_{xy}) just dominates, Table 5.3. This result was not surprising following the results from Chapter 4, which also showed that earthward velocity was dominant across all planes. It can be seen in Table 5.3 that the mean V_{xy} across all planes in both flow directions is 1.5 km s^{-1} during the growth phase, 0.6 km s^{-1} during the expansion phase and 1.7 km s^{-1} during the recovery phase. Comparing these results to the sample counts in each substorm phase seen in Table 5.2, this result is unsurprising since there is generally a good deal more earthward ion flow occurrences than tailward flows. In the equatorial plane for each substorm phase (Figures 5.4 (growth phase), 5.5 (expansion phase), 5.6 (recovery phase)), the earthward and tailward velocities are generally higher than the outer planes (which can be seen in Table 5.3), with earthward flow velocity dominating when the weighted average is calculated. The earthward velocity dominance at the equatorial plane is minimal, where the weighted mean $V_{xy} = 5.3$ km s^{-1} during the growth phase, $V_{xy} = 3.9$ km s^{-1} during the expansion phase and $V_{xy} = 7.0$ km s^{-1} during the recovery phase. These results likely follow the same reasoning as for Chapter 4, the equatorial plane is 9 R_E wide in the z-direction, 1 R_E wider than the idealised central plasma sheet dimensions proposed by *Zhang et al.* (2015a) and therefore likely still contains some tailward-dominant lobe data.

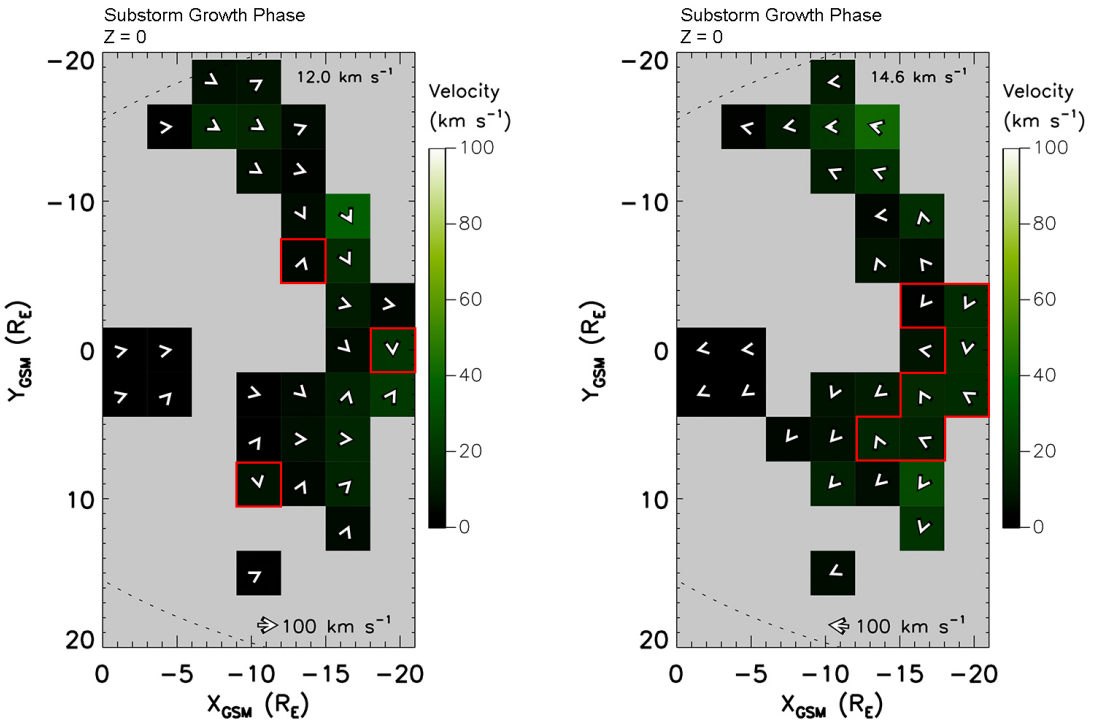

FIGURE 5.4: Ion velocity plots displaying tailward (left) and earthward (right) plasma flow during the substorm growth phase in the XY plane where Z = 0±4.5 R_E. The red boxes show vectors directed against the general flow direction of the plane.

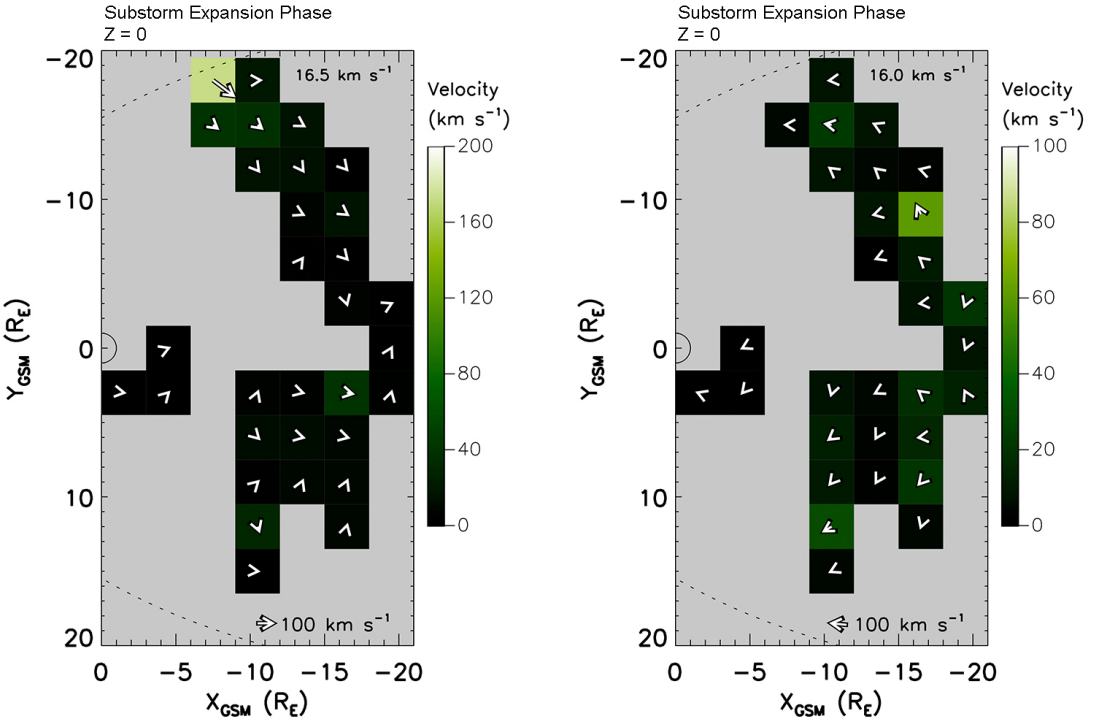

FIGURE 5.5: Ion velocity plots displaying tailward (left) and earthward (right) plasma flow during the substorm expansion phase in the XY plane where Z = 0±4.5 R_E.

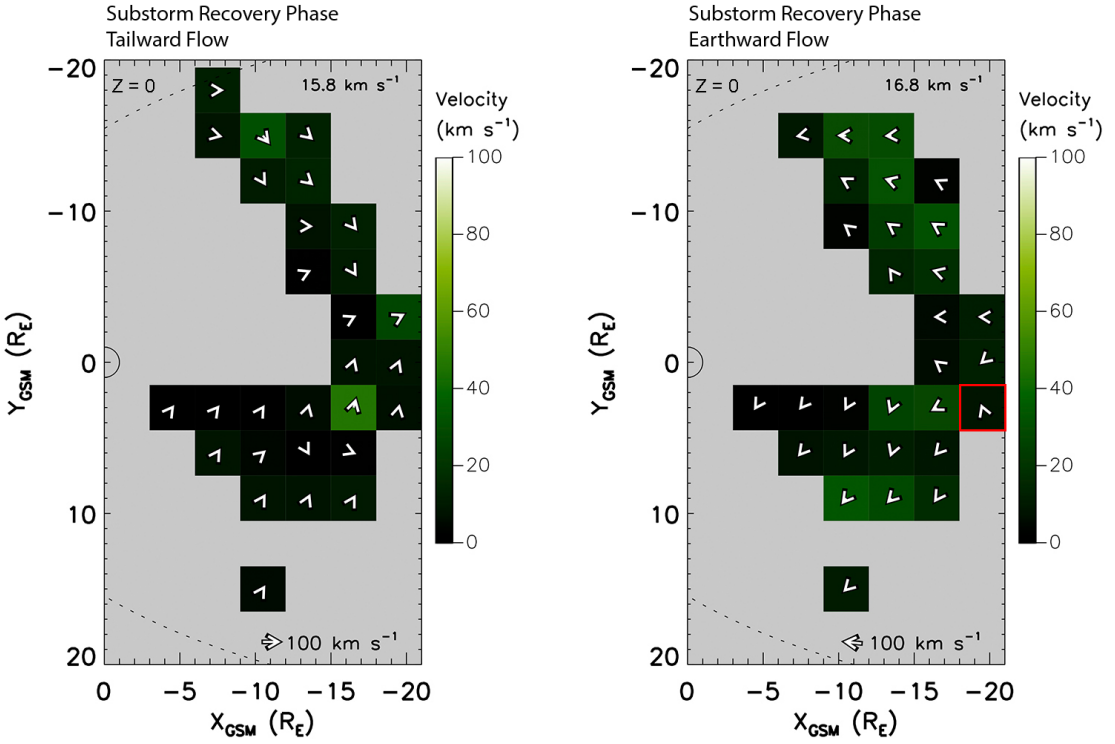

FIGURE 5.6: Ion velocity plots displaying tailward (left) and earthward (right) plasma flow during the substorm recovery phase in the XY plane where Z = 0±4.5 R_E. The red box show vectors directed against the general flow direction of the plane.

5.3.2.1 Earthward Ion Flows

This section discusses the behaviour of earthward directed ion flows for all three substorm phases.

Considering earthward flows for each substorm phase, across all XY planes, it can be seen that the growth phase has the slowest average earthward flows (8.7 km s^{-1}). The expansion and recovery phases have slightly faster average earthward flows, both having an average flow velocity of 9.5 km s^{-1}). When focussing on the equatorial plane (right plots of Figures 5.4, 5.5, 5.6), the growth phase has the slowest average earthward velocity of 14.6 km s^{-1}, with the expansion phase having a faster average earthward ion flow velocity of 16.0 km s^{-1}. The recovery phase has the fastest average earthward ion flow velocity with 16.8 km s^{-1}. These results agree with the study carried out by *Kissinger et al.* (2012), who found that the recovery phase had the largest occurrence rate of earthward fast flows, suggesting that the average velocity should be higher than the other two phases as a result. Kissinger also found that the growth phase had the lowest fast flow occurrence rate, the same result as in this chapter. Kissinger's study best compares to the research presented in this chapter as the spatial coverage bin sizes are more closely matched than with other similar studies. In the research carried out by *Juusola et al.* (2011), it was found that the expansion phase possessed the fewest

cases of slow plasma flow and thus suggesting that it had the largest average plasma flow velocity. The recovery phase was found to have just 1% more slow flow cases than the expansion phase. The growth phase again had the most cases of slow flow plasma flows and as such, it can be assumed that it had the lowest average ion flow velocity. In addition, such low average velocities suggest that throughout each substorm phase the majority of plasma flows are very slow with potentially infrequent faster flow bursts occurring sporadically. This notion is further supported by *Kissinger et al.* (2012), who found that the occurrence rate of fast earthward flows in the inner magnetosphere never exceeded 1.8% in any substorm phase. It is also supported by *Juusola et al.* (2011) who found that fast earthward flows occurred for no more than 11% of any substorm phase. All three studies support the idea that the average flow behaviour is generally slow throughout substorm events. Finally, the small disagreement of results between the study presented in this chapter, and Kissinger's and Juusola's findings about which phase possesses the fastest earthward flows, could again be due to the way the data has been managed, using slightly different bin and region sizes and as such, incorporating somewhat different data sets.

The average vector flow direction is the final observation to discuss. As previously mentioned, the direction of plasma flow must be taken with a healthy degree of scepticism because each spatial bin covers such a large area of the magnetotail that it is near impossible to determine where the data from each bin was collected in the z-direction to a good level of certainty. However, a series of plots at the original 3 R_E^3 spatial resolution can be seen in Appendix C, allowing comparisons to be made, providing somewhat more detail as to where the contributing vectors to each larger bin originated. Any of the larger bin plots which are not referenced explicitly in this section can also be seen in Appendix C.

Consider earthward ion flows in the equatorial plane for each substorm phase it is clear that deflections are present throughout with the growth phase flow pattern presenting some dawn-dusk asymmetry as well as appearing to be the most disordered substorm phase (the red boxes in Figure 5.4 show vectors directed against the general flow direction of the plane). It was suggested that perhaps the reason for this was due to noise in the data. However a study carried out in Chapter 4 section 4.3.4.4 applied a random perturbation to flow direction of each vector in the entire dataset used and found the change to have very little effect to the overarching results. This meant that the analysis technique used is robust and not unduly affected by some randomly angled vectors. From this, it can be implied that since the analysis procedure in the chapter is the same as Chapter 4, it is equally as robust and as such, the somewhat disordered nature of the growth phase is probably not as a result of background noise in the data. The dawn flank of the growth phase showed a good deal of sunward flow (right plot of Figure 5.4),

with some deflections toward the local midnight within a couple of R_E from the noon-midnight meridian. The dusk flank showed much more deflection, with the majority of bins presenting duskward flow with just a couple of bins possessing flow towards the local midnight. Close to the Earth, within a radial distance of about 5 R_E, flows are predominantly directed earthward.

The flow pattern of the expansion phase is a little more ordered than in the growth phase (Figure 5.5) and shows some dawn-dusk asymmetry. At larger distances from the equator in the dawn hemisphere, the flow direction is predominantly sunward, with a few vectors gently deflected towards the dawn flank. On the dawn-side close to the equator, ion flows are either earthward or strongly deflected towards the equator. On the dusk side, the deflections appear to roughly average out to show earthward flow, although there are a couple of stronger duskward deflection in the mid-to-near-earth tail and one strong deflection towards midnight at the furthest point from Earth. Further out into the dusk hemisphere ion flows are consistently directed duskward. Finally within a radial distance of about 5 R_E, the flow is fairly sunward with slight duskward deflection. During the expansion phase, *Kissinger et al.* (2012) found at local midnight that the ion flow was mostly earthward and further out away from midnight, there was some deflection towards the flanks, however no clear pattern could be discerned. This somewhat agrees with the research in this chapter, however, the flow pattern appears to be somewhat more ordered here, which is likely due to the use of V_{perp} rather than V_{bulk}.

The plasma flow pattern of the recovery phase appears to be the most ordered of the three substorm phases in the study with just one bin seemingly bucking the trend (red box in Figure 5.6). The dawn flank present sunward flow at the periphery of the dataset with a dawnward directed deflections closer to local midnight. While there are still only two bins occupied at local midnight, the flow pattern is somewhat earthward on average with slight deflections both towards the dusk and dawn flanks. In the dusk hemisphere, the flow pattern is consistently deflected towards the dusk flank.

Overall when looking at earthward flows during the three substorm phases, it is quite clear from comparing Figures 5.4, 5.5, 5.6 that the recovery phase has the most ordered flow pattern while the growth phase has the least ordered pattern. The level of deflection is difficult to assess through visual comparison alone. During the *Kissinger et al.* (2012) study, she found that deflections were generally smaller within 15 R_E than in the region between 15 and 20 R_E. However the results presented in this chapter's study do not entirely agree with this. In the dawn hemisphere for the growth and expansion phases, yes this is the case, however in the dusk hemisphere, deflections appear to be reasonably consistent at all distances from Earth. Looking at the recovery phase, Figure 5.6, it

appears the ion flow deflections are much more uniform, except for perhaps the most distant bins from Earth which exhibit stronger deflections.

5.3.2.2 Tailward Ion Flows

This short section discusses the behaviour of tailward directed ion flows for all three substorm phases.

Considering tailward flows for each substorm phase across all three XY spatial planes, it can be seen that the growth phase has the slowest average tailward flows (8.0 $\mathrm{km\,s^{-1}}$), the expansion phase has slightly faster average tailward flows (10.0 $\mathrm{km\,s^{-1}}$), and the recovery phase has the fastest tailward flows (10.4 $\mathrm{km\,s^{-1}}$). When focussing on the equatorial plane (left plots of Figures 5.4, 5.5, 5.6), the growth phase still has the slowest average tailward ion flow velocity of 12.0 $\mathrm{km\,s^{-1}}$, but now the expansion phase has the fastest average tailward ion flow of 16.5 $\mathrm{km\,s^{-1}}$. The recovery phase has a slightly slower average tailward flow velocity 15.8 $\mathrm{km\,s^{-1}}$.

In the growth phase, tailward flows at the dawn flank are gently deflected towards local midnight (left plot of Figure 5.4). Closer-in to the NMM, deflections mostly become more strongly directed towards local midnight. At midnight, ion flow is anti-sunward within 5 R_E of the Earth, however beyond 15 R_E, deflections become much stronger towards the dusk flank. In the dusk hemisphere, within 15 R_E from Earth, the flow is predominantly anti-sunward with three bins showing deviation from this. Beyond 15 R_E from Earth flows quickly turn towards local midnight and are mostly deflected strongly in this direction. As with the earthward flow patterns, it appears that tailward flow in the expansion phase appear to be generally more ordered than in the growth phase (left plot of Figure 5.5). In the dawn hemisphere, tailward flows are consistently deflected towards local midnight with the exception of just two bins. At local midnight, ion flow is close to anti-sunward within 5 R_E of the Earth, however beyond 15 R_E, deflections become much stronger towards the dawn flank. In the dusk hemisphere, anti-sunward flows with minimal deflections are present within 7.5 R_E from the NMM plane, and beyond this boundary much stronger deflections towards local midnight are predominantly seen. The tailward flows in the recovery phase appeared to be the most ordered of the three substorm phases. In the dawn hemisphere (top half of the leftward plot of Figure 5.6) there is clear split between ions flows being somewhat parallel to the NMM and others deflected towards the NMM. At local midnight, the flow direction is mainly deflected towards the dawn flank beyond 15 R_E. In the dusk hemisphere, strong deflections towards local midnight are present throughout.

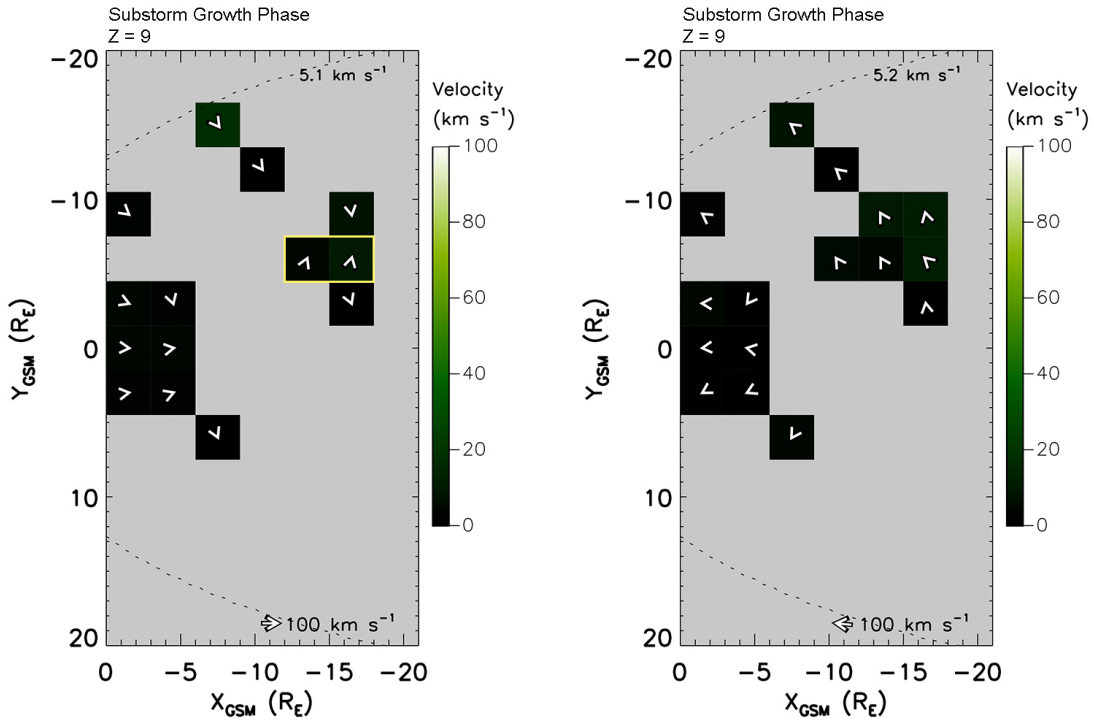

FIGURE 5.7: Ion velocity plots displaying tailward (left) and earthward (right) plasma flow during the substorm growth phase in the XY plane where Z = 9±4.5 R_E. The yellow box show vectors directed against the general flow direction of the plane.

5.3.2.3 Ion Flows Away From the Equatorial Plane

This short section discusses the behaviour of earthward and tailward directed ion flows in the outer planes of the three substorm phases.

Away from the equatorial plane, there is generally less data available in the northern hemisphere and as such the data spatial coverage is generally reduced, although in the growth phase it is more balanced. This is almost certainly due to the Cluster spacecraft spending less time in this region due to the orbital trajectory and its progression throughout the mission. In general, as previously mentioned, due to the lack of spatial coverage, it is very difficult to infer any specific flow patterns for any of the substorm phases. It is also worth noting that earthward flow is greatly reduced in these regions because there are periods in which the spacecraft lies out of the plasma sheet, where the outer planes are dominated by tailward flow data.

The northern hemisphere (positive Y values) of the growth phase shows a fairly sparse spatial distribution of earthward and tailward plasma flows (Figure 5.7). Earthward flows are mostly deflected towards the dawn flank in the dawn hemisphere. Within a radial distance of about 5 R_E of Earth, flows tend to be directed more earthward along the NMM, while there are slight dawnward/duskward deflections on the dawn and dusk sides respectively. Looking at the tailward flows in the same plane, the dawn flank

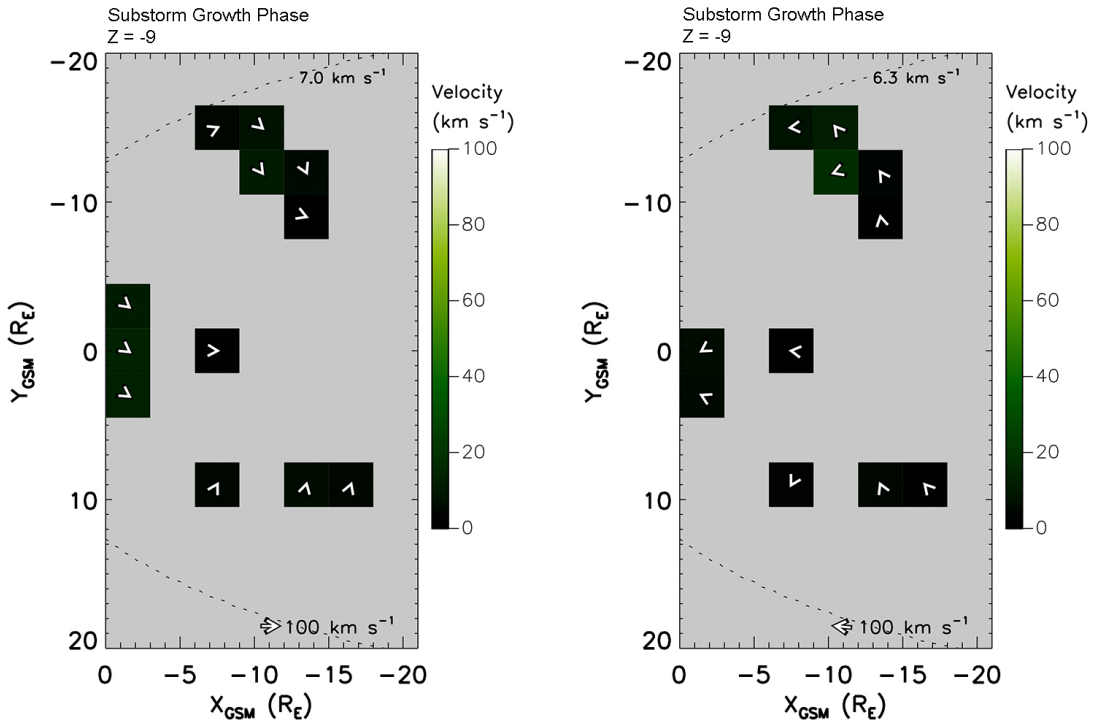

FIGURE 5.8: Ion velocity plots displaying tailward (left) and earthward (right) plasma flow during the substorm growth phase in the XY plane where Z = -9±4.5 R_E .

resents deflections directed towards the NMM with the two bins centred on Y = -6.5 R_E directed dawnward (yellow box). In the southern hemisphere (Figure 5.8), earthward flows in the dawn sector are mostly deflected dawnward. At local midnight flows are predominantly earthward and in the dusk hemisphere, flows are mostly directed towards the NMM with one bin directed duskward.

In the northern hemisphere of the expansion phase (Figure 5.9), there is almost no data available in the dusk hemisphere and not a great deal in the dawn hemisphere too. Within a radial distance of about 5 R_E from Earth, ion flows are roughly earthward at the NMM and again dawn and duskward deflections are present in their respective sides. In the dawn hemisphere flows are exclusively dawnward directed with the outermost vectors deflected very steeply. Looking at the tailward flows, within a radial distance of about 5 R_E from Earth, flows are almost parallel with the NMM with only very minor deflections towards the NMM. In the dawn hemisphere, ion flows are almost all deflected towards the NMM with the exception of one bin. The southern hemisphere (Figure 5.10) provides slightly more spatial coverage than the northern hemisphere. The earthward flows in the dawn hemisphere are gently deflected dawnward. At local midnight ion is almost exactly earthward. At the dusk terminator, deflections are strongly directed to the dusk, although at greater distances from earth, the flow pattern is directed towards the NMM. The tailward flows in the more distant regions of both the dawn and dusk hemispheres show fairly strong deflections towards the NMM while closer in, ions flows

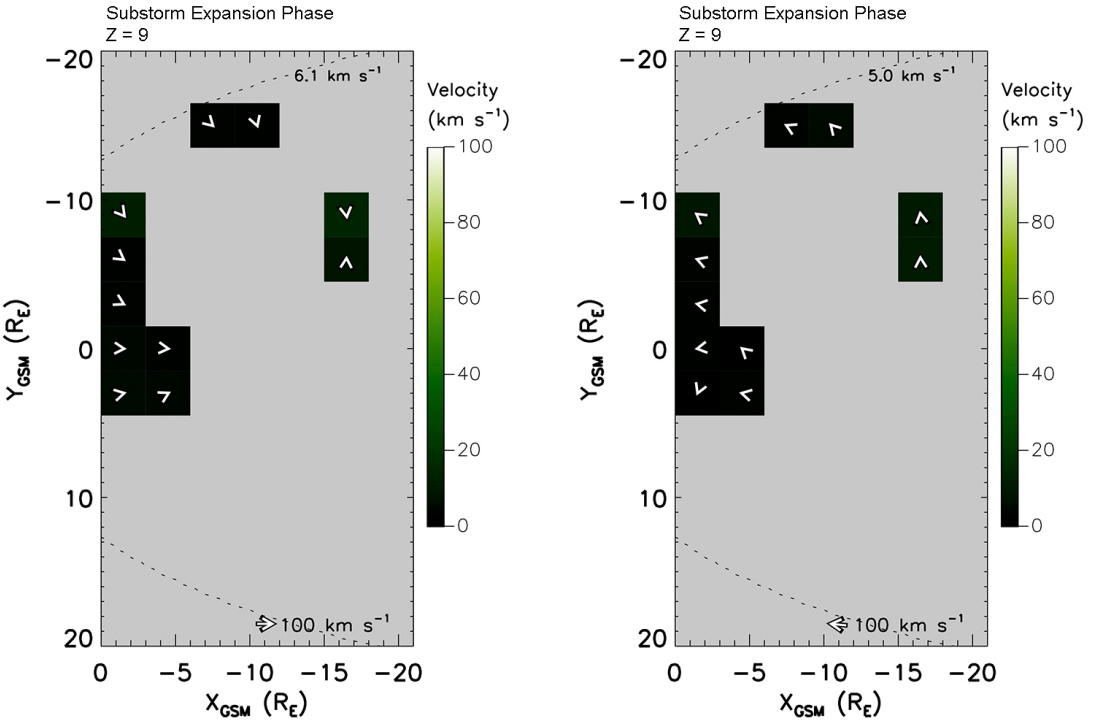

FIGURE 5.9: Ion velocity plots displaying tailward (left) and earthward (right) plasma flow during the substorm expansion phase in the XY plane where Z = 9±4.5 R_E .

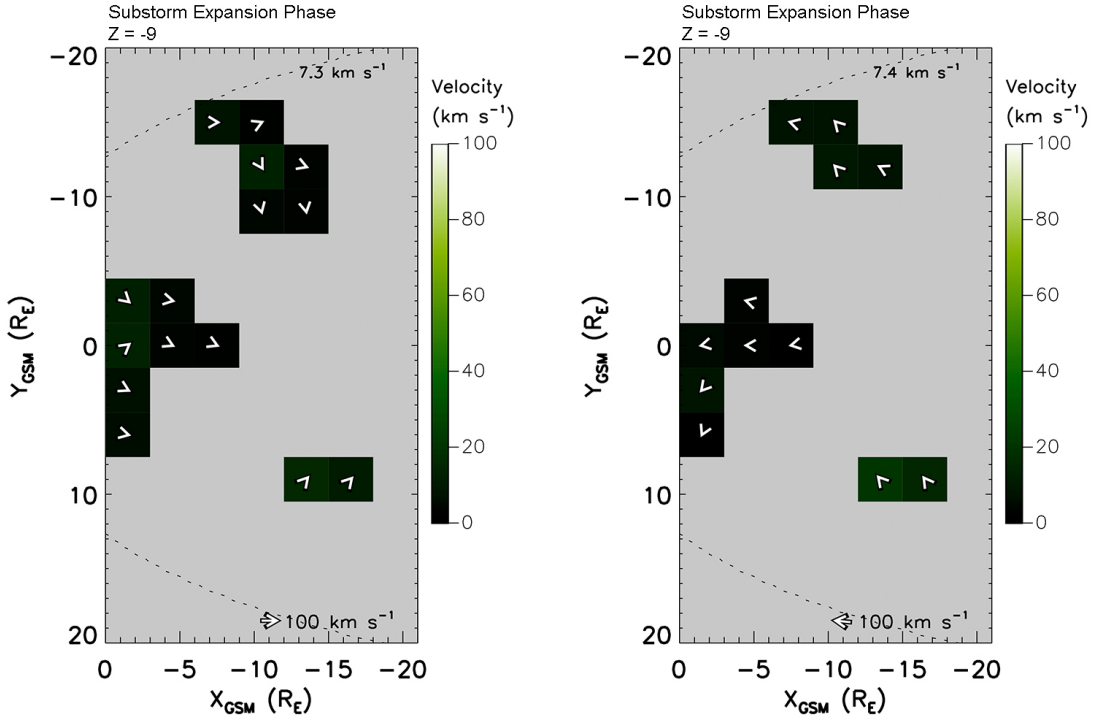

FIGURE 5.10: Ion velocity plots displaying tailward (left) and earthward (right) plasma flow during the substorm expansion phase in the XY plane where Z = -9±4.5 R_E .

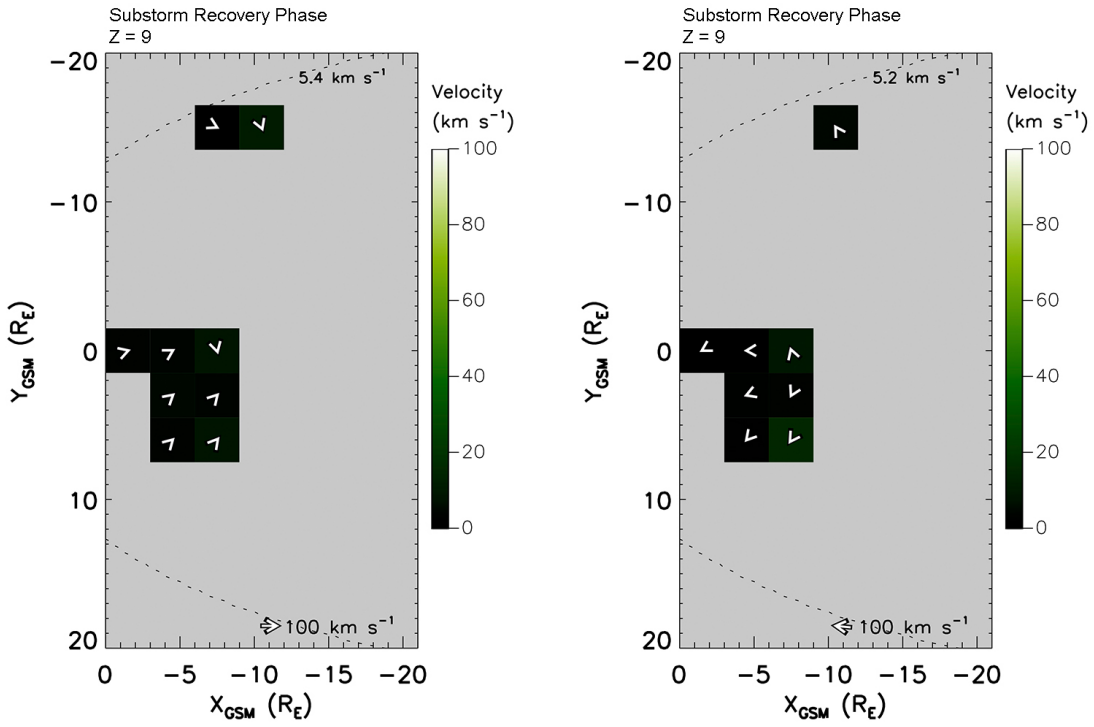

FIGURE 5.11: Ion velocity plots displaying tailward (left) and earthward (right) plasma flow during the substorm recovery phase in the XY plane where Z = 9±4.5 R_E .

appear to be orientated almost parallel to the NMM, with only minimal deflections away from this.

The northern hemisphere of the recovery phase (Figure 5.11) provides very little data beyond 10 R_E. Earthward flows at local midnight are near parallel to the NMM with the exception of one bin. In the dusk hemisphere, ion flows are deflected duskward. There is only one bin populated in the dawn hemisphere and its vector is directed dawnward. Tailward flows at local midnight are near parallel to the NMM with the exception of one bin. The rest of the vectors in both the dawn and dusk hemispheres are deflected towards local midnight. The southern hemisphere (Figure 5.12) provides much better coverage, although almost no data is present beyond Y = 10 R_E. On either side of local midnight, earthward flows throughout are generally directed towards the flanks with the exception of one bin. Tailward flows again show strong deflections towards local midnight throughout again with the exception of one bin.

Overall when looking at the outer planes, the take-home message is that across all the substorm phases earthward flows consistently show deflections towards the dawn and dusk flanks while tailward flows tend to present deflections towards local midnight.

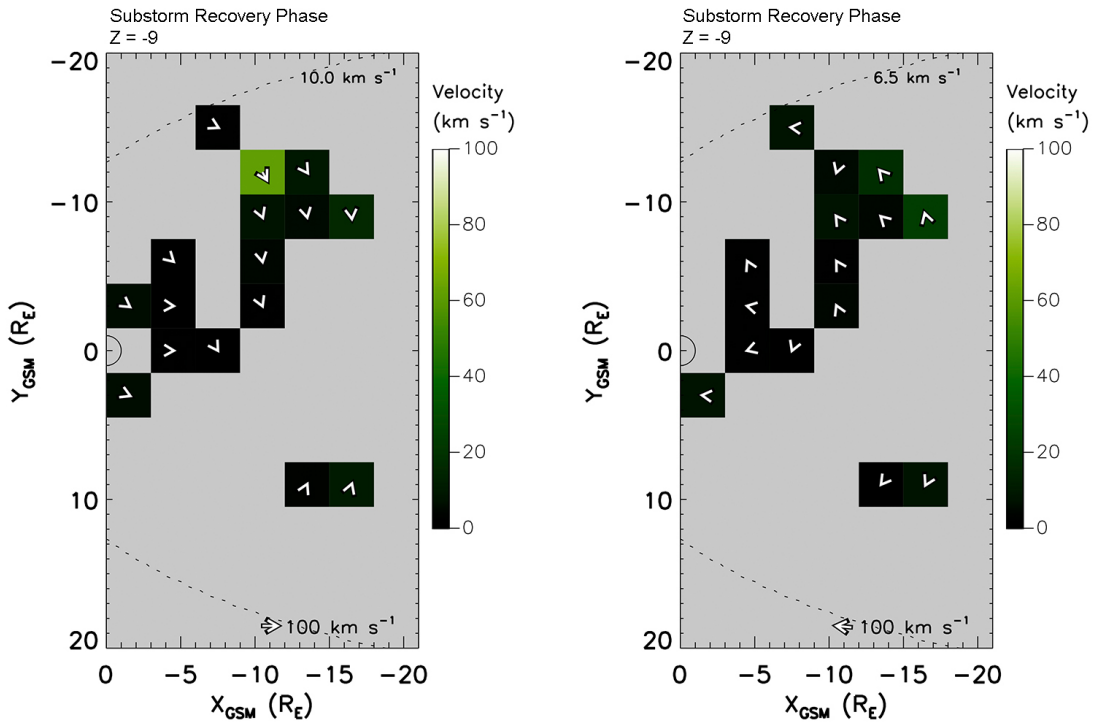

FIGURE 5.12: Ion velocity plots displaying tailward (left) and earthward (right) plasma flow during the substorm recovery phase in the XY plane where Z = -9±4.5 R_E .

5.3.3 Summary

When looking at all XY planes across all of the substorm phases, it was found that the dawn hemisphere generally has a greater spatial coverage than the dusk hemisphere in each plot. Across all planes and substorm phases, earthward flows had a higher occurrence rate than that of tailward ion flows. When just considering the equatorial plane, earthward flow dominates across all substorm phases with the recovery phase possessing the largest number of sample counts, followed by the expansion phase and finally the growth phase. When looking at previous studies, these results agreed with *Kissinger et al.* (2012), but did not agree with *Juusola et al.* (2011) who found there to be slightly more fast earthward flows in the growth phase than the expansion phase. The difference in results between the three studies could well be to do with how the data has been sampled and presented. Juusolas study used smaller spatial bins and an aberrated coordinate system, where both this chapters study and Kissingers did not. When looking at the data distribution for each individual substorm phase, it was found that the growth phase had a larger proportion of earthward flow than tailward flow occurrence. This was due to the heightened rate of dayside reconnection prevalent throughout this phase, which creates a flux pileup in the near-Earth magnetotail. Tailward flows are proportionally less frequent due to the lower rate of nightside reconnection in comparison to the rate of dayside reconnection. The expansion phase is the most balanced phase with regards

to flow direction and has the largest proportion of tailward flows across all phases. This is likely due to the rapid increase of the rate of nightside reconnection, which acts to increase the rate of tailward flows as some of the newly reconnected magnetic field lines are returned to the solar wind. Finally, the recovery phase has the largest proportion of earthward flow in comparison with the other two substorm phases. The likely reason for this result is that in this phase, the mid-tail region plasma sheet suddenly thickens with fast plasma flows at the plasma sheet boundary a region which is almost certainly included in the wider bins utilised in this study.

Across all planes and substorm phases, velocity in the earthward direction dominates with V_{xy} across all planes in both flow directions is 1.5 km s^{-1} during the growth phase, 0.6 km s^{-1} during the expansion phase and 1.7 km s^{-1} during the recovery phase. In the equatorial plane for each substorm phase, the earthward and tailward velocities are generally higher than the outer planes, with weighted-mean earthward-flow velocity dominating; V_{xy} is 5.3 km s^{-1} during the growth phase, 3.9 km s^{-1} during the expansion phase and 7.0 km s^{-1} during the recovery phase. When looking at earthward and tailward flows separately across all planes and substorm phases, it was found that the average earthward flow velocity was generally smaller than the average tailward flow velocity in the expansion and recovery phases. The growth phase has the slowest average earthward flows (8.7 km s^{-1}) and tailward flows (8.0 km s^{-1}), the expansion phase has slightly faster average earthward flows (9.5 km s^{-1} and tailward flows (10.0 km s^{-1}) than the growth phase, and the recovery phase has equally fast average earthward flows (9.5 km s^{-1}) but the fastest tailward flows (10.4 km s^{-1}). When only considering the equatorial plane, the growth phase still has the slowest average earthward and tailward ion flow velocity (14.6 km s^{-1} and 12.0 km s^{-1} respectively), but now the expansion phase has the fastest average tailward ion flow (16.5 km s^{-1}) and a faster average earthward ion flow velocity than the growth phase (16.0 km s^{-1}), and the recovery phase has the fastest average earthward ion flow velocity (16.8 km s^{-1}) and a slightly slower average tailward flow velocity (15.8 km s^{-1}). These earthward average-velocity substorm-distribution results were in agreement with *Kissinger et al.* (2012). However they were slightly different to the results found by *Juusola et al.* (2011), who found that the expansion phase had the largest average earthward velocity, followed by the recovery phase and finally the growth phase. This disagreement could be due to the way that data was binned and organised as there was only 1% difference between the amount of slow flows Juusola found in the expansion and recovery phases. In general, all three studies agree on the very low average velocities throughout the substorm event, further highlighting that the explosive energetic nature of substorms mostly consist of slow ion flows, interspersed with short duration fast flow events.

The final area of discussion was the observation of the average ion flow directions at the equatorial and outer planes for each substorm phase. In the equatorial plane, the growth phase earthward-flow pattern presenting some dawn-dusk asymmetry as well as appearing to be the most disordered substorm phase. The expansion phase appeared to be a little more ordered than the growth phase and possessed further evidence of dawn-dusk asymmetry. There were more deflections in the dusk hemisphere than in the dawn hemisphere were flows were predominantly sunward. The results here were generally more ordered than the equivalent results in the *Kissinger et al.* (2012) study. The earthward flows during the recovery phase were the most ordered of the three substorm phases, with the dawn hemisphere presenting mostly sunward ion flows with slight dawnward deflections. The dusk also showed mostly sunward flows, but this time with slightly duskward deflections. Still looking a the equatorial plane, tailward flows in the growth phase were found to be gently deflected at the dawn flank towards local midnight. In the dusk hemisphere, within 15 R_E from Earth, the flow is predominantly anti-sunward with only three bins showing deviation from this. Beyond 15 R_E from Earth, flows quickly turned towards local midnight. The expansion phase again appeared to be more ordered than the growth phase, although in the dawn hemisphere, deflections of the tailward flows were consistently directed towards the local midnight. In the dusk hemisphere, again a mix of anti-sunward and strong deflections towards local midnight were observed. Finally, the recovery phase appeared to be the most ordered substorm phase. In the dawn hemisphere there is clear split between ions flows being somewhat parallel to the NMM and others deflected towards the NMM. At local midnight, the flow direction is mainly deflected towards the dawn flank beyond 15 RE. In the dusk hemisphere, strong deflections towards local midnight are present throughout. Looking at the outer planes, away from the equatorial plane, the spatial coverage was severely limited and as such it was difficult to make specific meaningful conclusions for each substorm phase. Overall when looking at the outer planes, across all the substorm phases earthward flows consistently show deflections towards the dawn and dusk flanks while tailward flows tend to present deflections towards local midnight.

5.3.3.1 Key Results

There were a number of key original results shown in this section. Firstly in general there have not been any previous studies which study substorm intervals while considering ion moments of all velocities, although there have been two which looked at fast flow ion moment during these intervals, *Kissinger et al.* (2012); *Juusola et al.* (2011), they did not look at them for separate flow directions. In addition, both studied also focussed on ion bulk velocities rather than perpendicular ion velocities used in this study. Following

on from this, all results presented in this chapter are original and present a new set of results. With regards to tailward flows, the recovery phase presents the fastest weighted-mean average ion velocity, with the expansion phase being a little slower and the tailward flow in the growth phase being the slowest.

The first key original result was found when considering field-perpendicular earthward ion flows in the equatorial plane, the recovery phase has the fastest average ion-flow velocity with the expansion phase being a little slower and the growth phase being the slowest. This result agrees with but does not repeat the results presented by *Kissinger et al.* (2012), who found the same pattern when studying the relative proportions of fast flow moments (> 200 km s^{-1}). A similar study to Kissinger, carried out by *Juusola et al.* (2011), found the the average fast-flow earthward ion moment velocity to be slightly greater in the growth phase than the expansion phase, although there was on a 1% velocity difference. Again this study used a different dataset, utilising ion bulk-velocity moments and neglecting slow-flows, as well as applying an aberrated coordinate system, thus the result presented in this chapter is unique.

The next key original result was found while looking at the overall earthward ion-flow patterns in the equatorial plane. It was generally seen that there were dawn-dusk asymmetries present across each of the substorm phases with a good deal more deflections towards the flank in the dusk hemisphere than the dawn hemisphere. This was not presented in the study carried out by *Kissinger et al.* (2012) who reported a good deal of disorder in the fast flow patterns. It was also noted that in comparison to Kissinger's study, the ion flows generally appeared to follow a much more discernible flow pattern and possessing somewhat more order throughout.

All of the tailward ion-flow results presented in the chapter are essentially new results since there have been other studies discussing them in any great detail. Thus all the results summarised in section 5.3.2.2 are new.

5.4 Ion Flow During Substorm Events in the XZ Planes

5.4.1 Sample counts

Phase	Plane (Y = nR_e)	$N_{earthward}$	$N_{tailward}$	N_{total}	% EF	% TF
Growth	9	3400	1611	5011	67.9	32.1
	0	3680	5478	9158	40.2	59.8
	-9	3770	2312	6082	62.0	38.0
Total		10850	9401	20251	53.6	46.4
Expansion	9	3434	2506	5940	57.8	42.2
	0	4158	5950	10108	41.1	58.9
	-9	4586	3053	7639	60.0	40.0
Total		12178	11509	23687	51.4	48.6
Recovery	9	8918	3922	12840	69.5	30.5
	0	9083	10176	19259	47.2	52.8
	-9	10341	3987	14328	72.2	27.8
Total		28342	18085	46427	61.0	39.0

TABLE 5.4: Sample counts distribution for the XZ plane across 3 cuts in the y-direction for each substorm phase. The Y value given is the position on which the plane is centred. EF represents earthward flow and TF represents tailward flow.

This section will discuss the distribution of data analysed during the three substorm phases in the XZ plane. First, the spatial distribution of data across the three available planes for each substorm phase is analysed. The recovery phase has the largest amount of data available, this is due to the duration of the phase being 60% longer than the expansion and growth phases (Table 5.4). The latter had the least amount of data available. Overall, there is generally more earthward flow data than tailward flow data available. As previously discussed, while one would expect there to be generally more data available in the southern hemisphere due to the orbital trajectory of the Cluster spacecraft, it is clear from looking at the sample count plots that is is not entirely the case. For example Figure 5.13 clearly shows there to be more data contained within the northern hemisphere. There are two important factors which likely contributed to this. The first is the physical position in which the spacecraft were when the substorms began as each substorm phase duration is very short and thus there is a good chance that the Cluster spacecraft could just have been situated more frequently in the northern hemisphere when the events were triggered. The second reason could be down to the inclusion of the magnetosheath-removal procedure which likely stripped out a lot of the data available in the most southern regions containing data. It can also be seen that there is generally more spatial coverage and higher sample counts in the dawn hemisphere than the dusk hemisphere across all three substorm phases. It was also found that when observing the dawn region, there was also more data available in the northern hemisphere than in the dusk region. An example of this can be seen in Figures

5.14 (dawn hemisphere) and 5.15 (dusk hemisphere). This distribution has previously been discussed in Chapter 4 and it was observed that this asymmetrical data distribution was due to each Cluster spacecraft's orbital motion through the YZ plane.

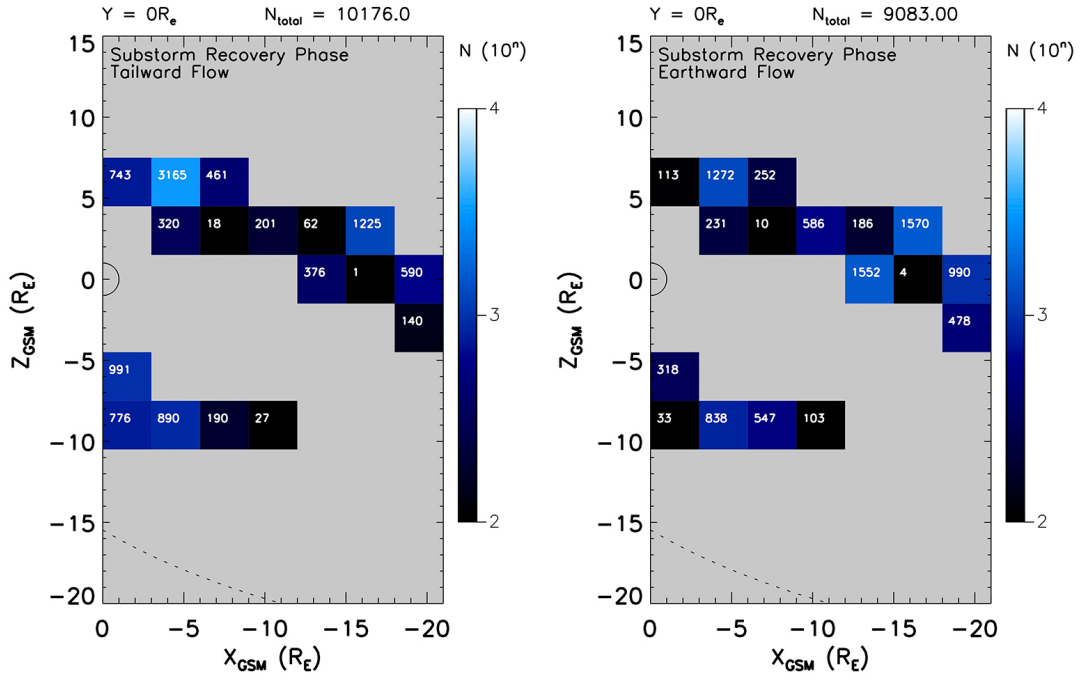

FIGURE 5.13: Sample count plot for the XY plane Z = 0 ± 4.5 R_E displaying tailward (left) and earthward (right) plasma flow during the substorm recovery phase.

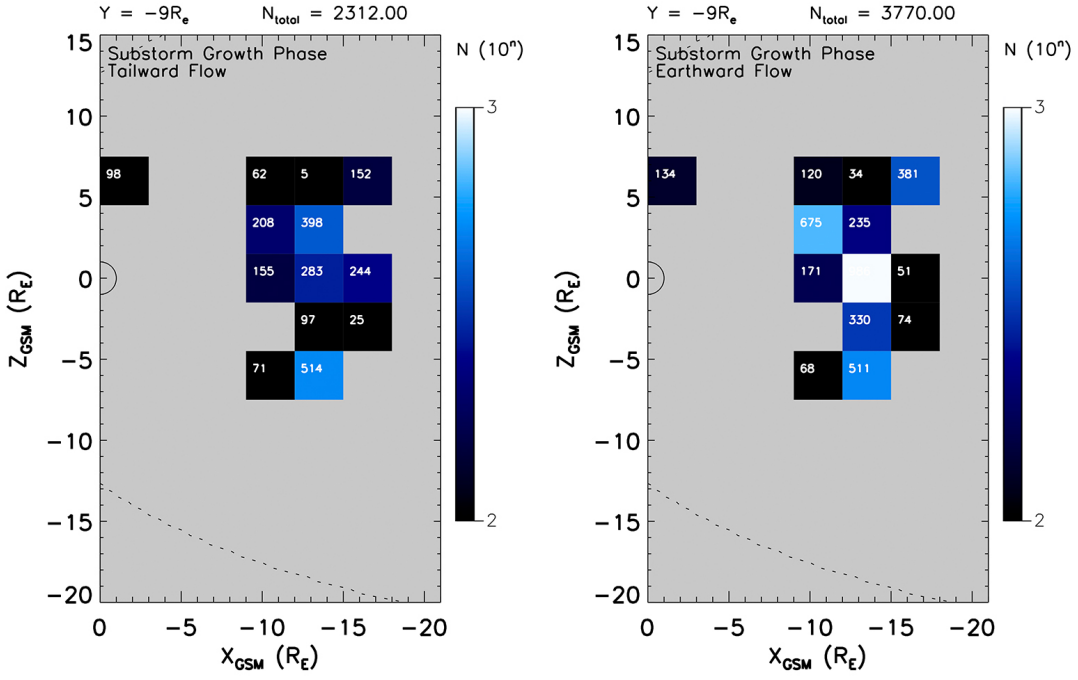

FIGURE 5.14: Sample count plot for the XY plane Z = -9 ± 4.5 R_E displaying tailward (left) and earthward (right) plasma flow during the substorm growth phase.

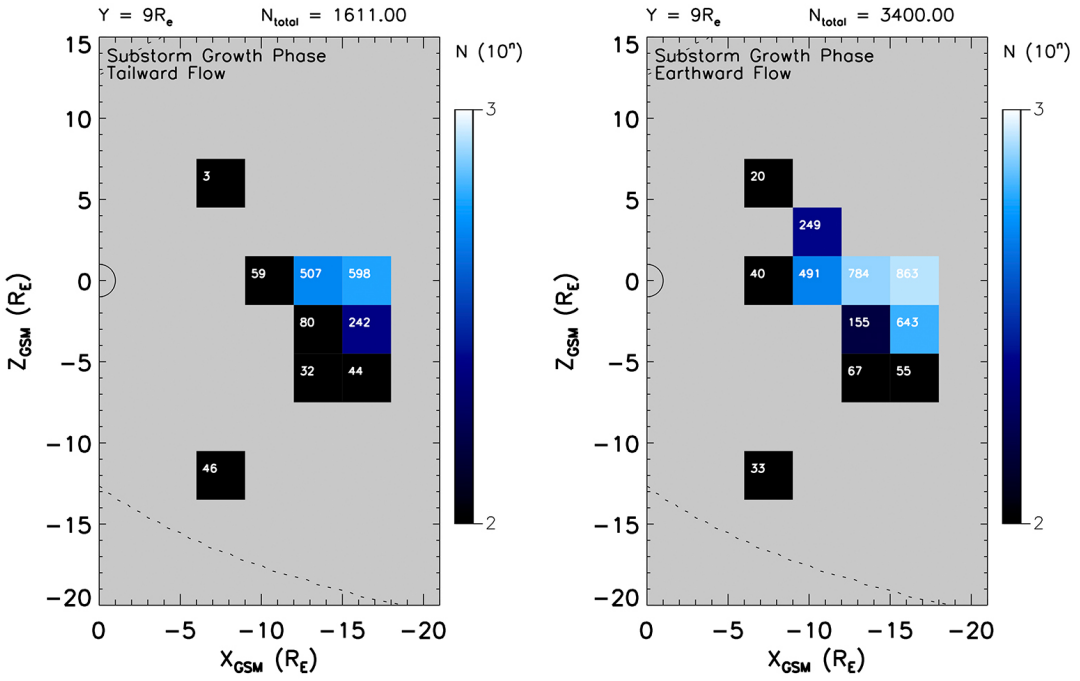

FIGURE 5.15: Sample count plot for the XY plane Z = 9 ± 4.5 R_E displaying tailward (left) and earthward (right) plasma flow during the substorm growth phase.

Considering all three planes for each substorm phase in the XZ direction, it is clear that overall there are more earthward directed plasma flow data than for tailward flow (Table 5.4). The recovery phase presents the largest difference, with earthward flow having 10257 more counts than tailward flow. It also has the smallest proportion of tailward ion flow (39.0 %) and the largest proportion of earthward flow (61.0 %). The growth has the next largest earthward/tailward count difference of 1449 counts. The expansion phase has the smallest difference with earthward flows having just 669 more sample-counts contributing to the phase than tailward flows. It is also the most balance phase with 51.4 % of ion flows occurring in the earthward direction. Unlike the data distribution in the XY plane, tailward flows in the XZ plane are dominant in the noon-midnight meridian, the plane centred on Y = 0 R_E. An example of this can be seen in Figure 5.16. This is because the central plasma sheet, where the majority of earthward plasma flow occurs covers a smaller region-per-plane (about 1512 R_E^3) than the XY planes (about 8400 R_E^2) and as such, the magnetotail in the XZ plane contains proportionally more tailward magnetosheath and lobe data which may not have been removed with the Coxon and magnetosheath removal procedures. It was found that in the NMM plane, the most earthward flow data was collected during the recovery phase, followed by the expansion and then growth phase, with only about a 2.8% difference (of the total number of earthward flows measure in the equatorial plane) between the number of counts measured in the latter two phases.

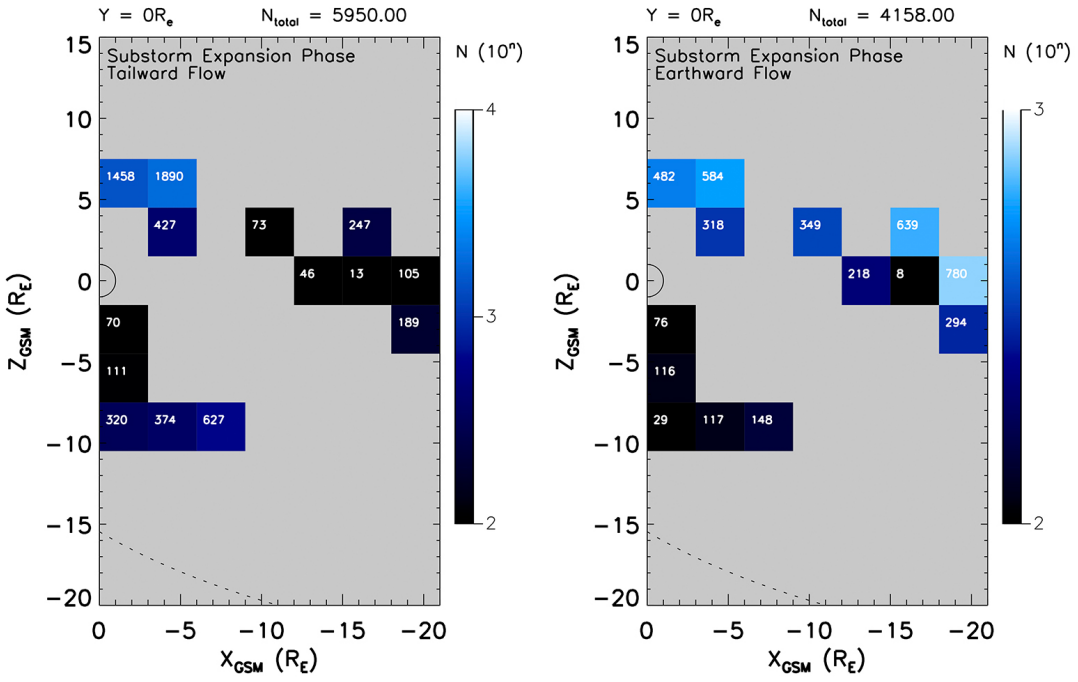

FIGURE 5.16: Sample count plot for the XY plane Z = 0 ± 4.5 R_E displaying tailward (left) and earthward (right) plasma flow during the substorm expansion phase.

5.4.2 Ion Velocity: Magnitude and Direction

Phase	Plane (Y=n±1.5 R_e)	V_{xz} Earthward [km s^{-1}]	V_{xz} Tailward [km s^{-1}]	Weighted Mean Av. V_{xz} [km s^{-1}]
Growth	9	8.3	6.5	3.5
	0	7.8	9.5	-2.5
	-9	9.3	8.3	2.6
Average		8.5	8.1	0.8
Expansion	9	12.7	7.9	4.0
	0	6.8	10.3	-3.3
	-9	9.7	7.3	2.9
Average		9.7	8.5	0.9
Recovery	9	9.1	6.9	4.2
	0	6.7	7.5	-0.8
	-9	14.3	12.9	6.7
Average		10.0	9.1	2.6

TABLE 5.5: V_{xz} distribution for the XZ plane across 3 cuts in the y-direction for each substorm phase. The Y value given is the position on which the plane is centred. EF represents earthward flow and TF represents tailward flow.

When considering both earthward and tailward perpendicular ion flows together in the XZ plane, on average across all planes observed and all substorm phases, earthward ion velocity (V_{xz}) dominates, Table 5.5. This result supports the results in Chapter 4 and section 5.3.2, which also found that earthward velocity was dominant for all times. It can be seen in Table 5.5 that the weighted mean V_{xz} across all planes is 0.8 km s^{-1}

during the growth phase, 0.9 km s^{-1} during the expansion phase and 2.6 km s^{-1} during the recovery phase. These average velocities are very similar to those observed in the XY plane. Looking only at the NMM, the plane centred on Y = 0 R_E, tailward ion flow velocities are faster each substorm phase.

Considering earthward and tailward flows separately for each substorm phase, it can be seen that the weighted-mean average earthward plasma flow velocity is faster than the average tailward flow velocity across all three XZ spatial planes (Table 5.5). The growth phase has the slowest earthward flows (8.5 km s^{-1}) and a tailward ion velocity of 8.1 km s^{-1}. The expansion phase has faster earthward (9.7 km s^{-1}) and tailward flows (8.5 km s^{-1}) than the growth phase. The recovery phase has the fastest earthward (10.0 km s^{-1}) and tailward flows (9.1 km s^{-1}). When focussing on the noon-midnight meridian plane, the recovery phase has the slowest average earthward flow velocity (6.7 km s^{-1}) but the slowest average tailward flow velocity (7.5 km s^{-1}). The growth phase has the fastest average earthward flow (7.8 km s^{-1}) and an average tailward flow of 9.5 km s^{-1}). The expansion phase has the fastest average tailward flow of 10.3 km s^{-1} and an average earthward flow velocity of 6.8 km s^{-1}. The average velocity results in the NMM were found to be lower than those in the equatorial plane for the same substorm phases. This difference in results was probably down to the spatial distribution of data in each plane as well as some potential magnetosheath contamination which was missed by the sheath-removal algorithm. In the equatorial plane, the spatial coverage extended right out to the magnetopause, allowing ions to interact with the solar wind and thus become accelerated to greater velocities. Since the spatial coverage rarely neared the magnetopause, this is the likely reason for the velocity disparity. Finally, as with the XY planes, the average earthward and tailward flows are slow, not exceeding 14.3 km s^{-1} for any substorm phase. These results further highlight the magnetotail is generally a slow moving system in comparison to other regions such as the solar wind, even during energetic substorm events.

The average vector flow direction is the final observation to be discussed. As previously mentioned, the direction of plasma flow must be treated with caution when using the plots. Each spatial bin covers such a large area of the magnetotail that it is very difficult to determine where the data from each bin was collected in the z-direction to a good level of certainty. However, a series of plots at the original 3 R_E^3 spatial resolution can be seen in Appendix C, allowing comparisons to be made, providing somewhat more detail as to where the contributing vectors to each larger bin originated. Considering earthward ion flows in the equatorial plane for each substorm phase (Figures 5.17, 5.18, 5.19), it is clear that deflections are present throughout, although there is little evidence of asymmetric behaviour.

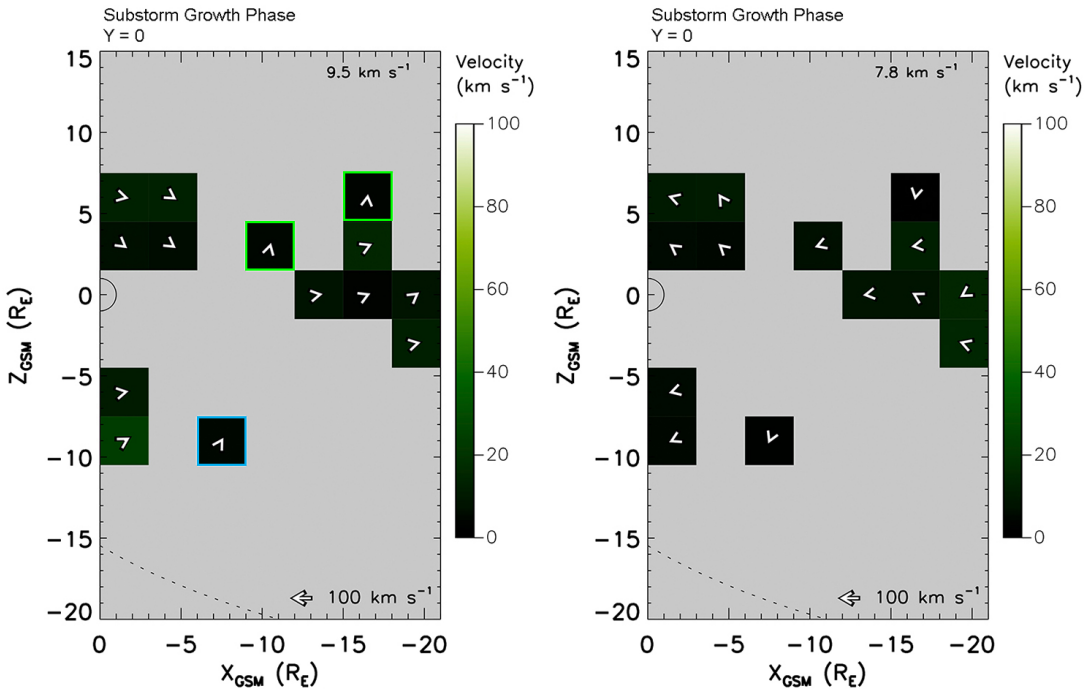

FIGURE 5.17: Ion velocity plots displaying tailward (left) and earthward (right) plasma flow during the substorm growth phase in the XZ plane where Y = 0±4.5 R_E .

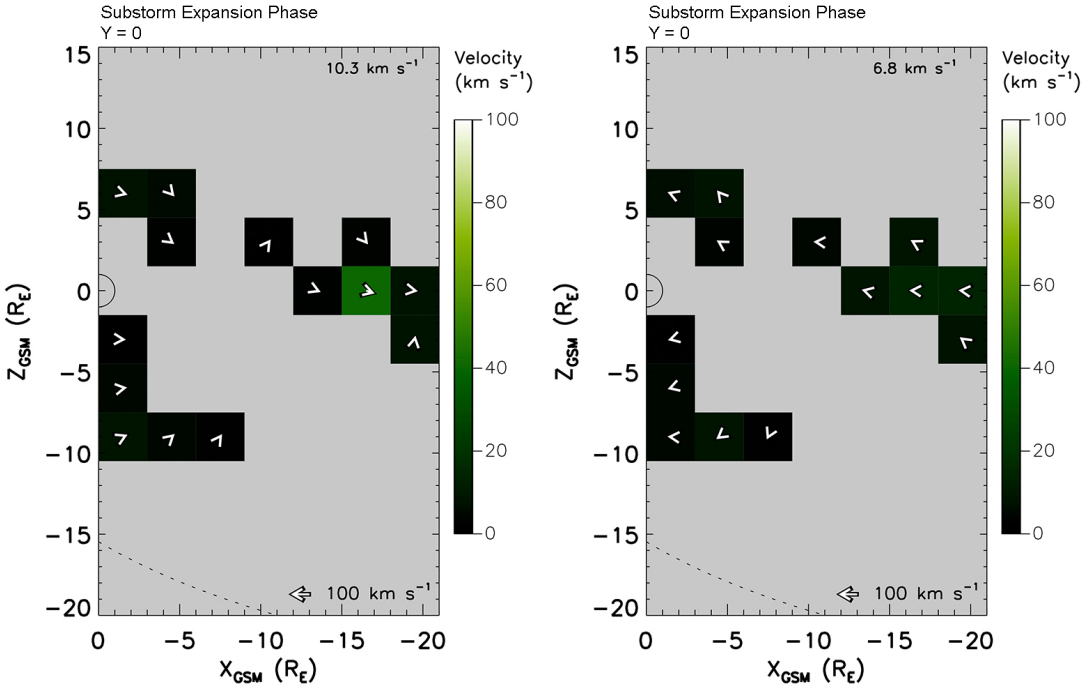

FIGURE 5.18: Ion velocity plots displaying tailward (left) and earthward (right) plasma flow during the substorm expansion phase in the XZ plane where Y = 0±4.5 R_E .

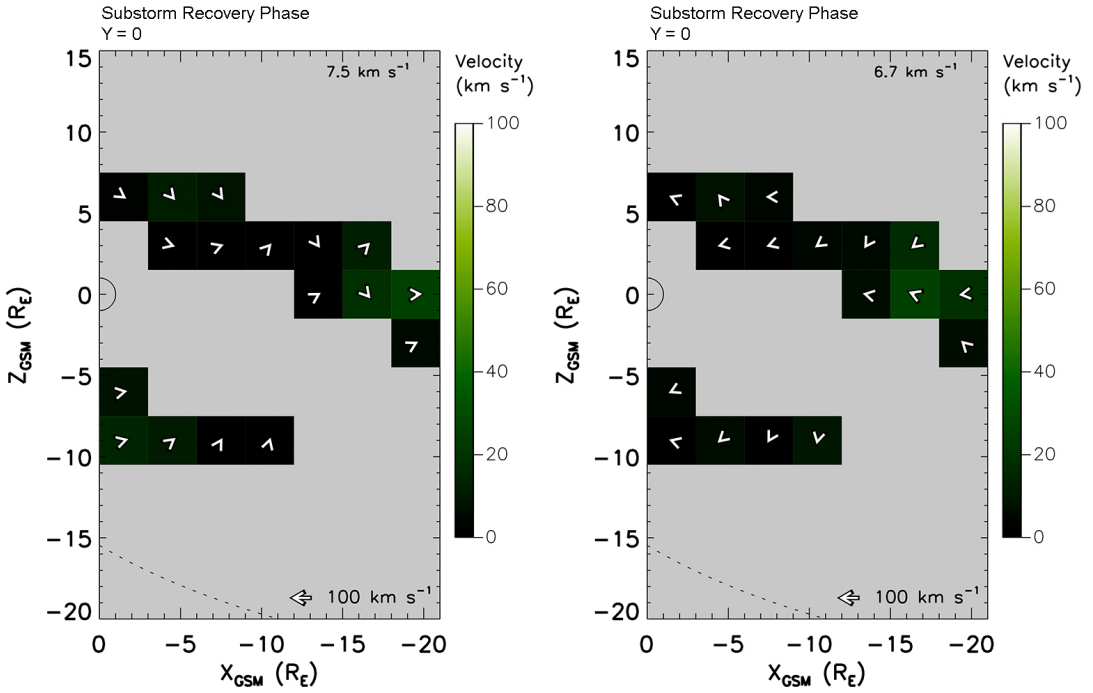

FIGURE 5.19: Ion velocity plots displaying tailward (left) and earthward (right) plasma flow during the substorm recovery phase in the XZ plane where Y = 0±4.5 R_E .

Looking at earthward ion flow in the noon-midnight meridian (centred upon Y = 0 R_E) of the growth phase, the ion flows within the northern hemisphere are predominantly sunward with stronger deflections present towards the northern terminator. The ion flow at the equatorial plane is mostly earthward with only a little deviation from this direction. The data coverage is limited in the southern hemisphere, although generally the ion flows are deflected towards the southern flank. The earthward flow pattern of the expansion phase appears to be very similar to the growth phase. The earthward plasma flow pattern of the recovery phase appears to be the least deflected of the three substorm phases in the study. The northern hemisphere presents predominantly sunward flow with minor northward deflections found close to the northern terminator. At the equatorial plane, there is little deviation from the earthward direction. In the southern hemisphere, flows are deflected more towards the southern flank and are little stronger at greater distances from the Earth. In general, it is clear that deflections in the XZ plane across all substorm phases are small in comparison to those found in the XY plane. This shows that there is possibly less plasma transported up and over the Earth in the Z-direction, with the system favouring transport around the sides of the Earth in the Y-direction instead.

Looking at tailward flows in the NMM plane of the growth phase, the northern hemisphere shows gentle deflections towards the local midnight with two anomalously directed bins (green boxes in Figure 5.17) which are strongly deflected towards the northern flank.

At the equatorial plane, flows are mostly anti-sunward (roughly parallel to the equatorial plane). In the southern hemisphere, ion flows are generally deflected gently towards the local midnight with one bin (blue box in Figure 5.17) showing a much stronger deflection in the same direction. The expansion phase tailward flow pattern in the same plane is very similar to that of the growth phase, with the only difference being that the deflections present are more consistently directed towards the Z = 0 R_E boundary and are also occasionally stronger than in the growth phase. The tailward flows in the recovery phase perhaps present slightly more-pronounced signs of convective ion flow. The northern hemisphere during the recovery phase shows more deflections towards the equatorial plane (EQ plane) with distance from it. Closer in, flows become more parallel to the EQ plane with some variation beyond X = -10 R_E. The same can be said for the flows along the equatorial plane. The southern hemisphere presents consistent defections towards the EQ plane. In general, it is clear that tailward flows experience somewhat more deflections in the z-direction than for earthward flows, showing that anti-sunward flow (somewhat parallel to the EQ plane) is marginally less dominant during tailward ion flow times than sunward flow is during earthward ion flow times.

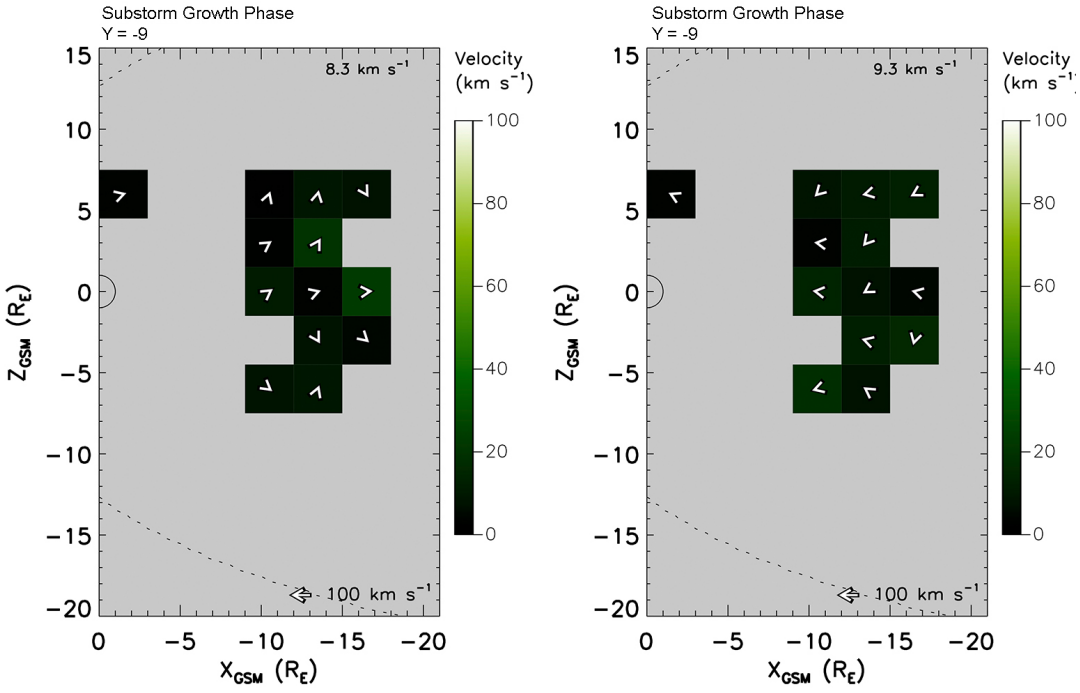

FIGURE 5.20: Ion velocity plots displaying tailward (left) and earthward (right) plasma flow during the substorm growth phase in the XZ plane where Y = -9±4.5 R_E .

Considering all substorm phases away from the equatorial plane, the data spatial coverage is somewhat reduced. There is generally more data available in the dawn hemisphere, which also has greater spatial coverage in the northern hemisphere than in the dusk hemisphere. The reasons for these spatial distributions have been discussed previously. Looking at the dawn hemisphere of the growth phase (Figure 5.20, right plot),

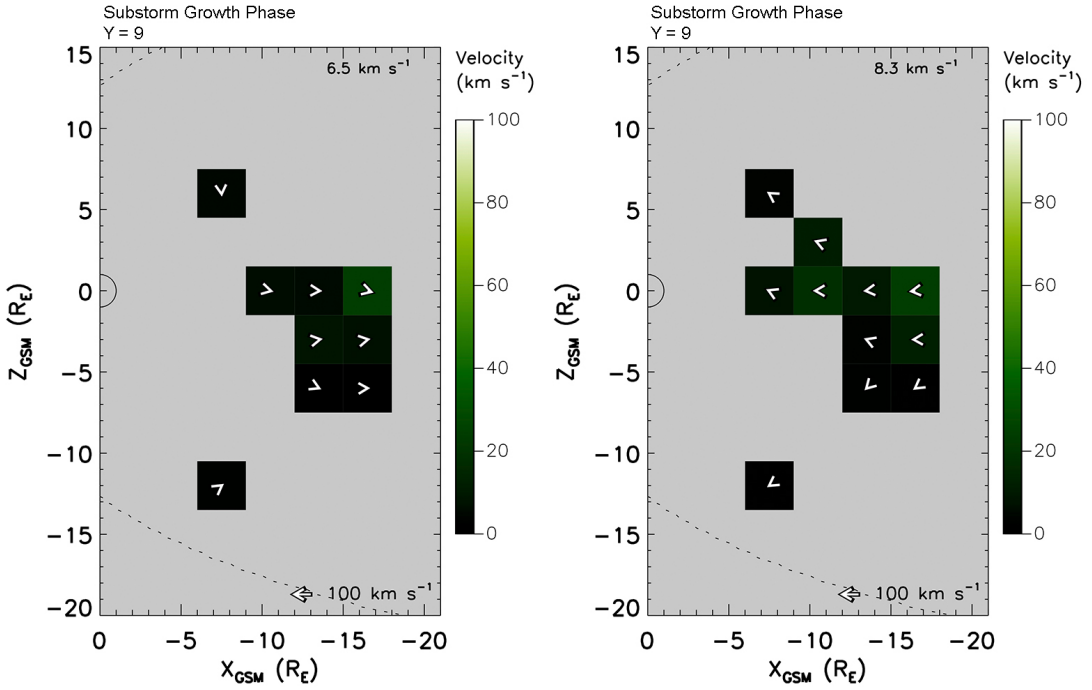

FIGURE 5.21: Ion velocity plots displaying tailward (left) and earthward (right) plasma flow during the substorm growth phase in the XZ plane where Y = 9±4.5 R_E .

earthward flows in the northern hemisphere are predominantly sunward, roughly parallel with the EQ plane, with only minor deflections towards it. The same can be said for flows along the EQ plane. In the southern hemisphere, flows are again predominantly sunward, with one vector strongly deflected towards the southern flank, and another slightly deflected towards the equatorial plane. Looking at the tailward flows in the same plane, northern hemisphere are mostly deflected towards the northern flank with the exception of the most distant bin from Earth which is strongly directed towards local midnight. In the southern hemisphere of the dawn sector, the flows are almost all directed towards the southern flank with the exception of one vector which is strongly deflected towards the equatorial plane. The flows directed along the equatorial plane are strongly aligned with the x-axis. The earthward flows in the dusk hemisphere (Figure 5.21, right plot) are mostly sunward close to the EQ plane with deflections towards the high-latitude magnetopause away from this. Tailward flows in this plane are much the same, with the two most distant bins from the EQ plane exhibiting strong deflections towards it.

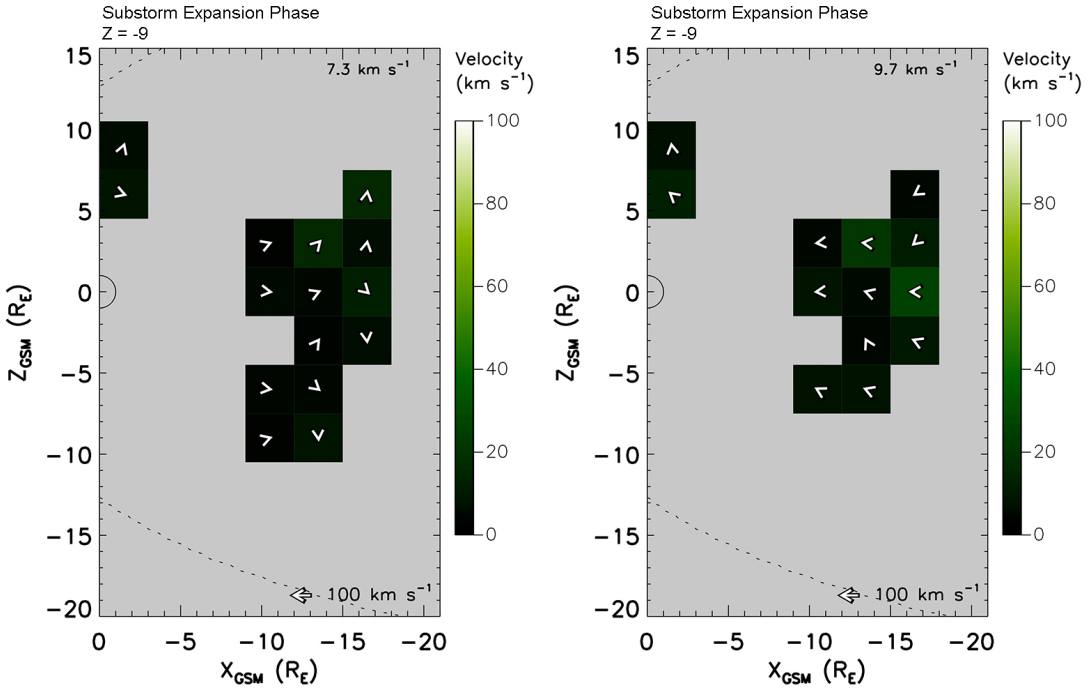

FIGURE 5.22: Ion velocity plots displaying tailward (left) and earthward (right) plasma flow during the substorm expansion phase in the XZ plane where Y = -9±4.5 R_E .

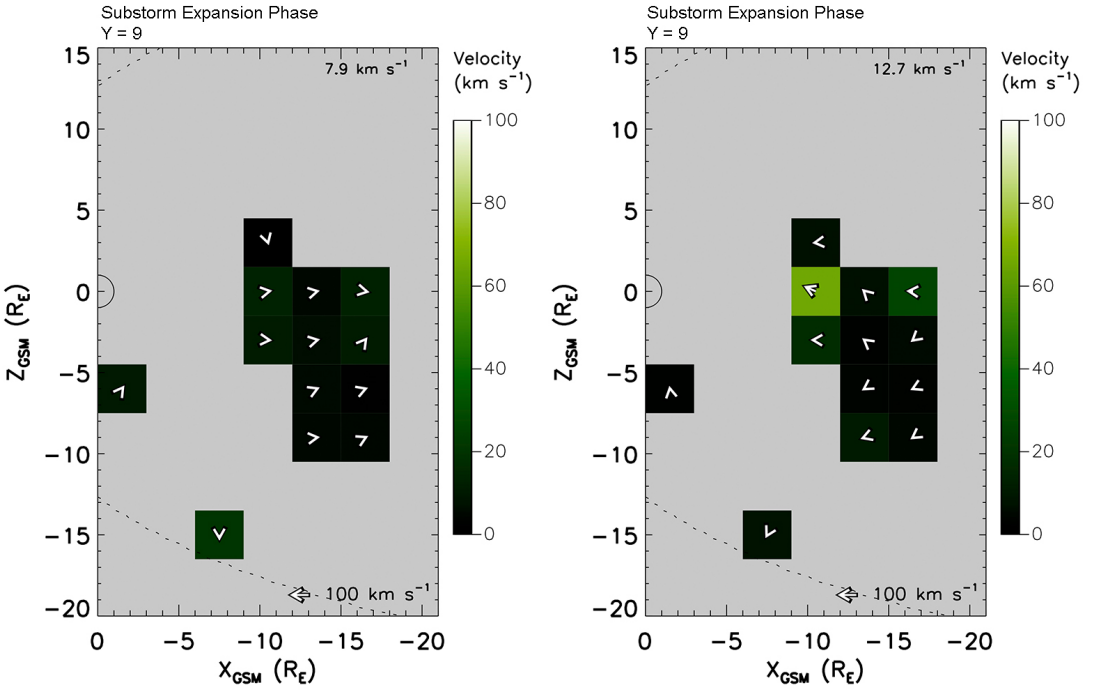

FIGURE 5.23: Ion velocity plots displaying tailward (left) and earthward (right) plasma flow during the substorm expansion phase in the XZ plane where Y = 9±4.5 R_E .

Looking at the earthward flows in the dawn hemisphere of the expansion phase (Figure 5.22, right plot), sunward flow dominates throughout with some deflection towards the equatorial plane and stronger deflections in the northern direction at the terminator. Tailward flows in this hemisphere are minimally deflected towards the flanks within 15 R_E from the Earth, becoming greatly deflected towards the flanks beyond this. There are also strong deflections present at the northern terminator. In the dusk hemisphere (Figure 5.23, right plot), earthward flows are considerably more ordered than the dawn hemisphere with only minimal deflections towards the flanks throughout. The tailward ion flows are dominated by anti-sunward flows with one additional southward deflection in the southern hemisphere and two quite strongly deflected vectors towards the equatorial plane.

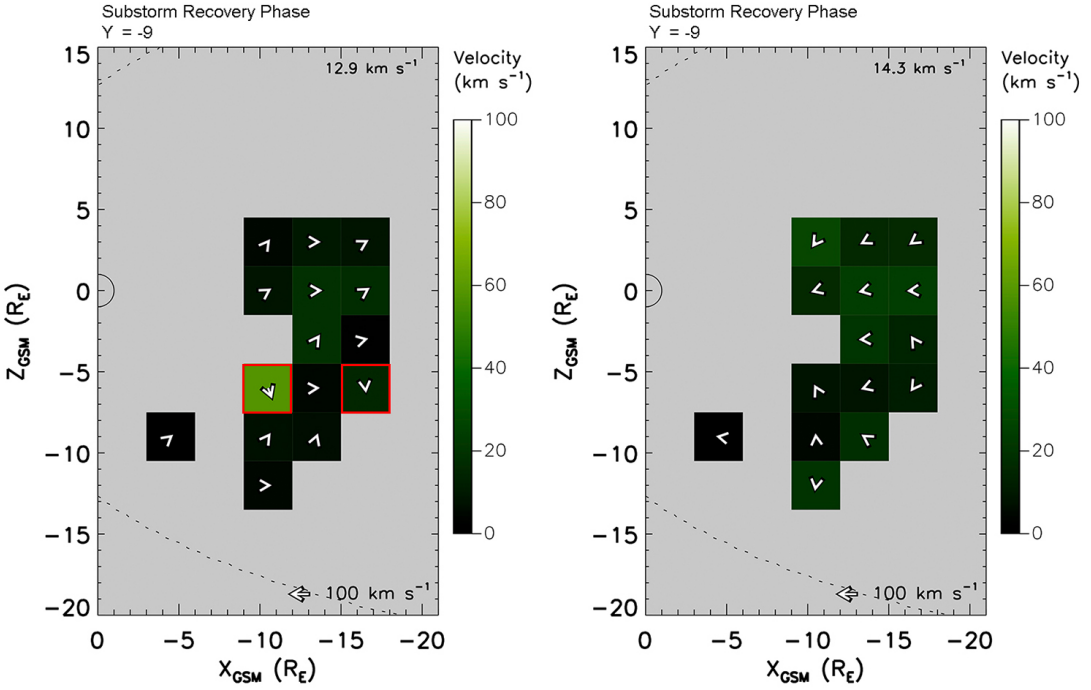

FIGURE 5.24: Ion velocity plots displaying tailward (left) and earthward (right) plasma flow during the substorm recovery phase in the XZ plane where Y = -9±4.5 R_E .

Looking at the dawn hemisphere of the recovery phase (Figure 5.24, right plot), earthward flows are deflected towards the equatorial plane throughout with stronger deflections present in the southern hemisphere. Tailward flows (left plot) in the northern hemisphere are slightly deflected towards the northern flank while flows in the southern hemisphere are mostly directed towards equatorial plane with the exception of two bins (red boxes) which are directed towards the southern flank. The direction of these two bins could be attributed to statistical fluctuations however. In the dusk hemisphere (Figure 5.25, left plot), tailward flows in the northern hemisphere are generally directed towards equatorial plane. At the equatorial plane, flows are somewhat directed towards

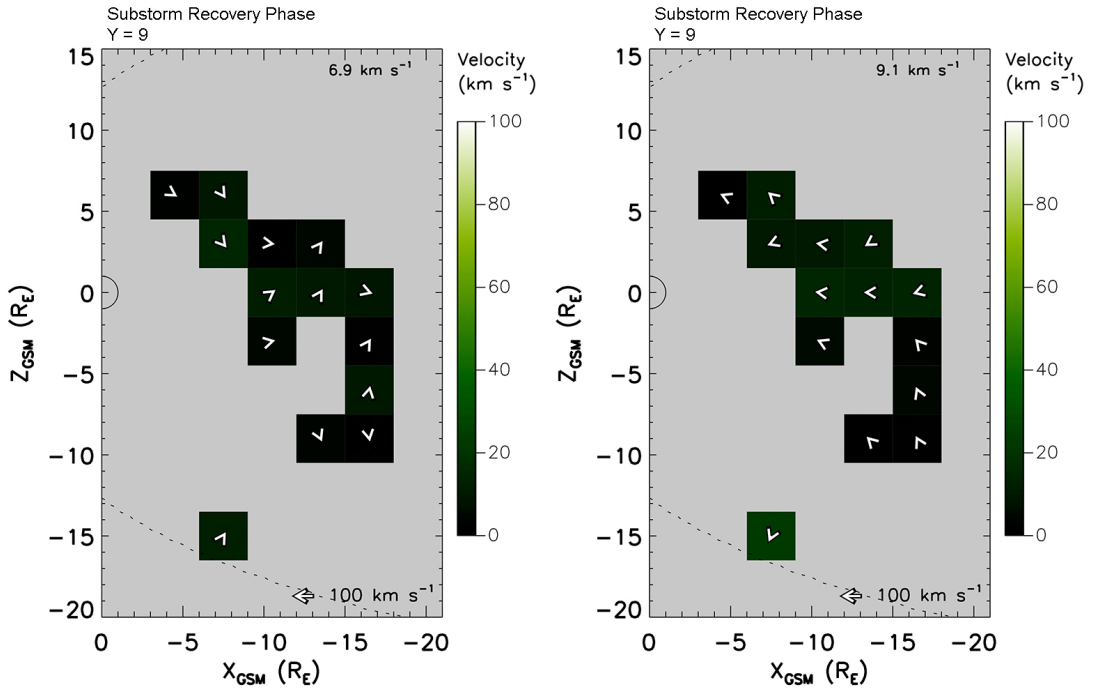

FIGURE 5.25: Ion velocity plots displaying tailward (left) and earthward (right) plasma flow during the substorm growth phase in the XZ plane where Y = 9±4.5 R_E .

the northern flank. In the southern hemisphere, the flow pattern is quite inconsistent, being split both strongly towards equatorial plane and the southern flank. Looking at the earthward flows (right plot of the same Figure), the pattern is much more consistent with minimal deflections in the northern sector and at the EQ plane, and strong deflections present towards equatorial plane in the southern hemisphere.

5.4.3 Summary

When looking at all XZ planes across all of the substorm phases, it was found that the recovery phase had the largest amount of data, this was because it's duration is 60% longer than the growth and expansion phases. The latter had the least amount of data available. The recovery phase has the smallest proportion of tailward ion flow and the largest proportion of earthward ion flows. The expansion phase proportionally has the lowest earthward ion flow occurrence rate and thus the highest proportion of tailward ion flows. The orbital trajectory of the Cluster spacecraft can be seen within the data and there is more spatial coverage across all substorm phases in the dawn hemisphere and with it, more coverage in the northern hemisphere than in the dusk hemisphere. Looking at all planes and substorm phases, there was more earthward data collected than tailward plasma flow data. When only considering the NMM plane (centred about Y = 0 R_E), tailward flow dominates across all substorm phases. This contrasts with

the equatorial plane and it was decided that this difference was caused by the NMM containing a smaller volume of central plasma sheet than the equatorial plane and as a result, a larger proportion of magnetospheric tailward-lobe data was included in the NMM results than was included in the equatorial plane results.

Considering tailward and earthward flows together while looking cross all planes and substorm phases, the weighted mean velocity in the earthward direction is just higher than that in the tailward direction. When looking at earthward and tailward flows separately across all planes and substorm phases, it was found that the average earthward flow velocity was generally slightly higher than the average tailward flow velocity. When only considering the NMM plane, weighted-mean earthward velocities were found to be faster than tailward flows. The recovery phase had the largest earthward velocity (10.0 km s^{-1}), the expansion phase was the next fastest (9.7 km s^{-1}) and finally average earthward flows in the growth phase were the slowest (9.3 km s^{-1}). It was found that the weighted-mean tailward velocity was largest during the recovery phase (9.1 km s^{-1}), next fastest during the expansion phase (8.5 km s^{-1}) and slowest during the growth phase (8.1 km s^{-1}). The average earthward velocity results in the NMM were found to be a little higher than those in the equatorial plane for the same substorm phases, while tailward flows were slower in the expansion and recovery phases. Finally, very low average velocities were found throughout the substorm event, further highlighting that the explosive energetic nature of substorms mostly consist of slow ion flows, interspersed with short duration fast flow events.

The final area of discussion was the observation of average ion flow directions both in the NMM plane and outer planes for each substorm phase. First, earthward flows were discussed for the growth phase of the central NMM plane, and in general they appeared to be fairly ordered with few inconsistent deflections. In the northern hemisphere of the growth phase, earthward ion flows were predominantly sunward with stronger deflections present towards the northern terminator. In the southern hemisphere, generally the ion flows are deflected towards the southern flank. Tailward flows in the the growth phase generally exhibited a gently curved convective ion flow directed towards equatorial plane. The expansion phase had very similar flow patterns to the growth phase for both earthward and tailward ion flows, although deflections present are more consistently directed towards equatorial plane (tailward ion flow direction) and are occasionally stronger than in the growth phase. The earthward flow pattern during the recovery phase appeared to be the least deflected of the three substorm phases in the study and was dominated by sunward flows throughout, with only minor deflections toward the flanks. The tailward flows in the recovery phase perhaps present slightly more-pronounced signs of convective ion flow. In general, it is clear that deflections in the XZ plane across all substorm phases are small in comparison to those found in the XY plane. This shows that there

is possibly less plasma transported up and over the Earth in the Z-direction, with the system favouring transport around the sides of the Earth in the Y-direction instead.

When looking at the outer planes away from the NMM, the spatial coverage was severely limited and this was most noticeable on the dusk side. It was clear, especially when the low-count bins were neglected that generally for earthward flows, sunward flow dominated with slight deflections towards equatorial plane in the northern hemispheres. At equatorial plane, there is little deviation from the ions flows being directed roughly parallel to the x-axis. In the southern hemispheres, again earthward flows are predominantly directed sunward with minimal deviations from this. Tailward flows present more deflections with more deflections towards the flanks in the northern and southern hemispheres. The flows directed along equatorial plane are strongly aligned with the x-axis.

5.4.3.1 Key Results

There were a number of key original results shown in this section. Firstly in general there have not been any previous studies which study substorm intervals while considering ion moments of all velocities and focussing primarily on the XZ plane, the NMM. Following on from this, all results presented in this chapter are original and present a new set of results.

The first key original result was found when considering field-perpendicular earthward ion flows in the noon-midnight meridian plane, the recovery phase has the fastest average ion-flow velocity with the expansion phase being a little slower and the growth phase being the slowest. This follows the same pattern as in the equatorial plane and thus provides further new evidence in support of the results collected in the study carried out by *Kissinger et al.* (2012). This pattern is also repeated for the average tailward velocities. In addition, the tailward flows were generally also marginally slower than the earthward flows.

When looking at the average earthward ion flow velocities, the fastest average velocities was found during both the recovery and expansion phases, with both having an average V_{xz} of 9.5 km s^{-1}. The growth phase presented the slowest average earthward velocity of 8.7 km s^{-1}. When looking at the average tailward flow velocities, it was found that the recovery phase again had the highest value of 10.4 km s^{-1}, which the expansion and growth phases were a little slower with their average V_{xz}'s being measured at 10.0 km s^{-1} and 8.0 km s^{-1} respectively.

The next key original result was found while looking at the overall earthward ion-flow patterns in the equatorial plane. It was found that they were generally fairly symmetrical

about the equatorial plane, although deflections when present tended to be a little stronger in the southern hemisphere. Fro this it can be said that there were still some dawn-dusk asymmetries present across each of the substorm phases, although they were generally less distinct than in the XY planes. Across all three substorm phases the level of disorder appeared to be a good deal less than in the XY planes. The recovery phase again appeared to be the most ordered phase, although there isn't much difference between the three. In general, it is clear that deflections in the XZ plane across all substorm phases are small in comparison to those found in the XY plane. This shows that there is possibly less plasma transported up and over the Earth in the Z-direction, with the system favouring transport around the sides of the Earth in the Y-direction instead.

Chapter 6

Electron Flow in the Terrestrial Magnetotail

6.1 Introduction

Throughout the research presented in this thesis, it has become apparent that previous studies focus on ion moment data when discussing plasma flows, convection and transportation throughout the Earth's magnetosphere. However, positively charged ions are not the only particle which can be used for these studies. Electrons in principle can also be used as they too obey the rules of the frozen-in theory (section 2.4.3) and are confined to the same magnetic field lines as ions.

Perhaps a key reason why ion moments have historically been used for the study of plasma flows is that the bulk kinetic energy of electrons is smaller than their thermal energy and so when their energy distribution is measured, the thermal energy component dominated the results. This can be comparable to the magnitude of the spacecraft potential so the electrons are deflected (this affects their angle of arrival) and also low energy populations become hard to see. Ions on the other hand usually have bulk kinetic energy that is comparable to or larger than the thermal energy, so their bulk kinetic energy can be seen, which is up in the keV range, way above the spacecraft potential. Therefore in general it is easier to carry out measurements on ions. Once studies begin on one particular particle population type, if comparisons are to be made with previous studies, the only logical decision would be to use ion moments for a current study to enable the clearest and most comparable results. Furthermore, electron moments have not been used in the study of large scale magnetospheric plasma flows, even though the electron detectors used on more modern spacecraft are much more reliable. This Chapter will examine electron flows in the terrestrial magnetotail using Cluster's PEACE

field-perpendicular electron moment data to establish the possibility of recreating the magnetospheric plasma flow results found by the CIS ion instrument in Chapter 4.

One of the key Cluster mission objectives was to use its multi-point measurement capabilities to examine structures and events in finer detail as to determine behaviour at the smallest scales. While electron moments have not been used in large scale studies to examine plasma flows in the magnetotail, they have been frequently used in conjunction with other data sets to examine the properties of other magnetospheric phenomena for both short time-scale case studies and larger statistical studies. One such study was carried out by *Walsh et al.* (2011b) who focussed on the pitch angle distribution (defined in Section 2.3.1.1) of electrons and ions within the terrestrial magnetosphere, using data returned by Cluster's PEACE instrument in the 2002 tail season. Walsh found that ions followed the widely accepted picture; a boundary layer made up of earthward streaming and bidirectional field-aligned particles, which eventually gives way to a predominantly isotropic plasma sheet. The electron distributions are substantially different from the ionic picture. A boundary layer made up of bidirectional field-aligned electrons is observed, but it soon yields to perpendicular-dominated electrons close to the neutral sheet. Walsh's results suggest that in general, there is no extended, isotropic electron plasma sheet. A later study carried out by *Walsh et al.* (2013a) conducted a survey of electron pitch angle distribution properties in the magnetotail plasma sheet to investigate where the pitch angle electron anisotropy in this region originated from. Using PEACE electron data from the 2001-2006 tail seasons, Walsh found that during intervals of steady northward and southward IMF, a cold component of electrons that were frequently present produced a pitch angle anisotropy such that parallel differential energy flux dominates at sub-keV energies. Walsh suggested that the cold electrons originated from the ionosphere and that when the magnetosphere experienced steady northward IMF, they were transported to the plasma sheet by large-scale field-aligned current systems that connect the magnetosphere and ionosphere together. When the magnetosphere experiences steady southward IMF, the cold electrons are seen more frequently with a distribution pattern showing a dawn-dusk asymmetry. Under this IMF condition, it was not clear whether the ionosphere was still the source of these electrons and no specific transportation mechanism was defined. Another study carried out examining the pitch angle/energy distribution of anisotropic electrons in the Earth's magnetotail by *Artemyev et al.* (2014) utilized nine years of Cluster PEACE data. Artemyev found that there was no significant dependence of the anisotropic electron population on plasma flows and as a result, the local level of geomagnetic activity does not correlate with these populations.

While it appears no studies have directly used electron moments for the analysis of

magnetospheric plasma flows, the PEACE instrument team have carried out a cross-calibration between the CIS and PEACE instruments to verify the PEACE inter-anode correction factor *Fazakerley et al.* (2013). It was expected that the PEACE $V_{\perp z}$ parameter (the z-component of the field-perpendicular velocity vector) should be consistent with the convection velocity calculated by the CIS instrument and as such, the PEACE instrument team compared the $V_{\perp z}$ values calculated by the CIS-CODIF detector and the PEACE-HEEA detector by subtracting the latter from the first. The results obtained showed that the $V_{\perp ZPEACE}$ values were not perfectly correlated with the $V_{\perp ZCODIF}$, suggesting that either or both sensors do not provide the true value of $V_{\perp z}$. If the results from both instruments are perfect, then the difference between $V_{\perp ZPEACE}$ and $V_{\perp ZCODIF}$ values should be zero, or at least very close to it depending on whether differential flows associated with electric currents were present. In conclusion, some differences in the ion and electron flow patterns should be expected, although this should have been minimised by the calibrations applied to both CIS and PEACE instruments.

6.2 Data Selection, Organisation and Visualisation

The methodology for this chapter's study, as well as the organisation and visualisation of the data are essentially the same as for the first study described in Chapter 4; the only difference is that PEACE instruments field-perpendicular onboard moment data are now being used instead. It includes all relevant PEACE electron data flags as well as the magnetosheath and magnetospheric lobe removal procedures.

The PEACE instrument was operational on all four Cluster spacecraft during the investigation's time interval, this means that there should be a great deal more data available than there was from CIS. In addition, if it is possible to obtain similar results to those found in Chapter 4, then the data from both instruments could be used together, greatly improving the data coverage for future studies

6.3 Electron Flow in the XY Plane

6.3.1 Number Density

Plane (Z=nR$_e$)	N$_{earthward}$	N$_{tailward}$	N$_{total}$	% Earthward	% Tailward
12	115	187	302	38.1	61.9
9	52896	156155	205891	25.3	74.7
6	216071	508841	724912	29.8	70.2
3	318148	390528	708676	44.9	55.1
0	342294	396050	738344	46.4	53.6
-3	295985	306991	602976	49.1	50.9
-6	176083	276328	452411	38.9	61.1
-9	128584	472508	601092	21.4	78.6
-12	42465	15081	193279	22.0	78.0
-15	5835	16051	21886	26.7	73.3
Totals	1578476	2538720	4117196	38.3	61.7

TABLE 6.1: Field-perpendicular electron number density distribution for the XY plane across 13 cuts in the z-direction. The Z value given is the position on which the plane is centred on.

This section presents the spatial distribution of the field-perpendicular electron moments in the XY-planes, any figures not explicitly discussed in this chapter can be seen in Appendix D).

It was found that there is 1.66 times more electron data (N$_{e-total}$ = 4117196) available than ion data (N$_{i-total}$ = 1530362). This suggests that spatial coverage will be greatly improved and therefore the reliability of the results should be increased too. In addition, more data was collected in the southern hemisphere (1871644 counts) than the northern hemisphere (1639781 counts). There was greater spatial coverage of electron data than the ion dataset across all planes in the southern hemisphere than in the northern hemisphere; this means more bins are occupied in the negative XY planes than the positive ones. This spatial distribution mirrors the number of data points found in each hemisphere. It is possible that since the data is now coming from twice as many spacecraft, there will be a greater spatial coverage, so even when the spacecraft are relatively close together, they could easily span the boundary of spatial bins which perhaps were not previously entered.

When looking at the spatial distribution in the northern hemisphere, as seen with the CIS data, there is an asymmetrical data distribution with the greatest coverage found on the dawn side (example in Figure 6.1). The coverage recedes with distance away from the equatorial plane, in both dawn and dusk hemispheres. The distribution across each individual plane in the southern hemisphere is generally more sparse than the northern half, however due to the orbital trajectory, there are more planes populated to greater

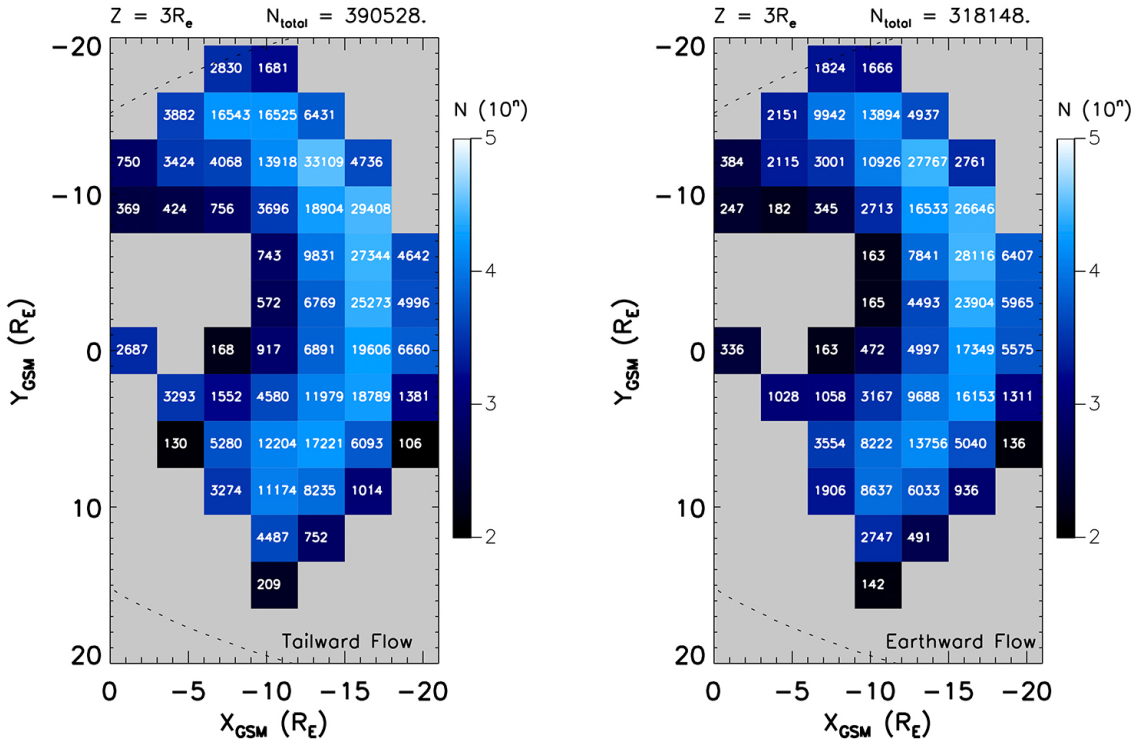

FIGURE 6.1: Field-perpendicular electron velocity number density plots displaying tailward (left) and earthward (right) plasma flow in the XY plane Z = 3±1.5 R_e.

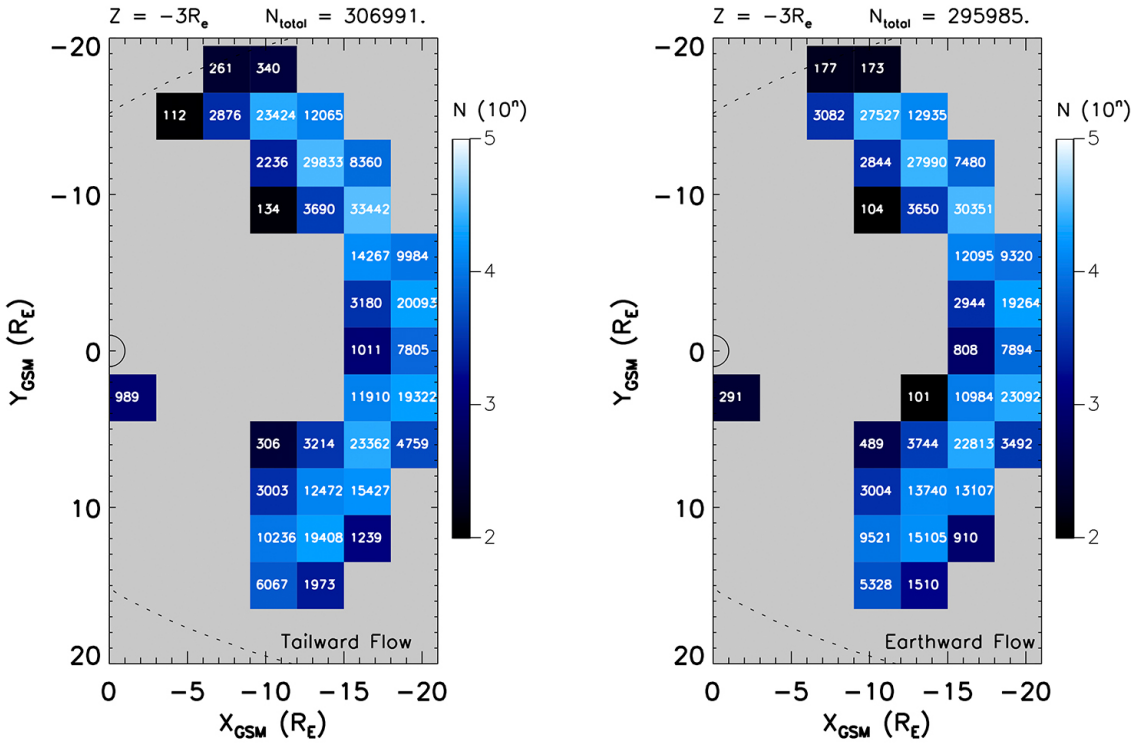

FIGURE 6.2: Field-perpendicular electron velocity number density plots displaying tailward (left) and earthward (right) plasma flow in the XY plane Z = -3±1.5 R_e.

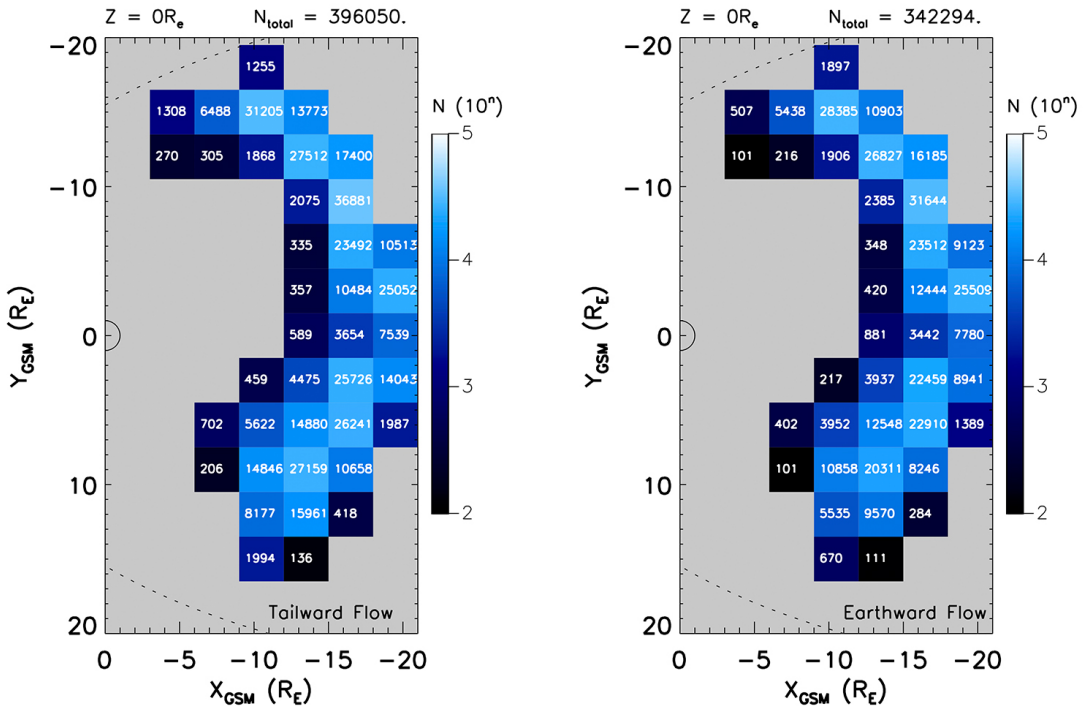

FIGURE 6.3: Field-perpendicular electron velocity number density plots displaying tailward (left) and earthward (right) plasma flow in the XY plane Z = 0±1.5 R_e.

distances from the equatorial plane. As with the CIS data set, the majority of data is concentrated at mid-to-distant tail regions, X < -9 R_E (example in Figure 6.2). The spatial coverage in this hemisphere generally increases out to the plane centred upon Z = -9 R_E before reducing again at further distances from the equatorial plane. In the plane centred about Z = -3 R_E, the spacial coverage is roughly symmetrical about the NMM. However this symmetry breaks down with distance from the equatorial plane with more data found in the dusk hemisphere. Eventually only the dusk hemisphere and the NMM remain occupied out to the plane centred upon Z = -15 R_E. For the equatorial plane, as with the CIS data set, the inner edge of the data distribution is the more sparsely populated, and the most densely occupied bins lying at radial and distances greater than about 10 R_E, with a couple of low density bins at the periphery of the dataset. These spatial distribution patterns and the number density gradient are both artefacts of the Cluster spacecraft trajectories. There is also a slight dawn-dusk asymmetric spatial distribution, while the number of bins occupied in each hemisphere are the same, the dawn side extends further out towards the magnetopause and the dusk side covers more area at closer in towards the NMM.

Looking at the tailward (left) and earthward (right) number density plots of Figure 6.3 along with Table 6.1, it can clearly be seen that on average, there is more tailward directed plasma flow than earthward flow; in fact tailward flow occurs 61.7% of the time.

This appears to be a somewhat unexpected result since when considering the results found in Chapter 4 looking at ion flows in the same region, earthwards flows were in fact dominant, occurring 56.0% of the time.

It is unlikely that the tailward dominance found in this chapter can be attributed solely to the inclusion of predominantly tailward-directed magnetospheric lobe and magnetosheath data considering much of it has been removed through the use of the Coxon and magnetosheath removal procedures. However since both methods are not perfectly accurate, there will be some data collected during these intervals included of course, although it is incredibly unlikely to have such a grand effect as seen here. Since both electrons and ions follow the frozen-in theory, although the results were not expected to be exactly the same, they were expected to be somewhat more similar than what was found. Delving deeper into how the data was distributed, it was found that every plane of the electron data collected showed tailward flow dominance, whereas for the ion data, the planes covering the region 4.5 R_E > Y > -7.5 R_E (containing the central plasma sheet) were dominated by earthward flows.

This flip in flow direction dominance across the two data sets presents a warning flag. On first inspection it is unclear what could be the cause of the tailward flow dominance. One possible reason could be down to the calibration of the instruments. The following section will investigate what could be happening with the data or the particles to create this disagreement in flow directions.

6.3.2 Electron Flow Investigation

It has been suggested throughout this thesis that the inclusion of additional lobe data within the equatorial plane could be the reason for the large proportions of tailward flow seen in this plane. This investigation was carried out in order to establish what is causing the tailward electron flow dominance found in this plane; whether it is still due to extra lobe data being included because the planes extend out to |Z| = 4.5 R_E rather than the suggested |Z| = 4 R_E from Zhang's idealised plasma sheet dimensions; or whether a different reason for this result is present.

The study carried out by *Zhang et al.* (2015a) has been discussed in detail in Chapter 4, however, one element of the study has yet to be evaluated. The paper utilises ion data from the CIS HIA instrument on the Cluster 3 spacecraft from 2001 to 2006. The paper shows that on average, there is more earthward than tailward plasma flow with the most data situated at around X = -16R_e (Figure 6.4).The data constraints explicitly described by Zhang and implemented for his ion data selection are shown below:

- Spatial restraints of -19 R_e <X < -10 R_e, -10 R_e < Y < 10 R_e and -4 R_e < Z < 4 R_e. This defines the effective plasma sheet.
- The duration of earthward/tailward flows (V_x >0 / V_x < 0) exceed three minutes. Used to eliminates short term flow direction fluctuation.
- B_z >0. Ensures that no data contained within tailward-moving plasmoids and data tailward of the x-line are included.

Two further data constraints were inferred from the *Zhang et al.* (2015a) paper but could not be verified as to whether they were actually implemented as the discussion within the paper was limited as were communications with the author. The additional criteria are provided below:

- A slow-flow velocity cutoff was implemented. While the value was not explicitly mentioned, Zhang used the *Angelopolous et al.* (1993) paper as a reference which founda slow ion flow value of 50 km s^{-1}.
- $\beta > 0.1$. Again it was not explicitly mentioned that this cutoff was used, however when Zhang was discussing the effective plasma sheet region used in the study, he had the plasma beta value in brackets. From this inference, it was also used.

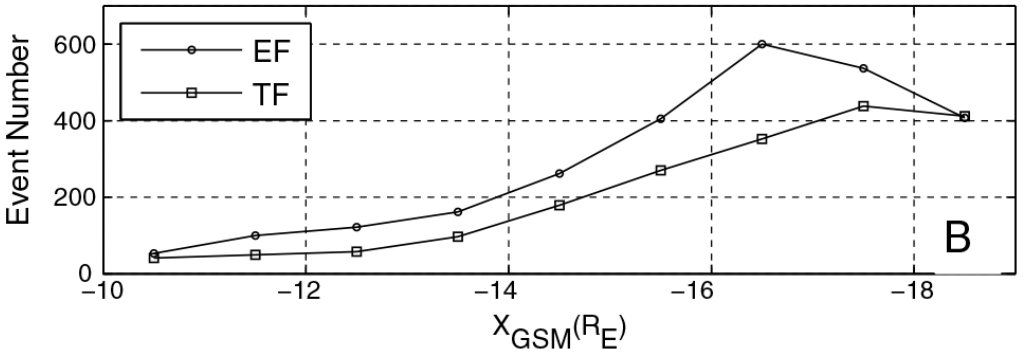

FIGURE 6.4: Case numbers of tailward Flow/earthward flow as a function of X_{GSM} (*Zhang et al.*, 2015a).

The earthward-tailward flow distribution plot is a useful way to distinguish which flow direction is dominant and as such it was decided to create one for the electron data set. It was important to ensure the accuracy of the results, therefore Zhang's plot was recreated first. The ion moment data was binned into smaller 1 R_E bins in the x-direction and the data-constraints discussed above were applied to the data set. The final plot is seen in 6.5.

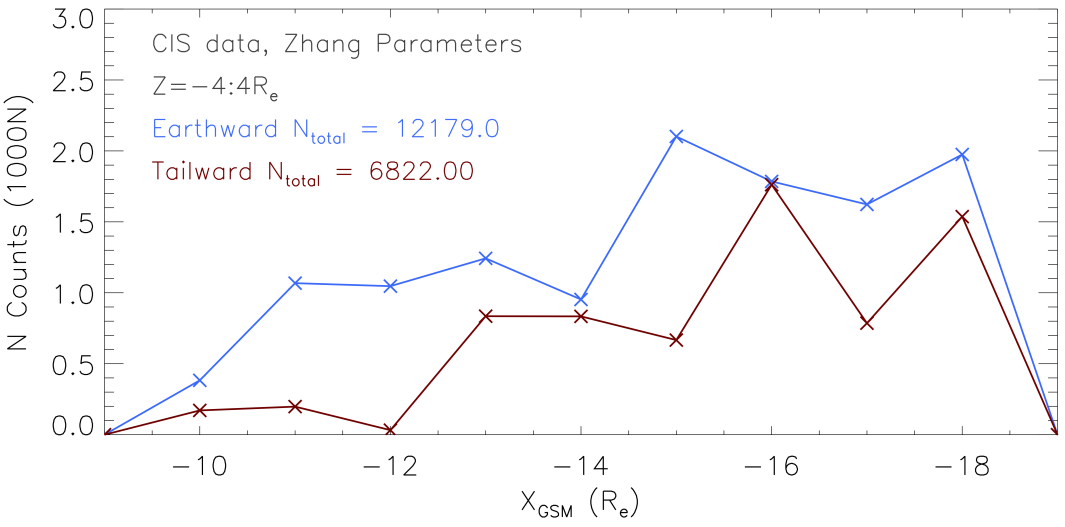

FIGURE 6.5: Plasma flow direction distribution plots using Zhang's parameters and CIS ion data. Shows the number of data counts as a function of X_{GSM} for the region -4 R_e < Z <4 R_e.

Both figures 6.4 and 6.5 use four second spin-resolution data, however there is clearly a fairly large difference in counts across the plots with Figure 6.5 generally having up to around 10-times more counts at some distances from Earth. It is believed that this disparity stems from the fact that Zhang was not perfectly clear which data selection criteria were used to generate his results. From this, they needed to be inferred from what was discussed in his paper (*Zhang et al.*, 2015a). The initial plot create (not shown here) only using the data selection criteria explicitly discussed in the paper resulted in having up to around 25-times more counts at some distances from Earth, clearly something was missing. A more careful read of the paper lead to the inference of the fourth and fifth data criteria (shown above) which may have been used. It was implement them into the study. They brought the counts down somewhat closer to Zhang's results (Figure 6.5).

Clearly the two figures (6.4 and 6.5) are not exactly the same, although the plot created as part of this study shows earthward flow dominance throughout, as Zhang's does. A notable difference is that Zhang's figure is much smoother than the recreated plot; the counts in both earthward and tailward curves increase consistently with distance up to about 16.5 R_E. On the other hand, while the counts in the recreated plot also increase with distance, it is much less consistent. Overall, the recreated plot does follow the same trend as the original Zhang plot and therefore it is adequate for the investigation.

The next step in the investigation was to use the same procedure made to recreate Zhang's event number plot to produce the electron flow direction distribution plot. Only PEACE data from C3 was used to do this and the result can be seen in Figure 6.6. The aim was to establish how the earthward and tailward plasma flows are distributed

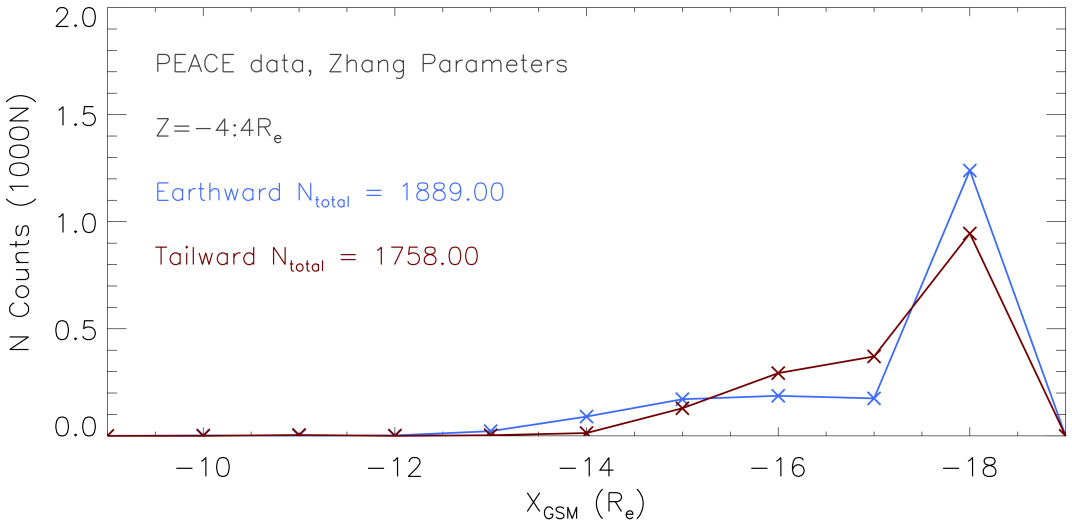

FIGURE 6.6: Plasma flow direction distribution plots using Zhang's initial and additional parameters, and PEACE electron data. Shows the number of data counts as a function of X_{GSM} in the region -4R_e <ZR_e <-4R_e.

and whether one flow direction is significantly dominant over the other as well as how it compares with the ion data plot. It was found that there was about 5 times less data available when using PEACE data than CIS data, a somewhat peculiar result since there was considerably more PEACE data available (when combining data from all four spacecraft) that CIS data (when combining data from the C1 and C3 spacecraft). However, after some further examination, the disparity found was likely to do with how much data each individual spacecraft collected. There was about 16×10^6 raw data counts available from the CIS instrument on Cluster 3 and there was about 1.7×10^6 raw data counts available from the PEACE instrument on Cluster 3. In general it was found that for the CIS instrument C3 was the greatest ion data contributor while for the PEACE instrument, C2 provided the greatest amount of electron data, considerably more than C3.

Looking at Figure 6.6, which includes all of Zhang's data cutoffs, it can be seen that earthward flows tend to dominate more often than tailward flows. This appears to be the opposite result than what was presented at the beginning of this chapter. However, if the velocity cutoff of 50 km s^{-1} is removed from the dataset, it is clear from Figure 6.7 that tailward flows quickly become dominant. It can be assumed from this pair of figures that the tailward flow occurrence dominance seen in Table 6.1 comes predominantly from flows with velocities less than 50 km s^{-1}. Looking back at Figure 6.6, tailward and earthward flows are almost non-existent in the region of x > -13 R_E. Counts begin to increase with distance from the Earth with earthward flows dominating the region -13 > x > -15.25 R_E, tailward flows then dominating the region -15.25 > x > -17.5 R_E before both peaking at x = -18 R_E.

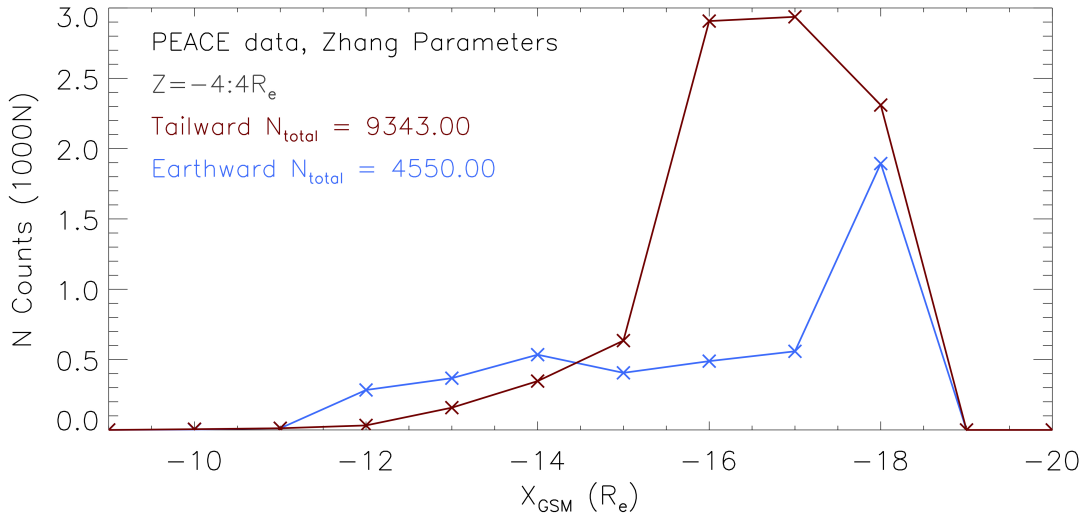

FIGURE 6.7: Plasma flow direction distribution plots using Zhang's initial parameters and PEACE electron data. Shows the number of data counts as a function of X_{GSM} in the region -4R_e <ZR_e <4R_e.

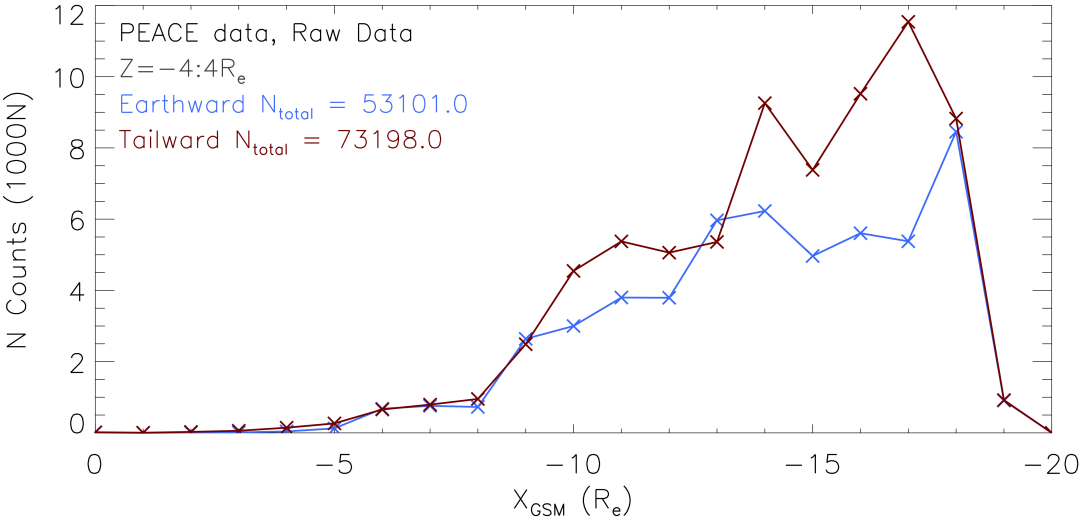

FIGURE 6.8: Plasma flow direction distribution plots using only raw PEACE electron data. Shows the number of data counts as a function of X_{GSM} for the region -4 R_e < Z <4 R_e.

One possible reason for the flow direction disparity could be that one of Zhang's data parameters not used in the main investigation, could have been the cause of the discrepancy. In order to establish whether this was the case, an earthward-tailward flow distribution plot was created without the application of Zhang's parameters using PEACE electron data, Figure 6.8. Across the X-range, it is clear that tailward flow is dominant throughout with the number density peaking at -14R_e and at -17R_e.

This result shows that one of the parameters is not the cause of the flow direction difference. Another possible reason for the observed flow direction disagreement could

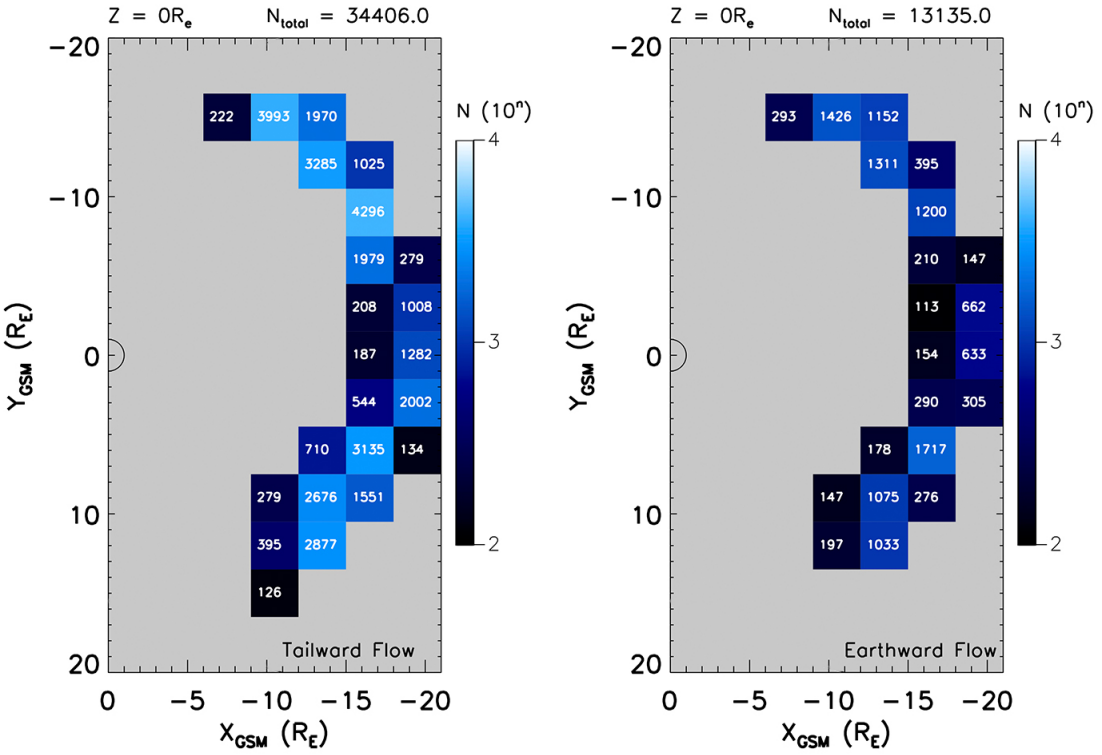

FIGURE 6.9: Electron bulk velocity number density plots displaying tailward (left) and earthward (right) plasma flow in the XY plane. Z = 0±1.5 R$_e$.

stem from the conversion from bulk-velocity moments to field-perpendicular moments within the PEACE dataset. To test whether this had a significant effect, a number density plot for the central-most plane was created using PEACE bulk velocity moments, which can be seen in Figure 6.9. It is clear that tailward flows are still dominant, occurring 72.4% of the time. This very quick check indicates that the flow direction disagreement was not caused by using different velocity moments.

Overall, it is still not clear what could have been the cause of these intriguing flow direction results, although the change in flow direction occurrence dominance between Figures 6.6 and 6.7 due to the inclusion of the 50 km s^{-1} velocity cutoff is the strongest indicator that perhaps the ratio between fast (greater than 50 km s^{-1} in this instance) and slow flows (less than 50 km s^{-1}) could differ quite significantly between the CIS and PEACE datasets.

On final possible reason for the flow direction dominance discrepancies could be due to some unresolved issue with the raw PEACE on-board moment data sets. A study carried out by *Geach et al.* (2005), applying a numerical method to correct spacecraft on-board-calculated electron moments found that generally, the magnitude of the velocity require some correction in the solar wind and lobe/plasma sheet regions, where the overall correction value can be dominated by the velocity estimation parameter in their

procedure. It is clear then that while the results presented throughout this thesis have not been reported before, other studies have pointed out that there are some issues with the initial PEACE on-board moment data sets. Finally, following communications with the Cluster instrument's primary investigator (PI) it was assumed that this data discrepancy has not been previously raised and therefore is a new finding.

6.4 Summary

The majority of the electron sample count distribution results mirror the spatial results seen in Chapter 4 although there was generally much more data available as all four Cluster spacecraft provided PEACE electron moments. The main finding in this chapter was found when comparing earthward and tailward flows across all of the XY planes; it was found that tailward electron flows were dominant for every plane, even for the central three planes, which when the same investigation was carried out using ion moment data (Chapter 4), earthward ion flow occurrence rates were dominant. This result seemed particularly peculiar and as such, a series of investigations were carried out to establish what could have been the cause of this flow direction disparity.

The first section investigation carried out was to recreate the ion flow distribution figure (6.4) from the study carried out by *Zhang et al.* (2015a). This was done to ensure the procedure used in this thesis was as close as possible to that used by Zhang. While both plots clearly showed overall earthward flow dominance across the whole region, there was up to 10 times more data at some distances from Earth. This was almost certainly due to the fact that from the discussion in Zhang's paper, it was not perfectly clear exactly which data selection criteria he used, thus there was an element of uncertainty when recreating his plot.

The second part of the investigation carried out was to compare Zhang's ion flow distribution figure to the same plot created using PEACE electron moment data, Figure 6.6. It was found that there was about 5 times less data available when using PEACE data than CIS data. While initially this was somewhat surprising, after looking at the raw data availability, it was clear that there was about 9 times more raw data available from the CIS instrument than the PEACE instrument on the Cluster 3 spacecraft. Interestingly, after applying all of Zhang's data cutoffs, earthward flows tended to dominate more often than tailward flows. This appeared to be the opposite result than what was presented at the beginning of this chapter. However removing the 50 km s^{-1} velocity cutoff produced Figure 6.7. It was instantly clear that tailward flows once again dominate, from this it can be assumed that the tailward flow occurrence dominance seen in Table 6.1 comes predominantly from flows with velocities less than 50 km s^{-1}. In

general this result highlighted that the flow direction disparity was not an artefact of the procedure in which the ion moment data had been processed in Chapter 4. To further this, another flow distribution plot was made using the raw unprocessed PEACE electron moments (Figure 6.8) to establish whether the Zhang parameters had any influence on the result. Again, tailward flows were seen to be dominant and as such, the reason for the flow direction disparity was tending towards the data set, rather than the data processing. One final investigation was carried out to evaluate whether the observed flow direction disagreement could stem from the conversion from bulk-velocity moments to field-perpendicular moments within the PEACE dataset. Another figure was created using CIS bulk velocity moments and the results can be seen in Figure 6.9. It is clear that tailward flows are still dominant, hence the use of PEACE field-perpendicular electron moment data was also not the cause of the flow direction disparity.

The interesting results found in this chapter combined with the results found in Chapter 4 (which are in general agreement with a multitude of similar magnetospheric plasma flow studies carried out in the past), suggest that the difference in flow-direction dominance between Figures 6.5 and 6.7 could be caused by a couple of factors. The first being that the tailward flow dominance descends from a large volume of slow flow in that direction, with the fast flows occurring more in the earthward direction. A second reason for the flow-direction difference could descend from the PEACE dataset rather than the way in which the data has been processed. A study carried out by *Geach et al.* (2005), applying a numerical method to correct spacecraft on-board-calculated electron moments found that generally, the magnitude of the velocity required little correction, although they went on to conclude that this is not true in the solar wind and lobe/plasma sheet regions, where the overall correction value can be dominated by the velocity estimation parameter in their procedure. Their conclusions with regards to the accuracy of the electron moments collected in the plasma sheet suggested that the reliability or consistency of the electron moments could be questionable at times where the velocity estimation parameter was dominant. After communications with the Cluster instrument's primary investigator (PI) it was assumed that this possible data discrepancy has not been previously raised and therefore is a new finding, requiring further investigation in the future.

Chapter 7

Summary and Further Work

7.1 Ion flow in the Terrestrial Magnetosphere

This study has examined the spatial distribution and plasma dynamics within the terrestrial magnetosphere using Cluster observations. The dynamics and flow behaviour of plasma are fundamental properties of the magnetosphere and determining the properties of ion and electron flows within the magnetosphere can provide valuable insight into energy and moment transport throughout the system as well as improving the picture of the general behaviour of the magnetosphere as well as during energetic substorm event. This chapter will review the results found throughout this study and look at possible ideas to improve and extend it in the future.

7.1.1 Ion Flow in the XY Plane

7.1.1.1 Sample Counts

Using perpendicular ion velocity moment observations collected by the CIS instrument on-board Cluster 1 and Cluster 3 spacecraft, key ion distribution and flow characteristics were obtained when initially looking at the XY planes. The initial investigation was carried out to establish confidence in the procedures used by attempting to recreate observations which have previously been reported.

When taking observations in the XY plane, it was found that there are much more ion velocity data available in the northern hemisphere than the southern hemisphere. When considering the Cluster spacecraft trajectory, one would expect the opposite to found, however, much of the most southerly data was removed due to contamination with data collected in the magnetosheath and lobe. There was further data asymmetry between

the dawn and dusk hemispheres about the equatorial plane, although this effect was more prolific in the northern hemisphere with this distribution appearing more symmetrical in the southern hemisphere. When looking at the most commonly studied plane, the central equatorial plane ($z = 0 \pm 1.5\,R_E$, it can be seen that the most densely populated bins are at radial distances greater than $10\,R_E$, a phenomena which is believed to be an artefact of the spacecraft orbit. The final key observation made when considering the sample count plots was that there was a greater occurrence of plasma flow in the earthward direction than there was in the tailward direction. Previous studies (*Juusola et al.*, 2011; *Zhang et al.*, 2015a) generally agree with this.

This study generally provides a unique set of results as not only does if focus on magnetospheric convection through the use of the perpendicular ion velocity component (the most similar previous studies by *Juusola et al.* (2011) and *Zhang et al.* (2015a) use bulk ion flow), it also includes all magnetotail data rather then using narrow bands of data in the XY and XZ plane as Zhang and Juusola do respectively. This allowed the analysis of a much larger magnetospheric area, providing a much better picture of the global behaviour of ion flows on the nightside of the Earth.

7.1.1.2 Ion Flows in the XY Plane

When investigating ion flow velocity and direction, it was found that the weighted-mean average perpendicular tailward ion flow velocity of V_{xy} = -6.4 $km\,s^{-1}$ dominated across all planes. Overall, 94.9% of all ion flows were found to have velocities lower than $100\,km\,s^{-1}$, a result which almost exactly agrees with the *Juusola et al.* (2011) study. When treating earthward and tailward flows separately, it was found that the average earthward and tailward field-perpendicular ion flow velocity was $19.1\,km\,s^{-1}$ and $28.6\,km\,s^{-1}$ respectively. The combination of these ion velocity results highlight that on average over large time scales, the magnetosphere appears to be a fairly slow moving system interspersed with bursts of energetic fast flows, a finding which again has been previously reported.

Finally a dawn-dusk asymmetry of ion flow is prominent in the most central planes. While strong flow deflections are present at greater distances from the equatorial plane, the asymmetry breaks down. Tailward ion flows certainly dominate in the outer regions. For planes above the equatorial plane with positive z-positions, the deflection of tailward flows appear greater than the earthward flows.

The key results in this section were essentially supporting the results from previous studies (*Juusola et al.*, 2011; *Zhang et al.*, 2015a) and therefore at first glance do not appear to bring anything new to the table. However it must be remembered that the

most similar previous studies used bulk-ion velocity moments, not perpendicular-velocity moments and as such, the results are a new alternative outlook which come to the same conclusions. This study also reaches out in the much greater areas above and below the equatorial plane then previous studies and thus the flow behaviour here has not previously been reported on in any great detail.

7.1.1.3 Key Original Results

The key results in this section were essentially supporting the results from previous studies (*Juusola et al.*, 2011; *Zhang et al.*, 2015a) and therefore at first glance do not appear to bring anything new to the table. However it must be remembered that the most similar previous studies used bulk-ion velocity moments, not perpendicular-velocity moments and as such, the results are a new alternative outlook which come to the same conclusions. This study also reaches out in the much greater areas above and below the equatorial plane then previous studies and thus the flow behaviour here has not previously been reported on in any great detail.

7.1.2 Ion Flow in the XZ Plane

7.1.2.1 Sample Counts

When taking observations in the XZ plane, it was found that there are more ion velocity data available in the dawn hemisphere than the dusk hemisphere, except for the region between y = 1.5 R_E and y = 7.5 R_E where the opposite is true. It was also found that on the dawn side, more bins are occupied in the north, whereas on the dusk side, more bins are occupied in the south. This data distribution is likely caused by the orbital inclination in the YZ plane, creating this seasonal effect. In general, there were found to be more earthward flows than tailward flows across all of the XY-planes. However in the central three planes tailward-directed ion flows occurred more frequently than earthward flows. This is likely due to there being less plasma sheet data contained within each XZ-plane in comparison to the XY-plane plots and potentially proportionally more contaminant magnetosheath and tail-lobe data being contained within each plane. Beyond z = $\pm$ 4.5 R_E earthward flow dominates. This result suggests that the *Zhang et al.* (2015a) underestimated the size of the plasma sheet in the y-direction and as such provides strong evidence that at times the plasma sheet can extend out as far as 19.5 $_E$ in y-direction and extrapolating this, it could be said that during these periods, the magnetosphere could stretch as wide as 39 $_E$. Of course it is a dynamic such the plasma

sheet boundaries are not static, expanding and contracting with varying magnetospheric conditions.

7.1.2.2 Ion Flows in the XZ Plane

When investigating ion flow velocity and direction it was found that tailward flow velocity dominates with an overall ion flow velocity of V_{xz} = -4.1 km s^{-1} across all planes. This is 2.3 km s^{-1} greater than the average velocity in the XY planes, such a small difference indicates that V_x is the dominant velocity component throughout the magnetotail. In general, this result strengthens the idea that on average, over large time-scales, the magnetosphere is rather slow-moving system.

Considering the tailward and earthward flows separately, it was found that the average tailward flow velocity (34.6 km s^{-1}) is a good deal higher than the average earthward flow velocity of 19.9 km s^{-1}. These velocities are higher than the equivalent velocities in the XY planes, and as such, it shows that overall, $V_z > V_y$. This evidence suggests that ion flow is influenced most in the z-direction. Looking at the central three planes, tailward flow is still a little faster, on average 14.3 km s^{-1} compared to the average earthward flow of 13.1 km s^{-1}. These results are in contrast with a previous study by *McPherron et al.* (2011) who found the opposite occurred, however he did not include slow-flow ion data as the study in this chapter did. Finally, when looking at the weighted-average ion flow velocity in the magnetotail when disregarding flow direction, the result was found to be $|V_{xz}| = 26.4$ km s^{-1}. This result is much slower than the 50 km s^{-1} average found by *Baumjohann et al.* (1989)). These differences are almost certainly due to the data selection criteria used.

The ion flow patterns throughout the XZ planes do display some north-south asymmetries, although in the noon-midnight meridian plane (centred on y = 0 R_E), the earthward flow pattern is fairly symmetrical about equatorial plane with reasonably strong deflections away from the equatorial plane in both the northern and southern hemispheres. At the equatorial plane the flows are predominantly sunward. It was found that earthward flows were somewhat more disturbed and much less uniform in direction on either side of the EQ plane in comparison to the study carried out by *Zhang et al.* (2015a). However right along the equatorial plane, the flows were much more uniform and in line with Zhang's findings. When observing the tailward flow, evidence was present for north-south asymmetries, with the deflections towards equatorial plane somewhat stronger in the northern hemisphere than the southern hemisphere. There is also further evidence for flow reflection in the equatorial plane with the anti-sunward

plasma flow being present in the same plane as the sunward earthward flows. When comparing these results with *Zhang et al.* (2015a), again more tailward ion flow-deflections were found to be stronger and thus the new results show a much more disturbed system.

Looking away from the noon-midnight meridian plane into the dawn and dusk hemispheres, asymmetrical ion flow can be seen throughout. Considering the dawn hemisphere, earthward flows in the region surrounding the equatorial plane where y = -3 ± 1.5 R_E are minimally deflected. At the northern and southern terminators, the deflections are more prominent towards the flanks. The further away from the noon-midnight meridian observations are taken, the more reduced the deflections become. This flow pattern is repeated across the dawn hemisphere. In the dusk hemisphere, earthward flows in the northern hemisphere of plane y = 3 ± 1.5 R_E are mostly sunward with minimal deflections and the southern hemisphere presents stronger deflections towards the southern flank. Across the rest of the dusk hemisphere, the flow pattern is much the same with the deflections in the southern hemisphere generally reducing with distance from the NMM. As with the dawn hemisphere, tailward flows in the dusk hemisphere exhibit a more symmetrical ion flow pattern about the equator and directed towards it. Further out into the dusk hemisphere, the tailward ion flow deflections quickly dissipate resulting in a predominantly anti-sunward flow pattern.

7.1.2.3 Key Original Results

There were a number of key original results shown in Chapter 4. Firstly it was found that there were large earthward flow occurrence rates found at greater y-positions along the equatorial plane during the study of the XZ planes. These results provide strong evidence that at times the plasma sheet can extend out as far as 19.5 R_E in y-direction and extrapolating this, it could be said that during these periods, the magnetosphere could stretch as wide as 39 R_E. While it has been generally agreed that the plasma sheet covers the extent of the magnetosphere out to the magnetosheath, few studies have discussed the physical size of this region and all the most similar studies have focused on the use of bulk rather than perpendicular velocity moments.

The next key result is that on average, ion flows were much slower than those from in previous studies such as *Baumjohann et al.* (1989). When considering similar magnetotail volumes, the average ion flow velocity was found to be around 70% slower than Baumjohann. These differences are almost certainly due to the data selection criteria used by Baumjohann. His study only incorporated four months worth of data, only focused on the region containing the central plasma sheet and used bulk-ion velocity

moments. The study presented in this chapter used 6 years of perpendicular ion velocities moments collects across the entire magnetotail. In addition ion flows appeared to be more turbulent than those found in the *Zhang et al.* (2015a) study, who again used bulk ion velocity moments rather than perpendicular ion velocity moments.

Another key result is that when looking at the central region about the NMM, tailward flow is faster than earthward flows. These results contrast a previous study by *McPherron et al.* (2011) who found earthward flows were faster. However he did not include slow-flow ion data as the study in this chapter did. Thus a new result of tailward flows are on average marginally faster than earthward flows in the central region about NMM when considering all ion flow moment vectors.

The final key result presented in this chapter was the fact that asymmetrical ion flow patterns were found out away from the the NMM. This is new as there have been no previous studies that have looked at the north-south planes this far out into the y-direction of the magnetosphere before.

7.2 Magnetospheric Ion Flow During Substorm Phases

7.2.1 Ion Flow in the XY Plane during Substorm Phases

7.2.1.1 Sample Counts

This section reviews the second investigation, looking at ion flows in the magnetotail during the three substorm phases. When looking at all XY planes across all of the substorm phases, it was found that earthward flows had a higher occurrence rate than tailward ion flows. When just considering the equatorial plane, earthward flow dominates across all substorm phases with the recovery phase possessing the largest number of sample counts, followed by the expansion phase and finally the growth phase. When looking at previous studies, these results agreed with *Kissinger et al.* (2012), but not with *Juusola et al.* (2011) who found there to be slightly more fast earthward flows in the growth phase than the expansion phase. When looking at the data distribution for each substorm phase, it was found that the growth phase had a larger proportion of earthward flow than tailward flow occurrence. The expansion phase is the most balanced phase with regards to flow direction and has the largest proportion of tailward flows across all phases. Finally, the recovery phase has the largest proportion of earthward flow in comparison with the other two substorm phases. These results provide a good representation of how the magnetotail behaves during substorms and provides additional original support for Kissinger's 2012 study.

7.2.1.2 Ion Flows in the XY Plane

Across all planes and substorm phases, velocity in the earthward direction dominates with V_{xy} across all planes in both flow directions is 1.5 km s^{-1} during the growth phase, 0.6 km s^{-1} during the expansion phase and 1.7 km s^{-1} during the recovery phase. In the equatorial plane for each substorm phase, the earthward and tailward velocities are generally higher than the outer planes, with the weighted-mean earthward-flow velocity dominating in each phase. When looking at earthward and tailward flows separately across all planes and substorm phases, it was found that the average earthward flow velocity was generally smaller than the average tailward flow velocity in the expansion and recovery phases. The growth phase has the slowest average earthward and tailward flows, the expansion phase has slightly faster average earthward and tailward flows than the growth phase, and the recovery phase has equally fast average earthward flows (to the expansion phase) and the fastest tailward flows.

When only considering the equatorial plane, it was found that the average tailward velocity was largest during the expansion phase (16.5 km s^{-1}) and smallest in the growth phase (12.0 km s^{-1}). It was found that the recovery phase had the largest earthward velocity (16.8 km s^{-1}) and the growth phase had the slowest (14.6 km s^{-1}). These earthward average-velocity substorm-distribution results were in agreement with *Kissinger et al.* (2012). However they were slightly different to the results found by *Juusola et al.* (2011), who found that the expansion phase had the largest average earthward velocity, followed by the recovery phase and finally the growth phase. This disagreement could be due to the way that data was binned and organised as there was only 1% difference between the amount of slow flows Juusola found in the expansion and recovery phases. In general, all three studies agree on the very low average velocities throughout the substorm event, further highlighting that the explosive energetic nature of substorms mostly consist of slow ion flows, interspersed with short duration fast flow events.

Finally observations were carried out on the average ion flow directions across all planes for each substorm phase. In the equatorial plane, the growth phase earthward-flow pattern presenting some dawn-dusk asymmetry as well as appearing to be the most disordered substorm phase. The expansion phase appeared to be a little more ordered than the growth phase and possessed further evidence of dawn-dusk asymmetry. There were more deflections in the dusk hemisphere than in the dawn hemisphere were flows were predominantly sunward. The results here were generally more ordered than the equivalent results in the *Kissinger et al.* (2012) study. The earthward flows during the recovery phase were the most ordered of the three substorm phases, with the dawn hemisphere presenting mostly sunward ion flows with slight dawnward deflections. The dusk also showed mostly sunward flows, but with slightly more duskward deflections.

Still looking a the equatorial plane, tailward flows in the growth phase were found to be gently deflected at the dawn-edge towards the NMM. In the dusk hemisphere, within 15 R_E from Earth, the flow is predominantly anti-sunward with only a little deviation from this. Beyond 15 R_E from Earth, flows quickly turned towards the NMM. Tailward flows in the expansion phase again appeared to be more ordered than the growth phase, although in the dawn hemisphere, deflections were consistently directed towards the the NMM. In the dusk hemisphere, again a mix of anti-sunward and strong deflections towards the NMM were observed. Finally, the recovery phase appeared to be the most ordered substorm phase. In the dawn hemisphere there is clear split between ions flows being somewhat parallel to the NMM and others deflected towards the NMM. At the NMM, the flow direction is mainly deflected towards the dawn flank beyond 15 RE. In the dusk hemisphere, strong deflections towards the NMM are present throughout. Looking at the outer planes, away from the equatorial plane, the spatial coverage was severely limited and as such it was difficult to make specific meaningful conclusions for each substorm phase. Overall when looking at the outer planes, across all the substorm phases earthward flows consistently show deflections towards the dawn and dusk flanks while tailward flows tend to present deflections towards the NMM.

7.2.1.3 Key Original Results

There were a number of key original results shown in this Section 5.3. Firstly in general there have not been any previous studies which study substorm intervals while considering ion moments of all velocities, although there have been two which looked at fast flow ion moment during these intervals, *Kissinger et al.* (2012); *Juusola et al.* (2011). following on from this, all results presented in this chapter are original and present a new set of results. With regards to tailward flows, the recovery phase presents the fastest weighted-mean average ion velocity, with the expansion phase being a little slower and the tailward flow in the growth phase being the slowest.

The first key original result was found when considering field-perpendicular earthward ion flows in the equatorial plane, the recovery phase has the fastest average ion-flow velocity with the expansion phase being a little slower and the growth phase being the slowest. This result agrees with but does not repeat the results presented by *Kissinger et al.* (2012), who found the same pattern when studying the relative proportions of fast flow moments (> 200 km s^{-1}). A similar study to Kissinger, carried out by *Juusola et al.* (2011), found the the average fast-flow earthward ion moment velocity to be slightly greater in the growth phase than the expansion phase, although there was on

a 1% velocity difference. Again this study used a different dataset, utilising ion bulk-velocity moments and neglecting slow-flows, as well as applying an aberrated coordinate system, thus the result presented in this chapter is unique.

The next key original result was found while looking at the overall earthward ion-flow patterns in the noon-midnight meridian plane. It was generally seen that there were dawn-dusk asymmetries present across each of the substorm phases with a good deal more deflections towards the flank in the dusk hemisphere than the dawn hemisphere. This was not presented in the study carried out by *Kissinger et al.* (2012) who reported a good deal of disorder in the fast flow patterns. It was also noted that in comparison to Kissinger's study, the ion flows generally appeared to follow a much more discernible flow pattern and possessing somewhat more order throughout.

All of the tailward ion-flow results presented in the chapter are essentially new results since there have been other studies discussing them in any great detail. Thus all the results summarised in section 5.3.2.2 are new.

7.2.2 Ion Flow in the XZ Plane during Substorm Phases

7.2.2.1 Sample Counts

When looking at all XZ planes across all of the substorm phases, it was found that the recovery phase has the smallest proportion of tailward ion flow and the largest proportion of earthward ion flows. The expansion phase proportionally has the lowest earthward ion flow occurrence rate and thus the highest proportion of tailward ion flows. The orbital trajectory of the Cluster spacecraft can be seen within the data and there is more spatial coverage across all substorm phases in the dawn hemisphere and with it, more coverage in the northern hemisphere than in the dusk hemisphere. Looking at all planes and substorm phases, there was more earthward data collected than tailward plasma flow data. When only considering the NMM plane, tailward flow dominates across all substorm phases. This contrasts with the equatorial plane and it was decided that this difference was caused by the NMM containing a smaller volume of central plasma sheet than the equatorial plane and as a result, a larger proportion of magnetospheric tailward-lobe data was included in the NMM results than was included in the equatorial plane results.

7.2.2.2 Ion Flows in the XZ Plane

Considering tailward and earthward flows together while looking cross all planes and substorm phases, the weighted mean ion velocity in the earthward direction is just higher than that in the tailward direction. When only considering the NMM plane, weighted-mean earthward velocities were found to be faster than tailward flows. The recovery phase had the largest earthward velocity (10.0 km s^{-1}), the expansion phase was the next fastest (9.7 km s^{-1}) and finally average earthward flows in the growth phase were the slowest (9.3 km s^{-1}). It was found that the weighted-mean tailward velocity was largest during the recovery phase (9.1 km s^{-1}), next fastest during the expansion phase (8.5 km s^{-1}) and slowest during the growth phase (8.1 km s^{-1}). The average earthward velocity results in the NMM were found to be a little higher than those in the equatorial plane for the same substorm phases, while tailward flows were slower in the expansion and recovery phases. Finally, very low average velocities were found throughout the substorm event, further highlighting that the explosive energetic nature of substorms mostly consist of slow ion flows, interspersed with short duration fast flow events.

The final area of discussion was the observation of average ion flow directions both in the NMM plane and outer planes for each substorm phase.

Looking at the growth phase of the central NMM plane, earthward flows appeared to be fairly ordered with few inconsistent deflections. In the northern hemisphere, earthward ion flows were predominantly sunward with stronger deflections present towards the northern terminator. In the southern hemisphere, they are generally deflected towards the southern flank. Tailward flows in the the growth phased generally exhibited a gently curved convective ion flow directed towards the EQ plane. The expansion phase had very similar flow patterns to the growth phase for both earthward and tailward ion flows, although deflections present are more consistently directed towards the EQ plane (for tailward ion flows) and are occasionally stronger than in the growth phase. The earthward flow pattern during the recovery phase appeared to be the least deflected of the three substorm phases, dominated by sunward flows with only minor deflections toward the flanks. The tailward flows in the recovery phase perhaps present slightly more-pronounced signs of convective ion flow. In general, it is clear that deflections in the XZ plane across all substorm phases are small in comparison to those found in the XY plane. This shows that there is possibly less plasma transported up and over the Earth in the Z-direction, with the system favouring transport around the sides of the Earth in the Y-direction instead.

When looking at the outer planes away from the NMM, the spatial coverage was severely limited and this was most noticeable on the dusk side. It was clear, especially when the low-count bins were neglected that generally for earthward flows, sunward flow dominated with slight deflections towards the EQ plane in the northern hemispheres. At the EQ plane, there is little deviation from the ions flows being directed roughly parallel to the x-axis. In the southern hemispheres, again earthward flows are predominantly directed sunward with minimal deviations from this. Tailward flows present more deflections with more deflections towards the flanks in the northern and southern hemispheres. The flows directed along the EQ plane are strongly aligned with the x-axis.

7.2.2.3 Key Original Results

There were a number of key original results shown in this section. Firstly in general there have not been any previous studies which study substorm intervals while considering ion moments of all velocities and focussing primarily on the XZ plane, the NMM. Following on from this, all results presented in this chapter are original and present a new set of results.

The first key original result was found when considering field-perpendicular earthward ion flows in the noon-midnight meridian plane, the recovery phase has the fastest average ion-flow velocity with the expansion phase being a little slower and the growth phase being the slowest. This follows the same pattern as in the equatorial plane and thus provides further new evidence in support of the results collected in the study carried out by *Kissinger et al.* (2012). This pattern is also repeated for the average tailward velocities. In addition, the tailward flows were generally also marginally slower than the earthward flows.

When looking at the average earthward ion flow velocities, the fastest average velocities was found during both the recovery and expansion phases, with both having an average V_{xz} of 9.5 km s^{-1}. The growth phase presented the slowest average earthward velocity of 8.7 km s^{-1}. When looking at the average tailward flow velocities, it was found that the recovery phase again had the highest value of 10.4 km s^{-1}, which the expansion and growth phases were a little slower with their average V_{xz}'s being measured at 10.0 km s^{-1} and 8.0 km s^{-1} respectively.

The next key original result was found while looking at the overall earthward ion-flow patterns in the equatorial plane. It was found that they were generally fairly symmetrical about the equatorial plane, although deflections when present tended to be a little stronger in the southern hemisphere. Fro this it can be said that there were still some dawn-dusk asymmetries present across each of the substorm phases, although they were

generally less distinct than in the XY planes. Across all three substorm phases the level of disorder appeared to be a good deal less than in the XY planes. The recovery phase again appeared to be the most ordered phase, although there isn't much difference between the three. In general, it is clear that deflections in the XZ plane across all substorm phases are small in comparison to those found in the XY plane. This shows that there is possibly less plasma transported up and over the Earth in the Z-direction, with the system favouring transport around the sides of the Earth in the Y-direction instead.

7.3 Electron Flow in the Terrestrial Magnetosphere

This section reviews the final study carried out within this thesis, attempting to recreate the ion flows found in Chapter 4 and assessing whether it is possible to use PEACE electron moments for large scale magnetospheric flow studies. The majority of the electron sample count distribution results are similar to the results seen in Chapter 4. In addition, since there was generally much more data available as all four Cluster spacecraft provided PEACE electron moments, the spatial coverage was somewhat improved upon the coverage of the CIS dataset. The main finding in this chapter was found when comparing earthward and tailward flows across all of the XY planes; it was found that tailward electron flows were dominant for every plane, even for the central three planes. When the same investigation was carried out using ion moment data (Chapter 4), earthward ion flow occurrence rates were dominant. This result was somewhat unexpected and as such, a series of investigations were carried out to establish what could have been the cause of this flow direction disparity.

The first section investigation carried out was to recreate the ion flow distribution figure (6.4) from the study carried out by *Zhang et al.* (2015a). This was done to ensure the procedure used in this thesis was as close as possible to that used by Zhang. While both plots clearly showed overall earthward flow dominance across the whole region, there was up to 10 times more data at some distances from Earth. This was almost certainly due to the fact that from the discussion in Zhang's paper, it was not perfectly clear exactly which data selection criteria he used, thus there was an element of uncertainty when recreating his plot.

The second part of the investigation carried out was to compare Zhang's ion flow distribution figure to the same plot created using PEACE electron moment data. It was found that there was about 5 times less data available when using PEACE data than CIS data. Interestingly, after applying all of Zhang's data cutoffs, earthward flows tended to dominate more often than tailward flows. This appeared to be the opposite result than what

was presented at the beginning of this chapter. However after the removal of the 50 km s^{-1} velocity cutoff, tailward flows once again dominated. From this it could be assumed that the tailward flow occurrence dominance initially found came predominantly from flows with velocities less than 50 km s^{-1}. In general this result highlighted that the flow direction disparity was not an artefact of the procedure in which the ion moment data had been processed in Chapter 4. To further this, another flow distribution plot was made using the raw unprocessed PEACE electron moments to establish whether the Zhang parameters had an influence on the result. Again, tailward flows were seen to be dominant and as such, the reason for the flow direction disparity was tending towards the data set, rather than the data processing. One final investigation was carried out to evaluate whether the observed flow direction disagreement could stem from the conversion from bulk-velocity moments to field-perpendicular moments within the PEACE dataset. Another figure was created using CIS ion bulk velocity moments and it is clear that tailward flows were still dominant, hence the use of PEACE field-perpendicular electron moment data was also not the cause of the flow direction disparity.

The interesting results found in this chapter suggest that the difference in flow-direction dominance between the CIS and PEACE datasets could well descend from the PEACE dataset rather than the way in which the data has been processed. In addition, there was an earlier study found (*Geach et al.*, 2005) whose conclusions suggested that the reliability or consistency of the electron moments could be questionable at times where the velocity estimation parameter (calculated in the study) was dominant. It is thought that these conclusions further the notion that the cause of the flow direction disparity lies with the raw data and how it has been processed and corrected before being uploaded to the Cluster Science Archive. After communications with the Cluster instrument's primary investigator (PI) it was assumed that this data discrepancy has not been previously raised and therefore is a new finding, requiring further investigation in the future.

7.4 Key Results Overview

Throughout the thesis, many investigations were carried out, all of which delivered interesting and original results. This is a brief overview of the most important findings and original points or research. Firstly, it was clear throughout the thesis that data selection and plasma sheet identification criteria are of the utmost importance. This is because one slight change in criteria can dramatically change the outcome. This can be seen throughout my study and all of the others discussed within this thesis too. From this, it is clear that while the magnetosheath-contamination removal procedure

was somewhat successful in removing the undesired data from the studies in this thesis, it became apparent that not all of the data was removed. As such, more time could have been spent refining the algorithm to improve its accuracy and if this study is revisited in the future, this should be one of the first points to be considered.

The studies carried out within this thesis were also the first ones to focus on convective ion flow, that is using perpendicular ion velocities when looking and plasma flows within the terrestrial magnetosphere. All previous comparable studies focussed on ion bulk flow velocities for all times and during substorm events too. Furthermore, it was the first time any studies had been carried out on more distant regions of the magnetosphere, looking away from the near-equatorial and near-noon midnight meridian planes. Finally, in Chapter 6, it was found that in general tailward flows tend to dominate throughout the magnetotail when using PEACE electron data, however once a $50\,\mathrm{km\,s^{-1}}$ velocity cutoff was applied, earthward flows dominated. This is interesting as many of the previous studies which found earthward flows to dominate also neglected slow flows in their research. Thus including slow electron flow data dramatically changes the results found, a conclusion which reflects the first point made in this section.

7.5 Future Work and Improvements

There are a number of ways in which the studies carried out in this thesis could be improved upon or extended. First of all, the bin size could have been adjusted to 2 R_3^3. As discussed in Chapter 4, this could have provided additional detail for the ion flows, perhaps illustrating smaller-scale structures present within the system. However, while this change would go some way to improving the clarity of the ion flow directions, it would also mean cubing the number of plots needed to present the data, making the analysis and comparisons greatly more difficult to carry out. This could be used for all three investigations to similar effect.

The importance of fast flow bursts has been mentioned a number of times within this thesis with regards to energy and momentum transportation throughout the system. From this, perhaps another extension to the study could be to carry out a more detailed investigation of the distribution of flow velocities throughout the magnetotail. *Juusola et al.* (2011) carried out a study looking at how ion flows differed with velocity, a study which could be repeated with substorm times to establish what affect fast flows have on the different substorm phases. This could be extended further to looking at the specific times at which each phase begins, identifying any possible flow signatures, which could be used to refine substorm models or identification algorithms in the future. A different

angle on this idea could be to look at the particle velocity distribution with position, investigating whether faster of slower flows occur in more localised positions.

Asymmetrical flow patterns have been discussed throughout this thesis and as such are an important theme which could be explored further. The next step here could be to re-plot the various data-products using an aberrated GSM coordinate system as *Juusola et al.* (2011) did in her study. Juusola rotated her coordinate system clockwise by 4.8°. This could help to establish whether some the asymmetrical flow are generated though Earth's trajectory about the Sun and the angle at which the solar wind meets the magnetosphere.

When considering Chapter 5's study on substorms, perhaps the investigation carried out by *Nakamura et al.* (1994), observing the occurrence rate of tailward fast flows, could also be extended by using a larger data set as well as the wider coverage of Cluster. This could help to give a broader view on the little studied tailward flows. An important study which could be carried out in the future is a comparison between the varies substorm identification procedures, such as the method used by *Kissinger et al.* (2012) or the newer model created by *Forsyth et al.* (2015). It is clear that they are not all the same and return different results. For example, the SuperMAG substorm list returned a great deal less positive identifications of isolated substorm events that the procedure *Kissinger et al.* (2012) used in her study. In addition to this generalised study, it would be interesting to apply these alternative substorm identification procedures to the investigation carried out in Chapter 5 so assess how the results change.

The final suggestion for future work is also potentially the largest investigation; to continue the research into why the electron and ion moments return conflicting results. One possible avenue to explore could be to apply the numerical methods devised by *Geach et al.* (2005) to the PEACE dataset in use for the study described in Chapter 6. If the newly adjusted data shows proportionally more flow dominance in the earthward direction, it would be further evidence towards the dataset being the reason for the flow direction discrepancy. A further more in-depth idea for continuation of this study could be to examine the other physical plasma parameters (such as temperature, density, magnetic field strength, and pitch angle) of each dataset, comparing the results and establishing how they differ. This could help to ascertain whether the data differences are only rooted within the moment data, or more widespread across multiple datasets. If the reason behind the difference between the ion and electron flow distributions can be uncovered and remedied, it would provide a great deal more data for future plasma flow studies, and greatly improve the data coverage and reliability for studies on shorter duration magnetospheric phenomena, such as substorms.

Appendix A

XY Plane Ion Moment Figures

A.1 Sample Counts EQ Plane

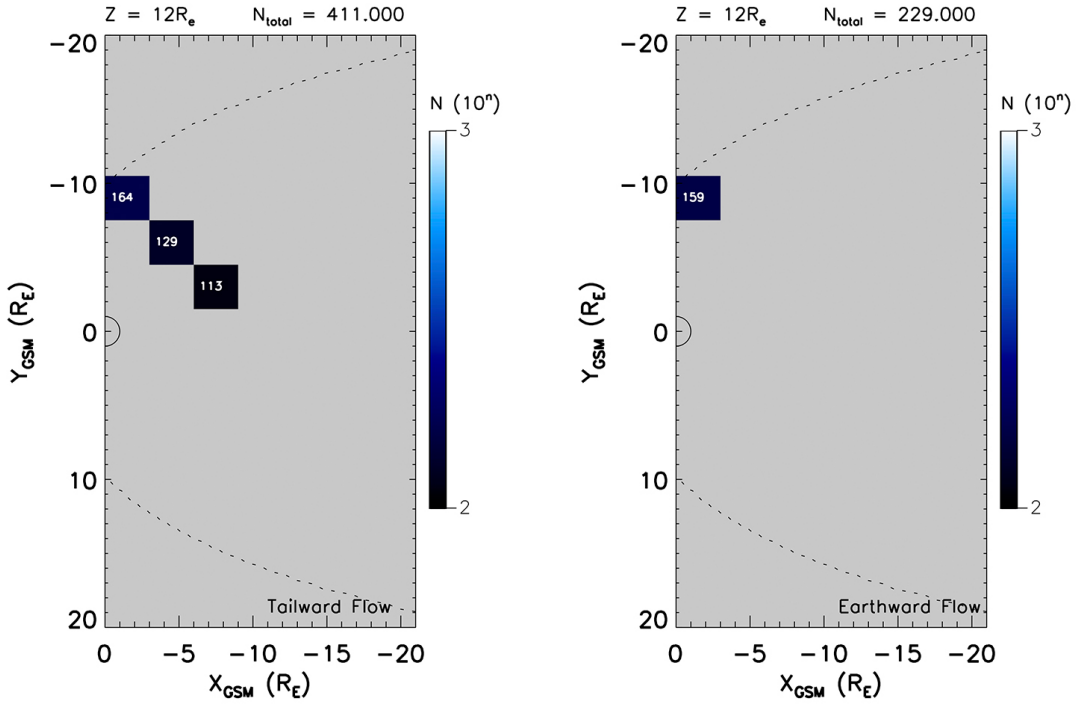

FIGURE A.1: Sample count plot for XY plane Z = 12 ± 1.5 R_e displaying tailward (left) and earthward (right) plasma flow.

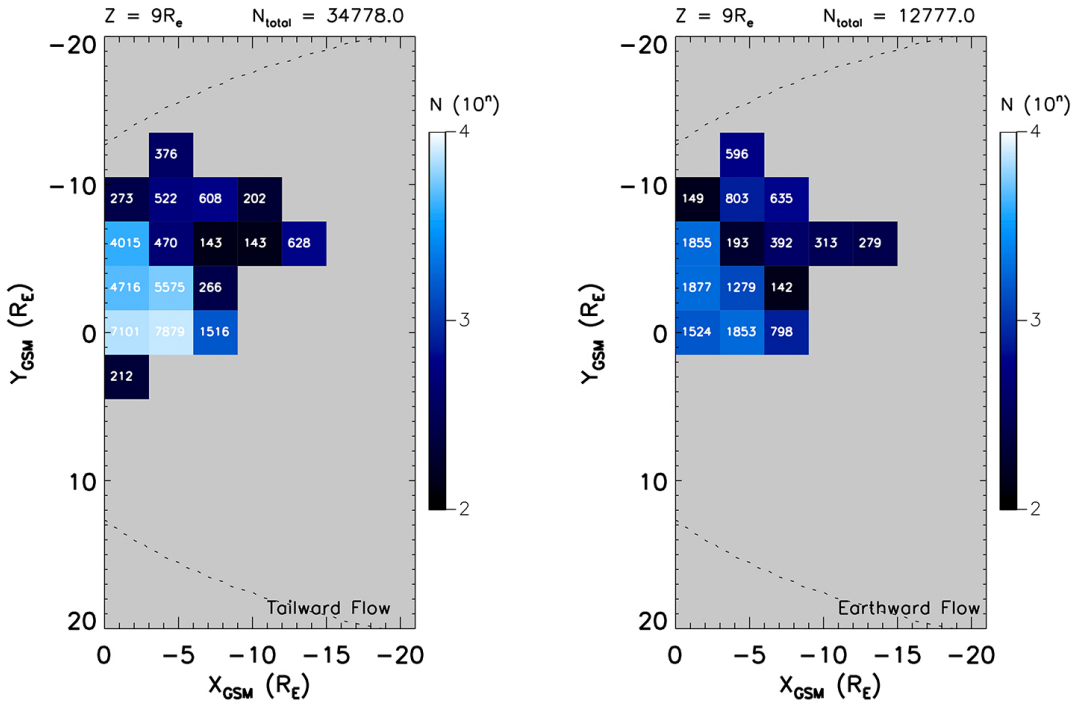

FIGURE A.2: Sample count plot for XY plane Z = 9 ± 1.5 R_e displaying tailward (left) and earthward (right) plasma flow.

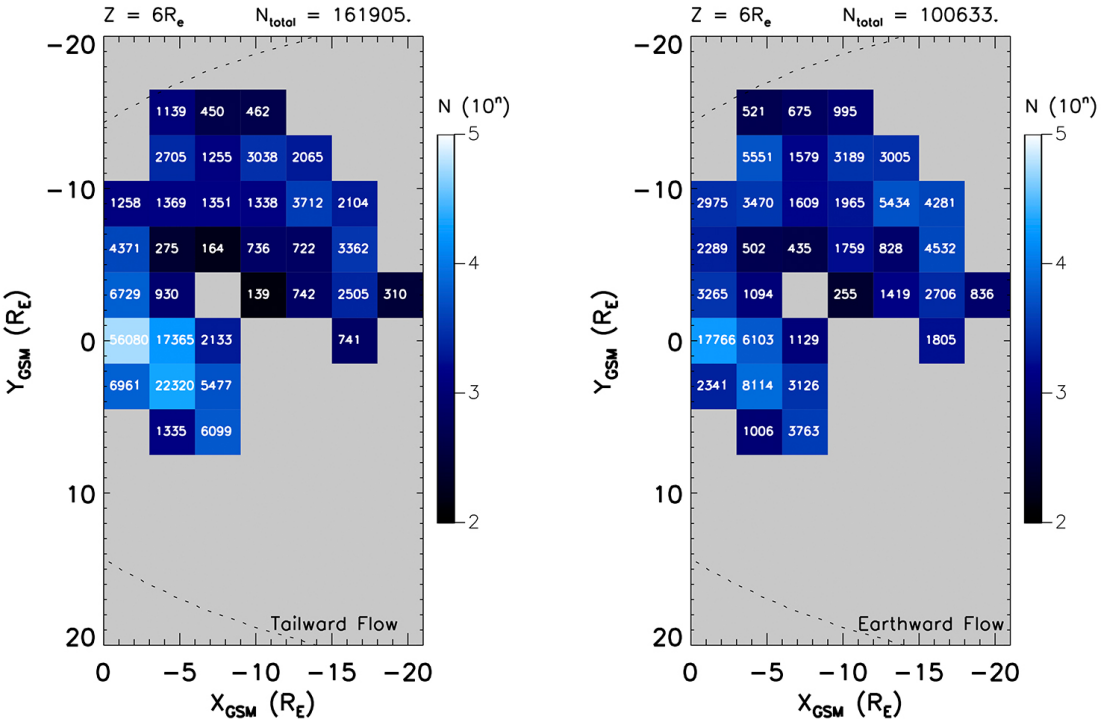

FIGURE A.3: Sample count plot for XY plane Z = 6 ± 1.5 R_e displaying tailward (left) and earthward (right) plasma flow.

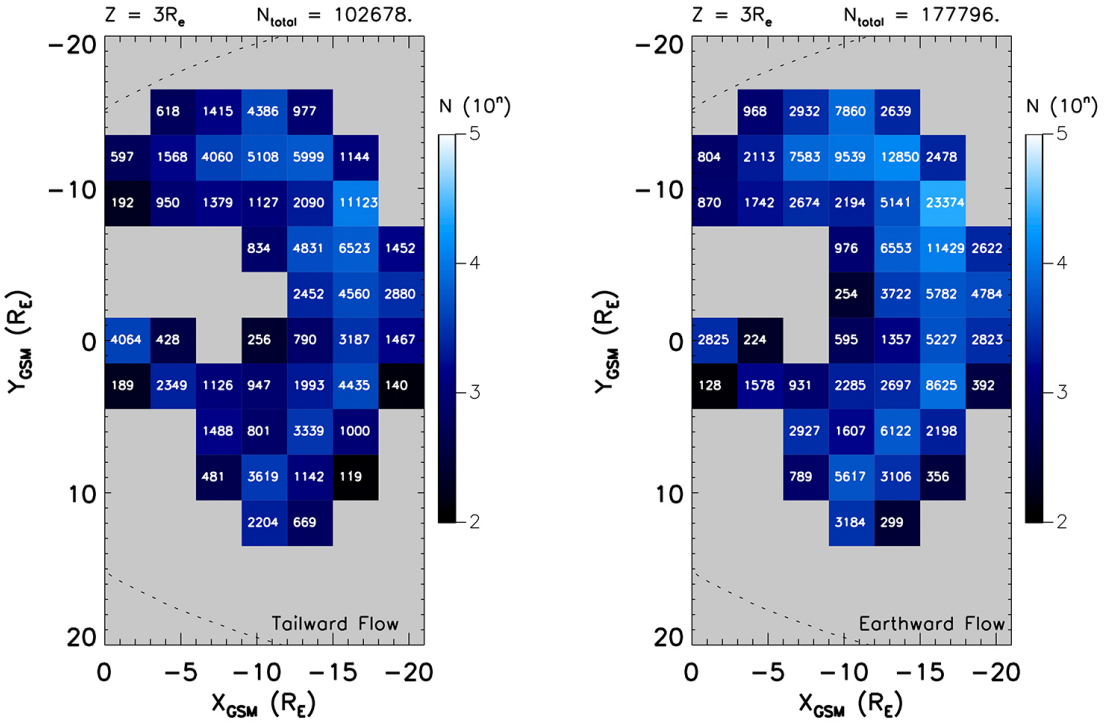

FIGURE A.4: Sample count plot for XY plane Z = 3 ± 1.5 R_e displaying tailward (left) and earthward (right) plasma flow.

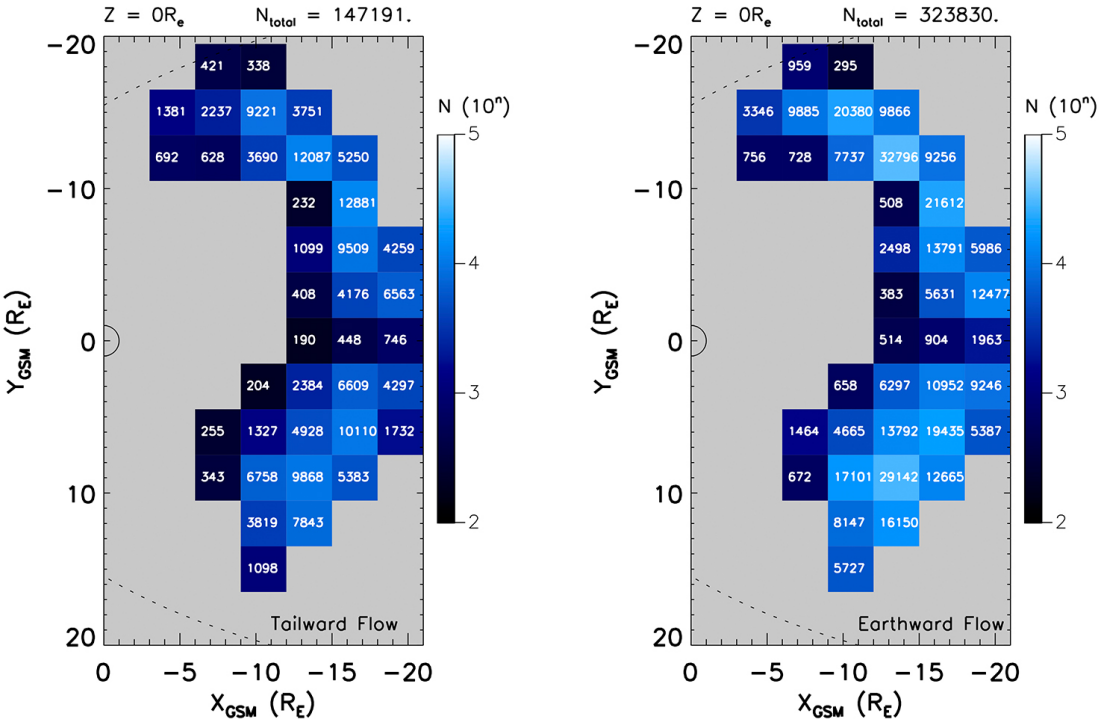

FIGURE A.5: Sample count plot for XY plane Z = 0 ± 1.5 R_e displaying tailward (left) and earthward (right) plasma flow.

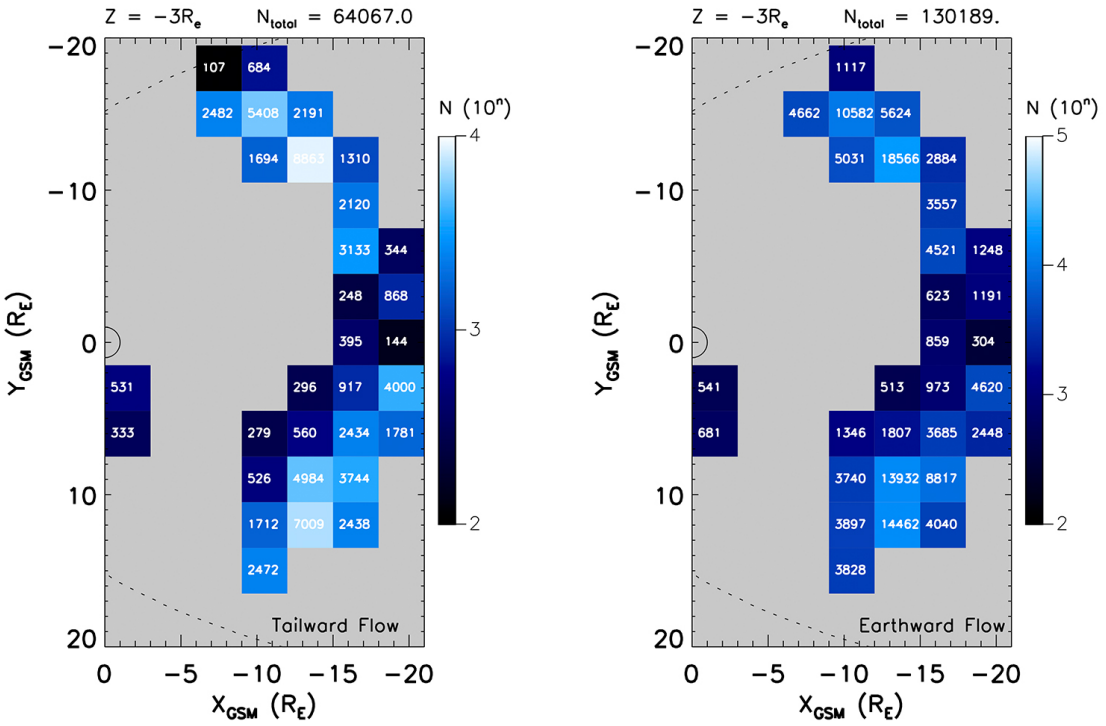

FIGURE A.6: Sample count plot for XY plane Z = -3 ± 1.5 R_e displaying tailward (left) and earthward (right) plasma flow.

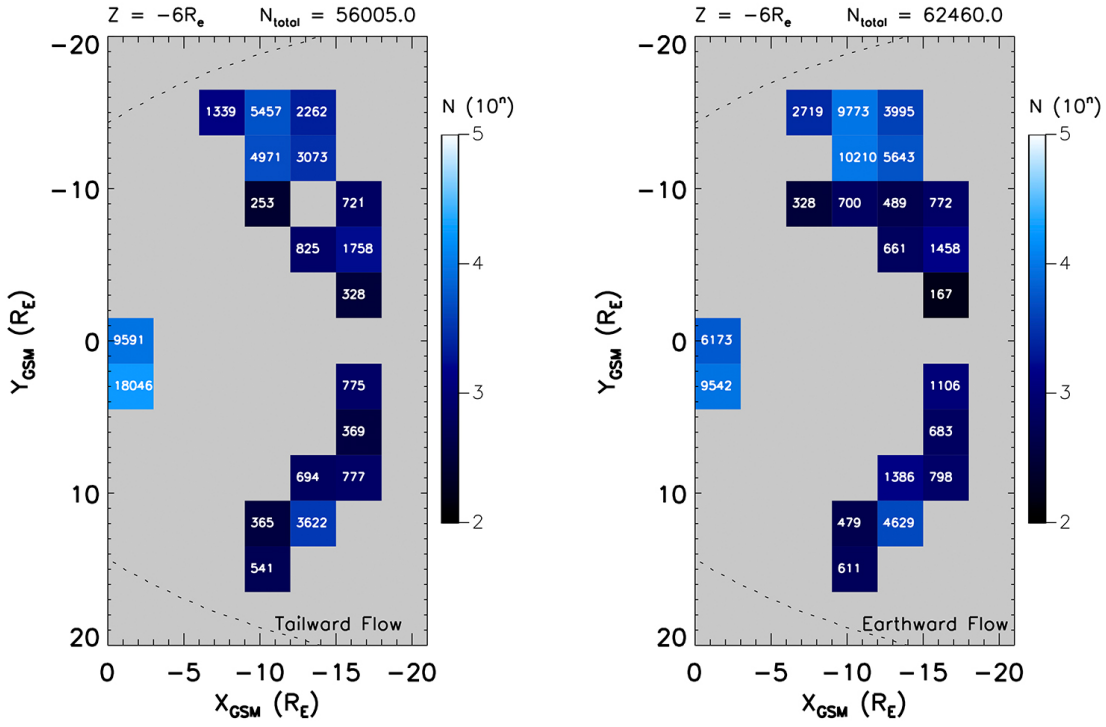

FIGURE A.7: Sample count plot for XY plane Z = -6 ± 1.5 R_e displaying tailward (left) and earthward (right) plasma flow.

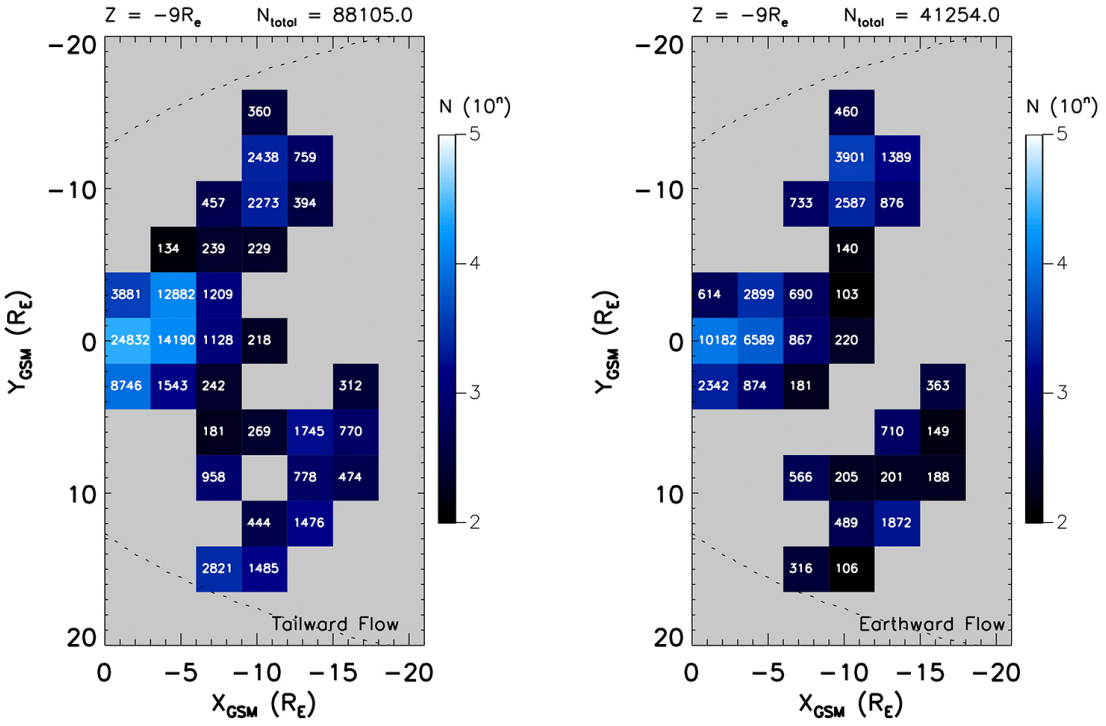

FIGURE A.8: Sample count plot for XY plane Z = 9 ± 1.5 R_e displaying tailward (left) and earthward (right) plasma flow.

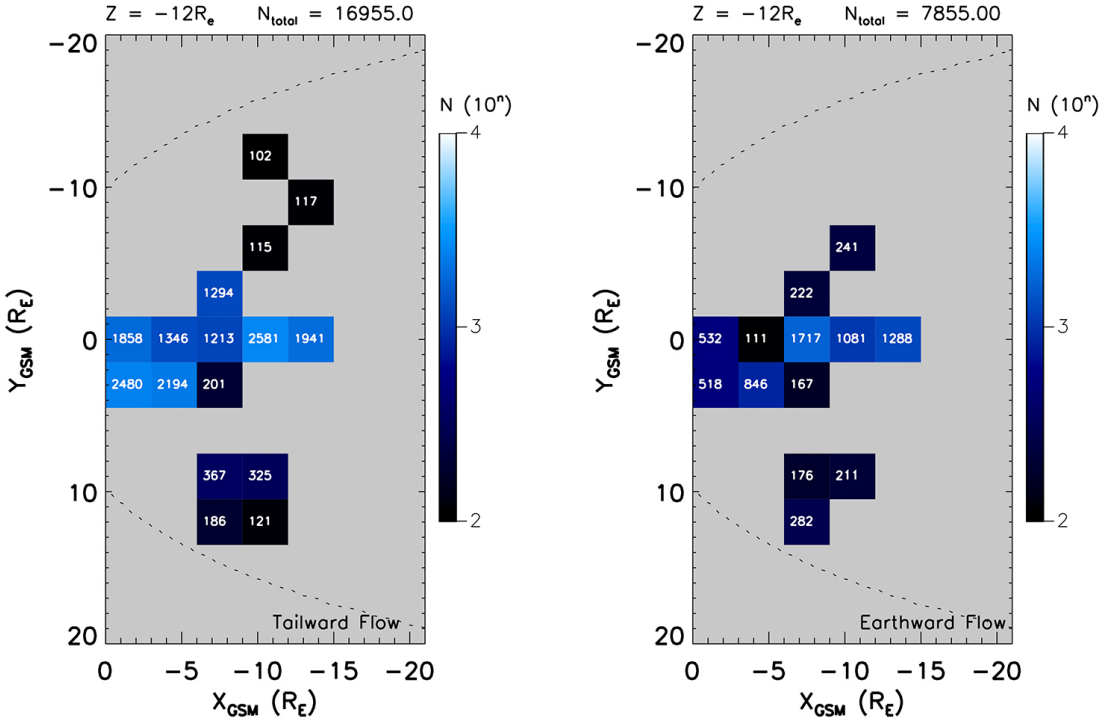

FIGURE A.9: Sample count plot for XY plane Z = -12 ± 1.5 R_e displaying tailward (left) and earthward (right) plasma flow.

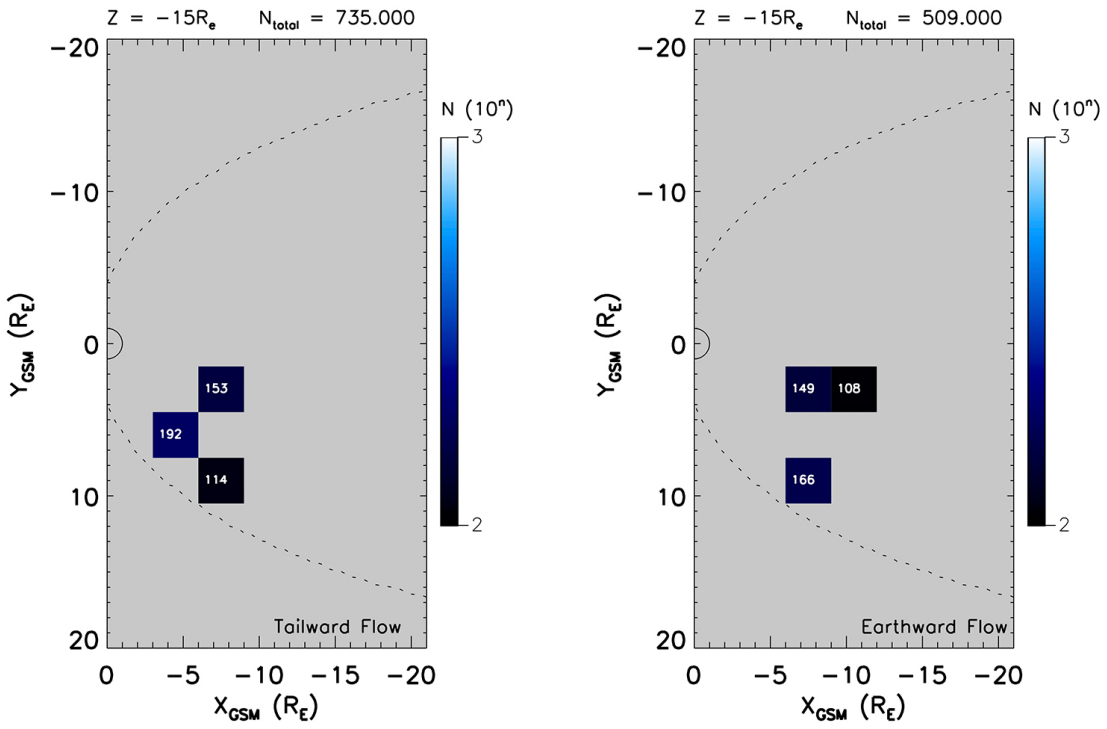

FIGURE A.10: Sample count plot for XY plane Z = -15 ± 1.5 R_e displaying tailward (left) and earthward (right) plasma flow.

A.2 Ion Velocity Plots - EQ Plane

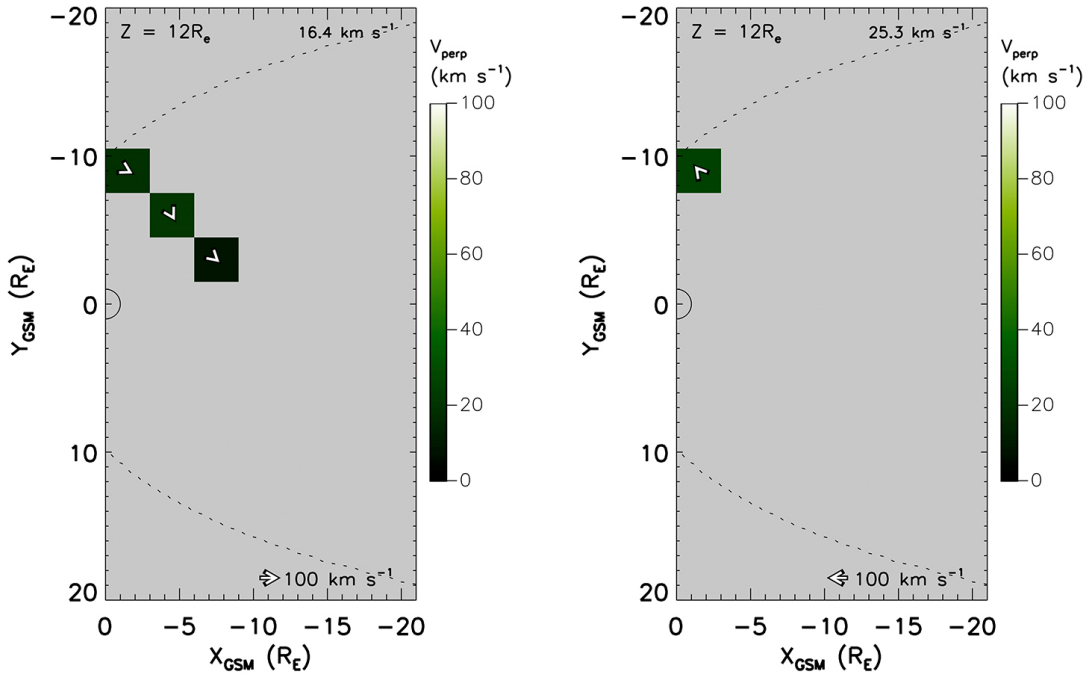

FIGURE A.11: Ion velocity plot for XY plane Z = 12 ± 1.5 R$_e$ displaying tailward (left) and earthward (right) plasma flow.

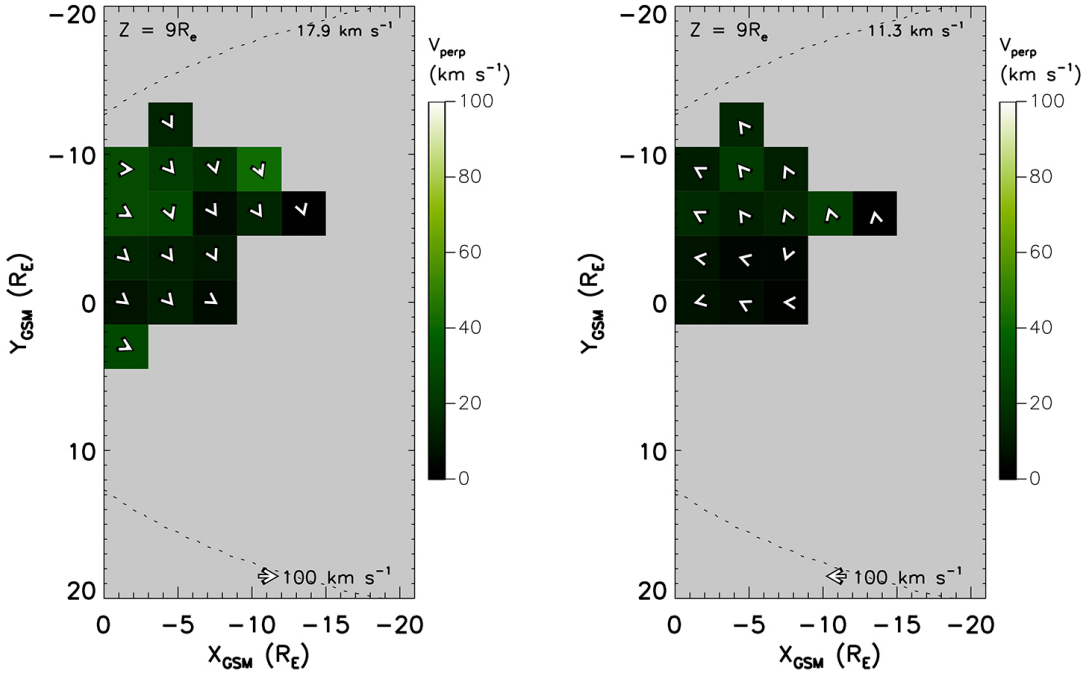

FIGURE A.12: Ion velocity plot for XY plane Z = 9 ± 1.5 R$_e$ displaying tailward (left) and earthward (right) plasma flow.

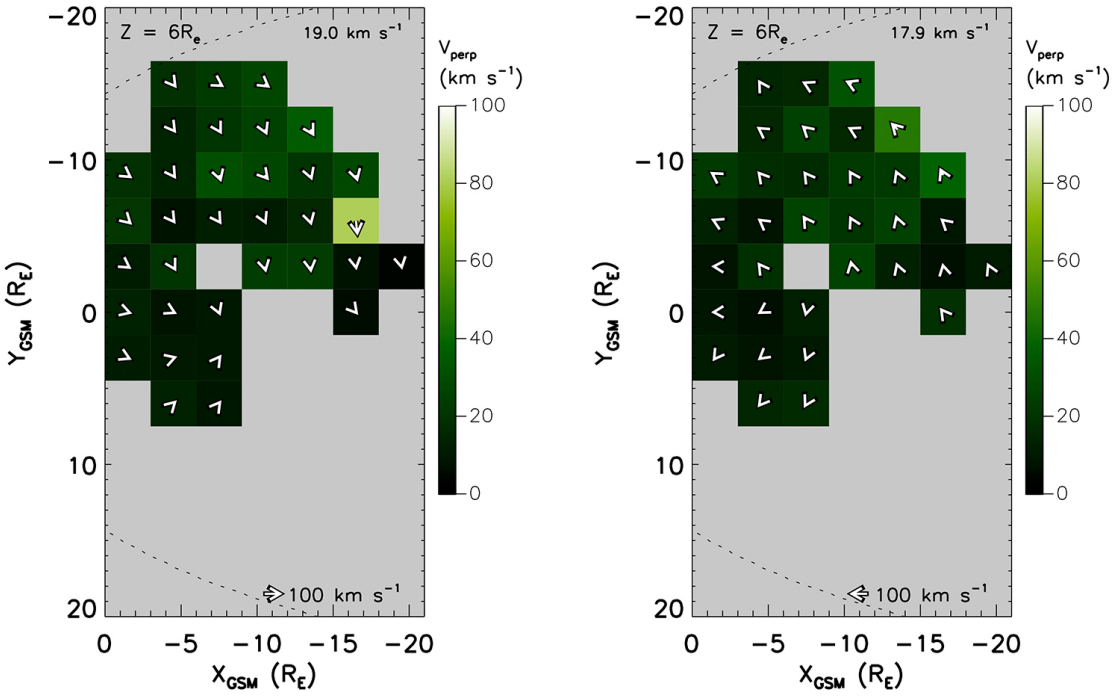

FIGURE A.13: Ion velocity plot for XY plane Z = 6 ± 1.5 R_e displaying tailward (left) and earthward (right) plasma flow.

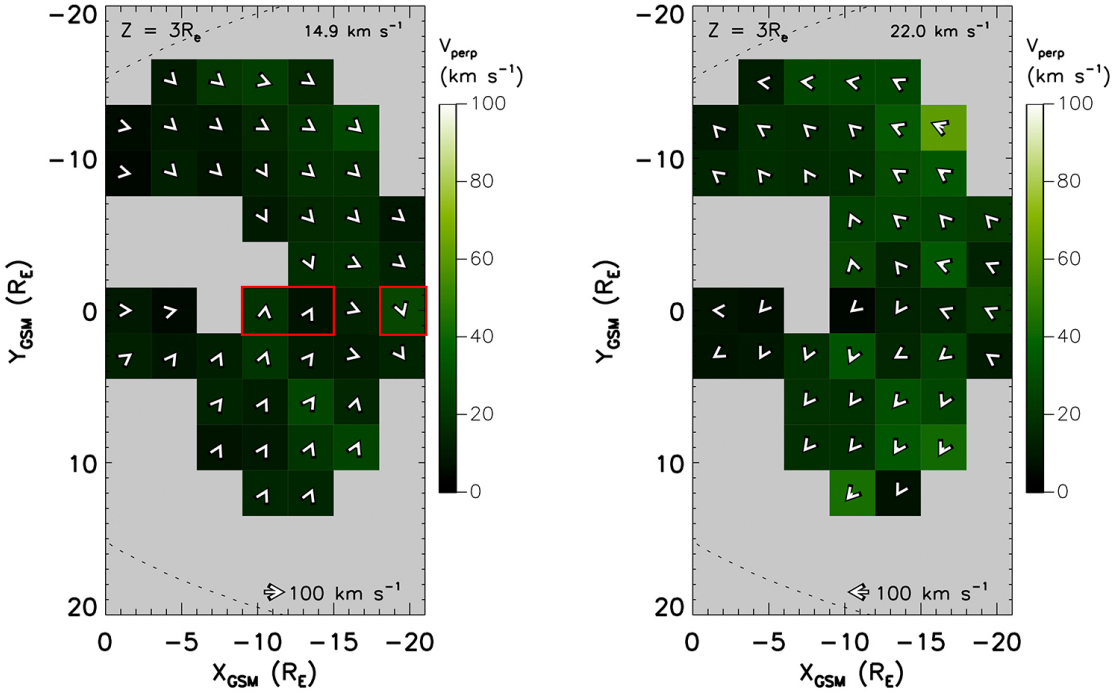

FIGURE A.14: Ion velocity plot for XY plane Z = 3 ± 1.5 R_e displaying tailward (left) and earthward (right) plasma flow.

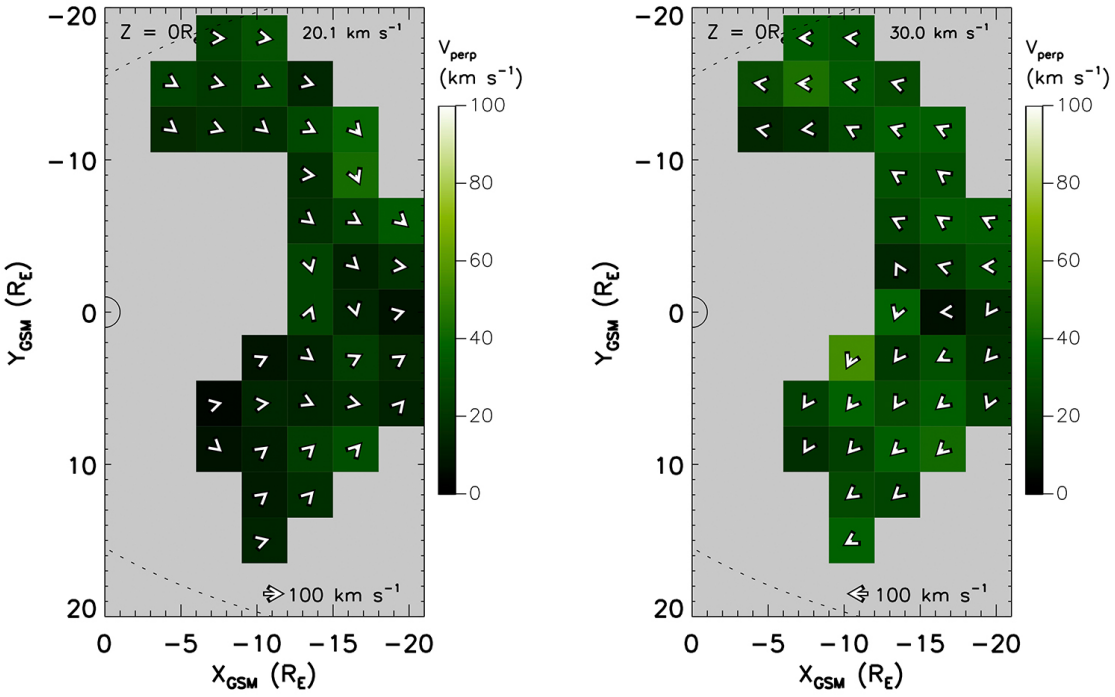

FIGURE A.15: Ion velocity plot for XY plane Z = 0 ± 1.5 R_e displaying tailward (left) and earthward (right) plasma flow.

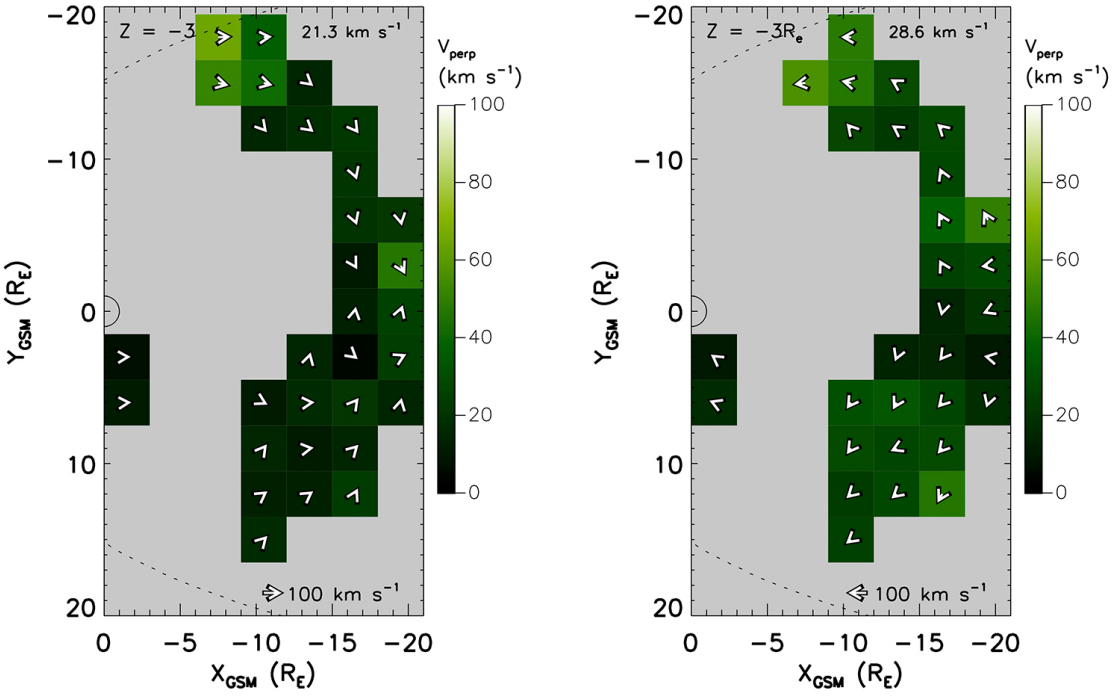

FIGURE A.16: Ion velocity plot for XY plane Z = -3 ± 1.5 R_e displaying tailward (left) and earthward (right) plasma flow.

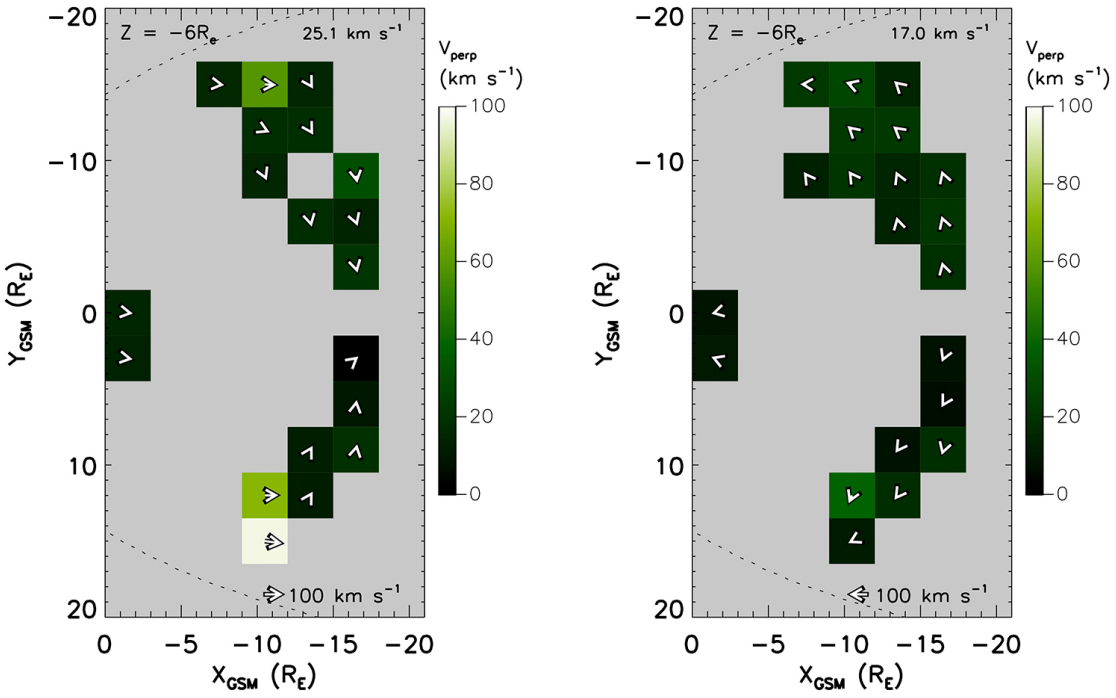

FIGURE A.17: Ion velocity plot for XY plane Z = -6 ± 1.5 R_e displaying tailward (left) and earthward (right) plasma flow.

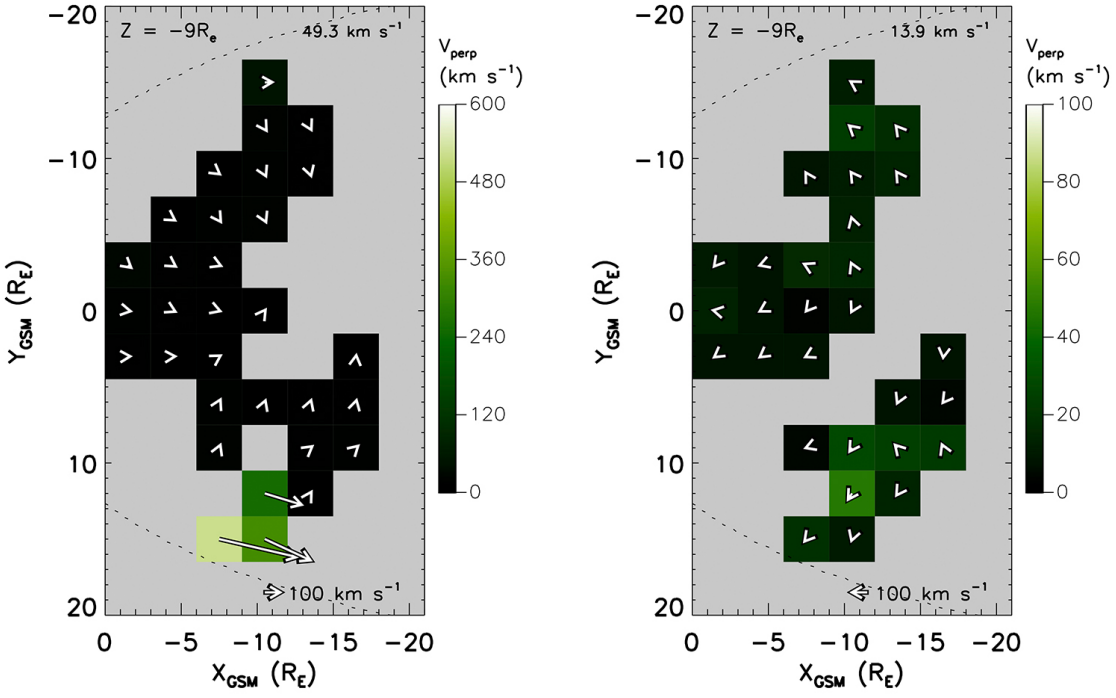

FIGURE A.18: Ion velocity plot for XY plane Z = -9 ± 1.5 R_e displaying tailward (left) and earthward (right) plasma flow.

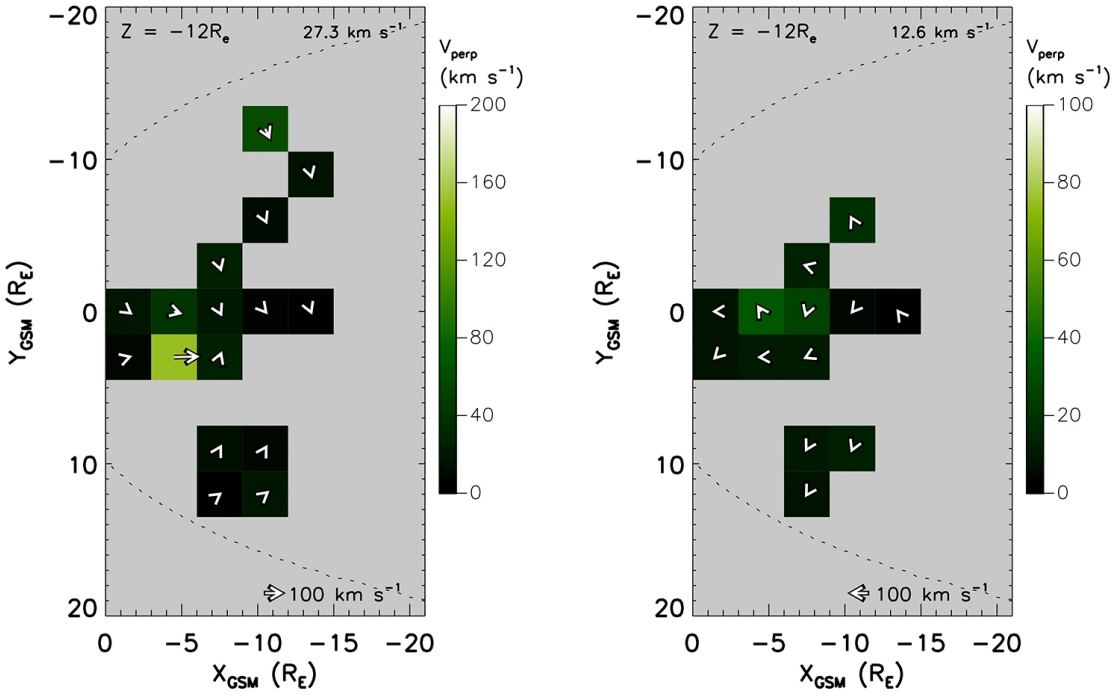

FIGURE A.19: Ion velocity plot for XY plane Z = -12 ± 1.5 R_e displaying tailward (left) and earthward (right) plasma flow.

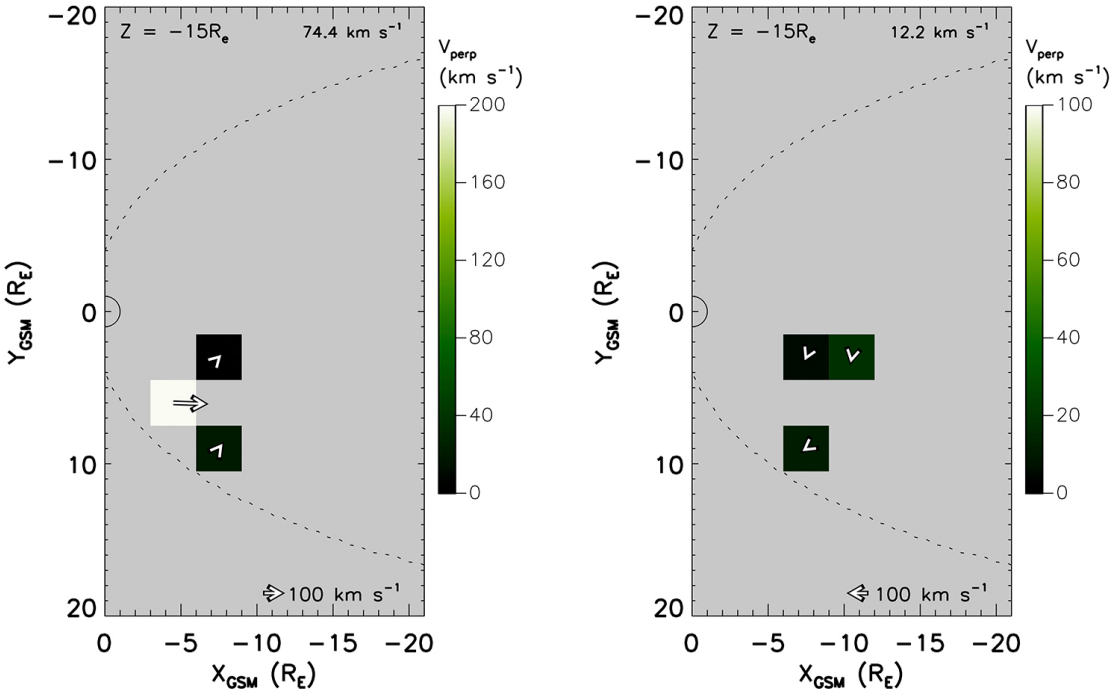

FIGURE A.20: Ion velocity plot for XY plane Z = -15 ± 1.5 R_e displaying tailward (left) and earthward (right) plasma flow.

Appendix B

XZ Plane Ion Moment Figures

B.1 Sample Counts - NMM Plane

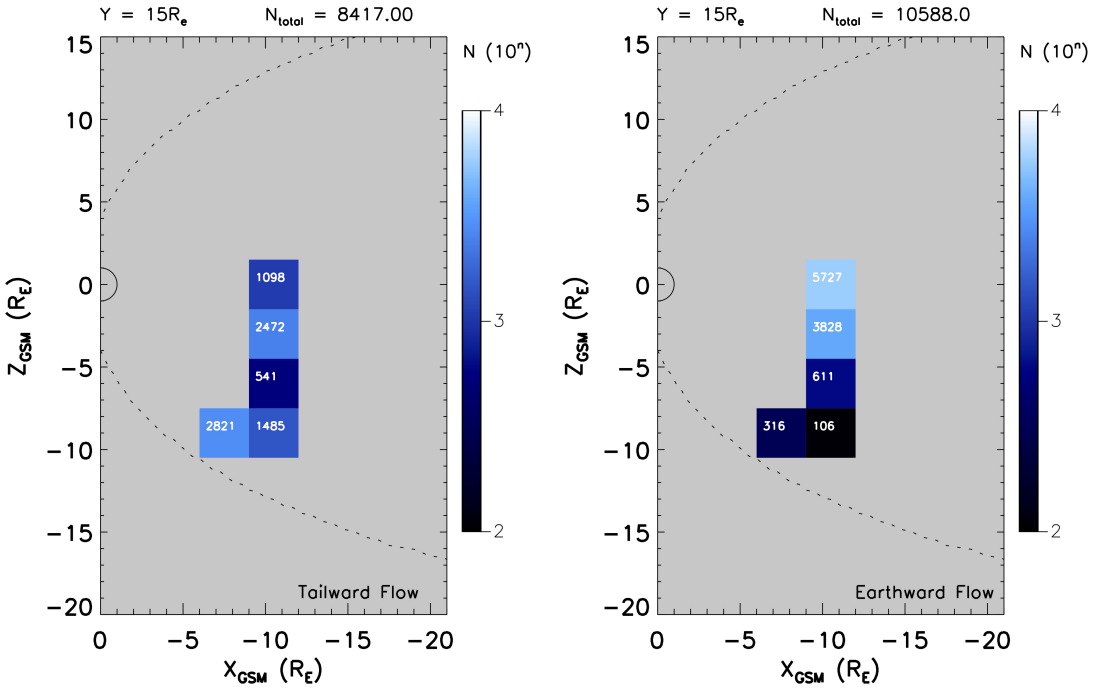

FIGURE B.1: Sample count plot for XZ plane Y = 15 ± 1.5 R$_e$ displaying tailward (left) and earthward (right) plasma flow.

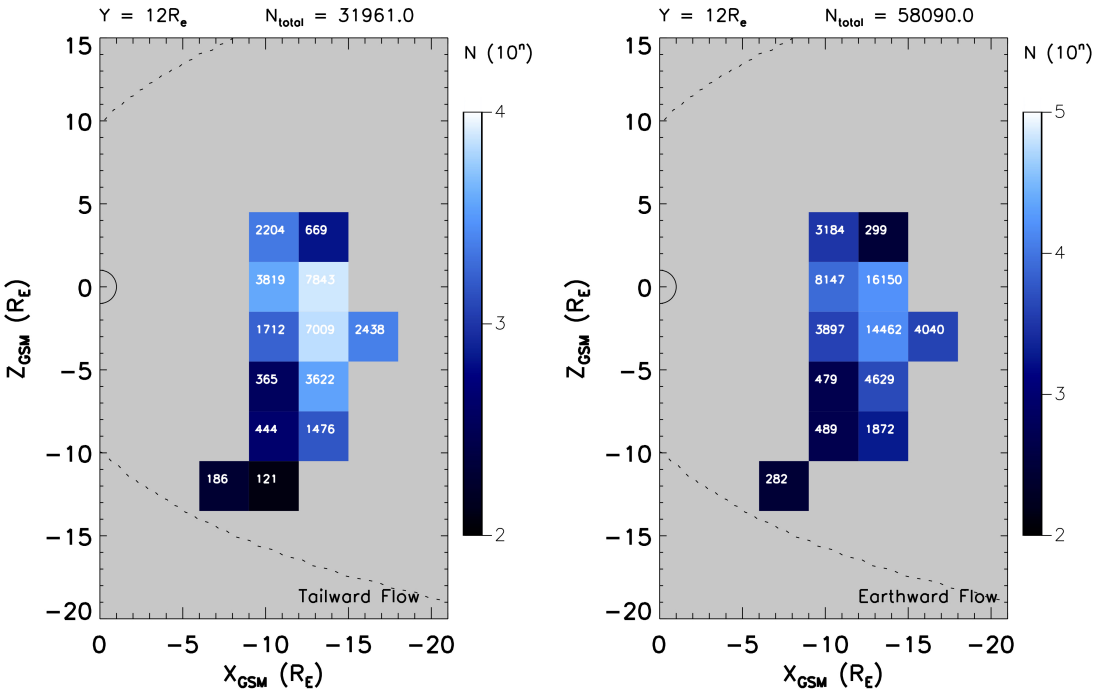

FIGURE B.2: Sample count plot for XZ plane $Y = 12 \pm 1.5\,R_e$ displaying tailward (left) and earthward (right) plasma flow.

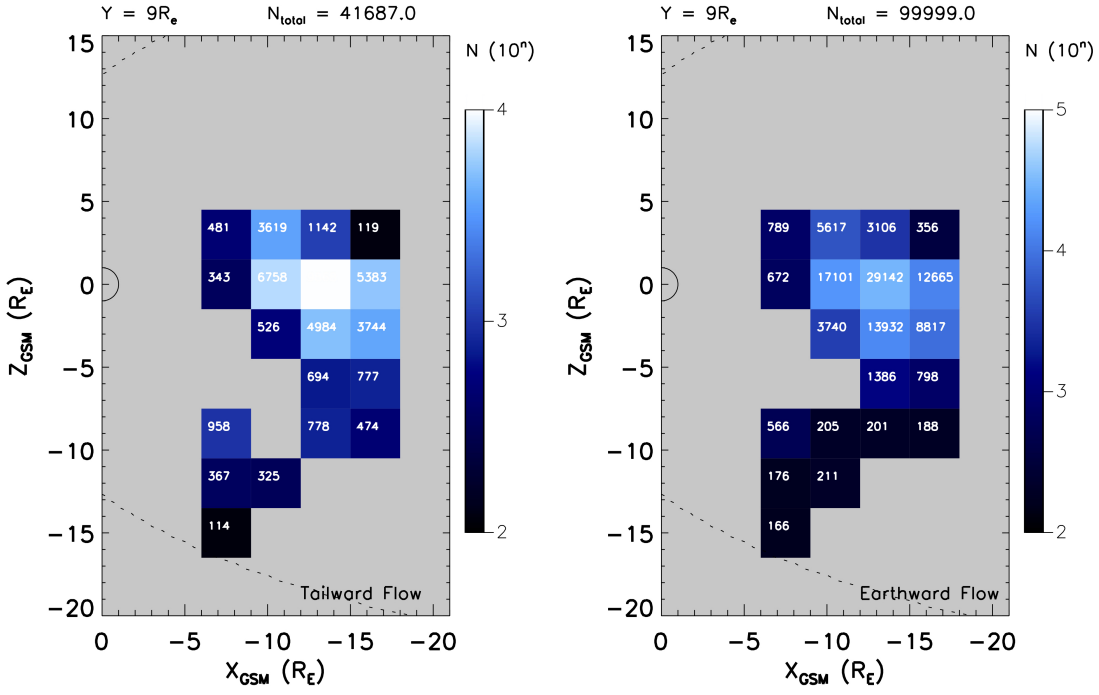

FIGURE B.3: Sample count plot for XZ plane $Y = 9 \pm 1.5\,R_e$ displaying tailward (left) and earthward (right) plasma flow.

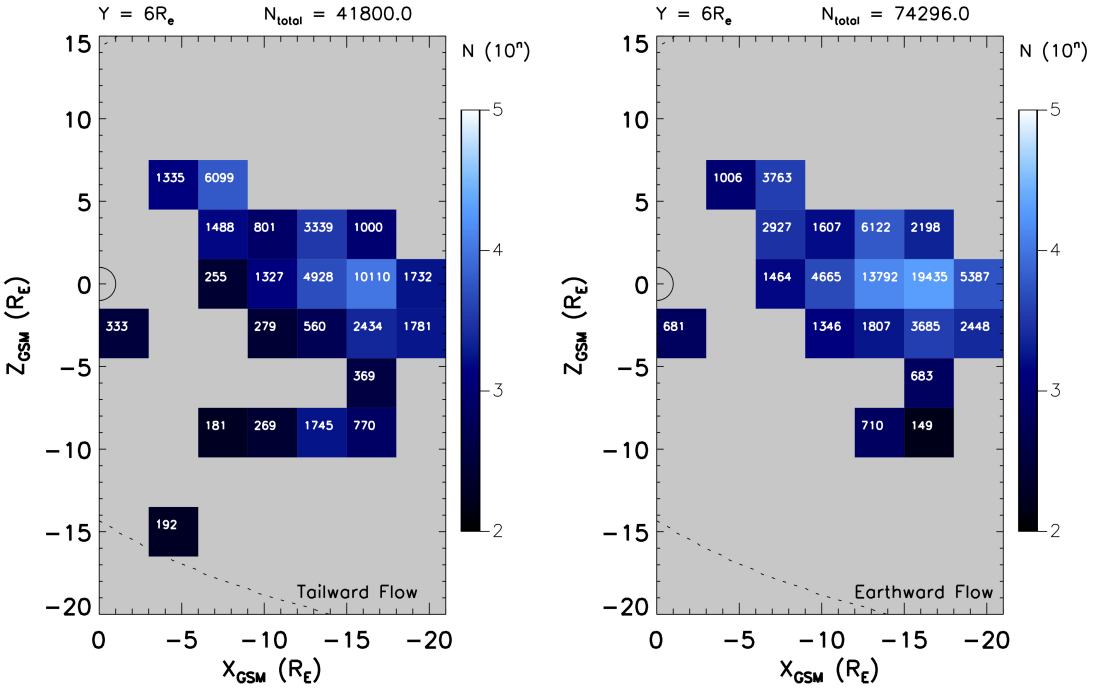

FIGURE B.4: Sample count plot for XZ plane Y = 6 ± 1.5 R_e displaying tailward (left) and earthward (right) plasma flow.

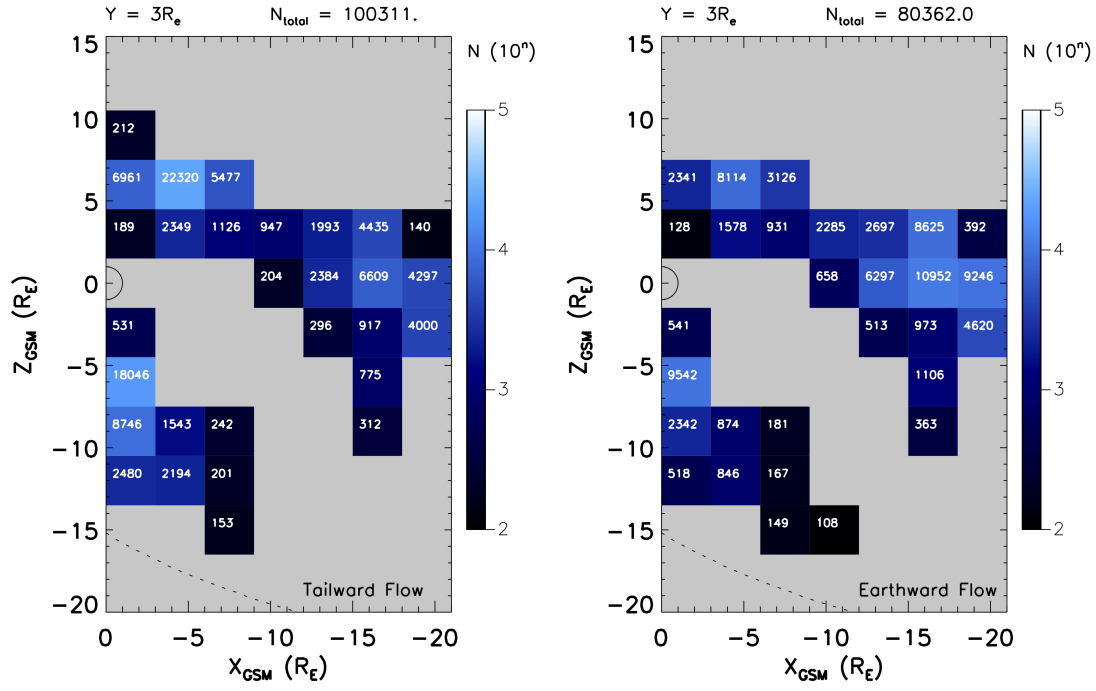

FIGURE B.5: Sample count plot for XZ plane Y = 3 ± 1.5 R_e displaying tailward (left) and earthward (right) plasma flow.

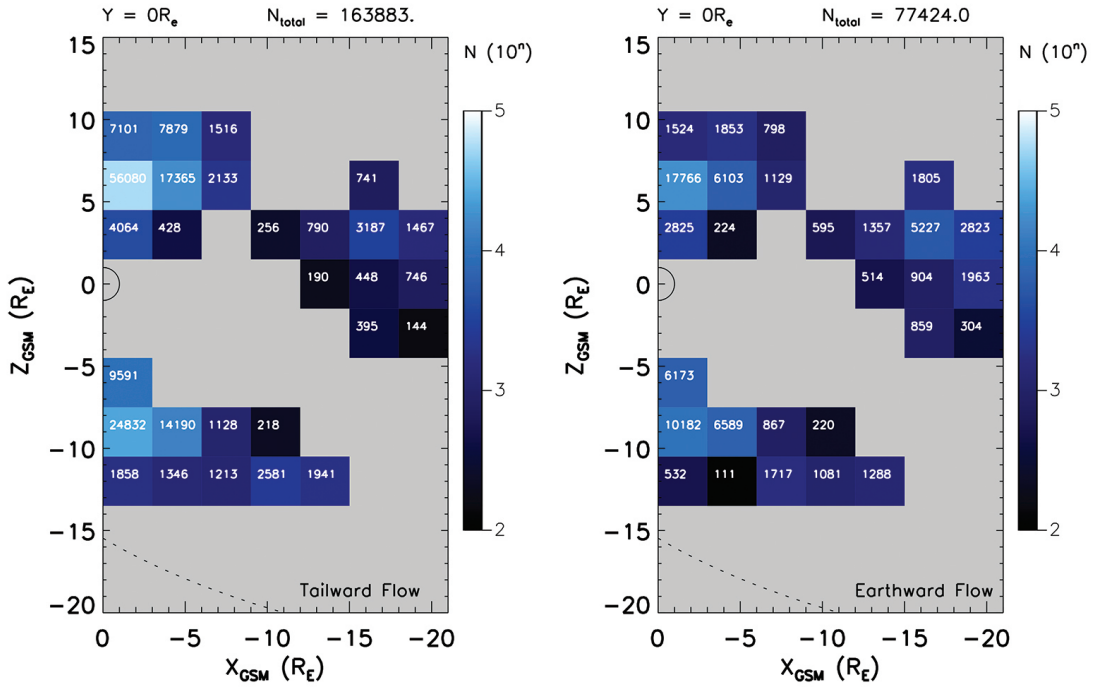

FIGURE B.6: Sample count plot for XZ plane Y = 0 ± 1.5 R_e displaying tailward (left) and earthward (right) plasma flow.

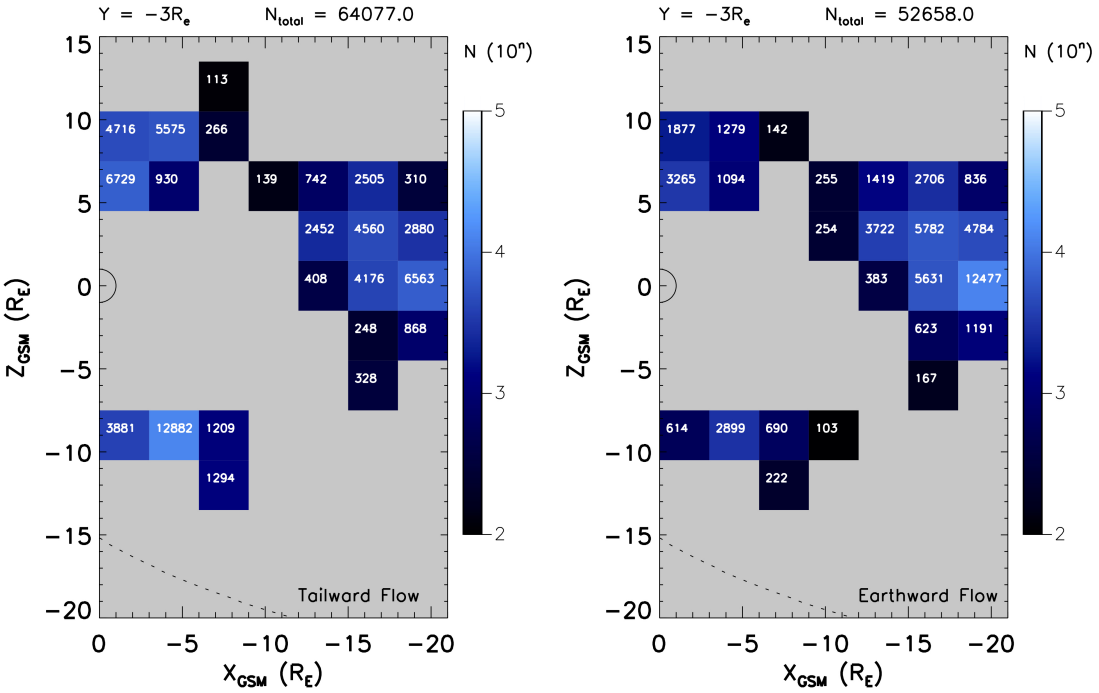

FIGURE B.7: Sample count plot for XZ plane Y = -3 ± 1.5 R_e displaying tailward (left) and earthward (right) plasma flow.

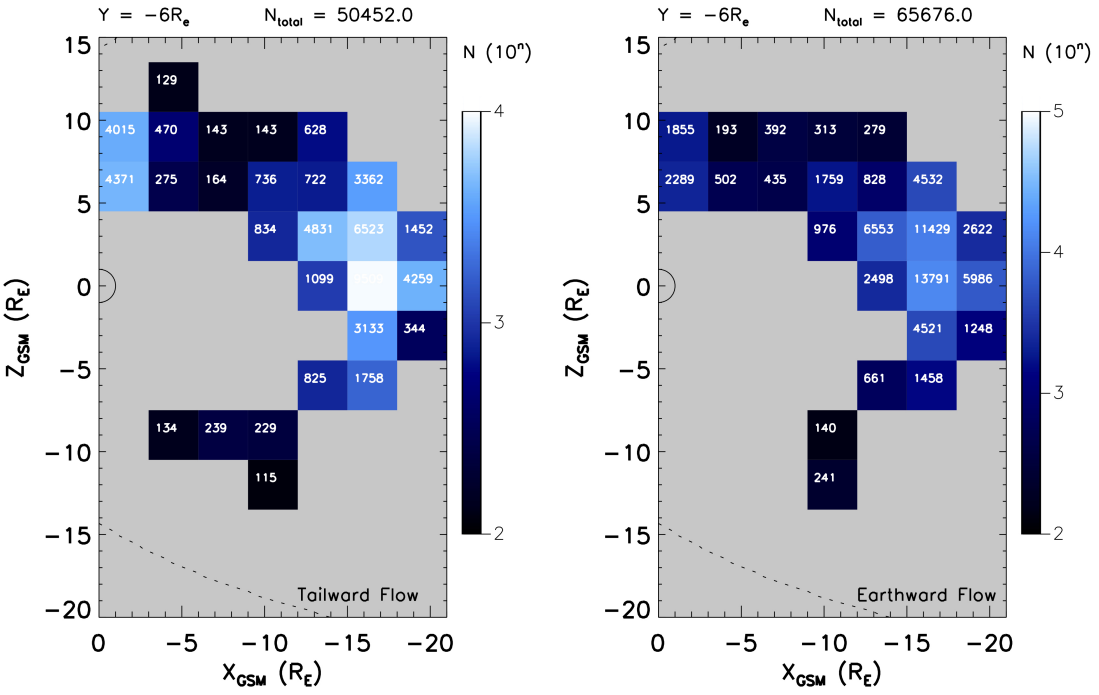

FIGURE B.8: Sample count plot for XZ plane Y = -6 ± 1.5 R_e displaying tailward (left) and earthward (right) plasma flow.

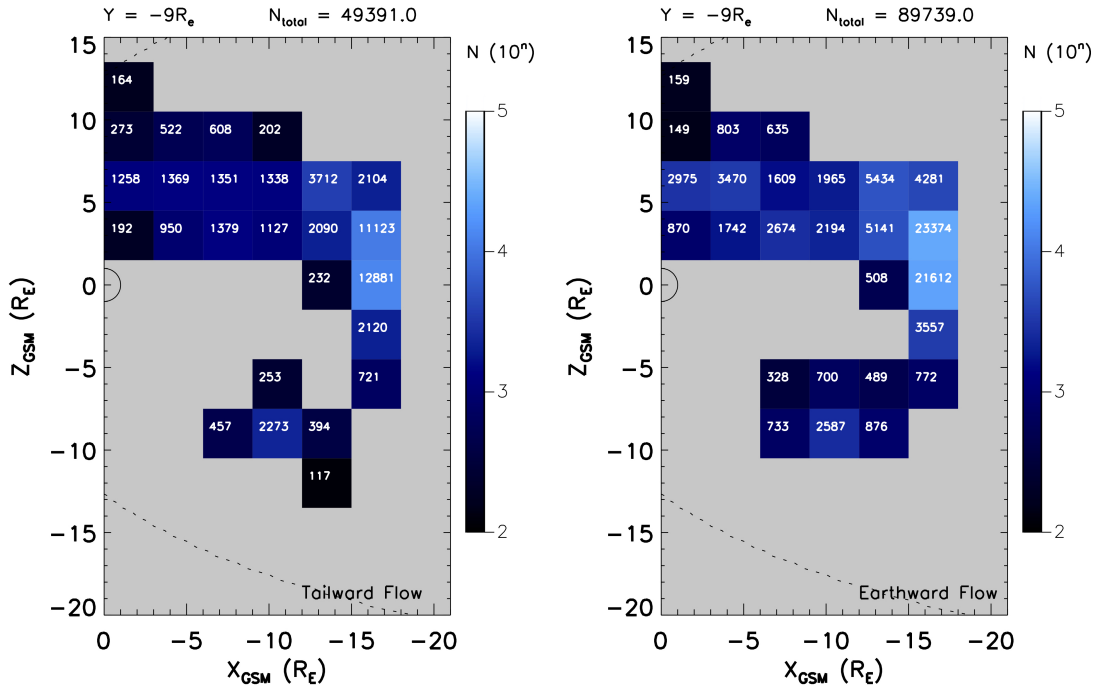

FIGURE B.9: Sample count plot for XZ plane Y = -9 ± 1.5 R_e displaying tailward (left) and earthward (right) plasma flow.

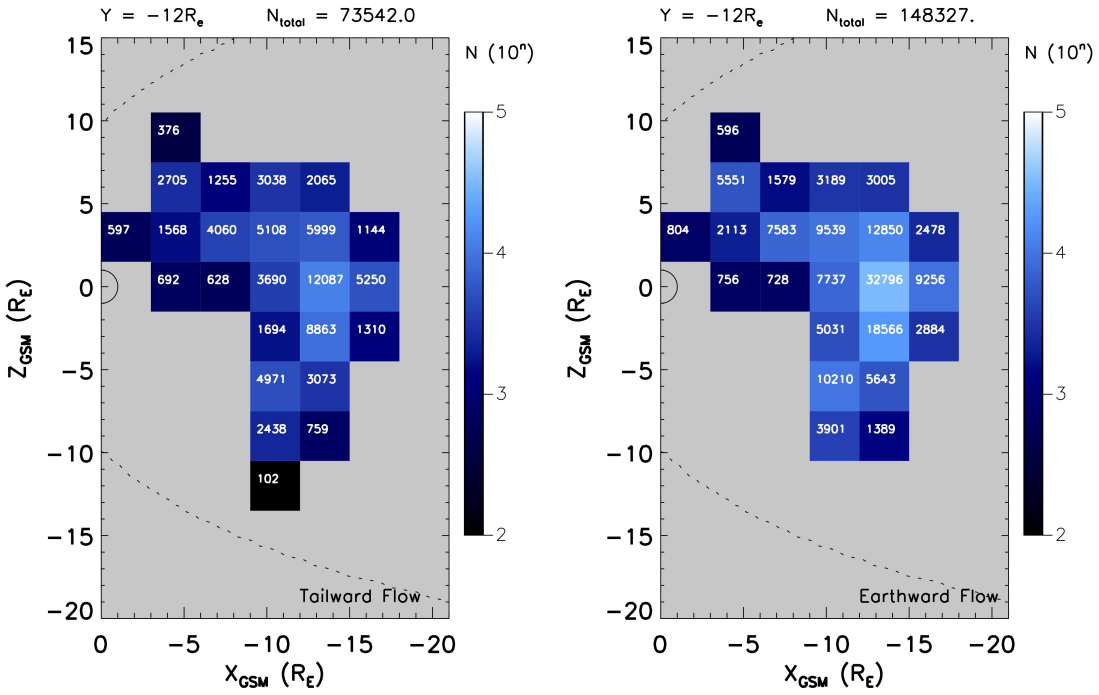

FIGURE B.10: Sample count plot for XZ plane Y = -12 ± 1.5 R_e displaying tailward (left) and earthward (right) plasma flow.

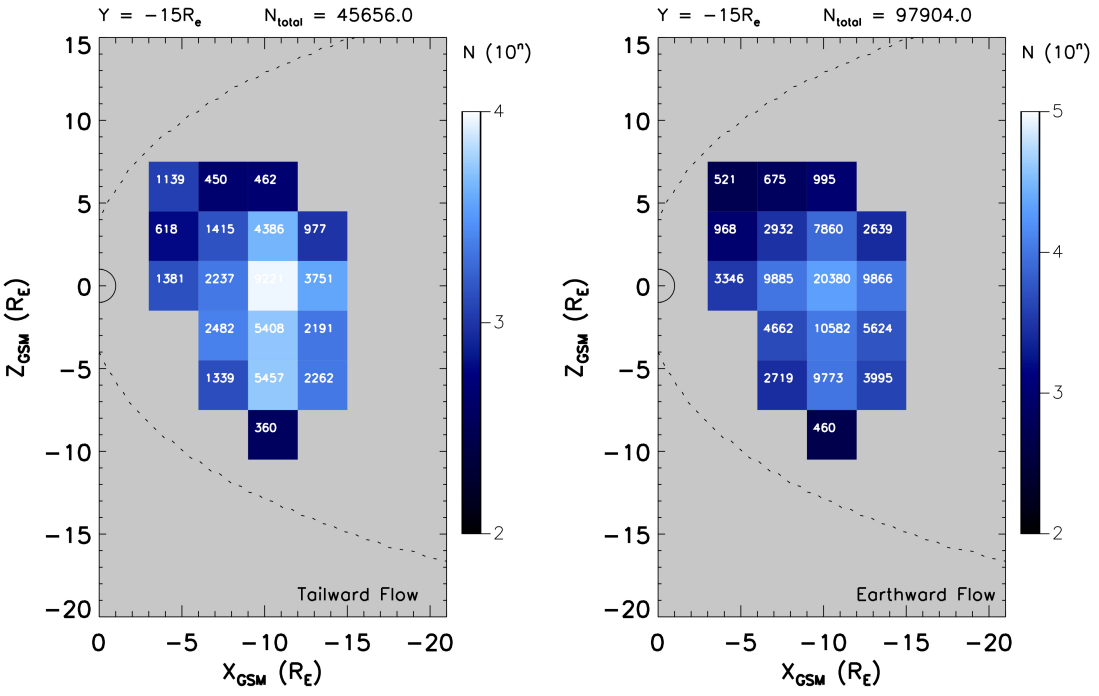

FIGURE B.11: Sample count plot for XZ plane Y = -15 ± 1.5 R_e displaying tailward (left) and earthward (right) plasma flow.

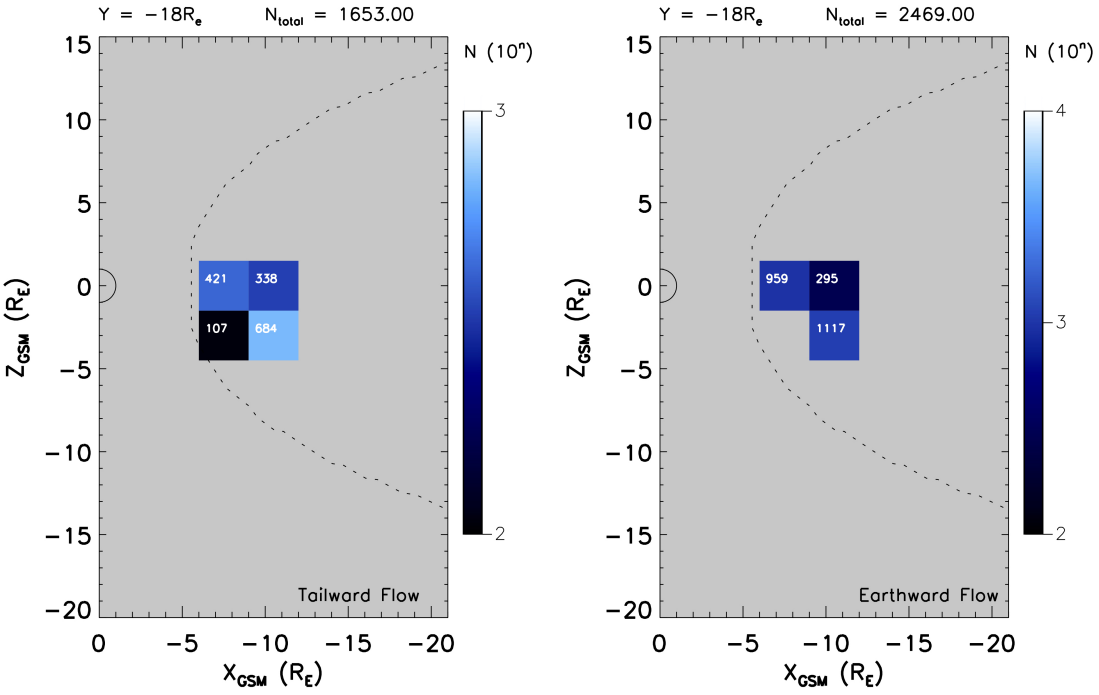

FIGURE B.12: Sample count plot for XZ plane Y = -18 ± 1.5 R_e displaying tailward (left) and earthward (right) plasma flow.

B.2 Ion Velocity Plots - NMM Plane

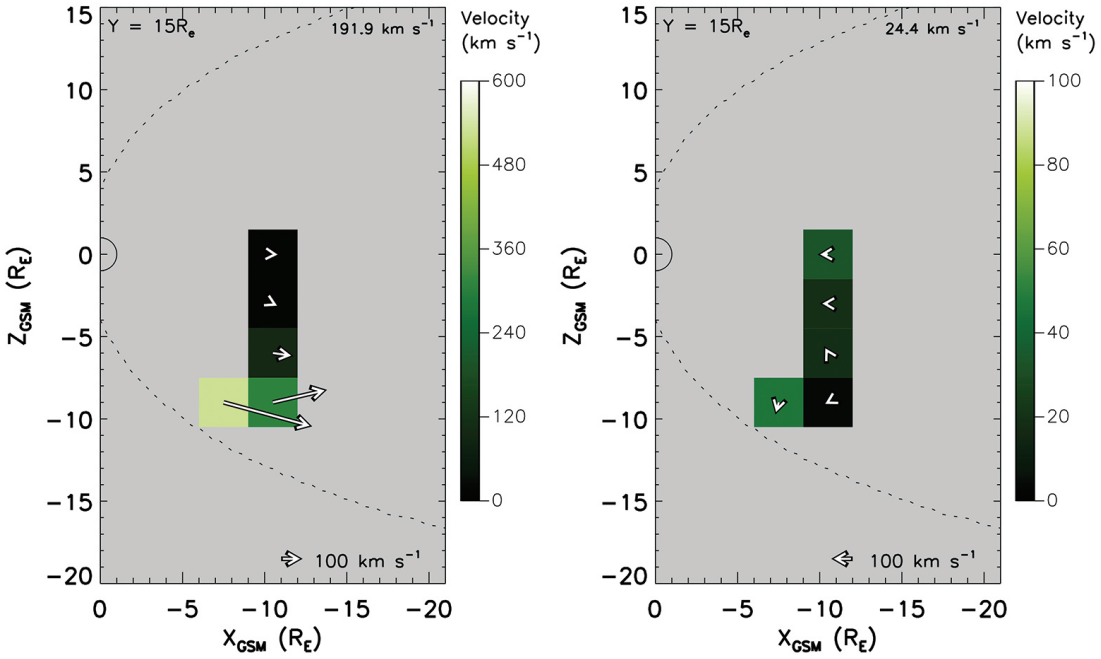

FIGURE B.13: Ion velocity plot for XY plane Y = 15 ± 1.5 R$_e$ displaying tailward (left) and earthward (right) plasma flow.

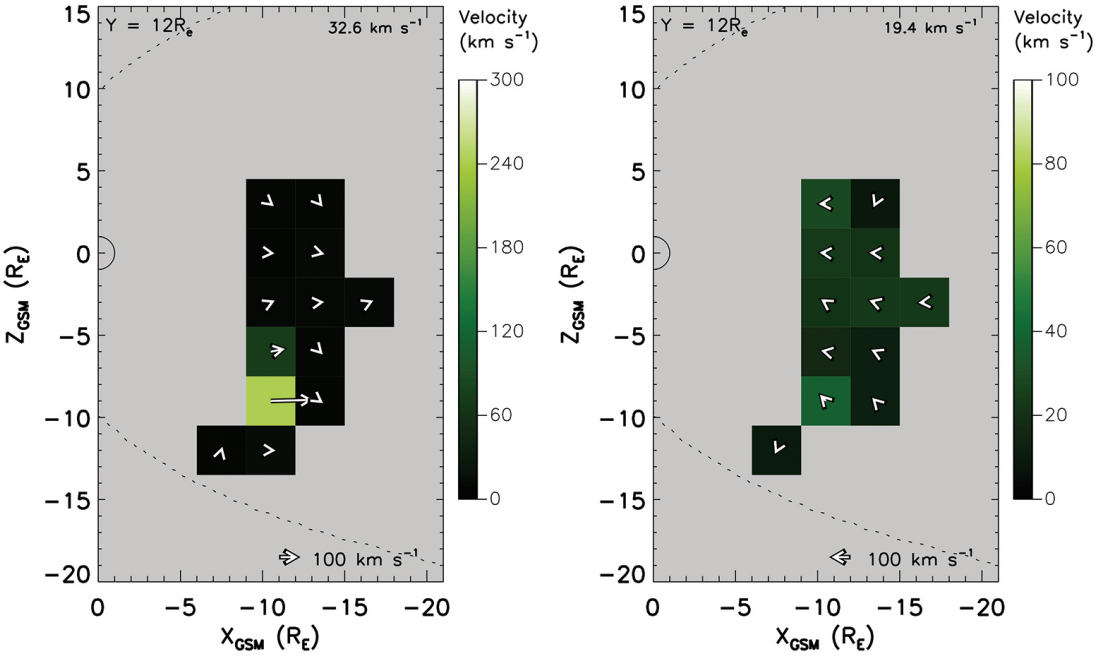

FIGURE B.14: Ion velocity plot for XY plane Y = 12 ± 1.5 R$_e$ displaying tailward (left) and earthward (right) plasma flow.

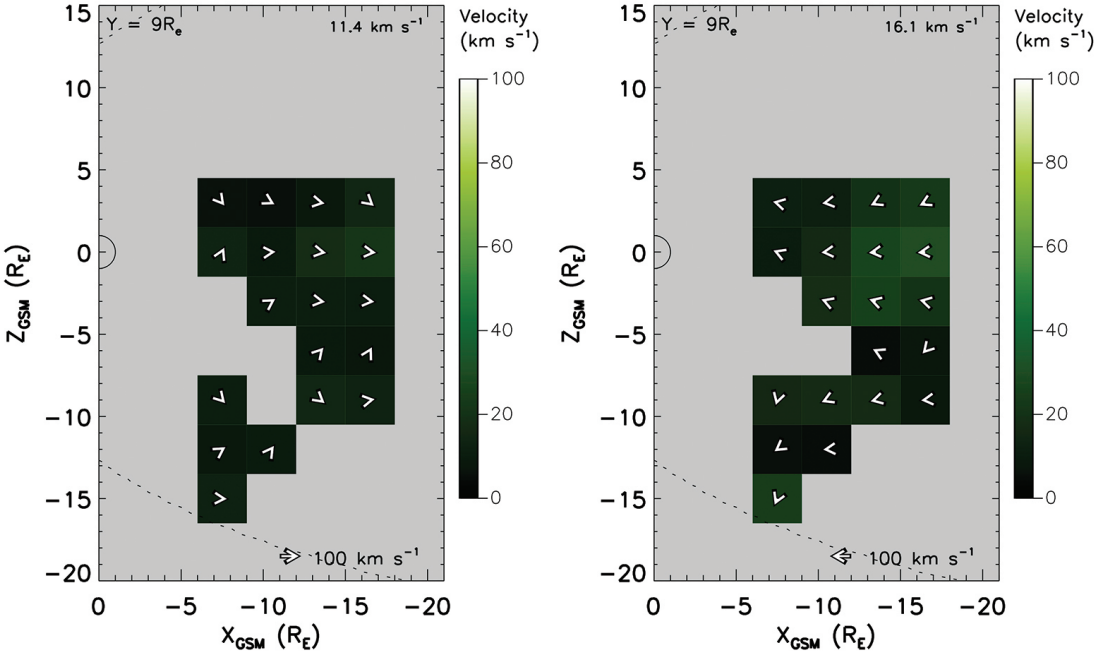

FIGURE B.15: Ion velocity plot for XY plane Y = 9 ± 1.5 R_e displaying tailward (left) and earthward (right) plasma flow.

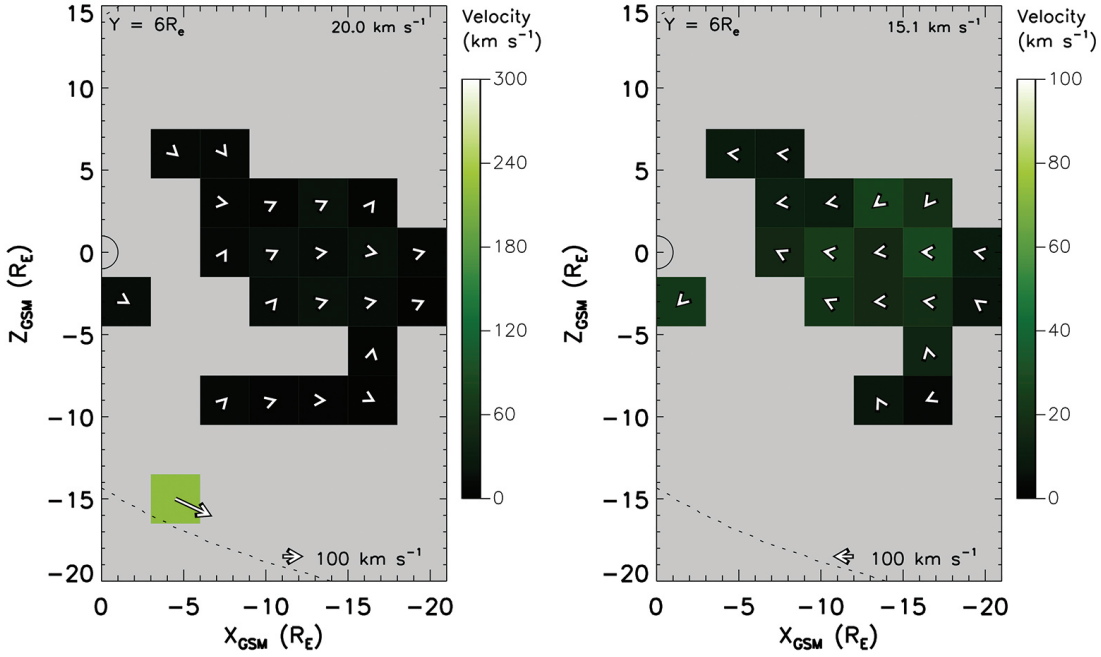

FIGURE B.16: Ion velocity plot for XY plane Y = 6 ± 1.5 R_e displaying tailward (left) and earthward (right) plasma flow.

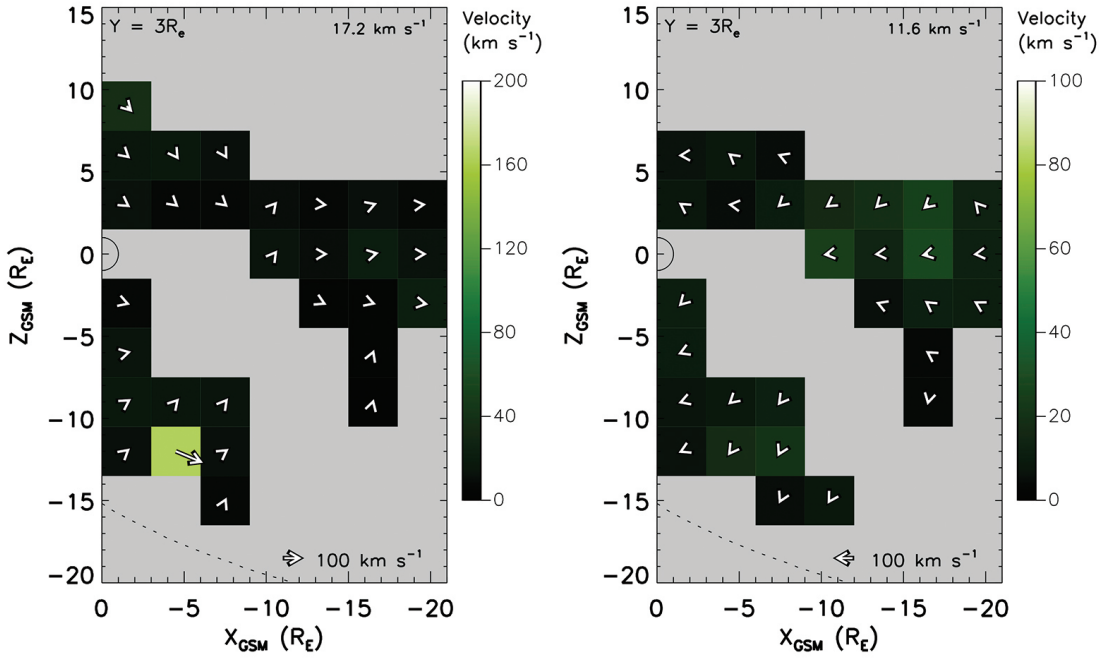

FIGURE B.17: Ion velocity plot for XY plane Y = 3 ± 1.5 R_e displaying tailward (left) and earthward (right) plasma flow.

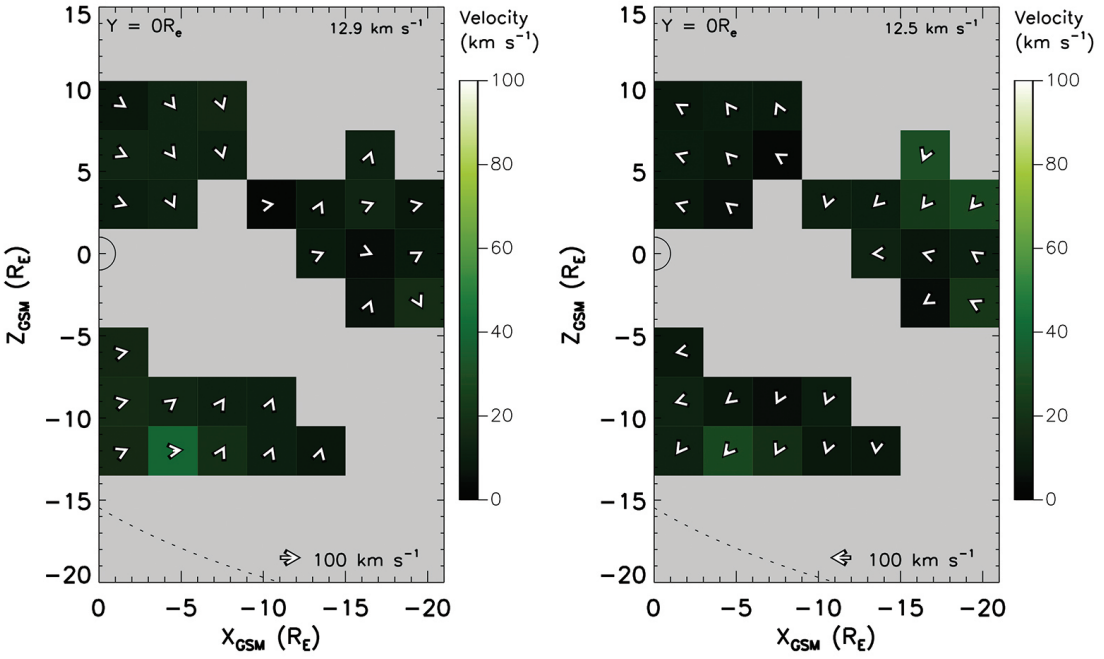

FIGURE B.18: Ion velocity plot for XY plane Y = 0 ± 1.5 R_e displaying tailward (left) and earthward (right) plasma flow.

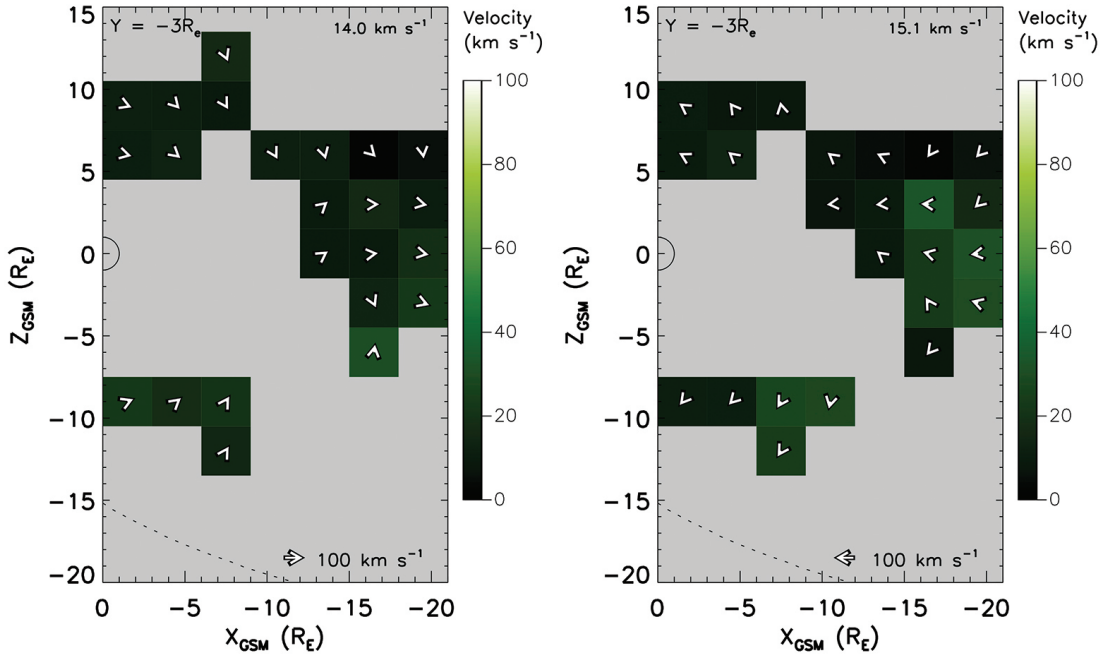

FIGURE B.19: Ion velocity plot for XY plane Y = -3 ± 1.5 R_e displaying tailward (left) and earthward (right) plasma flow.

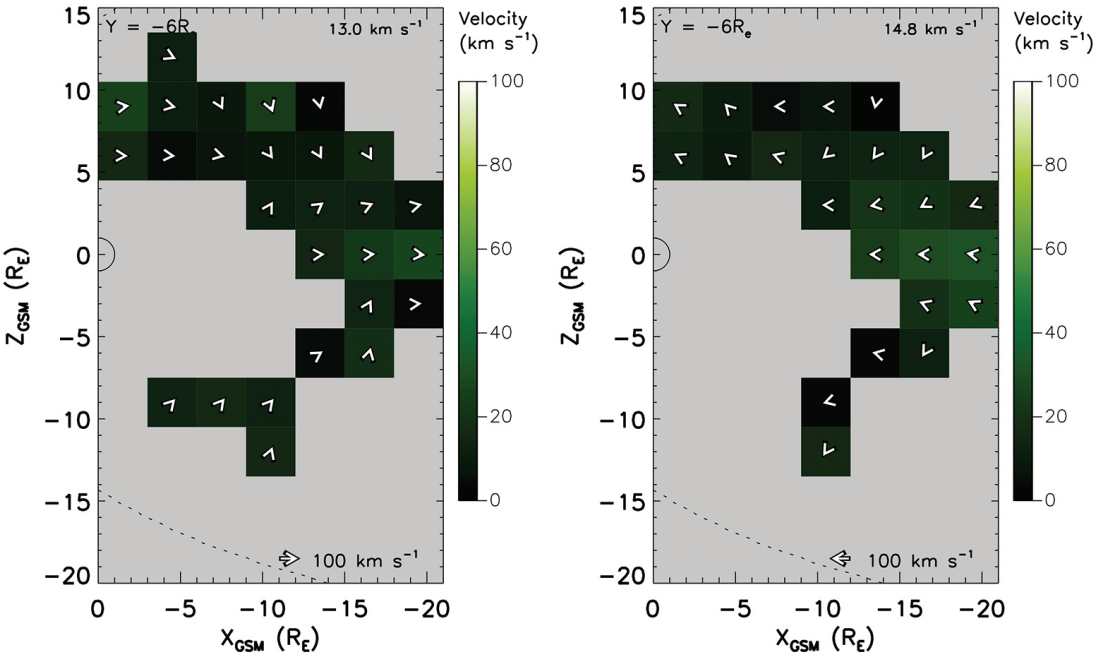

FIGURE B.20: Ion velocity plot for XY plane Y = -6 ± 1.5 R_e displaying tailward (left) and earthward (right) plasma flow.

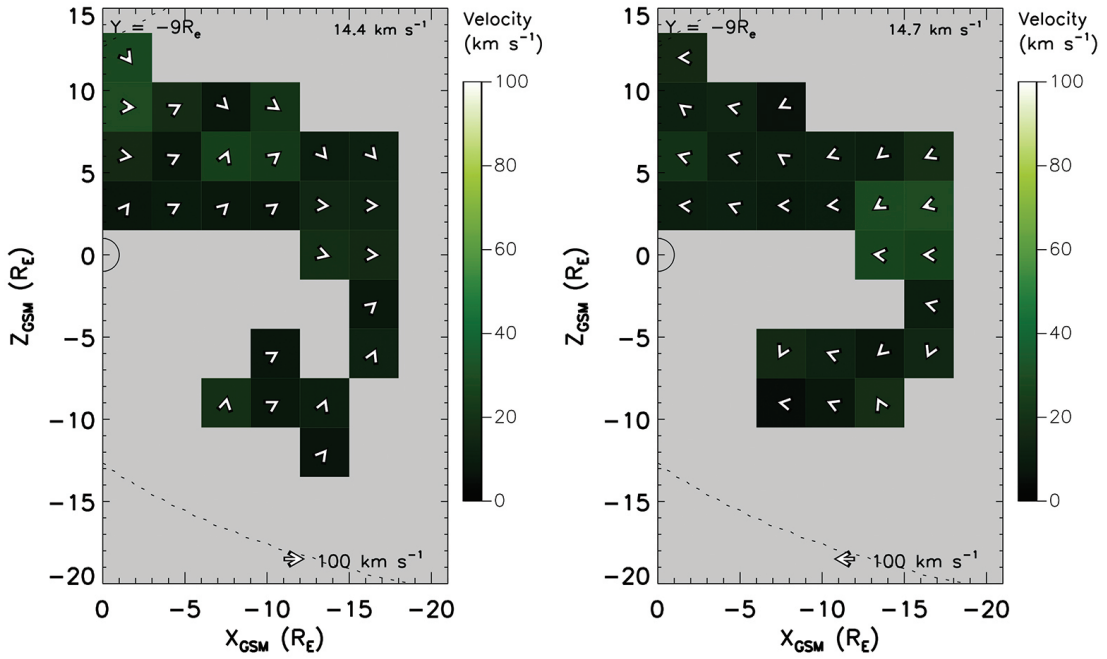

FIGURE B.21: Ion velocity plot for XY plane Y = -9 ± 1.5 R_e displaying tailward (left) and earthward (right) plasma flow.

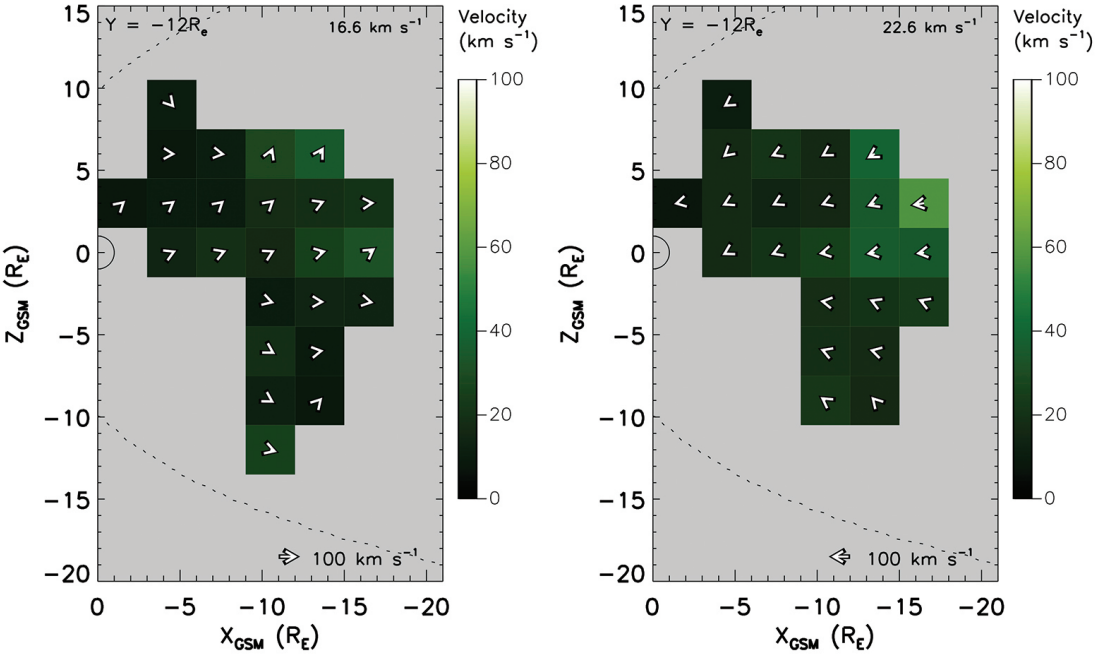

FIGURE B.22: Ion velocity plot for XY plane Y = -12 ± 1.5 R_e displaying tailward (left) and earthward (right) plasma flow.

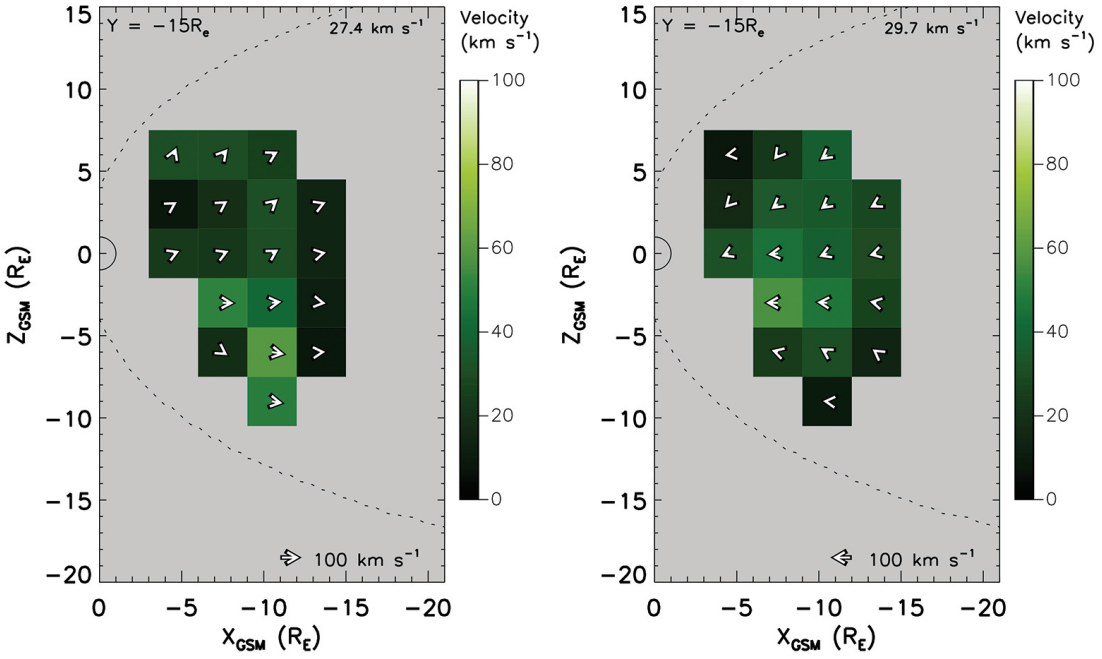

FIGURE B.23: Ion velocity plot for XY plane Y = -15 ± 1.5 R_e displaying tailward (left) and earthward (right) plasma flow.

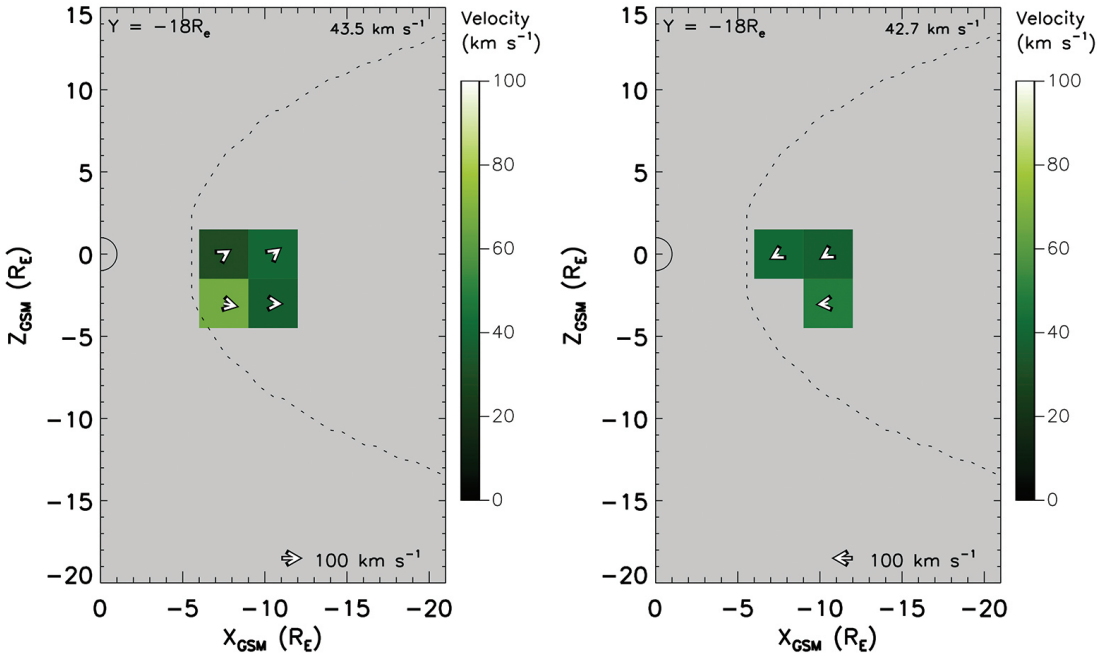

FIGURE B.24: Ion velocity plot for XY plane Y = -18 ± 1.5 R_e displaying tailward (left) and earthward (right) plasma flow.

Appendix C

Sample Count and Ion Flow Figures for All Substorm Phases

C.1 Sample Counts - EQ Plane

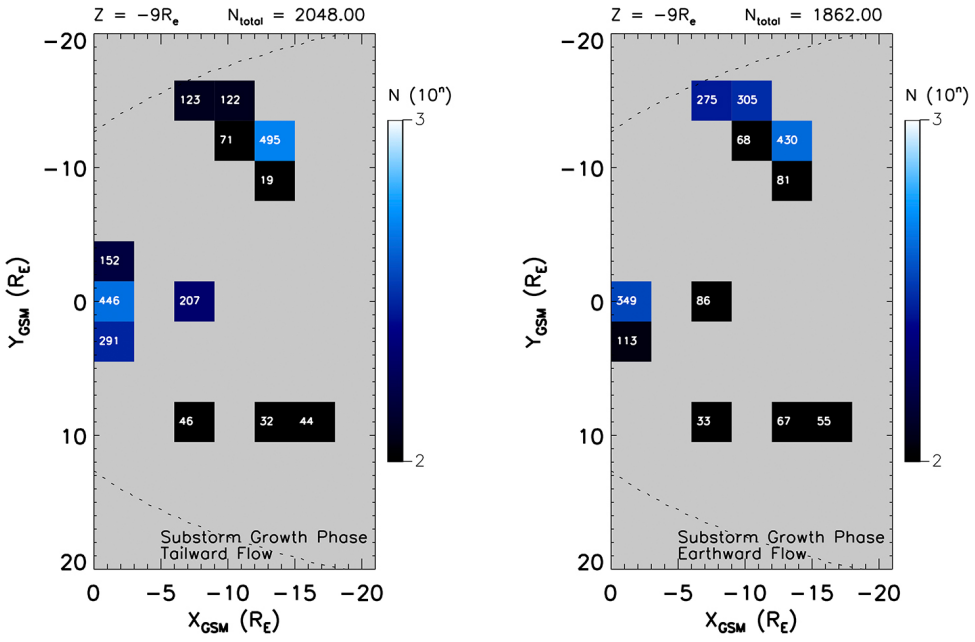

FIGURE C.1: Sample count plot for the XY plane Z = -9 ± 4.5 R_E displaying tailward (left) and earthward (right) plasma flow during the substorm growth phase.

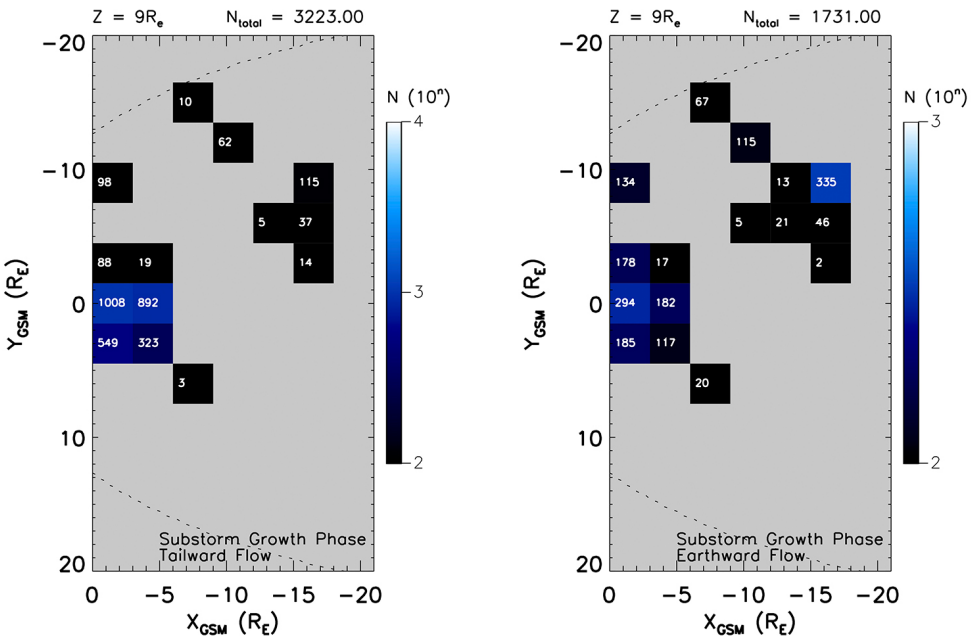

FIGURE C.2: Sample count plot for the XY plane Z = 9 ± 4.5 R_E displaying tailward (left) and earthward (right) plasma flow during the substorm growth phase.

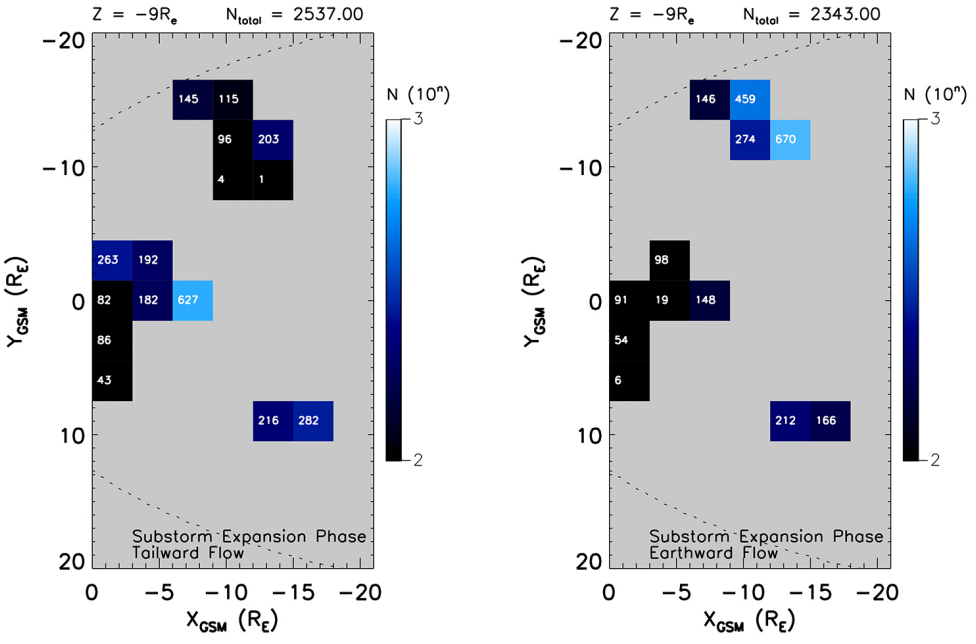

FIGURE C.3: Sample count plot for the XY plane Z = -9 ± 4.5 R_E displaying tailward (left) and earthward (right) plasma flow during the substorm expansion phase.

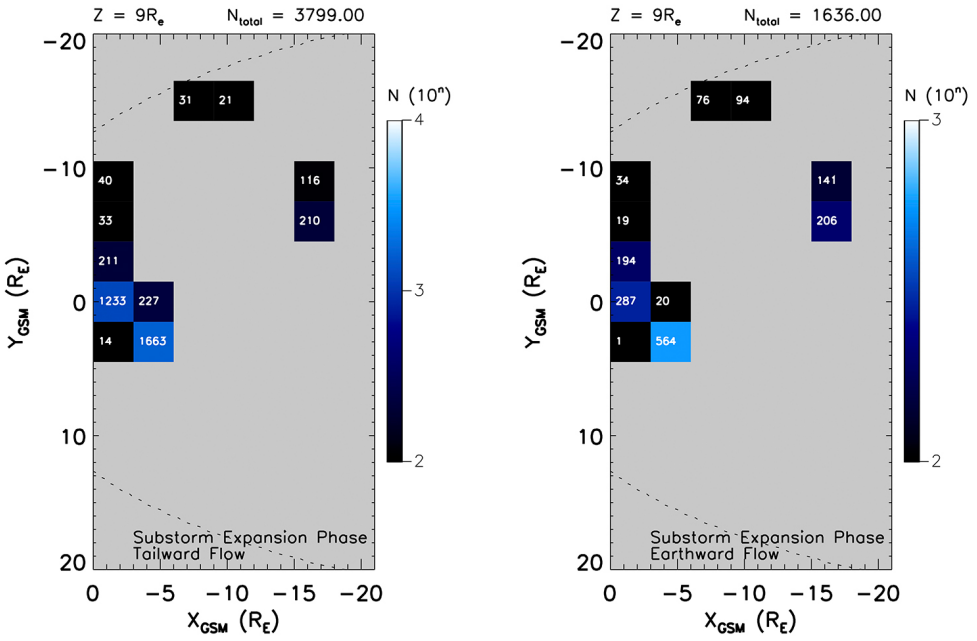

FIGURE C.4: Sample count plot for the XY plane Z = 9 ± 4.5 R_E displaying tailward (left) and earthward (right) plasma flow during the substorm expansion phase.

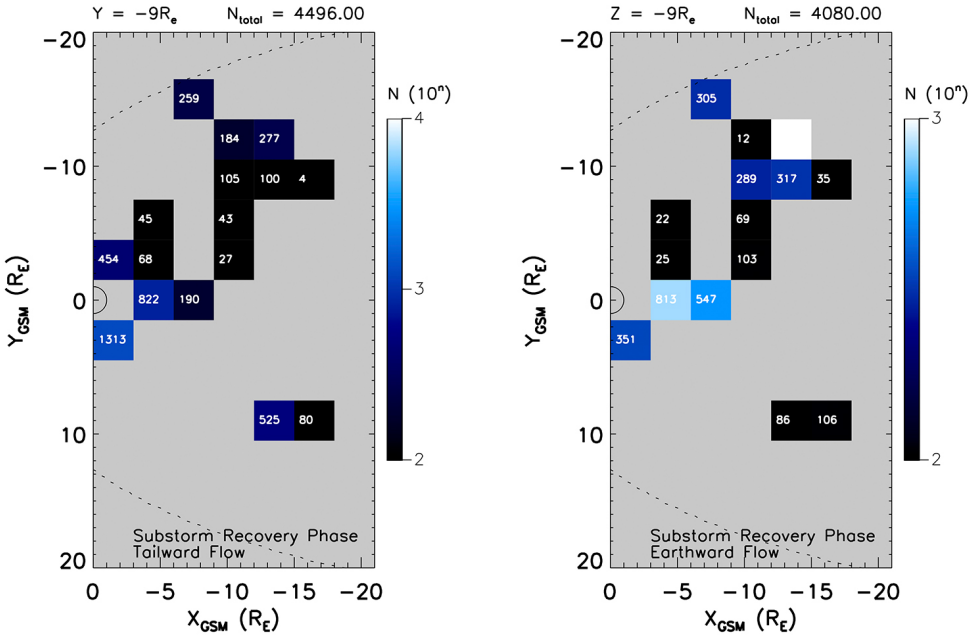

FIGURE C.5: Sample count plot for the XY plane Z = -9 ± 4.5 R_E displaying tailward (left) and earthward (right) plasma flow during the substorm recovery phase.

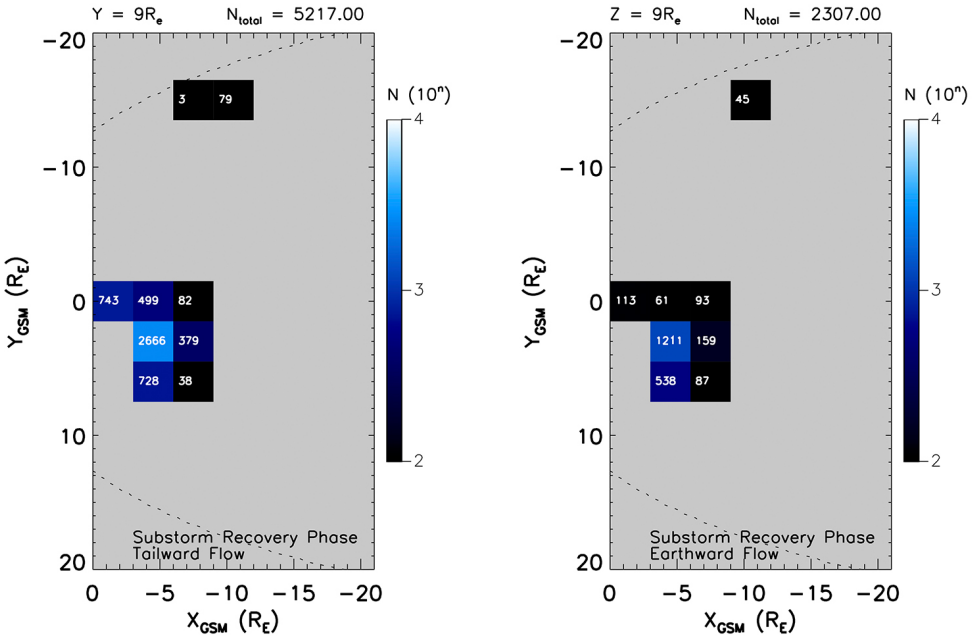

FIGURE C.6: Sample count plot for the XY plane Z = 9 ± 4.5 R_E displaying tailward (left) and earthward (right) plasma flow during the substorm recovery phase.

C.2 Ion Velocity Plots - EQ Plane

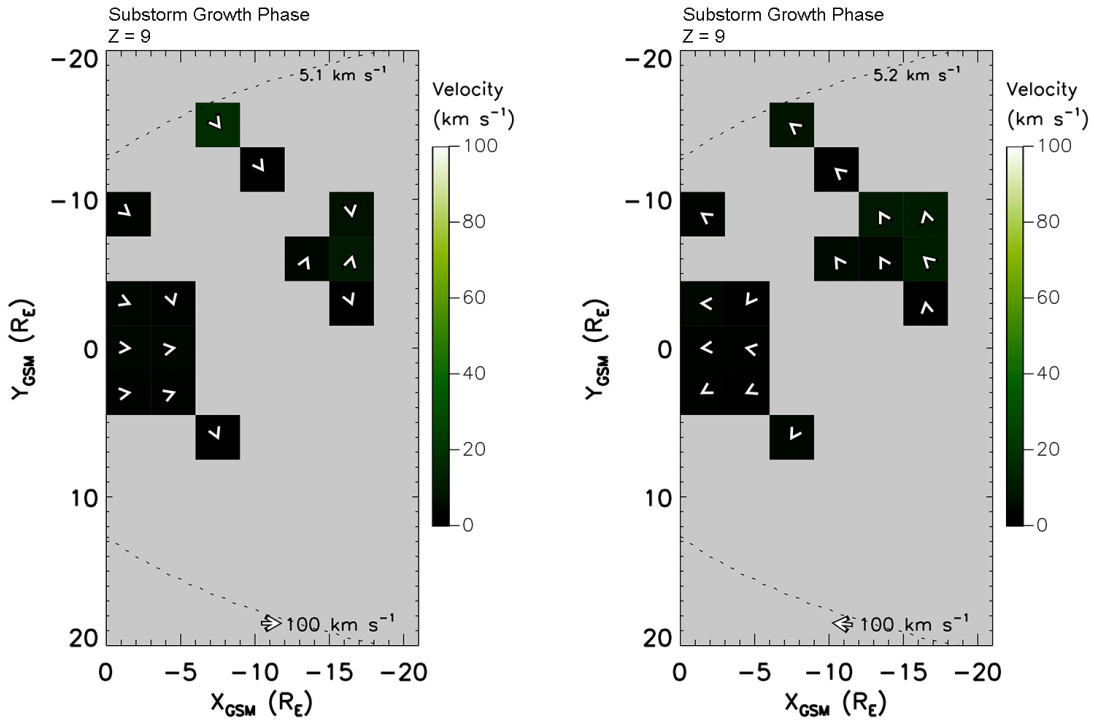

FIGURE C.7: Ion velocity plots displaying tailward (left) and earthward (right) plasma flow during the substorm growth phase in the XY plane where Z = 9±4.5 R_E .

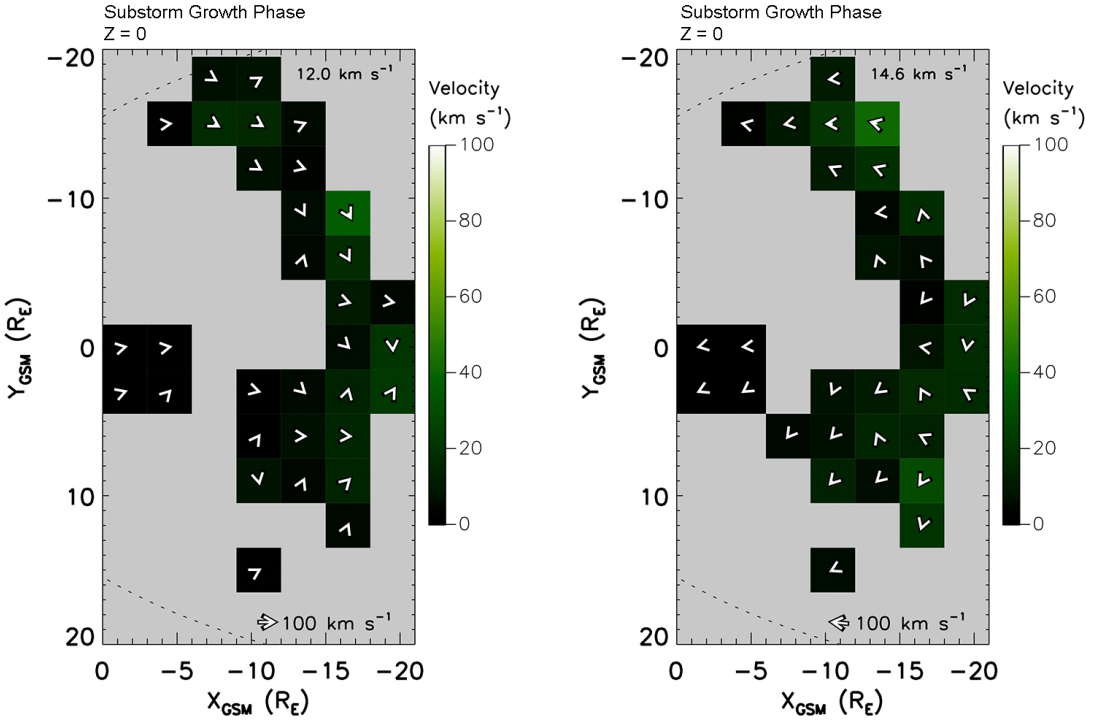

FIGURE C.8: Ion velocity plots displaying tailward (left) and earthward (right) plasma flow during the substorm growth phase in the XY plane where Z = 0±4.5 R_E .

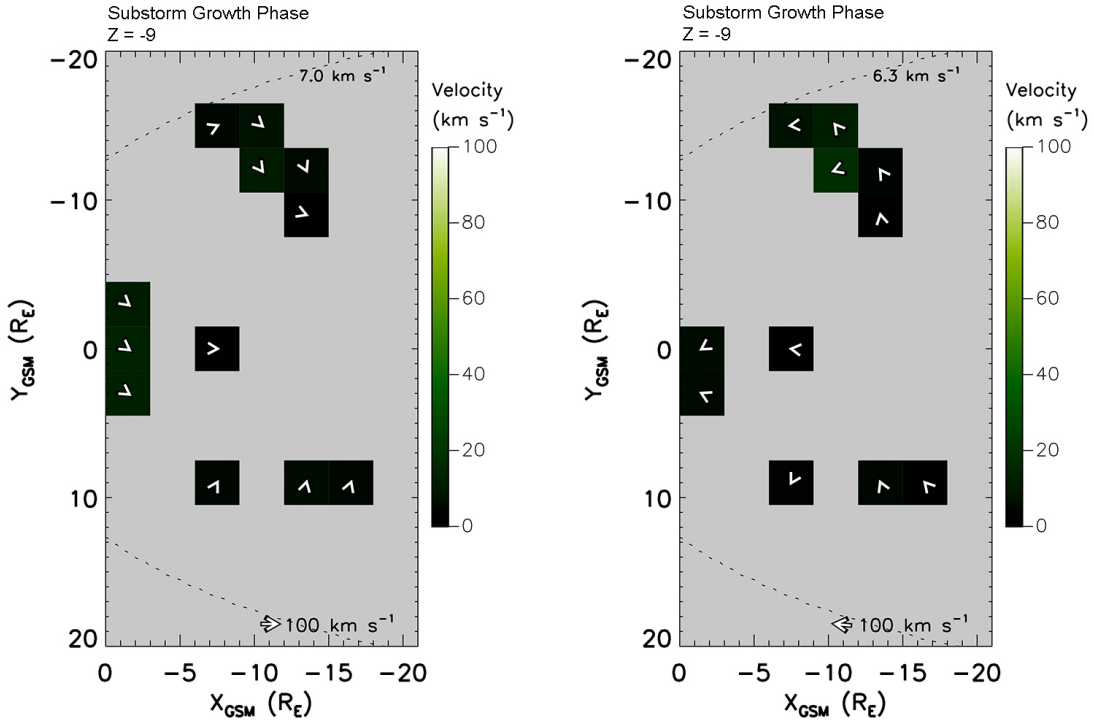

FIGURE C.9: Ion velocity plots displaying tailward (left) and earthward (right) plasma flow during the substorm growth phase in the XY plane where Z = -9±4.5 R_E .

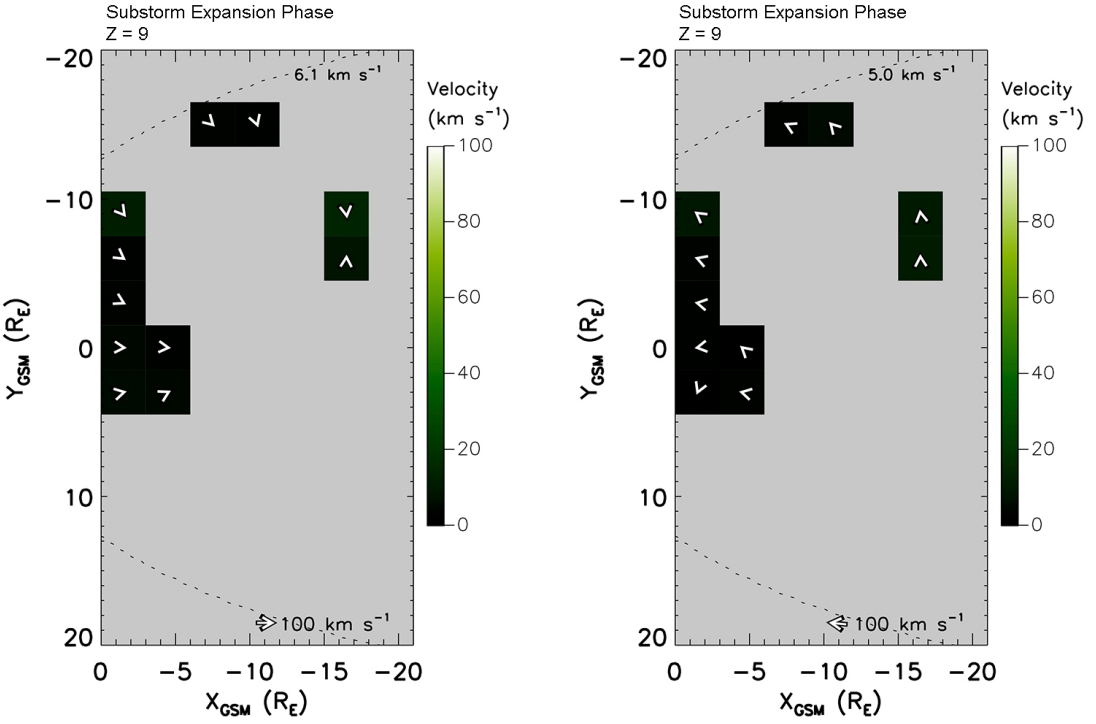

FIGURE C.10: Ion velocity plots displaying tailward (left) and earthward (right) plasma flow during the substorm expansion phase in the XY plane where Z = 9±4.5 R_E .

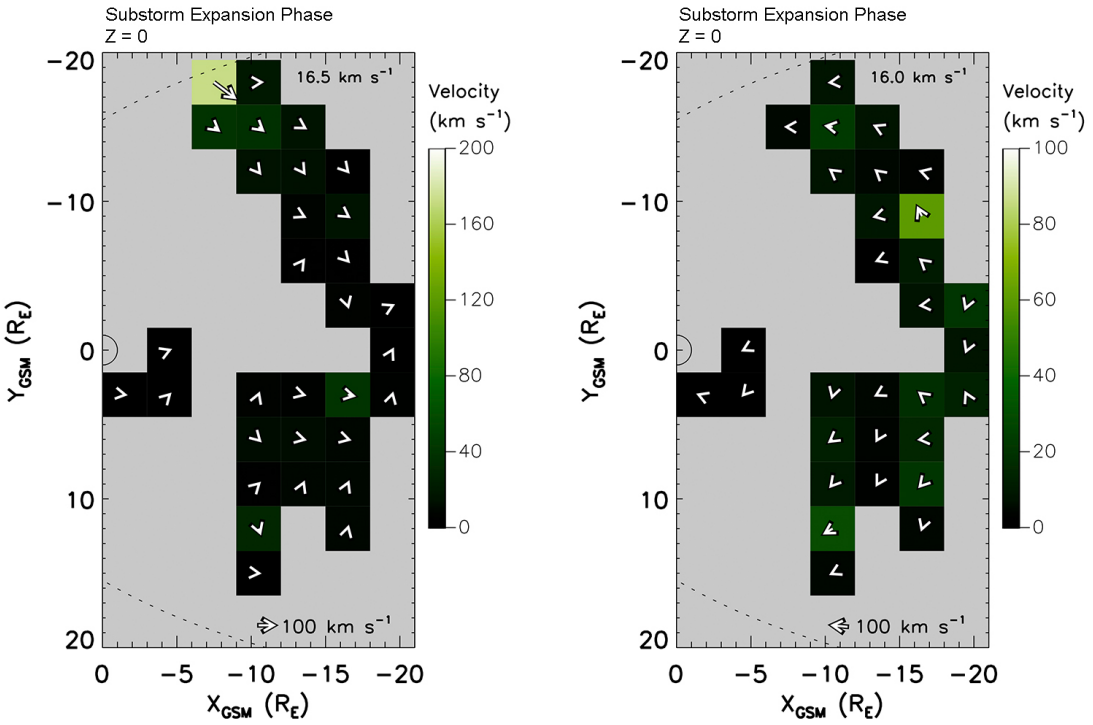

FIGURE C.11: Ion velocity plots displaying tailward (left) and earthward (right) plasma flow during the substorm expansion phase in the XY plane where Z = 0±4.5 R_E .

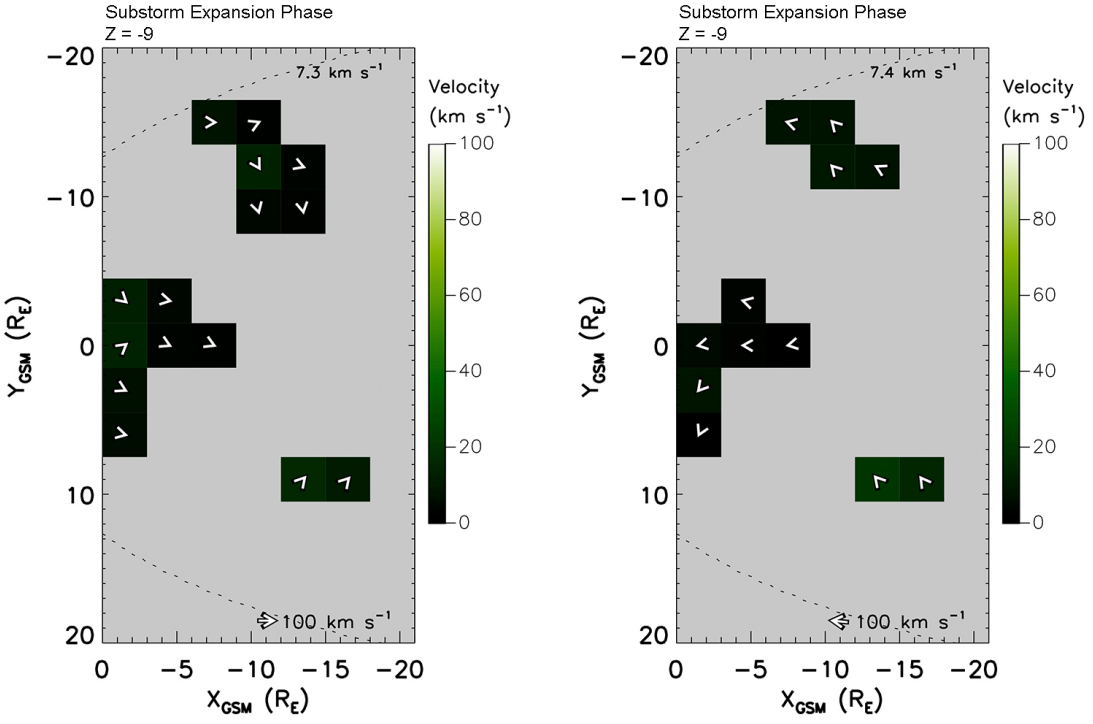

FIGURE C.12: Ion velocity plots displaying tailward (left) and earthward (right) plasma flow during the substorm expansion phase in the XY plane where Z = -9±4.5 R_E .

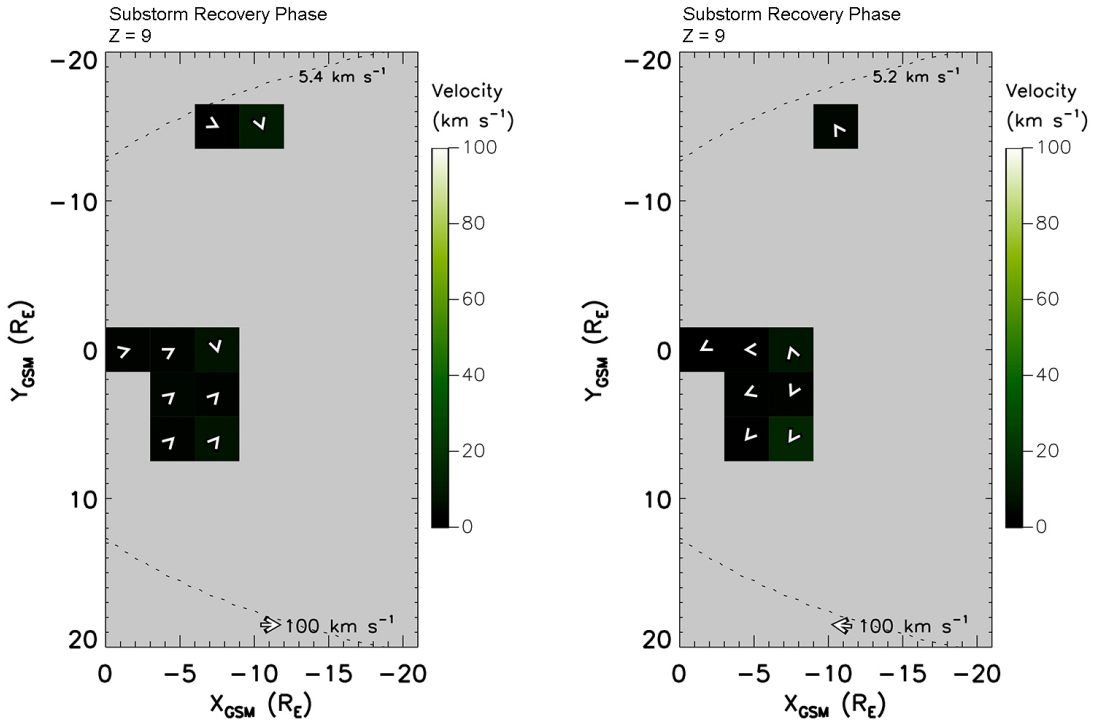

FIGURE C.13: Ion velocity plots displaying tailward (left) and earthward (right) plasma flow during the substorm growth phase in the XY plane where Z = 9±4.5 R_E .

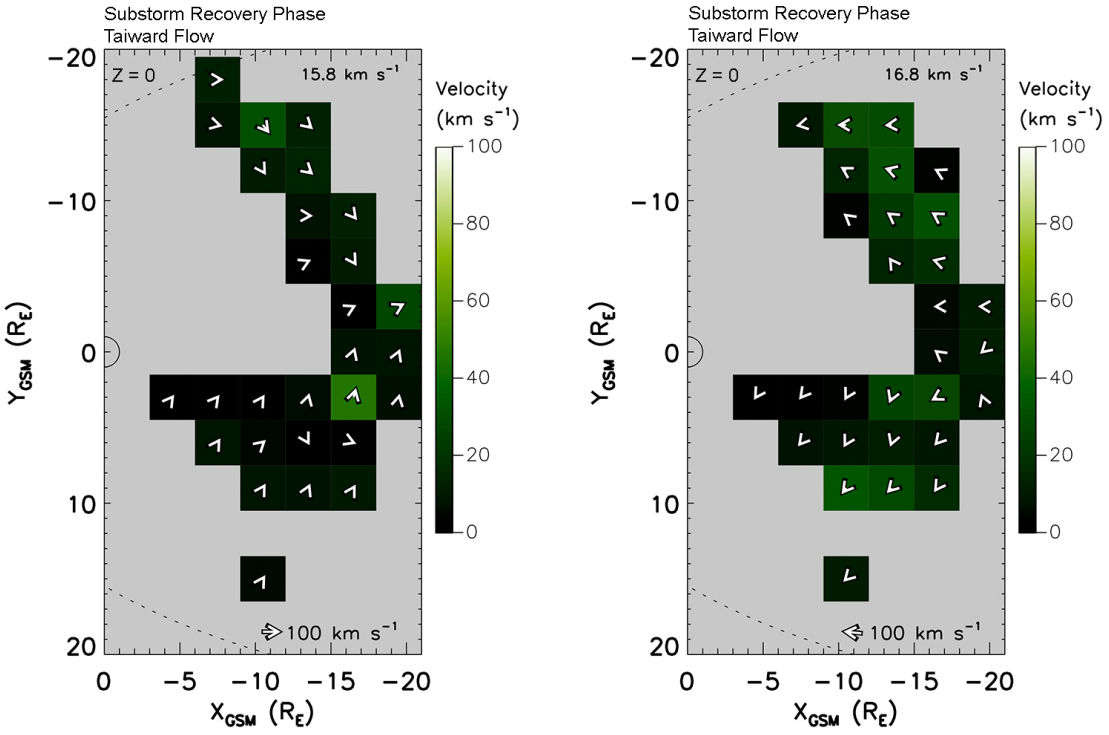

FIGURE C.14: Ion velocity plots displaying tailward (left) and earthward (right) plasma flow during the substorm recovery phase in the XY plane where Z = 0±4.5 R_E .

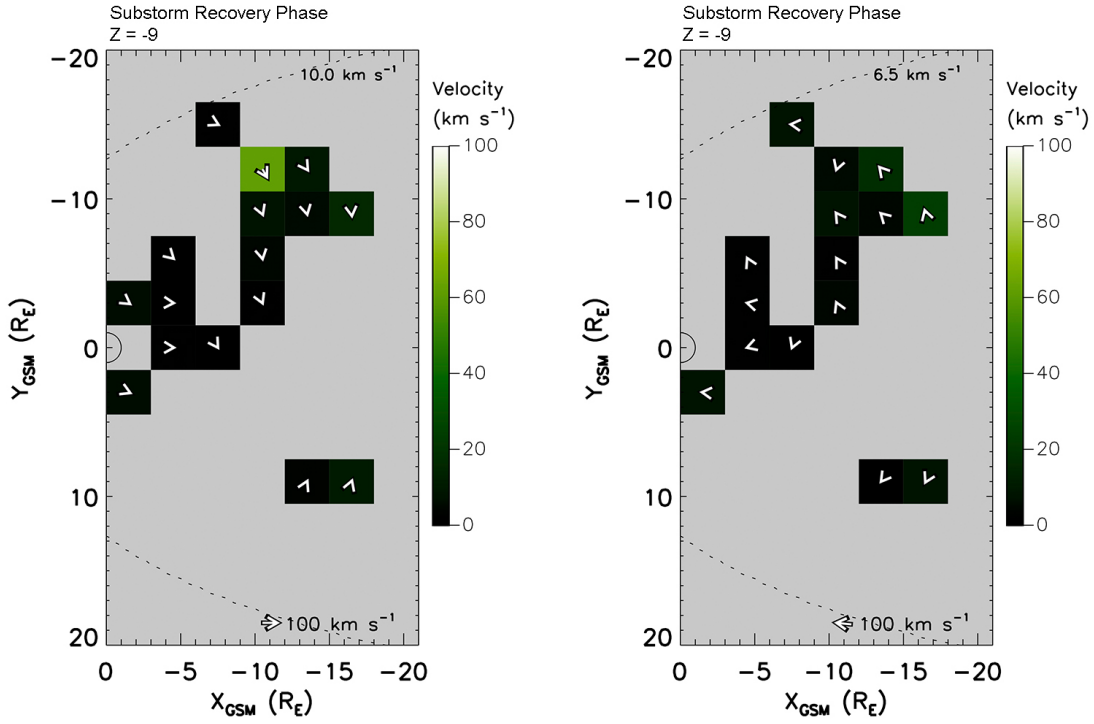

FIGURE C.15: Ion velocity plots displaying tailward (left) and earthward (right) plasma flow during the substorm recovery phase in the XY plane where Z = -9±4.5 R_E .

C.3 Sample Counts - NMM Plane

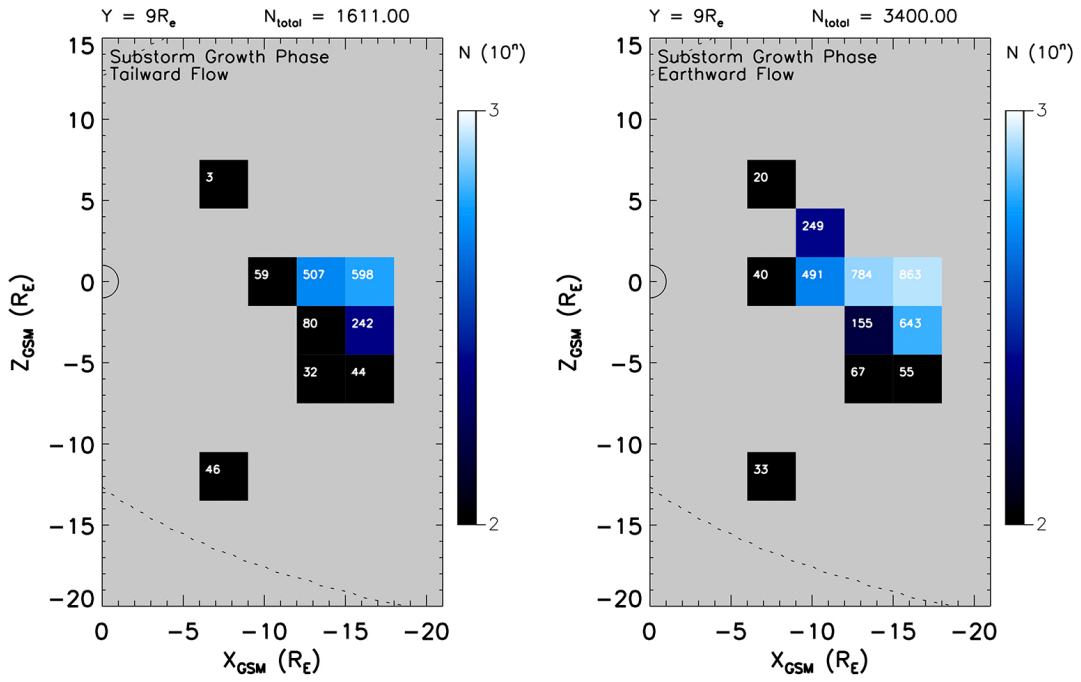

FIGURE C.16: Sample count plot for the XZ plane Y = 9 ± 4.5 R_E displaying tailward (left) and earthward (right) plasma flow during the substorm growth phase.

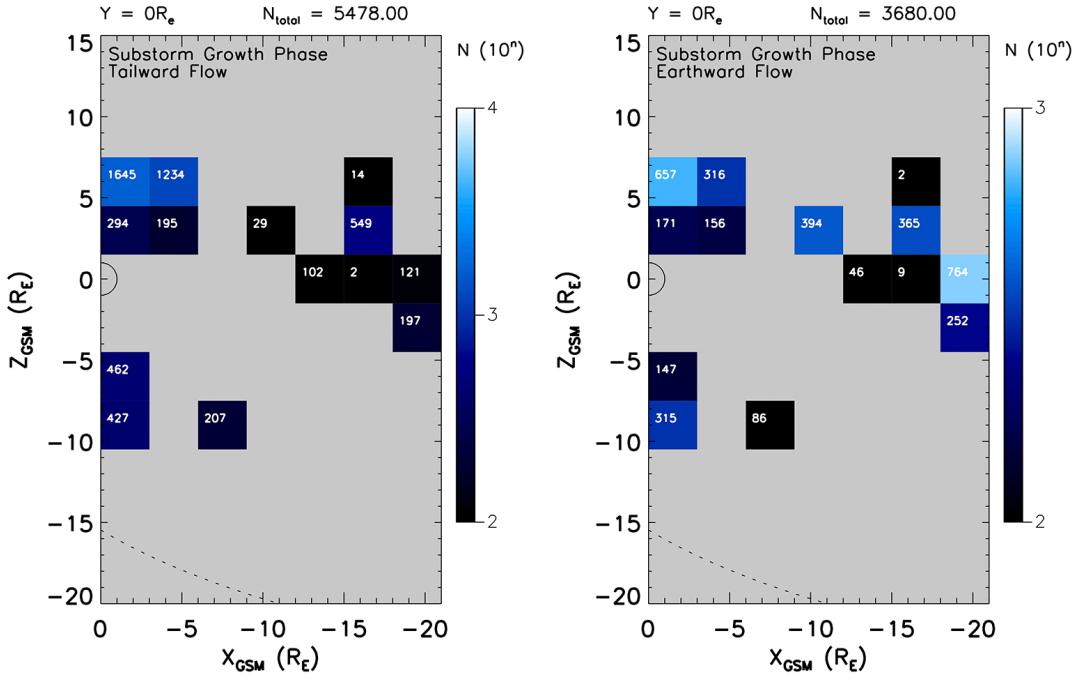

FIGURE C.17: Sample count plot for the XZ plane Y = 0 ± 4.5 R_E displaying tailward (left) and earthward (right) plasma flow during the substorm growth phase.

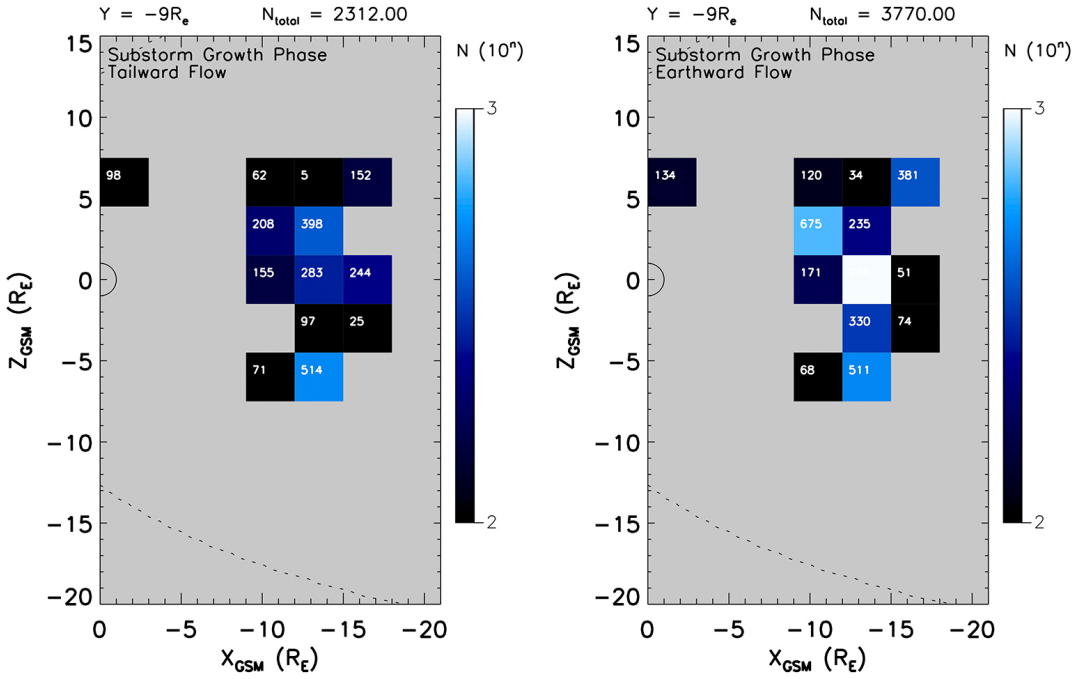

FIGURE C.18: Sample count plot for the XZ plane Y = -9 ± 4.5 R_E displaying tailward (left) and earthward (right) plasma flow during the substorm growth phase.

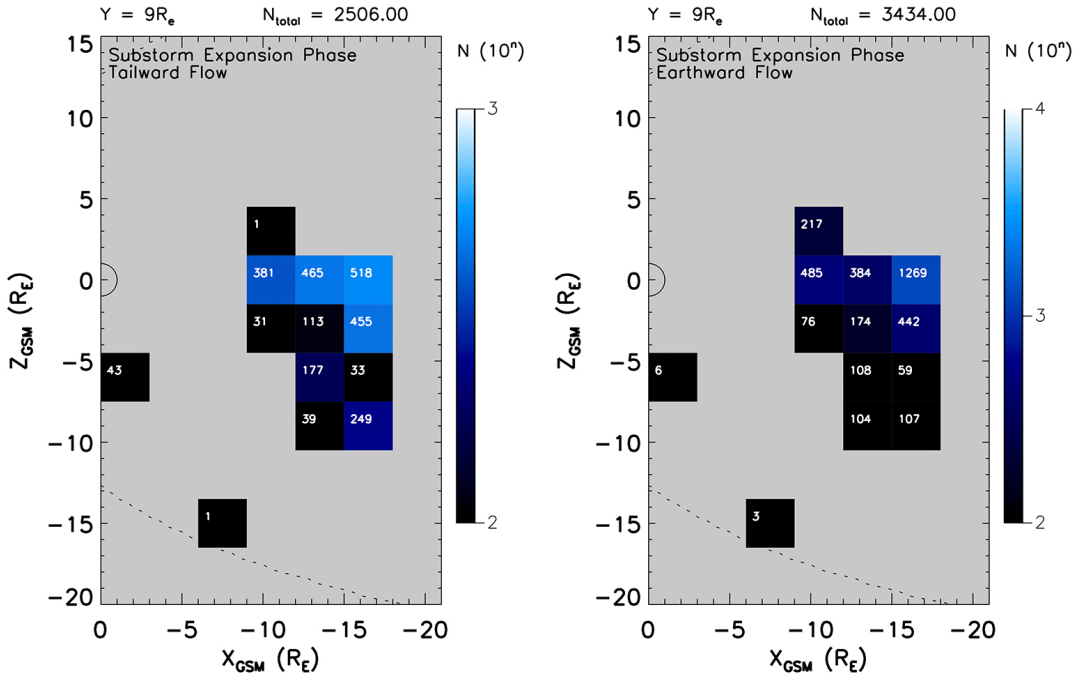

FIGURE C.19: Sample count plot for the XZ plane Y = 9 ± 4.5 R_E displaying tailward (left) and earthward (right) plasma flow during the substorm expansion phase.

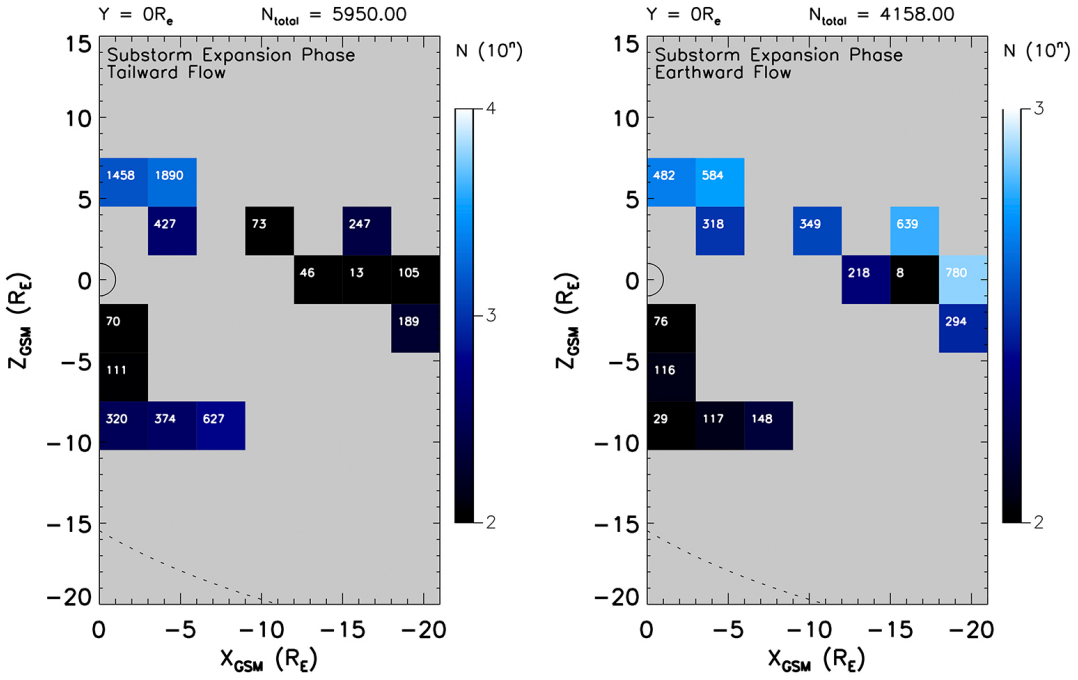

FIGURE C.20: Sample count plot for the XZ plane Y = 0 ± 4.5 R_E displaying tailward (left) and earthward (right) plasma flow during the substorm expansion phase.

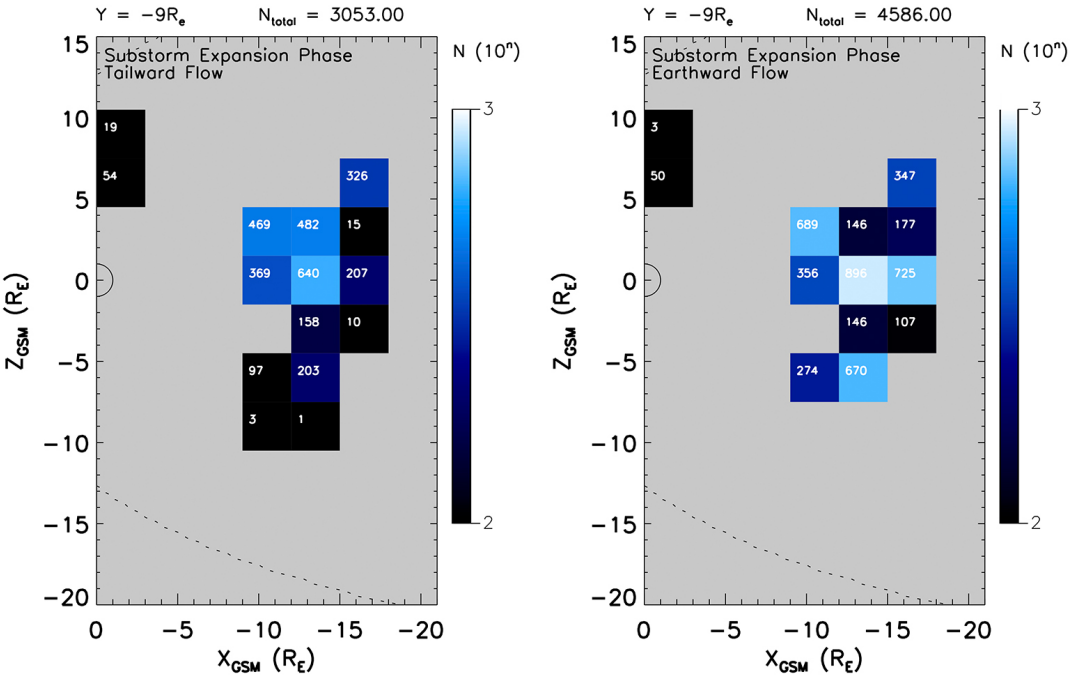

FIGURE C.21: Sample count plot for the XZ plane Y = -9 ± 4.5 R_E displaying tailward (left) and earthward (right) plasma flow during the substorm expansion phase.

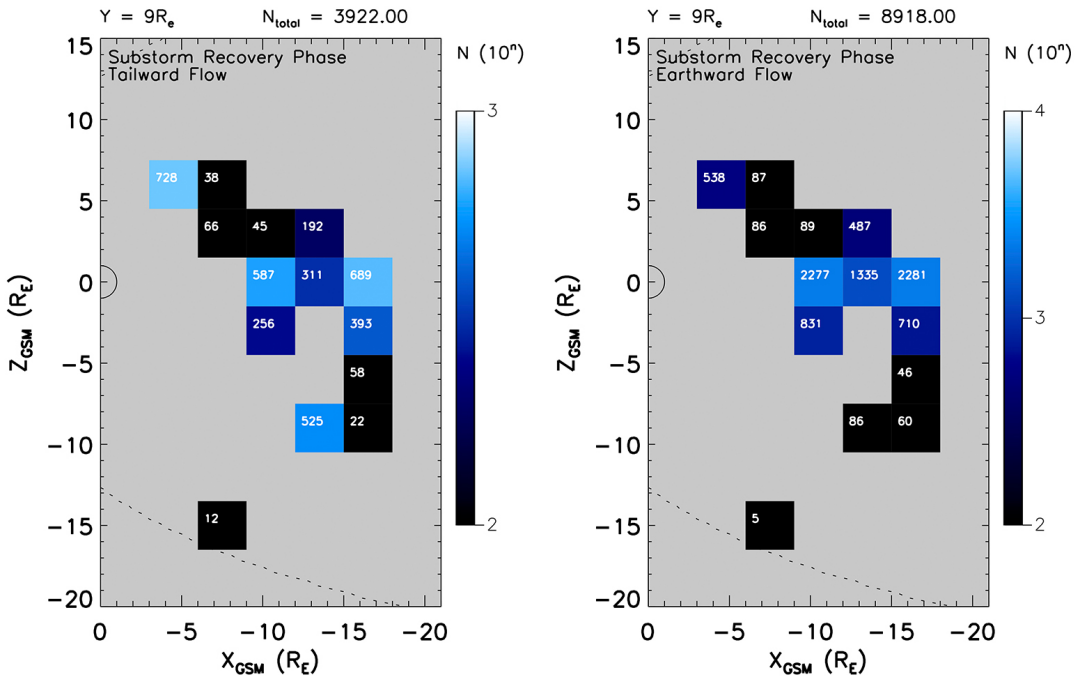

FIGURE C.22: Sample count plot for the XZ plane Y = 9 ± 4.5 R_E displaying tailward (left) and earthward (right) plasma flow during the substorm recovery phase.

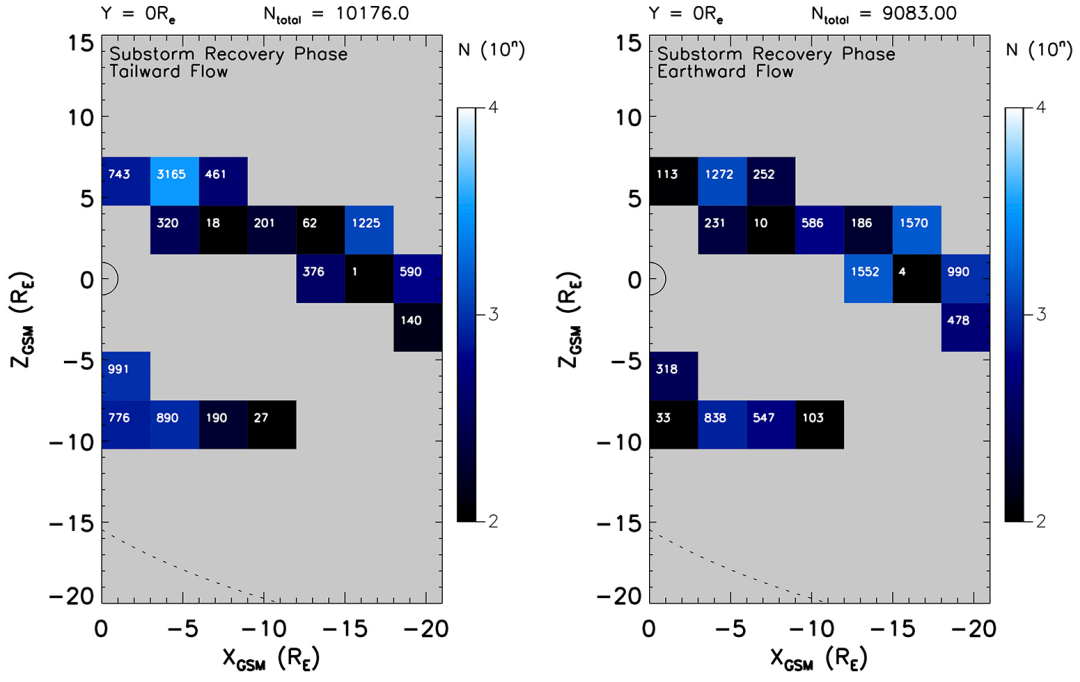

FIGURE C.23: Sample count plot for the XZ plane Y = 0 ± 4.5 R_E displaying tailward (left) and earthward (right) plasma flow during the substorm recovery phase.

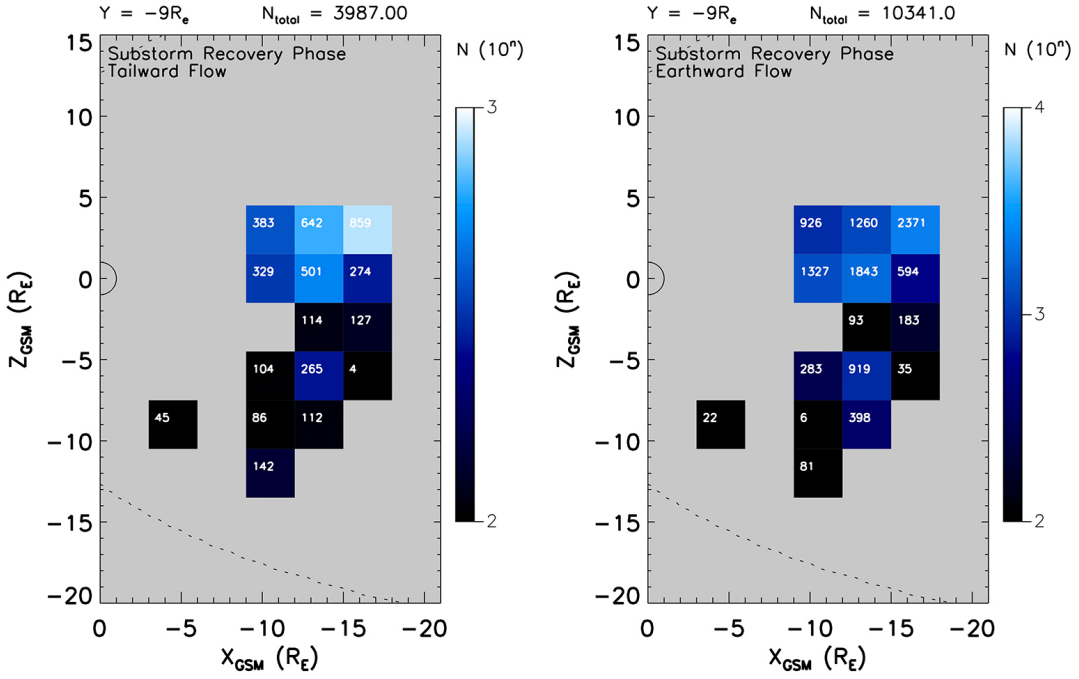

FIGURE C.24: Sample count plot for the XZ plane Y = -9 ± 4.5 R_E displaying tailward (left) and earthward (right) plasma flow during the substorm recovery phase.

C.4 Ion Velocity Plots - NMM Plane

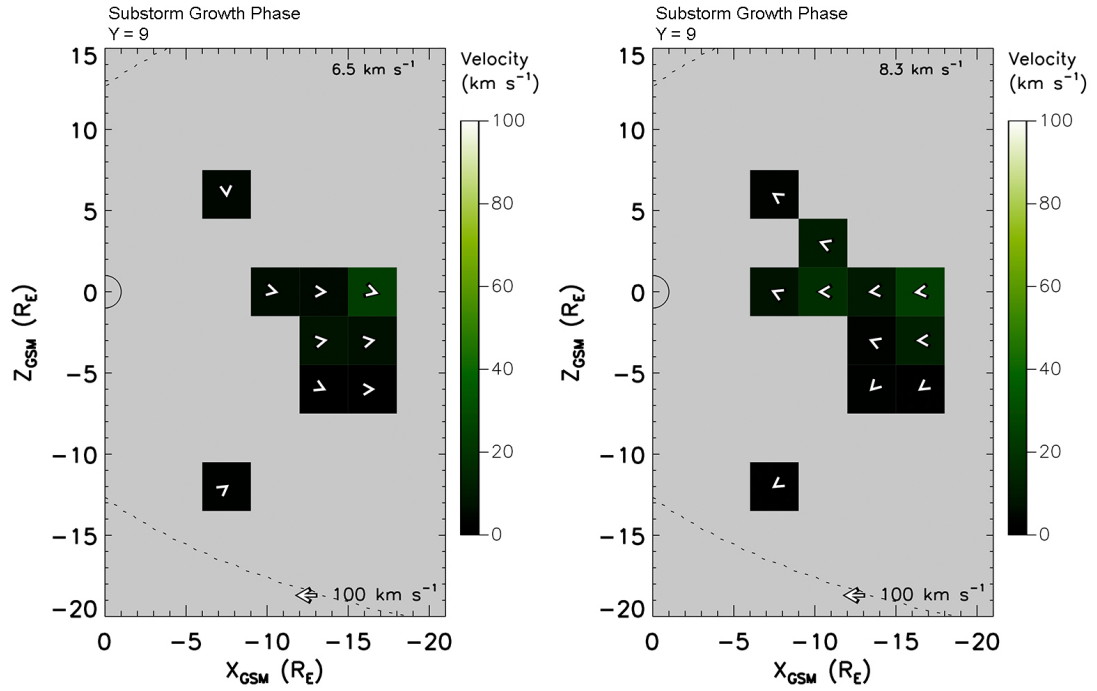

FIGURE C.25: Ion velocity plots displaying tailward (left) and earthward (right) plasma flow during the substorm growth phase in the XZ plane where Y = 9±4.5 R_E .

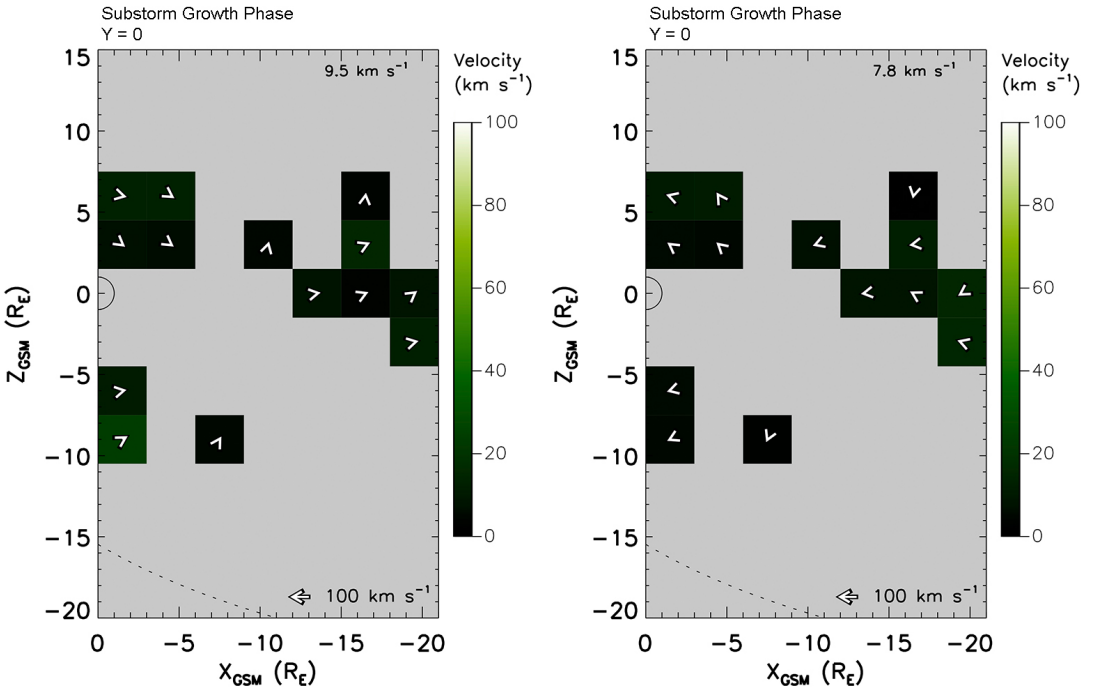

FIGURE C.26: Ion velocity plots displaying tailward (left) and earthward (right) plasma flow during the substorm growth phase in the XZ plane where Y = 0±4.5 R_E .

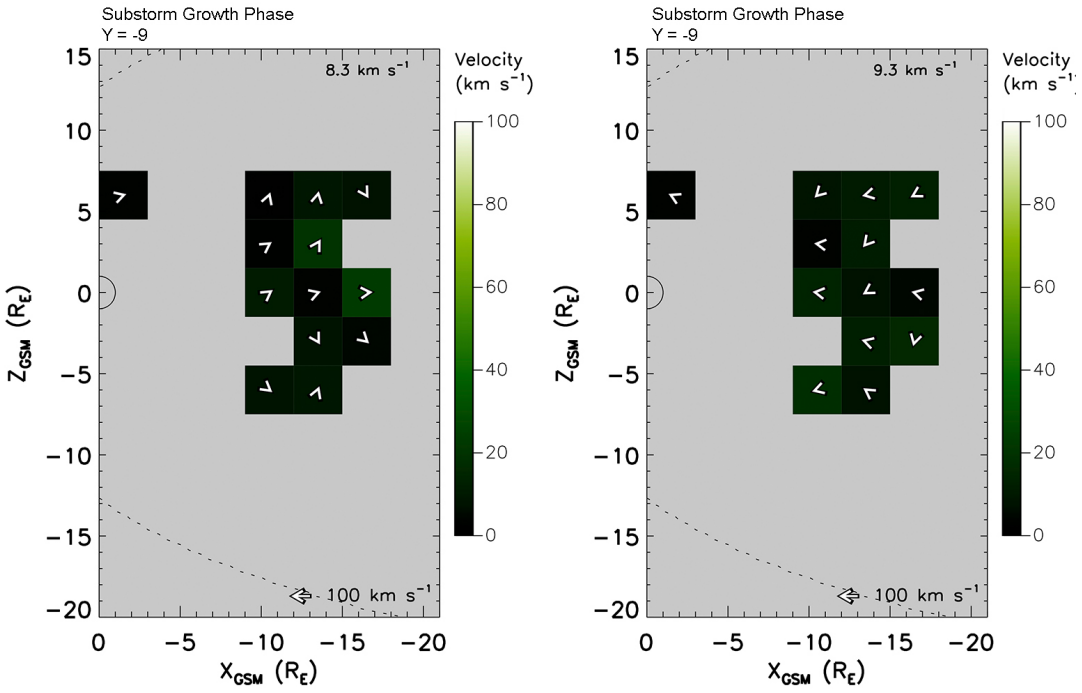

FIGURE C.27: Ion velocity plots displaying tailward (left) and earthward (right) plasma flow during the substorm growth phase in the XZ plane where Y = -9±4.5 R_E .

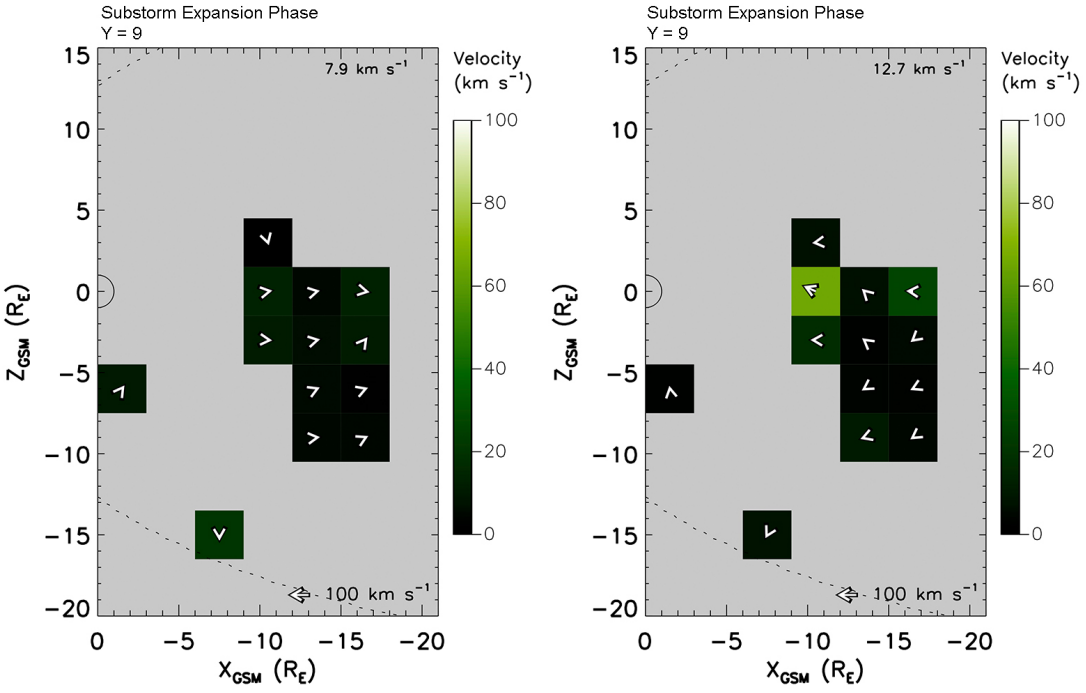

FIGURE C.28: Ion velocity plots displaying tailward (left) and earthward (right) plasma flow during the substorm expansion phase in the XZ plane where Y = 9±4.5 R_E .

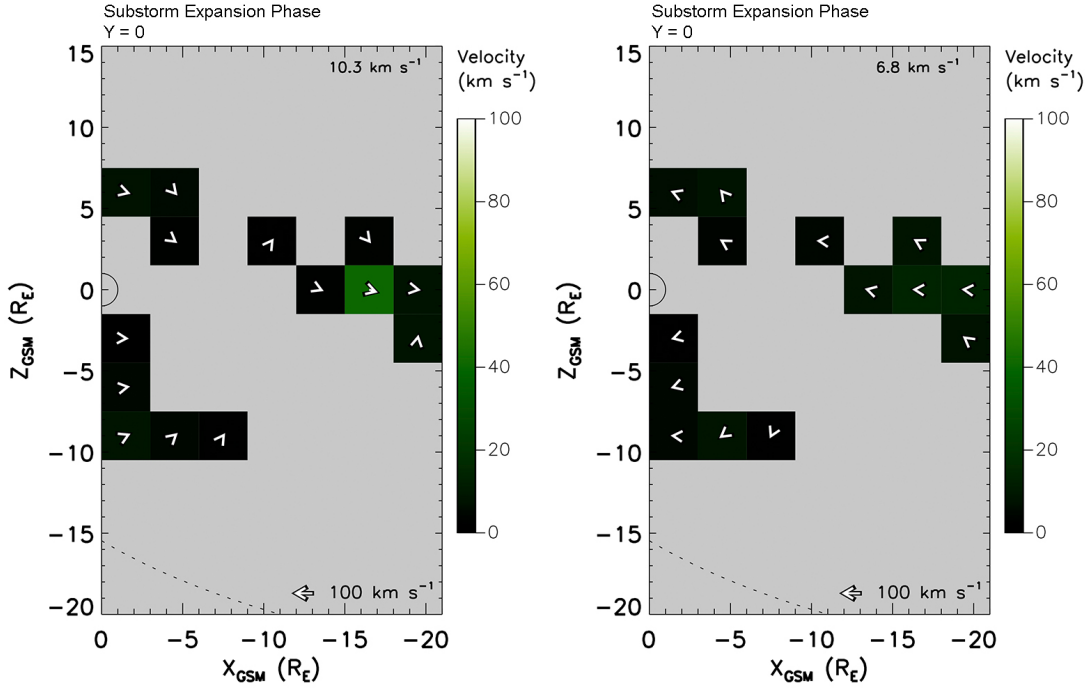

FIGURE C.29: Ion velocity plots displaying tailward (left) and earthward (right) plasma flow during the substorm expansion phase in the XZ plane where Y = 0±4.5 R_E .

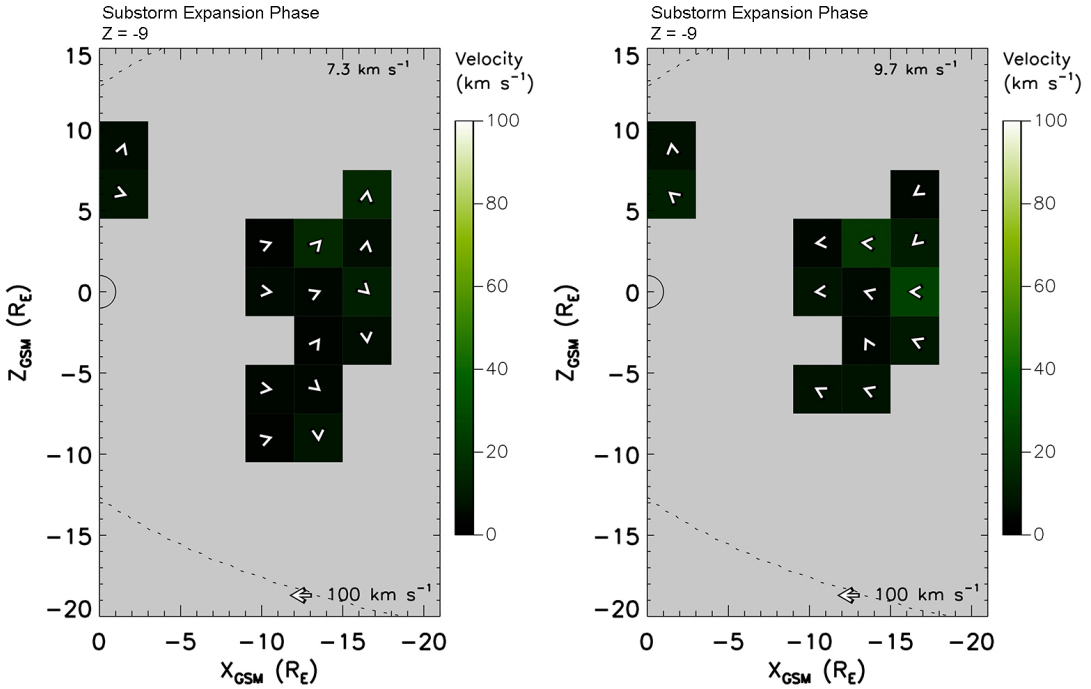

FIGURE C.30: Ion velocity plots displaying tailward (left) and earthward (right) plasma flow during the substorm expansion phase in the XZ plane where Y = -9±4.5 R_E .

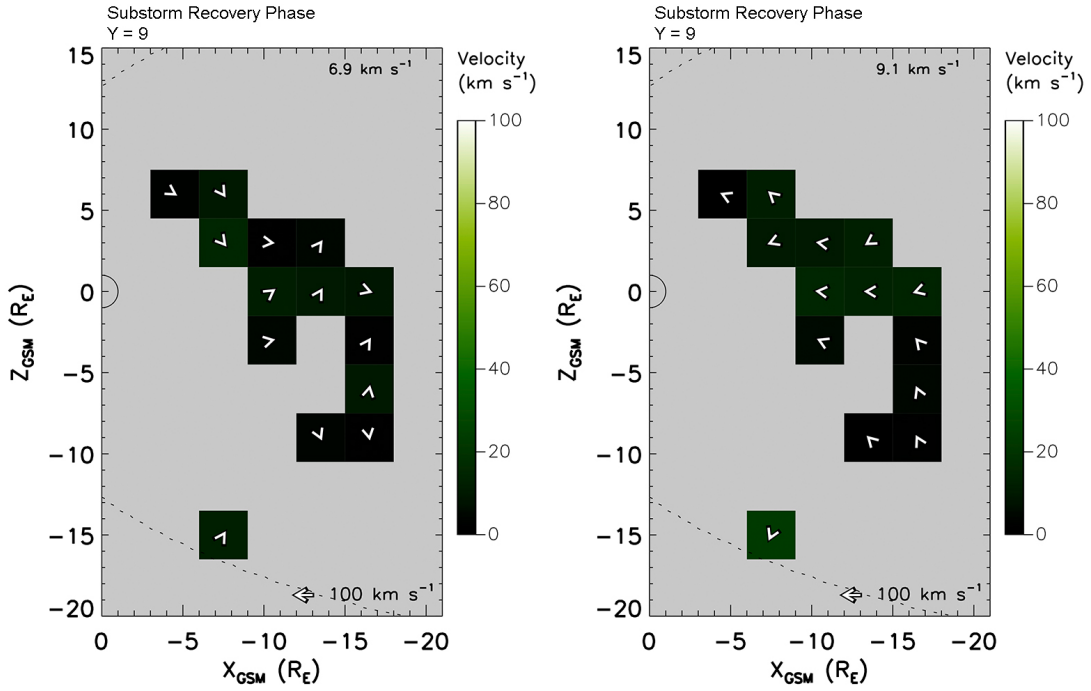

FIGURE C.31: Ion velocity plots displaying tailward (left) and earthward (right) plasma flow during the substorm growth phase in the XZ plane where Y = 9±4.5 R_E .

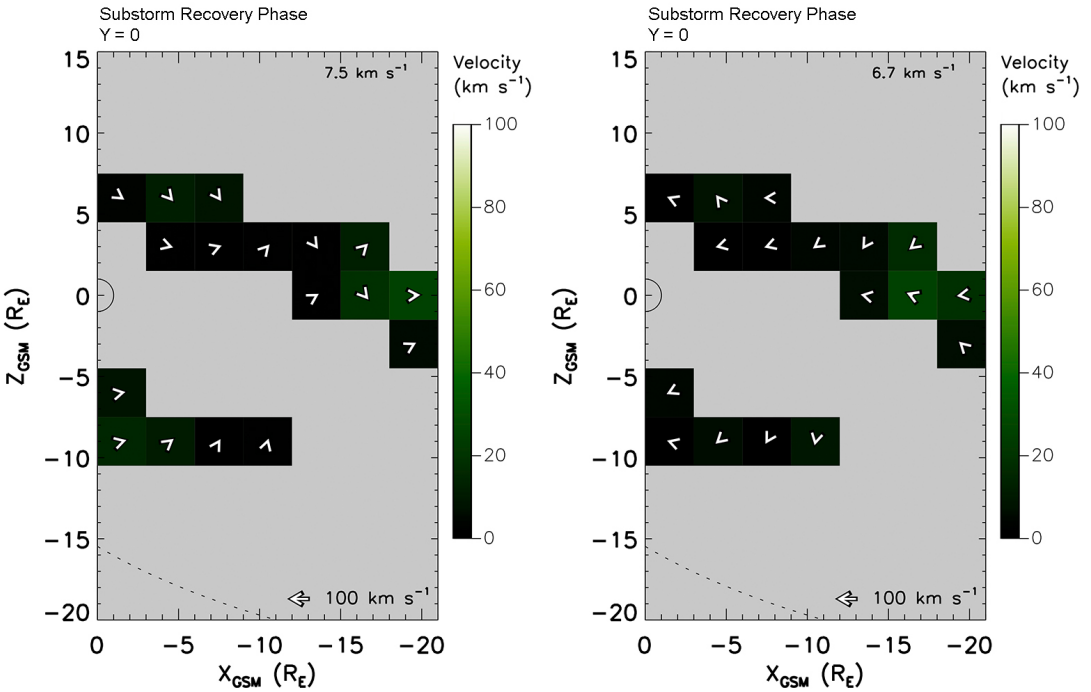

FIGURE C.32: Ion velocity plots displaying tailward (left) and earthward (right) plasma flow during the substorm recovery phase in the XZ plane where Y = 0±4.5 R_E .

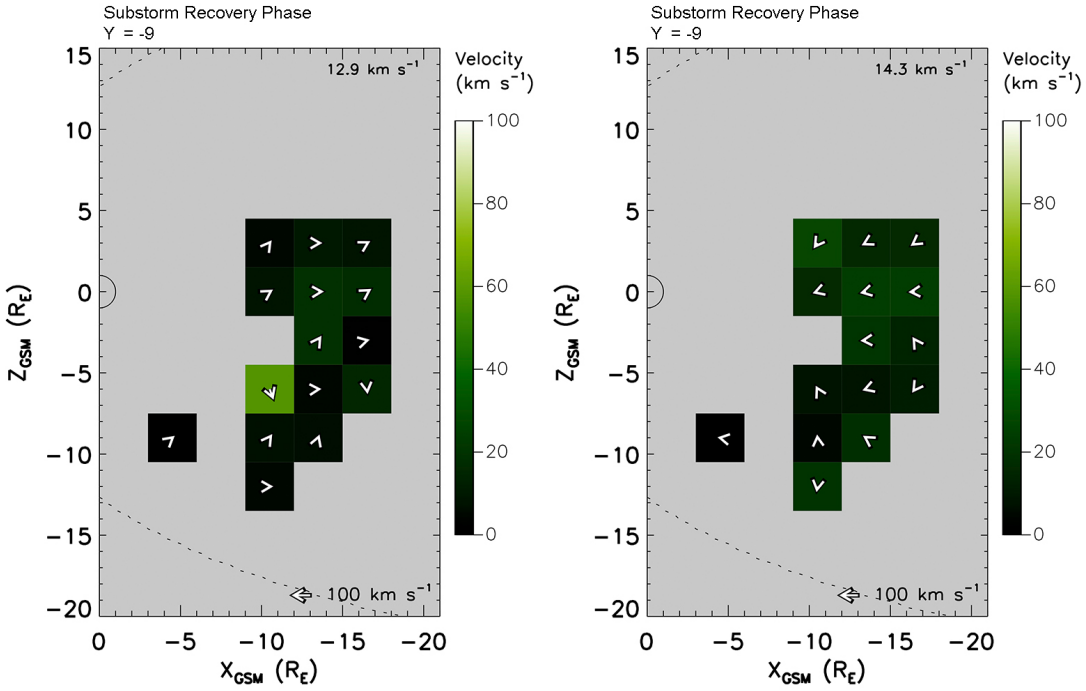

FIGURE C.33: Ion velocity plots displaying tailward (left) and earthward (right) plasma flow during the substorm recovery phase in the XZ plane where Y = -9±4.5 R_E .

Appendix D

Electron Flow Figures

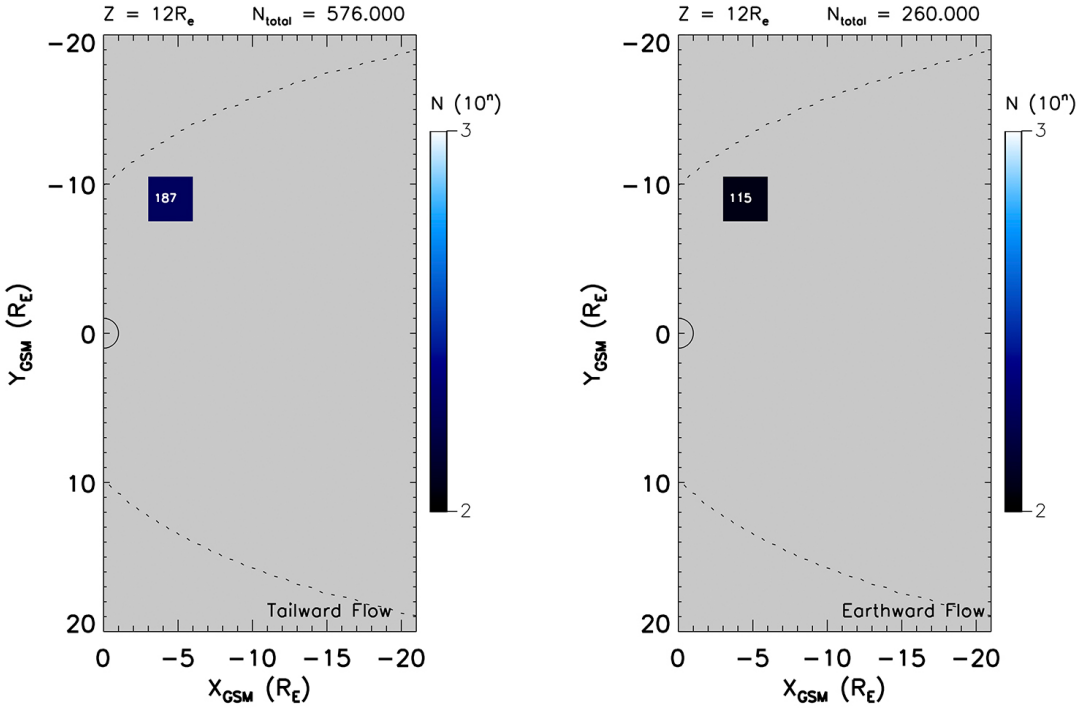

FIGURE D.1: Field-perpendicular electron number density plot for XY plane $Z = 12 \pm 1.5\,R_e$ displaying tailward (left) and earthward (right) plasma flow.

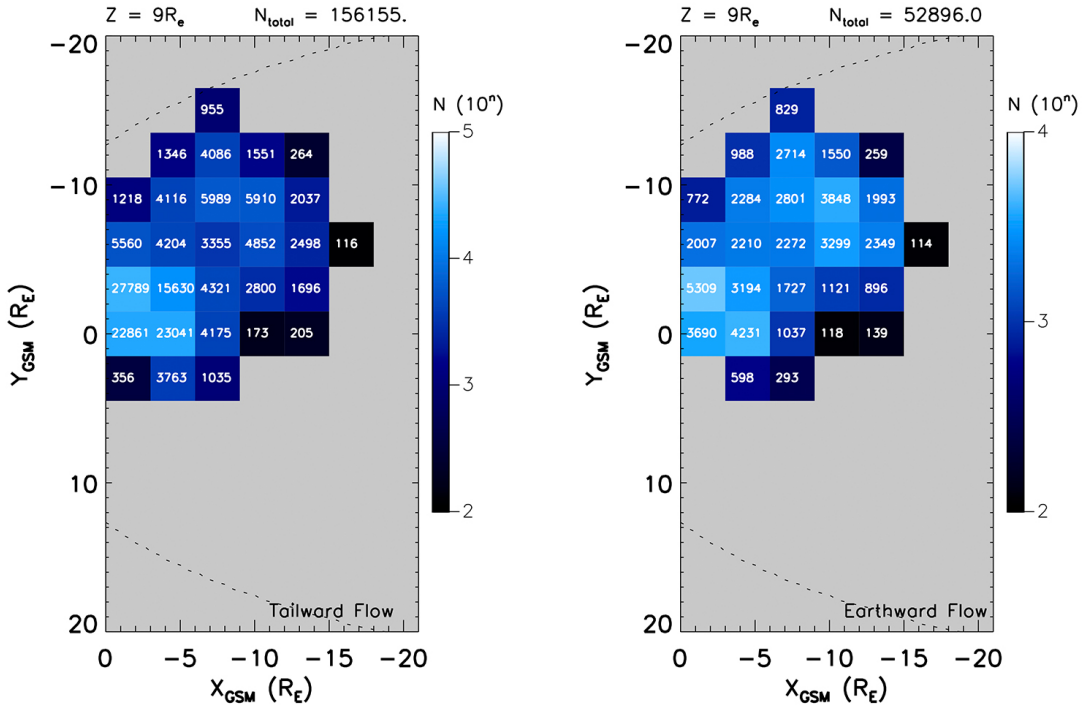

FIGURE D.2: Field-perpendicular electron number density plot for XY plane $Z = 9 \pm 1.5\,R_e$ displaying tailward (left) and earthward (right) plasma flow.

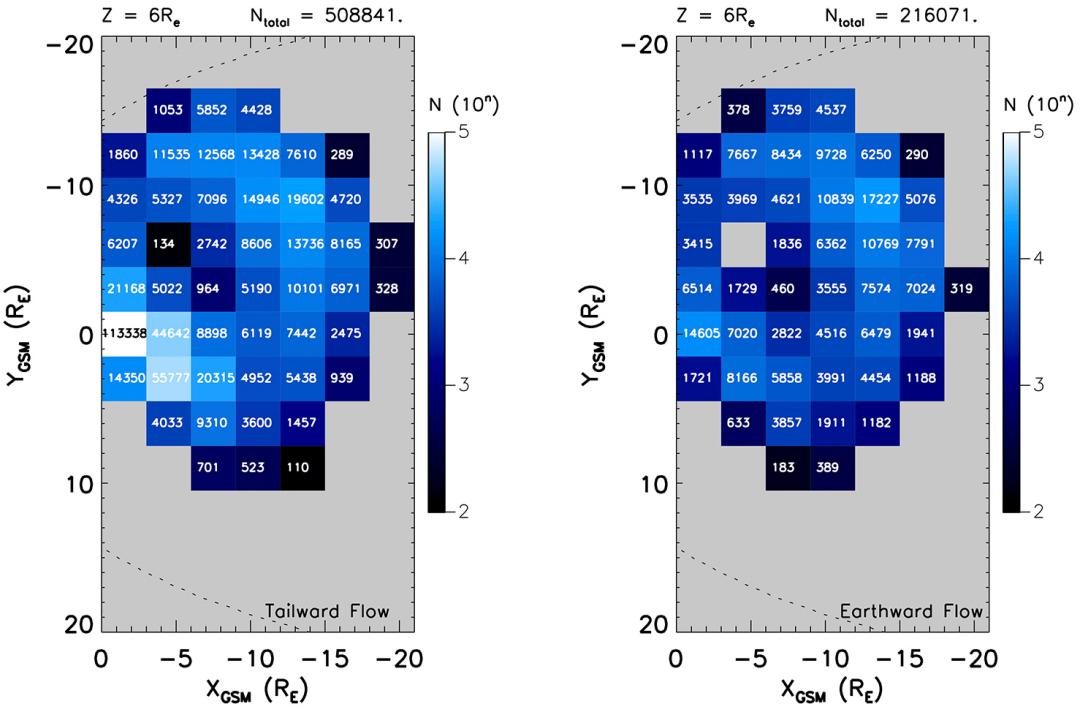

FIGURE D.3: Field-perpendicular electron number density plot for XY plane $Z = 6 \pm 1.5\,R_e$ displaying tailward (left) and earthward (right) plasma flow.

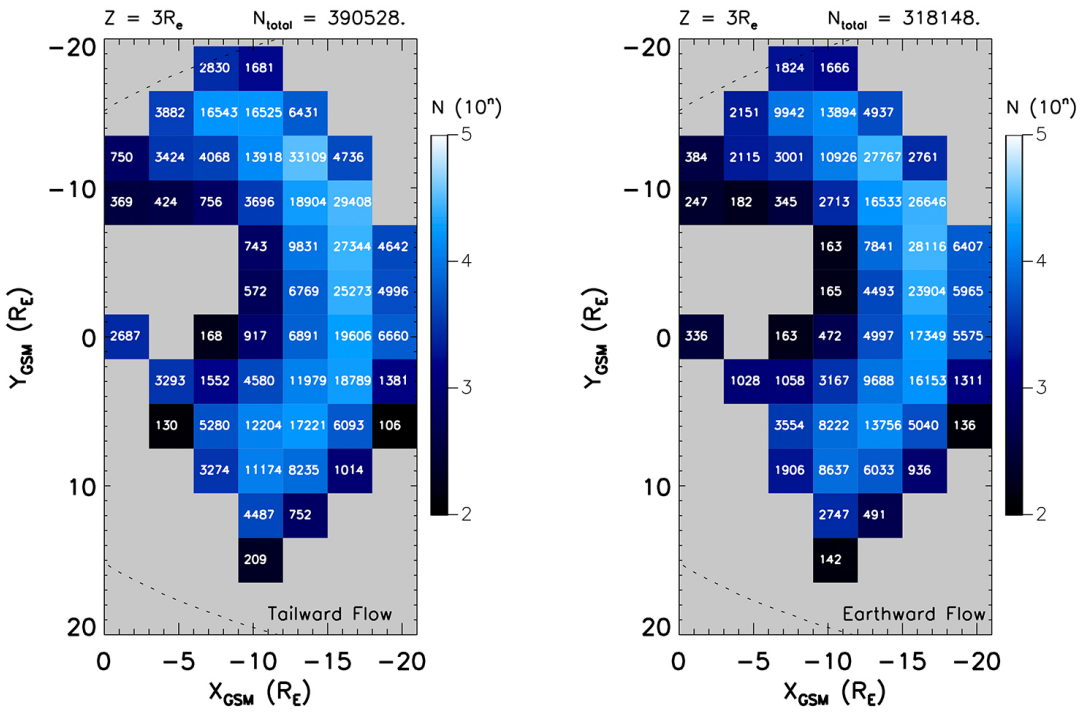

FIGURE D.4: Field-perpendicular electron number density plot for XY plane $Z = 3 \pm 1.5\,R_e$ displaying tailward (left) and earthward (right) plasma flow.

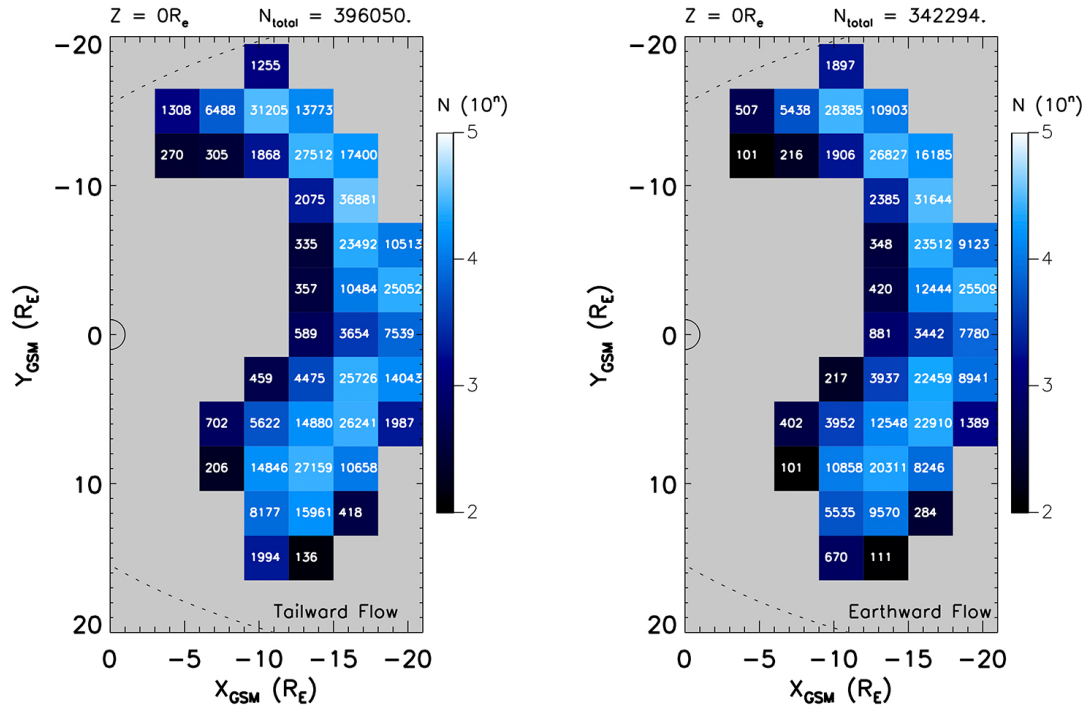

FIGURE D.5: Field-perpendicular electron number density plot for XY plane $Z = 0 \pm 1.5\,R_e$ displaying tailward (left) and earthward (right) plasma flow.

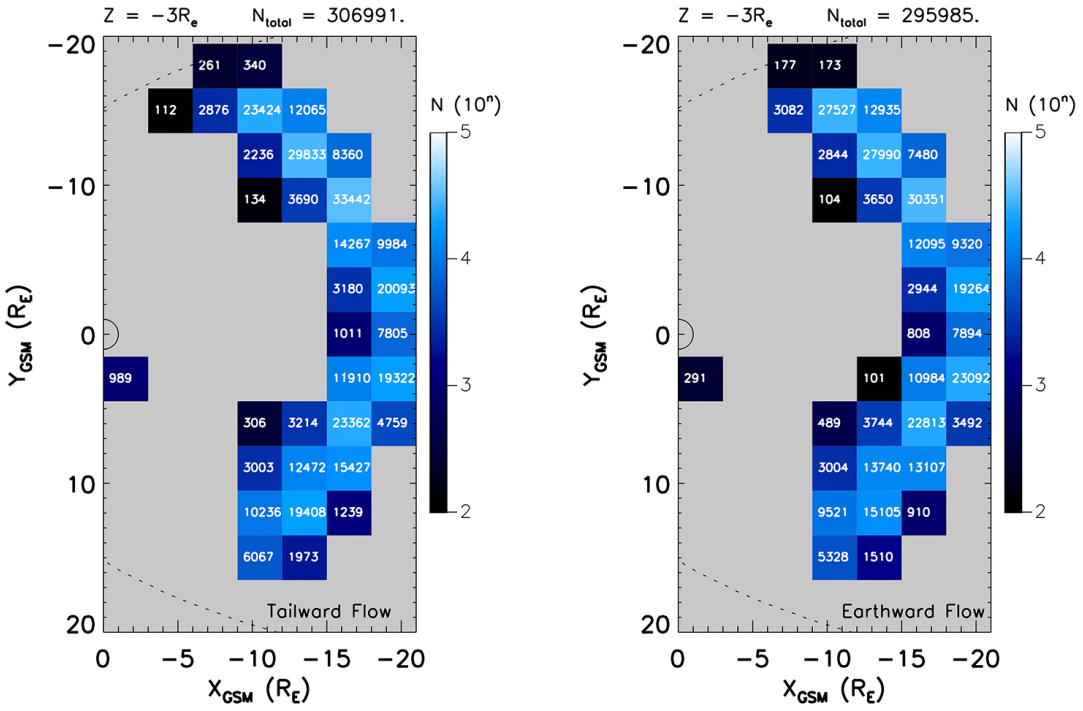

FIGURE D.6: Field-perpendicular electron number density plot for XY plane Z = -3 ± 1.5 R_e displaying tailward (left) and earthward (right) plasma flow.

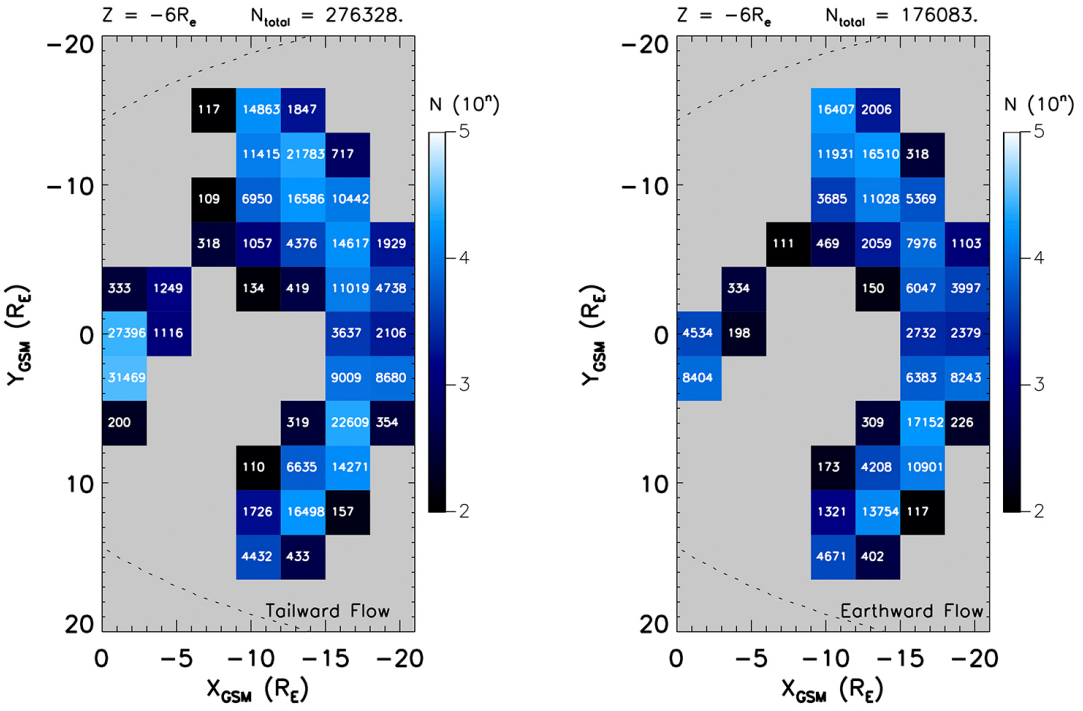

FIGURE D.7: Field-perpendicular electron number density plot for XY plane Z = -6 ± 1.5 R_e displaying tailward (left) and earthward (right) plasma flow.

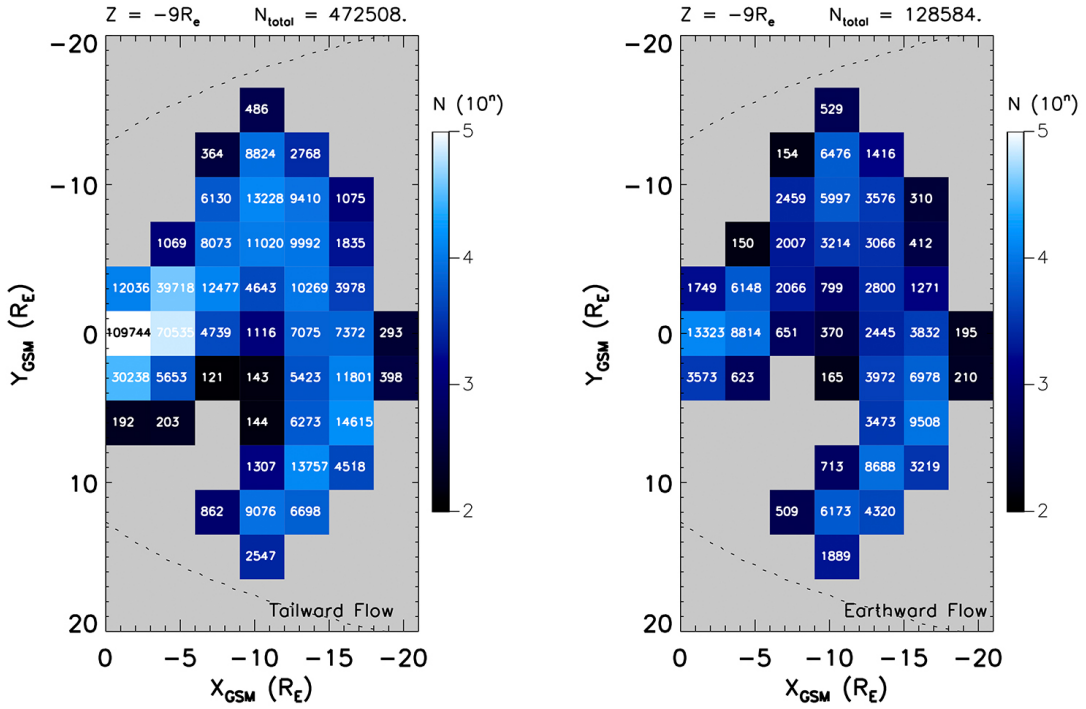

FIGURE D.8: Field-perpendicular electron number density plot for XY plane Z = 9 ± 1.5 R_e displaying tailward (left) and earthward (right) plasma flow.

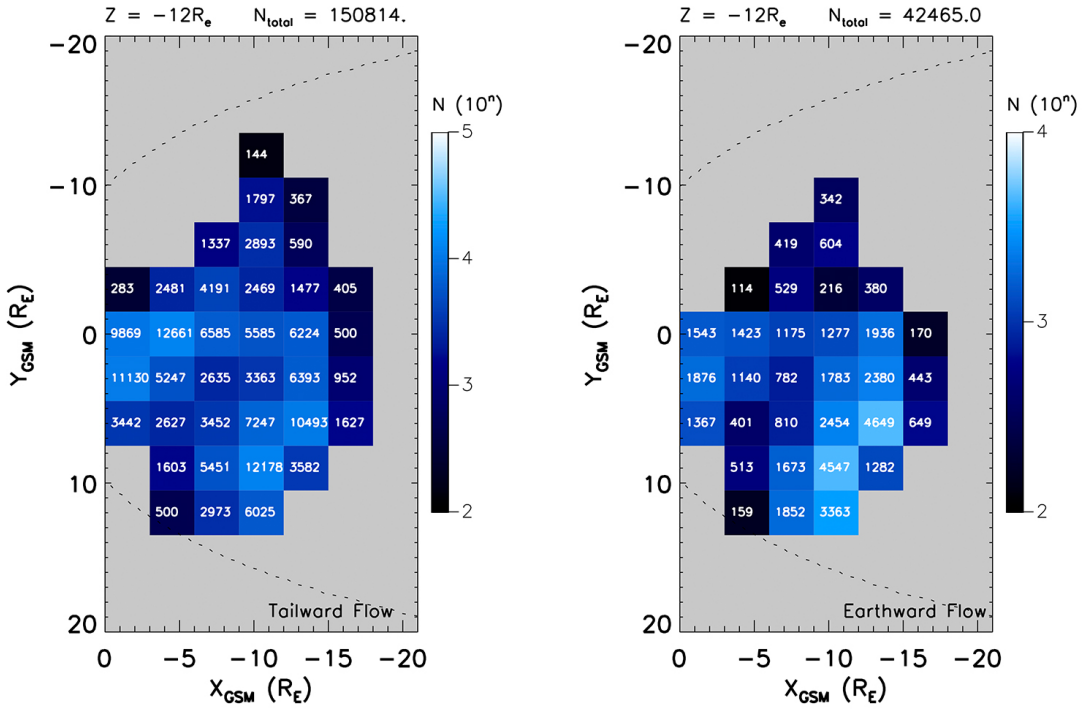

FIGURE D.9: Field-perpendicular electron number density plot for XY plane Z = -12 ± 1.5 R_e displaying tailward (left) and earthward (right) plasma flow.

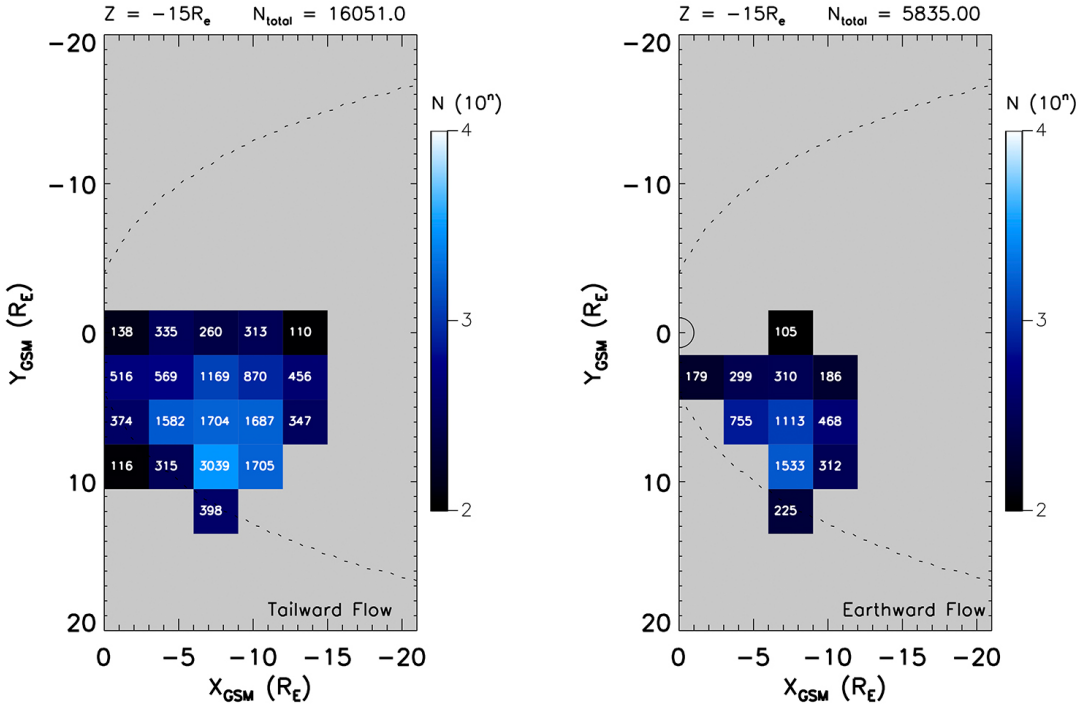

FIGURE D.10: Field-perpendicular electron number density plot for XY plane Z = -15 ± 1.5 R_e displaying tailward (left) and earthward (right) plasma flow.

Bibliography

Acuña, M. H. (2002), Space-based magnetometers, *Review of Scientific Instruments*, *73*(11), 3717–3736, doi:10.1063/1.1510570.

Akasofu, S. (1968), *Polar and Magnetospheric Substorms*, *strophysics and Space Science Library*, vol. 11, Springer Netherlands.

Akasofu, S., and S. Chapman (1961), The ring current, geomagnetic disturbance, and the van allen radiation belts, *Journal of Geophysical Research*, *66*(5), 1321–1350, doi:10.1029/JZ066i005p01321.

Akasofu, S.-I. (1964), The development of the auroral substorm, *Planetary and Space Science*, *12*, 273–282, doi:10.1016/0032-0633(64)90151-5.

Akasofu, S.-I. (1979), Interplanetary energy flux associated with magnetospheric substorms, *Planetary and space Science*, *27*, 425–431, doi:10.1016/0032-0633(79)90119-3.

Akasofu, S.-I. (1980), The solar wind-magnetosphere energy coupling and magnetospheric disturbances, *Planetary and Space Science*, *28*(5), 495 – 509, doi:https://doi.org/10.1016/0032-0633(80)90031-8.

Akasofu, S. I. (1981), Energy coupling between the solar wind and the magnetosphere, *Space Science Reviews*, *28*(2), 121–190, doi:10.1007/BF00218810.

Alfvén, H. (1942), Existence of electromagnetic-hydrodynamic waves, *Nature*, *150*, 405–406, doi:10.1038/150405d0.

Amm, O., and K. Kauristie (2002), Ionospheric signatures of bursty bulk flows, *Surveys in Geophysics*, *23*, 1–32, doi:10.1023/A:1014871323023.

André, M., and A. W. Yau (1997), Theories and observations of ion energization and outflow in the high latitude magnetosphere, *Space Science Reviews*, *80*(1), 27–48, doi:10.1023/A:1004921619885.

Angelopolous, V., C. F. Kennel, F. V. Coroniti, R. Pellat, H. E. Spence, M. G. Kivelson, R. J. Walker, W. Baumjohann, W. C. Feldman, J. T. Gosling, and C. T. Russell

(1993), Characteristics of ion flow in the quiet inner plasma sheet, *Geophysical Research Letters*, *20*, doi:10.1029/93GL00847.

Angelopoulos, V., W. Baumjohann, C. F. Kennel, F. V. Coroniti, M. G. Kivelson, R. Pellat, R. J. Walker, H. Lhr, and G. Paschmann (1992), Bursty bulk flows in the inner central plasma sheet, *Journal of Geophysical Research: Space Physics*, *97*(A4), 4027–4039, doi:10.1029/91JA02701.

Angelopoulos, V., C. F. Kennel, F. V. Coroniti, R. Pellat, M. G. Kivelson, R. J. Walker, C. T. Russell, W. Baumjohann, W. C. Feldman, and J. T. Gosling (1994), Statistical characteristics of bursty bulk flow events, *Journal of Geophysical Research: Space Physics*, *99*(A11), 21,257–21,280, doi:10.1029/94JA01263.

Angelopoulos, V., F. V. Coroniti, C. F. Kennel, M. G. Kivelson, R. J. Walker, C. T. Russell, R. L. McPherron, E. Sanchez, C.-I. Meng, W. Baumjohann, G. D. Reeves, R. D. Belian, N. Sato, E. Friis-Christensen, P. R. Sutcliffe, K. Yumoto, and T. Harris (1996), Multipoint analysis of a bursty bulk flow event on april 11, 1985, *Journal of Geophysical Research: Space Physics*, *101*(A3), 4967–4989, doi:10.1029/95JA02722.

Angelopoulos, V., T. D. Phan, D. E. Larson, F. S. Mozer, R. P. Lin, K. Tsuruda, H. Hayakawa, T. Mukai, S. Kokubun, T. Yamamoto, D. J. Williams, R. W. McEntire, R. P. Lepping, G. K. Parks, M. Brittnacher, G. Germany, J. Spann, H. J. Singer, and K. Yumoto (1997), Magnetotail flow bursts: Association to global magnetospheric circulation, relationship to ionospheric activity and direct evidence for localization, *Geophysical Research Letters*, *24*(18), 2271–2274, doi:10.1029/97GL02355.

Angelopoulos, V., J. P. McFadden, D. Larson, C. W. Carlson, S. B. Mende, H. Frey, T. Phan, D. G. Sibeck, K.-H. Glassmeier, U. Auster, E. Donovan, I. R. Mann, I. J. Rae, C. T. Russell, A. Runov, X.-Z. Zhou, and L. Kepko (2008), Tail reconnection triggering substorm onset, *Science*, *321*(5891), 931–935, doi:10.1126/science.1160495.

Arnoldy, R. L. (1971), Signature in the interplanetary medium for substorms, *Journal of Geophysical Research*, *76*(22), 5189–5201, doi:10.1029/JA076i022p05189.

Artemyev, A. V., A. P. Walsh, A. A. Petrukovich, W. Baumjohann, R. Nakamura, and A. N. Fazakerley (2014), Electron pitch angle/energy distribution in the magnetotail, *Journal of Geophysical Research: Space Physics*, *119*(9), 7214–7227, doi:10.1002/2014JA020350.

Asplund, M., N. Grevesse, A. J. Sauval, and P. Scott (2009), The chemical composition of the sun, *Annual Review of Astronomy and Astrophysics*, *47*, 481–522, doi:10.1146/annurev.astro.46.060407.145222.

Aubry, M. P., C. T. Russell, and M. G. Kivelson (1970), Inward motion of the magnetopause before a substorm, *Journal of Geophysical Research*, *75*(34), 7018–7031, doi:10.1029/JA075i034p07018.

Axford, W. I., and C. O. Hines (1961), A unifying theory of high-latitude geophysical phenomena and geomagnetic storms, *Canadian Journal of Physics*, *39*, 1433, doi:10.1139/p61-172.

Baker, D. N., T. I. Pulkkinen, E. W. Hones, R. D. Belian, R. L. McPherron, and V. Angelopoulos (1994), Signatures of the substorm recovery phase at high-altitude spacecraft, *Journal of Geophysical Research: Space Physics*, *99*(A6), 10,967–10,979, doi:10.1029/93JA02719.

Baker, D. N., T. I. Pulkkinen, V. Angelopoulos, W. Baumjohann, and R. L. McPherron (1996), Neutral line model of substorms: Past results and present view, *Journal of Geophysical Research: Space Physics*, *101*(A6), 12,975–13,010, doi:10.1029/95JA03753.

Balogh, A., M. W. Dunlop, S. W. H. Cowley, D. J. Southwood, J. G. Thomlinson, K. H. Glassmeier, G. Musmann, H. LÜHR, S. Buchert, M. H. AcuÑA, D. H. Fairfield, J. A. Slavin, W. Riedler, K. Schwingenschuh, and M. G. Kivelson (1997), The cluster magnetic field investigation, *Space Science Reviews*, *79*(1), 65–91, doi:10.1023/A:1004970907748.

Balogh, A., C. M. Carr, M. H. AcuÑA, M. W. Dunlop, T. J. Beek, P. Brown, K.-H. Fornacon, E. Georgescu, K.-H. Glassmeier, J. Harris, G. Musmann, T. Oddy, and K. Schwingenschuh (2001), The cluster magnetic field investigation: overview of in-flight performance and initial results, *Annales Geophysicae*, *19*(10/12), 1207–1217, doi:10.5194/angeo-19-1207-2001.

Baumjohann, W. (2002), Modes of convection in the magnetotail, *Physics of Plasmas*, *9*, 3665–3667, doi:10.1063/1.1499116.

Baumjohann, W., and K.-H. Glassmeier (1984), The transient response mechanism and Pi2 pulsations at substorm onset - Review and outlook, *Planetary and Space Science*, *32*, 1361–1370, doi:10.1016/0032-0633(84)90079-5.

Baumjohann, W., and R. Treumann (1997), *Basic Space Plasma Physics*, Imperial College Press.

Baumjohann, W., G. Paschmann, and C. A. Cattell (1989), Average plasma properties in the central plasma sheet, *Journal of Geophysical Research: Space Physics*, *94*(A6), 6597–6606, doi:10.1029/JA094iA06p06597.

Baumjohann, W., G. Paschmann, and H. Lhr (1990), Characteristics of high-speed ion flows in the plasma sheet, *Journal of Geophysical Research: Space Physics*, *95*(A4), 3801–3809, doi:10.1029/JA095iA04p03801.

Baumjohann, W., M. Hesse, S. Kokubun, T. Mukai, T. Nagai, and A. A. Petrukovich (1999), Substorm dipolarization and recovery, *Journal of Geophysical Research: Space Physics*, *104*(A11), 24,995–25,000, doi:10.1029/1999JA900282.

Bhavnani, K., U. S. A. F. S. Command, R. Vancour, and R. I. B. MA. (1991), *Coordinate Systems for Space and Geophysical Applications*, Phillips Laboratory, Air Force Systems Command.

Birkeland, K. (1908), *The Norwegian aurora polaris expedition 1902-1903*, no. v. 1, in The Norwegian Aurora Polaris Expedition 1902-1903, H. Aschelhoug and Co.

Birn, J., and M. Hesse (1991), The substorm current wedge and field-aligned currents in mhd simulations of magnetotail reconnection, *Journal of Geophysical Research: Space Physics*, *96*(A2), 1611–1618, doi:10.1029/90JA01762.

Birn, J., J. Raeder, Y. L. Wang, R. A. Wolf, and M. Hesse (2004), On the propagation of bubbles in the geomagnetic tail, *Annales Geophysicae*, *22*(5), 1773–1786, doi:10.5194/angeo-22-1773-2004.

Boakes, P. D., R. Nakamura, M. Volwerk, and S. E. Milan (2014), Eclat cluster spacecraft magnetotail plasma region identifications (20012009), *Dataset Papers in Science*, *2014*, 13 pages, doi:10.1155/2014/684305.

Cao, J., J. Duan, A. Du, Y. Ma, Z. Liu, G. C. Zhou, D. Yang, T. Zhang, X. Li, M. Vellante, H. Reme, I. Dandouras, E. Lucek, C. M. Carr, Q. Zong, and Q. Li (2008), Characteristics of middle- to low-latitude pi2 excited by bursty bulk flows, *Journal of Geophysical Research: Space Physics*, *113*(A7), n/a–n/a, doi:10.1029/2007JA012629, a07S15.

Cao, J. B., Y. D. Ma, G. Parks, H. Reme, I. Dandouras, R. Nakamura, T. L. Zhang, Q. Zong, E. Lucek, C. M. Carr, Z. X. Liu, and G. C. Zhou (2006), Joint observations by cluster satellites of bursty bulk flows in the magnetotail, *Journal of Geophysical Research: Space Physics*, *111*(A4), n/a–n/a, doi:10.1029/2005JA011322, a04206.

Carlson, C., D. Curtis, G. Paschmann, and W. Michel (1982), An instrument for rapidly measuring plasma distribution functions with high resolution, *Advances in Space Research*, *2*(7), 67 – 70, doi:http://dx.doi.org/10.1016/0273-1177(82)90151-X.

Chapman, S. (1918), An outline of a theory of magnetic storms, *Proceedings of the Royal Society of London A: Mathematical, Physical and Engineering Sciences*, *95*(666), 61–83, doi:10.1098/rspa.1918.0049.

Chapman, S., and V. C. A. Ferraro (1930), A new theory of magnetic storms, *Nature*, *126*, 129–130, doi:doi:10.1038/126129a0.

Chapman, S., and V. C. A. Ferraro (1931a), A new theory of magnetic storms, *Nature*, *126*, 129–130.

Chapman, S., and V. C. A. Ferraro (1931b), A new theory of magnetic storms, *Terrestrial Magnetism and Atmospheric Electricity*, *36*(2), 77–97, doi:10.1029/TE036i002p00077.

Chappell, C. R. (2015), The role of the ionosphere in providing plasma to the terrestrial magnetosphere—an historical overview, *Space Science Reviews*, *192*(1), 5–25, doi:10.1007/s11214-015-0168-5.

Chen, C. X., and R. A. Wolf (1999), Theory of thin-filament motion in earth's magnetotail and its application to bursty bulk flows, *Journal of Geophysical Research: Space Physics*, *104*(A7), 14,613–14,626, doi:10.1029/1999JA900005.

Chen, F. F. (2012), *The Earth's Ionosphere: Plasma Physics and Electrodynamics*, Springer US.

Chen, S.-H., and M. G. Kivelson (1991), On ultralow frequency waves in the lobes of the earth's magnetotail, *Journal of Geophysical Research: Space Physics*, *96*(A9), 15,711–15,723, doi:10.1029/91JA01422.

Coroniti, F., and C. F. Kennel (1972), Changes in magnetospheric configuration during the substorm growth phase, *Journal of Geophysical Research (1896-1977)*, *77*(19), 3361–3370, doi:10.1029/JA077i019p03361.

Corontini, F. V., and C. F. Kennel (1972), Changes in magnetospheric configuration during the substorm growth phase, *Journal of Geophysical Research*, *77*(19), 3361–3370, doi:10.1029/JA077i019p03361.

Cowley, S., and M. Lockwood (1992), Excitation and decay of solar wind-driven flows in the magnetosphere-ionosphere system, *Annales Geophysicae*, *10*, 103–115.

Cowley, S. W. H. (1981a), Magnetospheric and ionospheric flow and the interplanetary magnetic field, in *AGARD The Phys. Basis of the Ionosphere in the Solar-Terrest. System 14 p (SEE N81-23507 14-42)*, edited by S. W. H. Cowley.

Cowley, S. W. H. (1981b), Magnetospheric asymmetries associated with the y-component of the imf, *Planetary and Space Science*, *29*, 79–96, doi:10.1016/0032-0633(81)90141-0.

Cowley, S. W. H., J. A. Davies, A. Grocott, H. Khan, M. Lester, K. A. McWilliams, S. E. Milan, G. Provan, P. E. Sandholt, J. A. Wild, and T. K. Yeoman (2003), Solar-wind.

magnetosphere: Ionosphere interactions in the earth's plasma environment, *Philosophical Transactions: Mathematical, Physical and Engineering Sciences*, *361*(1802), 113–126.

Coxon, J. C., C. M. Jackman, M. P. Freeman, C. Forsyth, and I. J. Rae (2016), Identifying the magnetotail lobes with cluster magnetometer data, *Journal of Geophysical Research: Space Physics*, *121*(2), 1436–1446, doi:10.1002/2015JA022020, 2015JA022020.

Dandouras, I. A. B., and the CIS Team (2017), User guide to the cis measurements in the cluster active archive (caa), *Tech. Rep. CAA-EST-UG-CIS 3.7*.

Dessler, A. J., and E. N. Parker (1959), Hydromagnetic theory of geomagnetic storms, *Journal of Geophysical Research*, *64*(12), 2239–2252, doi:10.1029/JZ064i012p02239.

Dungey, J. W. (1961), Interplanetary Magnetic Field and the Auroral Zones, *Physical Review Letters*, *6*, 47–48, doi:10.1103/PhysRevLett.6.47.

Dungey, J. W. (1963), The structure of the exosphere, or adventures in velocity space, in geophysics: The earths environment, *Geophysical Journal International*, *8*(1), 505–550, doi:10.1111/j.1365-246X.1963.tb02903.x.

Dungey, J. W. (1965), The length of the magnetospheric tail, *Journal of Geophysical Research*, *70*(7), 1753–1753, doi:10.1029/JZ070i007p01753.

Eastman, T. E., L. A. Frank, W. K. Peterson, and W. Lennartsson (1984), The plasma sheet boundary layer, *Journal of Geophysical Research: Space Physics*, *89*(A3), 1553–1572, doi:10.1029/JA089iA03p01553.

Eastman, T. E., L. A. Frank, and C. Y. Huang (1985), The boundary layers as the primary transport regions of the earth's magnetotail, *Journal of Geophysical Research: Space Physics*, *90*(A10), 9541–9560, doi:10.1029/JA090iA10p09541.

Elphinstone, R. D., J. S. Murphree, L. L. Cogger, D. Hearn, M. G. Henderson, and R. Lundin (1991), *Observations of Changes to the Auroral Distribution Prior to Substorm Onset*, 257–275 pp., American Geophysical Union, doi:10.1029/GM064p0257.

Escoubet, C. P., R. Schmidt, and M. L. Goldstein (1997), *Cluster - Science and Mission Overview*, pp. 11–32, Springer Netherlands, Dordrecht, doi:10.1007/978-94-011-5666-0_1.

Fairfield, D. H., and L. J. Cahill (1966), Transition region magnetic field and polar magnetic disturbances, *Journal of Geophysical Research*, *71*(1), 155–169, doi:10.1029/JZ071i001p00155.

Fairfield, D. H., and G. D. Mead (1975), Magnetospheric mapping with a quantitative geomagnetic field model, *Journal of Geophysical Research*, *80*(4), 535–542, doi:10.1029/JA080i004p00535.

Farley, T. A., and N. L. Sanders (1962), Pitch angle distributions and mirror point densities in the outer radiation zone, *Journal of Geophysical Research*, *67*(6), 2159–2168, doi:10.1029/JZ067i006p02159.

Fazakerley, A., N. Doss, A. Lahiff, I. Rozum, D. Kataria, H. Bacai, C. Anekallu, B. Mihaljcic, M. West, and A. Asnes (2013), Calibration report of the peace measurements in the cluster active archive (caa), *Tech. rep.*, European Space Agency.

Feldstein, Y., and G. Starkov (1967), Dynamics of auroral belt and polar geomagnetic disturbances, *Planetary and Space Science*, *15*(2), 209 – 229, doi:https://doi.org/10.1016/0032-0633(67)90190-0",url="http://www.sciencedirect.com/science/article/pii/0032063367901900.

Fok, M., T. E. Moore, G. R. Wilson, J. D. Perez, X. X. Zhang, P. C. Brandt, D. G. Son, Mitchell, E. C. Roelof, J. Jahn, C. J. Pollock, and R. Wolf (2003), Global ena image simulations, *Space Science Reviews*, *109*, 77–103, doi:https://doi.org/10.1023/B:SPAC.0000007514.56380.fd.

Forsyth, C., I. J. Rae, J. C. Coxon, M. P. Freeman, C. M. Jackman, J. Gjerloev, and A. N. Fazakerley (2015), A new technique for determining substorm onsets and phases from indices of the electrojet (sophie), *Journal of Geophysical Research: Space Physics*, *120*(12), 10,592–10,606, doi:10.1002/2015JA021343, 2015JA021343.

Frank, L. A. (1967), On the extraterrestrial ring current during geomagnetic storms, *Journal of Geophysical Research*, *72*(15), 3753–3767, doi:10.1029/JZ072i015p03753.

Geach, J., S. J. Schwartz, V. Génot, O. Moullard, A. Lahiff, and A. N. Fazakerley (2005), A corrector for spacecraft calculated electron moments, *Annales Geophysicae*, *23*, 931–943.

Gjerloev, J. W. (2012), The supermag data processing technique, *Journal of Geophysical Research: Space Physics*, *117*(A9), n/a–n/a, doi:10.1029/2012JA017683, a09213.

Goertz, C. K., and R. A. Smith (1989), The thermal catastrophe model of substorms, *Journal of Geophysical Research: Space Physics*, *94*(A6), 6581–6596, doi:10.1029/JA094iA06p06581.

Griffiths, D. (2013), *Introduction to Electrodynamics*, Always learning, Pearson.

Grocott, A., T. K. Yeoman, R. Nakamura, S. W. H. Cowley, H. U. Frey, H. Rème, and B. Klecker (2004), Multi-instrument observations of the ionospheric counterpart of a bursty bulk flow in the near-earth plasma sheet, *Annales Geophysicae*, *22*(4), 1061–1075, doi:10.5194/angeo-22-1061-2004.

Grosz, A., M. Haji-Sheikh, and S. Mukhopadhyay (2016), *High Sensitivity Magnetometers*, Smart Sensors, Measurement and Instrumentation, Springer International Publishing.

Haaland, S., A. Runov, and C. Forsyth (2017), *Dawn-Dusk Asymmetries in Planetary Plasma Environments*, pp. i–xvi, American Geophysical Union (AGU), doi:10.1002/9781119216346.fmatter.

Haerendel, G., G. Paschmann, N. Sckopke, H. Rosenbauer, and P. C. Hedgecock (1978), The frontside boundary layer of the magnetosphere and the problem of reconnection, *Journal of Geophysical Research: Space Physics*, *83*(A7), 3195–3216, doi:10.1029/JA083iA07p03195.

Hapgood, M. (1992), Space physics coordinate transformations: A user guide, *Planetary and Space Science*, *40*(5), 711 – 717, doi:https://doi.org/10.1016/0032-0633(92)90012-D.

Heelis, R. A. (1982), The polar ionosphere, *Reviews of Geophysics*, *20*(3), 567–576, doi:10.1029/RG020i003p00567.

Heppner, J. P., and N. C. Maynard (1987), Empirical high-latitude electric field models, *Journal of Geophysical Research: Space Physics*, *92*(A5), 4467–4489, doi:10.1029/JA092iA05p04467.

Hines, C. O. (1986), Origins of the 1961 axford-hines paper on magnetospheric convection, *Eos, Transactions American Geophysical Union*, *67*(33), 634–634, doi:10.1029/EO067i033p00634-02.

Hones, E. W., Jr. (1976), The magnetotail - its generation and dissipation, in *Physics of Solar Planetary Environments*, edited by D. J. Williams, pp. 558–571.

Hones Jr., E. W. (1985), The poleward leap of the auroral electrojet as seen in auroral images, *Journal of Geophysical Research: Space Physics*, *90*(A6), 5333–5337, doi:10.1029/JA090iA06p05333.

Hori, T., K. Maezawa, Y. Saito, and T. Mukai (2000), Average profile of ion flow and convection electric field in the near-earth plasma sheet, *Geophysical Research Letters*, *27*(11), 1623–1626, doi:10.1029/1999GL003737.

Hsu, T.-S., and R. L. McPherron (2012), A statistical analysis of substorm associated tail activity, *Advances in Space Research*, *50*, 1317–1343, doi:10.1016/j.asr.2012.06.034.

Huang, C. Y., and L. A. Frank (1986), A statistical study of the central plasma sheet: Implications for substorm models, *Geophysical Research Letters*, *13*(7), 652–655, doi: 10.1029/GL013i007p00652.

Hughes, W. (1995a), *The Magnetopause, Magnetotail and Magnetic Reconnection*, Cambridge atmospheric and space science series, 227-287 pp., Cambridge University Press.

Hughes, W. (1995b), *Magnetospheric configuration*, Cambridge atmospheric and space science series, 288-329 pp., Cambridge University Press.

Ieda, A., S. Machida, T. Mukai, Y. Saito, T. Yamamoto, A. Nishida, T. Terasawa, and S. Kokubun (1998), Statistical analysis of the plasmoid evolution with geotail observations, *Journal of Geophysical Research: Space Physics*, *103*(A3), 4453–4465, doi:10.1029/97JA03240.

Jackman, C. M., and C. S. Arridge (2011), Statistical properties of the magnetic field in the kronian magnetotail lobes and current sheet, *Journal of Geophysical Research: Space Physics*, *116*(A5), n/a–n/a, doi:10.1029/2010JA015973, a05224.

Jacquey, C., J. A. Sauvaud, and J. Dandouras (1991), Location and propagation of the magnetotail current disruption during substorm expansion: Analysis and simulation of an isee multi-onset event, *Geophysical Research Letters*, *18*(3), 389–392, doi:10. 1029/90GL02789.

James, M. K. (2015), Ulf waves driven by recently-injected energetic particle populations abstract, Ph.D. thesis, University of Leicester.

Johnstone, A. D., C. Alsop, S. Burge, P. J. Carter, A. J. Coates, A. J. Coker, A. N. Fazakerley, M. Grande, R. A. Gowen, C. Gurgiolo, B. K. Hancock, B. Narheim, A. Preece, P. H. Sheather, J. D. Winningham, and R. D. Woodliffe (1997), Peace: A plasma electron and current experiment, *Space Science Reviews*, *79*(1), 351–398, doi:10.1023/A:1004938001388.

Juusola, L., N. stgaard, and E. Tanskanen (2011), Statistics of plasma sheet convection, *Journal of Geophysical Research: Space Physics*, *116*(A8), doi:10.1029/2011JA016479.

Kamide, Y. (1982), The relationship between field-aligned currents and the auroral electrojets - a review, *Space Science Reviews*, *31*, 127–243, doi:10.1007/BF00215281.

Kavanagh, L. D., J. W. Freeman, and A. J. Chen (1968), Plasma flow in the magnetosphere, *Journal of Geophysical Research*, *73*(17), 5511–5519, doi:10.1029/ JA073i017p05511.

Keika, K., R. Nakamura, M. Volwerk, V. Angelopoulos, W. Baumjohann, A. Retinò, M. Fujimoto, J. W. Bonnell, H. J. Singer, H. U. Auster, J. P. McFadden, D. Larson, and I. Mann (2009), Observations of plasma vortices in the vicinity of flow-braking: a case study, *Annales Geophysicae*, *27*(8), 3009–3017, doi:10.5194/angeo-27-3009-2009.

Kennel, C. (1996), *Convection and Substorms: Paradigms of Magnetospheric Phenomenology*, International Series on Astronomy and Astrophysics, Oxford University Press.

Kepko, L., M. G. Kivelson, and K. Yumoto (2001), Flow bursts, braking, and pi2 pulsations, *Journal of Geophysical Research: Space Physics*, *106*(A2), 1903–1915, doi:10.1029/2000JA000158.

Kissinger, J., R. L. McPherron, T.-S. Hsu, and V. Angelopoulos (2012), Diversion of plasma due to high pressure in the inner magnetosphere during steady magnetospheric convection, *Journal of Geophysical Research: Space Physics*, *117*(A5), doi:10.1029/2012JA017579.

Kivelson, M., and C. Russell (1995), *Introduction to Space Physics*, Cambridge atmospheric and space science series, Cambridge University Press.

Kletzing, C. A., J. D. Scudder, E. E. Dors, and C. Curto (2003), Auroral source region: Plasma properties of the high-latitude plasma sheet, *Journal of Geophysical Research (Space Physics)*, *108*, 1360, doi:10.1029/2002JA009678.

Kokubun, S., and R. L. McPherron (1981), Substorm signatures at synchronous altitude, *Journal of Geophysical Research: Space Physics*, *86*(A13), 11,265–11,277, doi:10.1029/JA086iA13p11265.

Le, G., J. A. Slavin, and R. J. Strangeway (2010), Space technology 5 observations of the imbalance of regions 1 and 2 field-aligned currents and its implication to the cross-polar cap pedersen currents, *Journal of Geophysical Research: Space Physics*, *115*(A7), doi:10.1029/2009JA014979, a07202.

Li, H., C. Wang, and S. Y. Fu (2014), Classification of fast flows in central plasma sheet: Superposed epoch analysis based on themis observations, *Journal of Geophysical Research: Space Physics*, *119*(9), 7199–7213, doi:10.1002/2014JA020105.

Lopez, R. E., and A. T. Y. Lui (1990), A multisatellite case study of the expansion of a substorm current wedge in the near-earth magnetotail, *Journal of Geophysical Research: Space Physics*, *95*(A6), 8009–8017, doi:10.1029/JA095iA06p08009.

Lopez, R. E., C. C. Goodrich, G. D. Reeves, R. D. Belian, and A. Taktakishvili (1994), Midtail plasma flows and the relationship to near-earth substorm activity: A case

study, *Journal of Geophysical Research: Space Physics*, *99*(A12), 23,561–23,569, doi:10.1029/94JA01771.

Lui, A. T. Y. (1991), A synthesis of magnetospheric substorm models, *Journal of Geophysical Research: Space Physics*, *96*(A2), 1849–1856, doi:10.1029/90JA02430.

Lui, A. T. Y. (2000), Tutorial on geomagnetic storms and substorms, *IEEE Transactions on Plasma Science*, *28*(6), 1854–1866, doi:10.1109/27.902214.

Lui, A. T. Y., R. E. Lopez, S. M. Krimigis, R. W. McEntire, L. J. Zanetti, and T. A. Potemra (1988), A case study of magnetotail current sheet disruption and diversion, *Geophysical Research Letters*, *15*(7), 721–724, doi:10.1029/GL015i007p00721.

Lui, A. T. Y., A. Mankofsky, C.-L. Chang, K. Papadopoulos, and C. S. Wu (1990), A current disruption mechanism in the neutral sheet: A possible trigger for substorm expansions, *Geophysical Research Letters*, *17*(6), 745–748, doi:10.1029/GL017i006p00745.

Ma, Y. D., J. B. Cao, R. Nakamura, T. L. Zhang, H. Reme, I. Dandouras, E. Lucek, and M. Dunlop (2009), Statistical analysis of earthward flow bursts in the inner plasma sheet during substorms, *Journal of Geophysical Research: Space Physics*, *114*(A7), n/a–n/a, doi:10.1029/2009JA014275, a07215.

McPherron, R. (1995), *Magnetospheric Dynamics*, Cambridge atmospheric and space science series, 288-329 pp., Cambridge University Press.

McPherron, R. L. (1970), Growth phase of magnetospheric substorms, *Journal of Geophysical Research*, *75*(28), 5592–5599, doi:10.1029/JA075i028p05592.

McPherron, R. L. (1979), Magnetospheric substorms, *Reviews of Geophysics*, *17*(4), 657–681, doi:10.1029/RG017i004p00657.

McPherron, R. L., C. T. Russell, and M. P. Aubry (1973), Satellite studies of magnetospheric substorms on august 15, 1968: 9. phenomenological model for substorms, *Journal of Geophysical Research*, *78*(16), 3131–3149, doi:10.1029/JA078i016p03131.

McPherron, R. L., T.-S. Hsu, J. Kissinger, X. Chu, and V. Angelopoulos (2011), Characteristics of plasma flows at the inner edge of the plasma sheet, *Journal of Geophysical Research: Space Physics*, *116*(A5), n/a–n/a, doi:10.1029/2010JA015923, a00I33.

Mende, S. B., H. U. Frey, V. Angelopoulos, and Y. Nishimura (2011), Substorm triggering by poleward boundary intensification and related equatorward propagation, *Journal of Geophysical Research: Space Physics*, *116*(A5), n/a–n/a, doi:10.1029/2010JA015733, a00I31.

Meng, C.-I., and K. Makita (1986), Dynamic variations of the polar cap, in *Solar Wind Magnetosphere Coupling*, *Astrophysics and Space Science Library*, vol. 126, edited by Y. Kamide and J. A. Slavin, pp. 605–631, doi:10.1007/978-90-277-2303-1_41.

Meyer-Vernet, N. (2007), *Basics of the Solar Wind*, Cambridge Atmospheric and Space Science Series, Cambridge University Press.

Mikaelian, T. (2009), Spacecraft charging and hazards to electronics in space, https://arxiv.org/pdf/0906.3884.pdf.

Milan, S. E., G. Provan, and B. Hubert (2007), Magnetic flux transport in the dungey cycle: A survey of dayside and nightside reconnection rates, *Journal of Geophysical Research: Space Physics*, *112*(A1), n/a–n/a, doi:10.1029/2006JA011642, a01209.

Mobius, E., G. Gloeckler, D. Hovestadt, F. M. Ipavich, B. Klecker, M. Scholer, H. Arbinger, H. Hofner, E. Kunneth, P. Laeverenz, A. Luhn, E. O. Tums, and H. Waldleben (1985), The time-of-flight spectrometer suleica for ions of the energy range 5-270 kev/charge on ampte irm, *IEEE Transactions on Geoscience and Remote Sensing*, *GE-23*(3), 274–279, doi:10.1109/TGRS.1985.289527.

Murphree, J. S., R. D. Elphinstone, L. L. Cogger, and D. Hearn (1991), *Viking Optical Substorm Signatures*, 241–255 pp., American Geophysical Union, doi:10.1029/GM064p0241.

Musmann, G. (2010), *Fluxgate Magnetometers for Space Research*, Books on Demand.

Nagai, T., M. Fujimoto, Y. Saito, S. Machida, T. Terasawa, R. Nakamura, T. Yamamoto, T. Mukai, A. Nishida, and S. Kokubun (1998), Structure and dynamics of magnetic reconnection for substorm onsets with geotail observations, *Journal of Geophysical Research: Space Physics*, *103*(A3), 4419–4440, doi:10.1029/97JA02190.

Nagai, T., H. Singer, T. Mukai, T. Yamamoto, and S. Kokubun (2000), Development of substorms in the near-earth tail, *Advances in Space Research*, *25*("7), 1651 – 1662, doi:https://doi.org/10.1016/S0273-1177(99)00680-8, proceedings of the DO.1 Symposium of COSPAR Scientific Commission D.

Nakamura, R., D. N. Baker, D. H. Fairfield, D. G. Mitchell, R. L. McPherron, and E. W. Hones (1994), Plasma flow and magnetic field characteristics near the midtail neutral sheet, *Journal of Geophysical Research: Space Physics*, *99*(A12), 23,591–23,601, doi:10.1029/94JA02082.

Narinder (2016), Ever wondered what sustains earths magnetic field?, https://narinderkw.wordpress.com/2016/10/17/ever-wondered-what-sustains-earths-magnetic-field/.

Ness, N. F. (1965), The earth's magnetic tail, *Journal of Geophysical Research*, *70*(13), 2989–3005, doi:10.1029/JZ070i013p02989.

Nishimura, Y., L. Lyons, S. Zou, V. Angelopoulos, and S. Mende (2010), Substorm triggering by new plasma intrusion: Themis all-sky imager observations, *Journal of Geophysical Research: Space Physics*, *115*(A7), n/a–n/a, doi:10.1029/2009JA015166, a07222.

Nishino, M. N., M. Fujimoto, G. Ueno, K. Maezawa, T. Mukai, and Y. Saito (2007), Geotail observations of two-component protons in the midnight plasma sheet, *Annales Geophysicae*, *25*(10), 2229–2245, doi:10.5194/angeo-25-2229-2007.

Ohtani, S., R. Yamaguchi, M. Nos, H. Kawano, M. Engebretson, and K. Yumoto (2002a), Quiet time magnetotail dynamics and their implications for the substorm trigger, *Journal of Geophysical Research: Space Physics*, *107*(A2), SMP 6–1–SMP 6–10, doi:10.1029/2001JA000116.

Ohtani, S., R. Yamaguchi, H. Kawano, F. Creutzberg, J. B. Sigwarth, L. A. Frank, and T. Mukai (2002b), Does the braking of the fast plasma flow trigger a substorm?: A study of the august 14, 1996, event, *Geophysical Research Letters*, *29*(15), 16–1–16–4, doi:10.1029/2001GL013785.

Ohtani, S., Y. Miyashita, H. Singer, and T. Mukai (2009), Tailward flows with positive bz in the near-earth plasma sheet, *Journal of Geophysical Research: Space Physics*, *114*(A6), doi:10.1029/2009JA014159, a06218.

Ohtani, S.-I., R. Fujii, M. Hesse, and R. L. Lysak (2000), Magnetospheric Current Systems, *Washington DC American Geophysical Union Geophysical Monograph Series*, *118*, doi:10.1029/GM118.

Owens, M. J., and R. J. Forsyth (2013), The heliospheric magnetic field, *Living Reviews in Solar Physics*, *10*(1), 5, doi:10.12942/lrsp-2013-5.

Panov, E. V., R. Nakamura, W. Baumjohann, V. Angelopoulos, A. A. Petrukovich, A. Retin, M. Volwerk, T. Takada, K.-H. Glassmeier, J. P. McFadden, and D. Larson (2010a), Multiple overshoot and rebound of a bursty bulk flow, *Geophysical Research Letters*, *37*(8), n/a–n/a, doi:10.1029/2009GL041971, l08103.

Panov, E. V., R. Nakamura, W. Baumjohann, V. A. Sergeev, A. A. Petrukovich, V. Angelopoulos, M. Volwerk, A. Retin, T. Takada, K.-H. Glassmeier, J. P. McFadden, and D. Larson (2010b), Plasma sheet thickness during a bursty bulk flow reversal, *Journal of Geophysical Research: Space Physics*, *115*(A5), n/a–n/a, doi:10.1029/2009JA014743, a05213.

Parker, E. N. (1958), Dynamics of the interplanetary gas and magnetic fields., *The Astrophysical Journal*, *128*, 664, doi:10.1086/146579.

Parker, E. N. (1963), *Interplanetary dynamical processes.*, New York, Interscience Publishers, 1963.

Paschmann, G., I. Papamastorakis, N. Sckopke, G. Haerendel, B. Sonnerup, S. J. Bame, J. R. Asbridge, J. Gosling, C. T. Russel, and R. C. Elphic (1979), Plasma acceleration at the earth's magnetopause: Evidence for reconnection, *282*.

Pedlosky, J. (1992), *Geophysical Fluid Dynamics*, Springer study edition, Springer New York.

Perreault, P., and S.-I. Akasofu (1978), A study of geomagnetic storms, *Geophysical Journal of the Royal Astronomical Society*, *54*(3), 547–573, doi:10.1111/j.1365-246X.1978.tb05494.x.

Petschek, H. E. (1964), Magnetic field annihilation, *NASA Special Publication*, *50*, 425.

Phillips, J., S. Bame, W. Feldman, B. Goldstein, J. Gosling, C. Hammond, D. McComas, M. Neugebauer, E. Scime, S. Suess, et al. (1995), Ulysses solar wind plasma observations at high southerly latitudes, *Science-AAAS-Weekly Paper Edition*, *268*(5213), 1030–1032.

Pontius, D. H., and R. A. Wolf (1990), Transient flux tubes in the terrestrial magnetosphere, *Geophysical Research Letters*, *17*(1), 49–52, doi:10.1029/GL017i001p00049.

Pulkkinen, T. I., N. Partamies, J. Kissinger, R. L. McPherron, K.-H. Glassmeier, and C. Carlson (2013), Plasma sheet magnetic fields and flows during steady magnetospheric convection events, *Journal of Geophysical Research: Space Physics*, *118*(10), 6136–6144, doi:10.1002/jgra.50574.

Rae, I. J., K. R. Murphy, C. E. J. Watt, G. Rostoker, R. Rankin, I. R. Mann, C. R. Hodgson, H. U. Frey, A. W. Degeling, and C. Forsyth (2014), Field line resonances as a trigger and a tracer for substorm onset, *Journal of Geophysical Research: Space Physics*, *119*(7), 5343–5363, doi:10.1002/2013JA018889.

Raj, A., T. Phan, R. P. Lin, and V. Angelopoulos (2002), Wind survey of high-speed bulk flows and field-aligned beams in the near-earth plasma sheet, *Journal of Geophysical Research: Space Physics*, *107*(A12), SMP 3–1–SMP 3–17, doi:10.1029/2001JA007547, 1419.

Rème, H., J. M. Bosqued, J. A. Sauvaud, A. Cros, J. Dandouras, C. Aoustin, J. Bouyssou, T. Camus, J. Cuvilo, C. Martz, J. L. MÉDALE, H. Perrier, D. Romefort,

J. Rouzaud, C. D'Uston, E. MÖBIUS, K. Crocker, M. Granoff, L. M. Kistler, M. Popecki, D. Hovestadt, B. Klecker, G. Paschmann, M. Scholer, C. W. Carlson, D. W. Curtis, R. P. Lin, J. P. Mcfadden, V. Formisano, E. Amata, M. B. Bavassano-CATTANEO, P. Baldetti, G. Belluci, R. Bruno, G. Chionchio, A. Di Lellis, E. G. Shelley, A. G. Ghielmetti, W. Lennartsson, A. Korth, H. Rosenbauer, R. Lundin, S. Olsen, G. K. Parks, M. Mccarthy, and H. Balsiger (1997), The cluster ion spectrometry (cis) experiment, *Space Science Reviews*, *79*(1), 303–350, doi:10.1023/A:1004929816409.

Rème, H., C. Aoustin, J. M. Bosqued, I. Dandouras, B. Lavraud, J. A. Sauvaud, A. Barthe, J. Bouyssou, T. Camus, O. Coeur-Joly, A. Cros, J. Cuvilo, F. Ducay, Y. Garbarowitz, J. L. Medale, E. Penou, H. Perrier, D. Romefort, J. Rouzaud, C. Vallat, D. Alcaydé, C. Jacquey, C. Mazelle, C. d'Uston, E. Möbius, L. M. Kistler, K. Crocker, M. Granoff, C. Mouikis, M. Popecki, M. Vosbury, B. Klecker, D. Hovestadt, H. Kucharek, E. Kuenneth, G. Paschmann, M. Scholer, N. Sckopke, E. Seidenschwang, C. W. Carlson, D. W. Curtis, C. Ingraham, R. P. Lin, J. P. McFadden, G. K. Parks, T. Phan, V. Formisano, E. Amata, M. B. Bavassano-Cattaneo, P. Baldetti, R. Bruno, G. Chionchio, A. Di Lellis, M. F. Marcucci, G. Pallocchia, A. Korth, P. W. Daly, B. Graeve, H. Rosenbauer, V. Vasyliunas, M. McCarthy, M. Wilber, L. Eliasson, R. Lundin, S. Olsen, E. G. Shelley, S. Fuselier, A. G. Ghielmetti, W. Lennartsson, C. P. Escoubet, H. Balsiger, R. Friedel, J.-B. Cao, R. A. Kovrazhkin, I. Papamastorakis, R. Pellat, J. Scudder, and B. Sonnerup (2001), First multispacecraft ion measurements in and near the earths magnetosphere with the identical cluster ion spectrometry (cis) experiment, *Annales Geophysicae*, *19*(10/12), 1303–1354, doi:10.5194/angeo-19-1303-2001.

Rostoker, G., and T. Eastman (1987a), A boundary layer model for magnetospheric substorms, *Journal of Geophysical Research: Space Physics*, *92*(A11), 12,187–12,201, doi:10.1029/JA092iA11p12187.

Rostoker, G., and T. Eastman (1987b), A boundary layer model for magnetospheric substorms, *Journal of Geophysical Research: Space Physics*, *92*(A11), 12,187–12,201, doi:10.1029/JA092iA11p12187.

Runov, A., V. A. Sergeev, W. Baumjohann, R. Nakamura, S. Apatenkov, Y. Asano, M. Volwerk, Z. Vörös, T. L. Zhang, A. Petrukovich, A. Balogh, J.-A. Sauvaud, B. Klecker, and H. Rème (2005), Electric current and magnetic field geometry in flapping magnetotail current sheets, *Annales Geophysicae*, *23*(4), 1391–1403.

Russell, C. T., and R. L. McPherron (1973), The magnetotail and substorms, *Space Science Reviews*, *15*(2), 205–266, doi:10.1007/BF00169321.

Sauvaud, J. A., A. Saint-Marc, J. Dandouras, H. Rme, A. Korth, G. Kremser, and G. K. Parks (1984), A multisatellite study of the plasma sheet dynamics at substorm onset, *Geophysical Research Letters*, *11*(5), 500–503, doi:10.1029/GL011i005p00500.

Schödel, R., W. Baumjohann, R. Nakamura, V. A. Sergeev, and T. Mukai (2001), Rapid flux transport in the central plasma sheet, *Journal of Geophysical Research: Space Physics*, *106*(A1), 301–313, doi:10.1029/2000JA900139.

Schunk, R., and A. Nagy (2009), *Ionospheres: Physics Plasma Physics, and Chemistry*, Cambridge Atmospheric and Space Science Series, 2 ed., Cambridge University Press, doi:10.1017/CBO9780511635342.

Seki, K., A. Nagy, C. M. Jackman, F. Crary, D. Fontaine, P. Zarka, P. Wurz, A. Milillo, J. A. Slavin, D. C. Delcourt, M. Wiltberger, R. Ilie, X. Jia, S. A. Ledvina, M. W. Liemohn, and R. W. Schunk (2015), A review of general physical and chemical processes related to plasma sources and losses for solar system magnetospheres, *Space Science Reviews*, *192*(1), 27–89, doi:10.1007/s11214-015-0170-y.

Sergeev, V. A., V. Angelopoulos, J. T. Gosling, C. A. Cattell, and C. T. Russell (1996), Detection of localized, plasma-depleted flux tubes or bubbles in the midtail plasma sheet, *Journal of Geophysical Research: Space Physics*, *101*(A5), 10,817–10,826, doi:10.1029/96JA00460.

Sergeev, V. A., V. Angelopoulos, and R. Nakamura (2012), Recent advances in understanding substorm dynamics, *Geophysical Research Letters*, *39*(5), n/a–n/a, doi:10.1029/2012GL050859, l05101.

Shiokawa, K., W. Baumjohann, and G. Haerendel (1997), Braking of high-speed flows in the near-earth tail, *Geophysical Research Letters*, *24*(10), 1179–1182, doi:10.1029/97GL01062.

Shue, J.-H., J. K. Chao, H. C. Fu, C. T. Russell, P. Song, K. K. Khurana, and H. J. Singer (1997), A new functional form to study the solar wind control of the magnetopause size and shape, *Journal of Geophysical Research: Space Physics*, *102*(A5), 9497–9511, doi:10.1029/97JA00196.

Sibeck, D. G., and V. Angelopoulos (2008), Themis science objectives and mission phases, *Space Science Reviews*, *141*(1), 35–59, doi:10.1007/s11214-008-9393-5.

Slavin, J. A., M. F. Smith, E. L. Mazur, D. N. Baker, E. W. Hones, T. Iyemori, and E. W. Greenstadt (1993), Isee 3 observations of traveling compression regions in the earth's magnetotail, *Journal of Geophysical Research: Space Physics*, *98*(A9), 15,425–15,446, doi:10.1029/93JA01467.

Slavin, J. A., R. P. Lepping, J. Gjerloev, D. H. Fairfield, M. Hesse, C. J. Owen, M. B. Moldwin, T. Nagai, A. Ieda, and T. Mukai (2003), Geotail observations of magnetic flux ropes in the plasma sheet, *Journal of Geophysical Research: Space Physics*, *108*(A1), SMP 10–1–SMP 10–18, doi:10.1029/2002JA009557, 1015.

Smith, R. A., C. K. Goertz, and W. Grossman (1986), Thermal catastrophe in the plasma sheet boundary layer, *Geophysical Research Letters*, *13*(13), 1380–1383, doi:10.1029/GL013i013p01380.

Szita, S., A. N. Fazakerley, P. J. Carter, A. M. James, P. Trvnek, G. Watson, M. Andr, A. Eriksson, and K. Torkar (2001), Cluster peace observations of electrons of spacecraft origin, *Ann. Geophys*, p. 1721.

Takahashi, K., L. J. Zanetti, R. E. Lopez, R. W. McEntire, T. A. Potemra, and K. Yumoto (1987), Disruption of the magnetotail current sheet observed by ampte/cce, *Geophysical Research Letters*, *14*(10), 1019–1022, doi:10.1029/GL014i010p01019.

Tascione, T. (1994), *Introduction to the Space Environment*, Intelligence Series, Krieger Pub.

timeanddate.com (1995-2017), Seasons: Meteorological and astronomical.

Vasyliunas, V. M. (1975), Theoretical models of magnetic field line merging, *Reviews of Geophysics*, *13*(1), 303–336, doi:10.1029/RG013i001p00303.

Walsh, A. (2009), New perspectives on magnetotail dynamic processes from combined cluster and double star observations, Ph.D. thesis, University College London.

Walsh, A. P., C. J. Owen, A. N. Fazakerley, C. Forsyth, and I. Dandouras (2011a), Average magnetotail electron and proton pitch angle distributions from cluster peace and cis observations, *Geophysical Research Letters*, *38*(6), doi:10.1029/2011GL046770.

Walsh, A. P., C. J. Owen, A. N. Fazakerley, C. Forsyth, and I. Dandouras (2011b), Average magnetotail electron and proton pitch angle distributions from cluster peace and cis observations, *Geophysical Research Letters*, *38*(6), n/a–n/a, doi:10.1029/2011GL046770, l06103.

Walsh, A. P., A. N. Fazakerley, C. Forsyth, C. J. Owen, M. G. G. T. Taylor, and I. J. Rae (2013a), Sources of electron pitch angle anisotropy in the magnetotail plasmasheet, *Journal of Geophysical Research: Space Physics*, *118*(10), 6042–6054, doi:10.1002/jgra.50553.

Walsh, B. M., D. G. Sibeck, Y. Wang, and D. H. Fairfield (2012), Dawn-dusk asymmetries in the earth's magnetosheath, *Journal of Geophysical Research: Space Physics*, *117*(A12), doi:10.1029/2012JA018240, a12211.

Walsh, B. M., D. G. Sibeck, Y. Nishimura, and V. Angelopoulos (2013b), Statistical analysis of the plasmaspheric plume at the magnetopause, *Journal of Geophysical Research: Space Physics*, *118*(8), 4844–4851, doi:10.1002/jgra.50458.

Walters, G. K. (1964), Effect of oblique interplanetary magnetic field on shape and behavior of the magnetosphere, *Journal of Geophysical Research*, *69*(9), 1769–1783, doi:10.1029/JZ069i009p01769.

Wang, C.-P., L. R. Lyons, J. M. Weygand, T. Nagai, and R. W. McEntire (2006), Equatorial distributions of the plasma sheet ions, their electric and magnetic drifts, and magnetic fields under different interplanetary magnetic field bz conditions, *Journal of Geophysical Research: Space Physics*, *111*(A4), n/a–n/a, doi:10.1029/2005JA011545, a04215.

Wang, C.-P., L. R. Lyons, T. Nagai, J. M. Weygand, and R. W. McEntire (2007), Sources, transport, and distributions of plasma sheet ions and electrons and dependences on interplanetary parameters under northward interplanetary magnetic field, *Journal of Geophysical Research: Space Physics*, *112*(A10), n/a–n/a, doi:10.1029/2007JA012522, a10224.

Wild, J. A. (2000), Electrodynamics of the auroral ionosphere during magnetospheric substorms, Ph.D. thesis, University of Leicester.

Wild, J. A. (2015), Dynamics of earth's magnetosphere: Stfc solar terrestrial physics advanced summer school lecture., Lancaster, Lancashire.

Wiza, J. L. (1979), Microchannel plate detectors, *Nuclear Instruments and Methods*, *162*(1), 587 – 601, doi:http://dx.doi.org/10.1016/0029-554X(79)90734-1.

Woolfson, M. (2000), The origin and evolution of the solar system, *Astronomy and Geophysics*, *41*(1), 1.12–1.19, doi:10.1046/j.1468-4004.2000.00012.x.

Yau, A. W., and M. André (1997), Sources of ion outflow in the high latitude ionosphere, *Space Science Reviews*, *80*(1), 1–25, doi:10.1023/A:1004947203046.

Young, H., R. Freedman, and A. Ford (2012), *University Physics with Modern Physics*, Addison-Wesley.

Zhang, L. Q., J. Y. Wang, W. Baumjohann, H. Rme, and M. W. Dunlop (2015a), Earthward and tailward flows in the plasma sheet, *Journal of Geophysical Research: Space Physics*, *120*(6), 4487–4495, doi:10.1002/2015JA021154.

Zhang, L. Q., W. Baumjohann, J. Y. Wang, H. Rme, M. W. Dunlop, and T. Chen (2015b), Statistical characteristics of slow earthward and tailward flows in the plasma

sheet, *Journal of Geophysical Research: Space Physics*, *120*(8), 6199–6206, doi:10.1002/2015JA021354, 2015JA021354.

Zhang, Q.-H., M. Lockwood, J. C. Foster, S.-R. Zhang, B.-C. Zhang, I. W. McCrea, J. Moen, M. Lester, and J. M. Ruohoniemi (2015c), Direct observations of the full dungey convection cycle in the polar ionosphere for southward interplanetary magnetic field conditions, *Journal of Geophysical Research: Space Physics*, *120*(6), 4519–4530, doi:10.1002/2015JA021172, 2015JA021172.

Zhu, X. (1993), Magnetospheric convection pattern and its implications, *Journal of Geophysical Research: Space Physics*, *98*(A12), 21,291–21,296, doi:10.1029/93JA01950.